

Energy efficiency optimization in large-scale multichannel electrical neuromodulation

Varkevisser, F.

DOI

[10.4233/uuid:58fa34ea-fb7f-445e-ad08-78cd7325b9c5](https://doi.org/10.4233/uuid:58fa34ea-fb7f-445e-ad08-78cd7325b9c5)

Publication date

2025

Document Version

Final published version

Citation (APA)

Varkevisser, F. (2025). *Energy efficiency optimization in large-scale multichannel electrical neuromodulation*. [Dissertation (TU Delft), Delft University of Technology].
<https://doi.org/10.4233/uuid:58fa34ea-fb7f-445e-ad08-78cd7325b9c5>

Important note

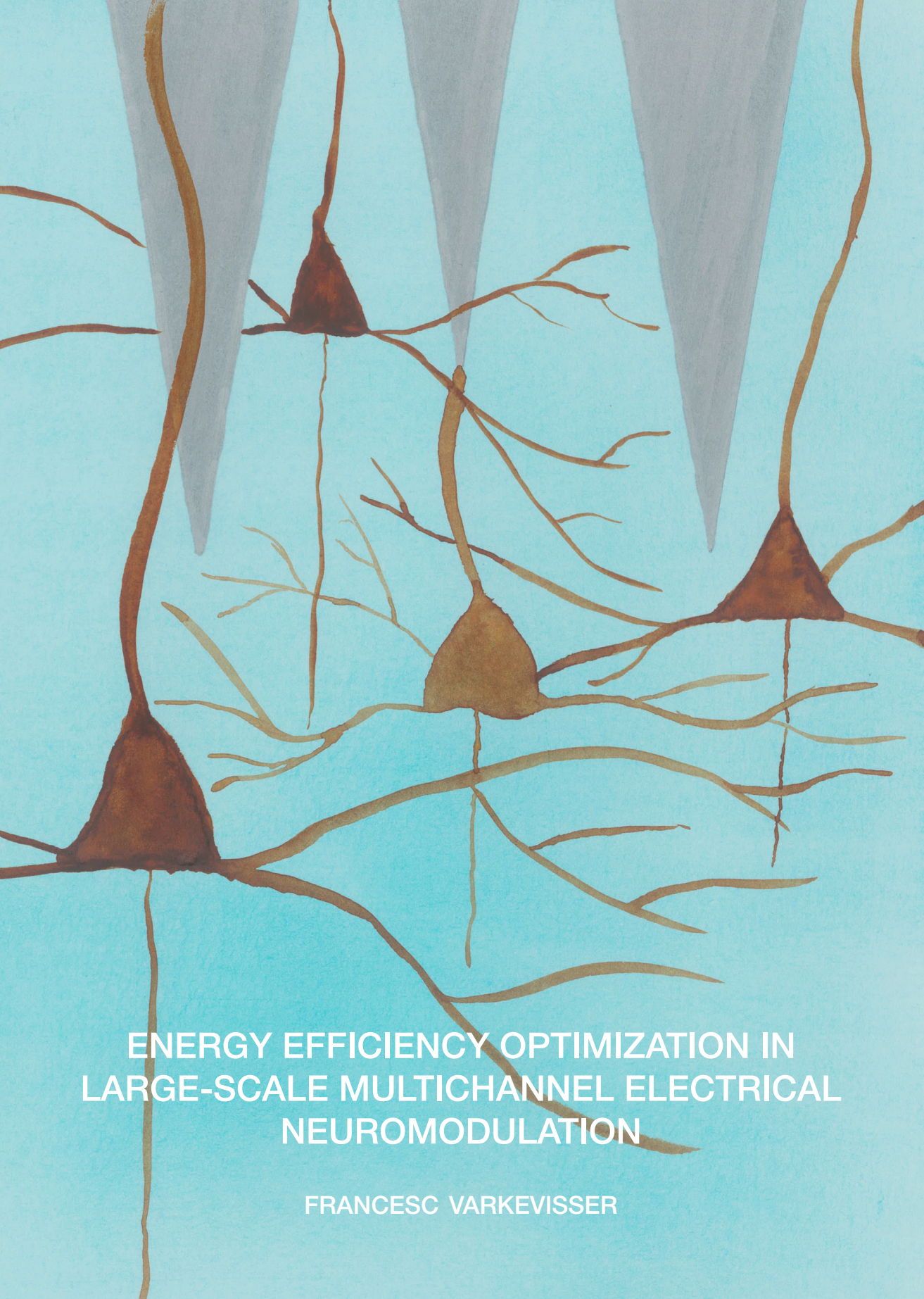
To cite this publication, please use the final published version (if applicable).
Please check the document version above.

Copyright

Other than for strictly personal use, it is not permitted to download, forward or distribute the text or part of it, without the consent of the author(s) and/or copyright holder(s), unless the work is under an open content license such as Creative Commons.

Takedown policy

Please contact us and provide details if you believe this document breaches copyrights.
We will remove access to the work immediately and investigate your claim.



ENERGY EFFICIENCY OPTIMIZATION IN
LARGE-SCALE MULTICHANNEL ELECTRICAL
NEUROMODULATION

FRANCESC VARKEVISSER

ENERGY EFFICIENCY OPTIMIZATION IN LARGE-SCALE MULTICHANNEL ELECTRICAL NEUROMODULATION

ENERGY EFFICIENCY OPTIMIZATION IN LARGE-SCALE MULTICHANNEL ELECTRICAL NEUROMODULATION

Dissertation

for the purpose of obtaining the degree of doctor
at Delft University of Technology
by the authority of the Rector Magnificus prof. dr. ir. T.H.J.J. van der Hagen
chair of the Board for Doctorates to be defended publicly on
Thursday 25 September 2025 at 17:30 o'clock.

by

Francesc VARKEVISSER

Master of Science in Electrical Engineering,
Delft University of Technology, The Netherlands,
born in Leiden, The Netherlands.

This dissertation has been approved by the promotor.

Composition of the doctoral committee:

Rector Magnificus	chairperson
Prof. dr. ir. W.A. Serdijn	Delft University of Technology, promotor
Dr. T.M. Lopes Marta da Costa	Delft University of Technology, copromotor

Independent members:

Prof. dr. P.J. French	Delft University of Technology
Prof. dr. ir. J.H.M. Frijns	Delft University of Technology and Leiden University, The Netherlands
Prof. dr. T.G. Constandinou	Imperial College London, United Kingdom
Prof. dr. P. Degenaar	Newcastle University, United Kingdom
Dr. S. Ghoreishizadeh	University College London, United Kingdom



Keywords: Electrical Neuromodulation, Energy Efficiency, ASIC, Pulse Shaping, Power Management, Voltage Regulation, Multichannel Stimulation

Printed by: Proefschriftspecialist

Artwork: Watercolor of cortical neurons and electrodes on cover and chapter title pages by F. Varkevisser

Copyright © 2025 by F. Varkevisser

ISBN 978-94-6518-118-9

An electronic version of this dissertation is available at
<http://repository.tudelft.nl/>.

*Het komt een soort van goed.
Niet perfect, maar goed genoeg.*

— Spinvis

CONTENTS

Summary	xi
Samenvatting	xiii
1 Introduction	1
1.1 Motivation	2
1.2 Aim of this work.	3
1.3 Thesis organization	4
2 Theoretical background	11
2.1 Principles of electrical stimulation	12
2.1.1 Neurophysiology of electrical stimulation	12
2.1.2 Methods and targets of electrical stimulation	14
2.1.3 Stimulation modes.	15
2.1.4 Stimulation waveform characteristics	16
2.1.5 Electrode configurations.	18
2.1.6 System-level design of neural interfaces	19
2.1.7 Typical stimulation parameters	20
2.2 Modeling of electrical stimulation	21
2.2.1 Modeling neuronal dynamics	22
2.2.2 Modeling electric fields and activation patterns	24
2.2.3 Modeling the electrode-tissue interface (ETI)	25
2.3 Discussion	27
3 State-of-the-art	35
3.1 Energy-efficient stimulation pulses	36
3.1.1 Pulse-shape optimization	36
3.1.2 Validation of non-rectangular pulses.	37
3.1.3 System implementations for non-rectangular pulses	40
3.2 Power management in implantable stimulators.	42
3.2.1 Wireless power delivery	43
3.2.2 Rectifier design	45
3.2.3 Voltage regulation	47
3.2.4 Regulating rectifiers	49
3.2.5 Power management strategies in multichannel stimulator systems	50
3.3 Design of multichannel stimulation systems	51
3.4 Discussion and research questions	53

4	Energy efficiency of pulse shaping in electrical stimulation	73
4.1	Introduction	74
4.2	Methods	76
4.2.1	Stimulation waveforms	76
4.2.2	Neuron models	76
4.2.3	Shape comparisons	79
4.2.4	Dynamic voltage scaling	80
4.2.5	Capacitive effects of electrode-tissue interface	80
4.3	Results	81
4.3.1	Single-axon fiber model	81
4.3.2	Biophysically realistic models	83
4.3.3	Dynamic voltage scaling	83
4.3.4	Effect of capacitive ETI	84
4.3.5	Generalization of results	86
4.4	Discussion	87
4.5	Conclusion	88
5	Power losses in multichannel electrical stimulation systems	93
5.1	Introduction	94
5.2	Methods	95
5.2.1	Data collection and extraction	95
5.2.2	Data analysis	99
5.2.3	Calculating power losses	100
5.3	Results	102
5.3.1	Voltage and load power distributions	102
5.3.2	Power losses for a fixed voltage supply	103
5.3.3	Power losses for global supply scaling	104
5.3.4	Power losses for a stepped supply	105
5.3.5	Comparison of scaling strategies	106
5.3.6	Effect of channel yield	108
5.4	Discussion	109
5.4.1	Circuit design considerations	109
5.4.2	Temporal changes	110
5.4.3	Limitations of current work	110
5.5	Conclusion	111
6	Autonomous output supply scaling for multichannel stimulation	117
6.1	Introduction	118
6.2	System architecture	121
6.3	Circuit design	123
6.3.1	Phase controller	124
6.3.2	Error amplifier	125
6.3.3	Voltage-controlled delay line	125
6.3.4	Comparator	126
6.3.5	Rectifier switch driver	127
6.3.6	Design of the feedback loop	127

6.4	System validation	130
6.4.1	Output pulses	130
6.4.2	Varying output conditions	132
6.4.3	Power efficiency	132
6.4.4	Efficiency in multichannel applications	134
6.4.5	Time division multiplexing.	135
6.4.6	In vitro measurements	136
6.4.7	Performance comparison with previous work	137
6.5	Discussion	140
6.6	Conclusion	141
7	Conclusions and recommendations	149
7.1	Efficiency improvements of pulse shaping	150
7.1.1	Summary of scientific contributions	150
7.1.2	Detailed conclusions.	150
7.2	Impact of channel variability on power efficiency.	151
7.2.1	Summary of scientific contributions	151
7.2.2	Detailed conclusions.	151
7.3	Power distribution in multichannel stimulator systems.	152
7.3.1	Summary of scientific contributions	152
7.3.2	Detailed conclusions.	152
7.4	Discussion	152
7.5	Recommendations for future work	153
7.6	Outlook	155
	Acknowledgements	157
	Curriculum vitae	163
	List of publications	165

SUMMARY

Electrical neuromodulation is an evolving therapeutic approach used to treat neurological conditions such as Parkinson's disease, epilepsy, and vision loss. Early systems, such as cardiac pacemakers and deep brain stimulators, typically utilized low-channel-count stimulation. Recent technological progress has enabled large-scale multichannel systems supporting hundreds or thousands of electrodes.

As channel counts increase, power consumption becomes a critical constraint for the scalability of implantable neurostimulators. While small systems often rely on implanted batteries, the substantial power demands of large-scale systems make battery-powered operation impractical. Wireless power transfer (e.g. inductive coupling) offers an alternative, but is fundamentally limited in the amount of power that can be safely delivered. Consequently, optimizing energy efficiency in large-scale multichannel neurostimulators is essential for maximizing channel count within the available power budget.

While prior studies evaluated pulse shaping mainly from a neurophysiological perspective, this thesis is the first to systematically analyze the relationship between pulse shape, physiological effectiveness, and circuit-level power consumption to identify optimal stimulation strategies. The results challenge existing perspectives by demonstrating that rectangular pulses lead to fewer circuit-level losses, making them competitive compared to non-rectangular alternatives. Although non-rectangular pulses can reduce neural activation thresholds, when circuit losses are included, they require 14 % to 51 % more energy than rectangular pulses. This suggests that rectangular pulses may be preferable for practical neurostimulator implementations.

A second contribution is the introduction of a quantitative framework to capture the impact of channel-to-channel variability on power efficiency. Due to inherent variations in electrode impedance and required stimulation amplitudes, individual channels have different power requirements. Conventional power management techniques often neglect this variability, resulting in low energy efficiency. Although several strategies have been proposed to enhance efficiency, a quantification of their efficacy is lacking in the literature. This thesis introduces a systematic methodology to analyze power losses in multichannel neurostimulation systems, enabling consistent benchmarking of existing strategies and providing a foundation for new application-specific approaches. Applying this methodology to previously published experimental data demonstrates that the effectiveness of power management strategies varies across applications, underscoring the necessity for application-specific optimization.

Building on these insights, the thesis proposes an advanced power-management approach designed specifically for the varying power needs of individual stimulation channels. This strategy incorporates a channel-specific regulating rectifier optimized for current-mode stimulation, capable of dynamically adjusting its output voltage without compliance monitoring. The rectifier quickly adapts to changing load conditions, enabling efficient time-division multiplexing and improved scalability in multichannel

neurostimulation systems. It achieves a median efficiency of 84 % on a dataset of intracortical visual stimulation, representing a 74 % improvement over conventional fixed supplies and 6 % compared to an 8-rail stepped supply.

In conclusion, this thesis offers critical insights into enhancing energy efficiency in multichannel electrical stimulation, contributing to advancing next-generation large-scale neurostimulator technologies. A key observation is the interdependence of multiple system-level factors, emphasizing the importance of a holistic optimization approach. Additionally, the findings highlight that optimal pulse width for minimizing activation energy varies significantly with pulse shape, underscoring the necessity of co-optimizing stimulation parameters for both physiological effectiveness and energy efficiency. The methods developed provide new perspectives on energy-efficient stimulator designs, and the proposed power-management approach shows promising results for efficient channel-specific voltage regulation and reduced output losses.

SAMENVATTING

Elektrische neuromodulatie is een opkomende therapeutische aanpak ter behandeling van neurologische aandoeningen zoals de ziekte van Parkinson, epilepsie en visusverlies. Vroege neuromodulatiesystemen, waaronder hartpacemakers en systemen voor diepe hersenstimulatie, maken doorgaans gebruik van stimulatie via een beperkt aantal kanalen. Recente technologische ontwikkelingen maken echter grootschalige multikanaalsystemen mogelijk, die honderden tot duizenden elektrodes kunnen stimuleren.

Met het toenemende aantal stimulatiekanalen vormt het energieverbruik een kritische belemmering voor de schaalbaarheid van implanteerbare neurostimulatoren. Hoewel kleinschalige systemen vaak werken op batterijvoeding, maakt de hoge energiebehoefte van multikanaalsystemen dit onpraktisch. Draadloze vermogensoverdrachtstechnieken, zoals inductieve koppeling, bieden hiervoor een alternatief door geïmplanteerde batterijen overbodig te maken. Deze techniek wordt echter beperkt door verschillende veiligheidsnormen. Daarom is optimalisatie van energie-efficiëntie essentieel om zoveel mogelijk kanalen te kunnen stimuleren binnen het beschikbare vermogensbudget. Dit proefschrift draagt bij aan dit doel door zich te richten op de efficiëntie van stimulatiepulsen en de vermogensverdeling in multikanaalsystemen.

Waar eerdere studies pulsvormgeving voornamelijk vanuit een neurofysiologisch perspectief hebben onderzocht, analyseert dit proefschrift voor het eerst systematisch de relatie tussen pulsvorm, fysiologische effectiviteit en energieverbruik op circuitniveau om optimale stimulatiestrategieën te identificeren. De resultaten dagen bestaande perspectieven uit door aan te tonen dat rechthoekige pulsen leiden tot minder verliezen op circuitniveau, waardoor zij concurrerend zijn ten opzichte van niet-rechthoekige alternatieven. Hoewel niet-rechthoekige pulsen de neurale activatiedrempel kunnen verlagen, leiden zij tot een toename van 14 tot 51 % in de benodigde energie ten opzichte van rechthoekige pulsen als circuitverliezen worden meegenomen. Dit suggereert dat rechthoekige pulsen de voorkeur verdienen voor praktische toepassingen van neurostimulatoren.

Een tweede bijdrage is de introductie van een systematische methode om de impact van kanaal-tot-kanaal variabiliteit op energie-efficiëntie te beschrijven. Door inherente verschillen in elektrode-impedantie en benodigde stimulatie-amplitudes hebben individuele kanalen uiteenlopende energiebehoeften. Conventionele vermogensbeheerstrategieën negeren deze variabiliteit vaak, wat leidt tot lage efficiëntie. Hoewel verschillende strategieën zijn voorgesteld om de efficiëntie te verbeteren, ontbreekt in de literatuur een systematische kwantificatie van hun effectiviteit. Dit proefschrift introduceert een methodologie om energieverliezen in multikanaalsystemen te analyseren, wat een kader biedt om bestaande strategieën te beoordelen en nieuwe strategieën te vergelijken. Toepassing van deze methode op eerder gepubliceerde experimentele data toont aan dat de effectiviteit van energiebeheer sterk applicatie-afhankelijk is, wat het belang van applicatiespecifieke optimalisatie benadrukt.

Voortbouwend op deze inzichten introduceert dit proefschrift een geavanceerde energiebeheerstrategie, die specifiek is ontworpen om rekening te houden met de variërende energiebehoeften per kanaal. Deze strategie maakt gebruik van kanaalspecifieke regulerende gelijkrichters, geoptimaliseerd voor stroomgestuurde elektrische stimulatie. De gelijkrichters passen de uitgangsspanning dynamisch aan op basis van veranderende belastingscondities, wat efficiënte time-division multiplexing mogelijk maakt en daarmee de schaalbaarheid van multikanaalsystemen bevordert. Hij behaalt een efficiëntie van 84 % op een dataset van intracorticale visuele stimulatie, wat een verbetering van 74 % betekent ten opzichte van conventionele vaste voedingen en 6 % ten opzichte van een voeding met 8 stappen.

Samenvattend biedt dit proefschrift nieuwe inzichten in het verbeteren van de energie-efficiëntie van multikanaals elektrische stimulatie, en levert het een bijdrage aan de ontwikkeling van de volgende generatie grootschalige neurostimulatoren. Een belangrijke observatie is de onderlinge afhankelijkheid van meerdere systeemfactoren, wat het belang benadrukt van een holistische optimalisatiebenadering. Bovendien tonen de resultaten aan dat de optimale pulsbreedte voor het minimaliseren van activatie-energie sterk varieert met de pulsvorm, wat de noodzaak onderstreept om stimulatieparameters zowel voor fysiologische effectiviteit als voor energie-efficiëntie gezamenlijk te optimaliseren. De ontwikkelde methoden bieden nieuwe perspectieven op energiezuinige stimulatorontwerpen, en de voorgestelde vermogensbeheerstrategie laat veelbelovende resultaten zien voor efficiënte kanaalspecifieke spanningsregeling en verminderde uitgangsverliezen.



1

INTRODUCTION

It's not what you look at that matters, it's what you see.

— Thoreau

1.1. MOTIVATION

ELECTRICAL neuromodulation is an increasingly important therapeutic approach with the potential to address a wide range of medical conditions, from neurological disorders like Parkinson's disease and epilepsy to sensory impairments such as hearing and vision loss [1–5]. The fundamental principle involves delivering controlled electrical pulses to neural tissue to modulate its activity, providing relief from symptoms or restoring lost sensory functions. For chronic treatments, implantable stimulator devices are preferred over non-invasive methods due to several advantages, such as improved targeting precision and more consistent stimulation over time. However, implantable devices introduce additional design challenges related to power efficiency [6–8], safety [8–10], and long-term reliability [11, 12]. A central requirement of any implantable stimulator is to generate pulses that are both effective in activating neurons and safe for the electrodes and tissue. This typically requires biphasic stimulation to prevent net charge build-up and electrode degradation, as well as flexibility in pulse parameters to improve stimulation efficiency and optimize the neural response [9, 10].

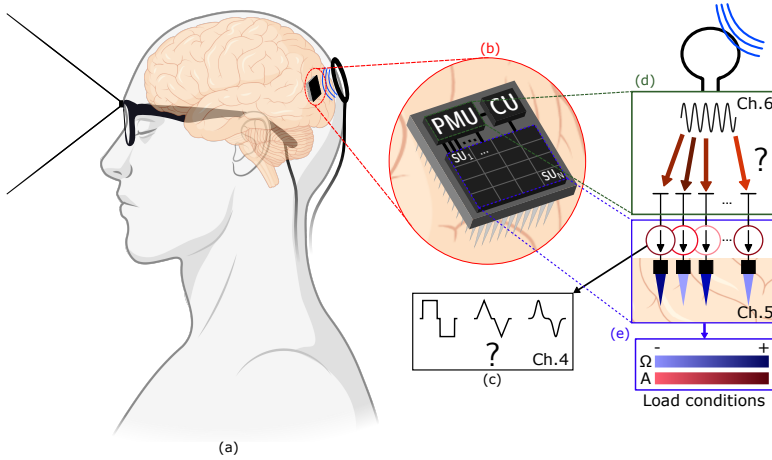


Figure 1.1: Illustration of an intracortical visual implant with challenges in energy efficiency of large-scale multichannel stimulator systems. (a) The patient's environment is captured by a camera worn on glasses, the information is processed and wirelessly sent to a device implanted in the visual cortex of the patient. (b) System-level overview of the stimulator, containing a power management unit (PMU), control unit (CU) and N stimulation units (SU_1-N). The system could contain more components, not depicted in this figure. (c) Depicting different pulse shapes that can be used to optimize the stimulation efficiency. (d) PMU, the power is wirelessly transferred to the implanted device. (e) SUs, depicting the inter-channel variation in current amplitude (A) and electrode impedance (Ω).

Early applications, such as cardiac pacemakers and deep brain stimulation, primarily use single channel or low-channel-count stimulation. A stimulation channel encompasses all components required to deliver controlled electrical stimulation to a specific site, including one or more electrodes, the electronic circuits to produce the stimulation signals, and the connections between them. Recent advancements in integrated circuit technology, microfabrication techniques, and electrode miniaturization have facilitated

the development of large-scale multichannel systems with hundreds or even thousands of electrodes. These advancements have opened the door for emerging applications, including cortical visual prostheses designed to restore vision to profoundly blind individuals by electrically stimulating the visual cortex, illustrated in Fig. 1.1 [13–15]. In this application, the surrounding environment of the patient is captured by a camera worn on glasses. The captured data is processed and transmitted wirelessly to a stimulator implanted in the patient's visual cortex. By sending electrical pulses to the electrodes, artificial perceptions of light known as phosphenes are elicited, with the goal of reconstructing meaningful visual patterns and improving users' quality of life [15–17].

Expanding the capabilities and effectiveness of cortical visual prostheses—and other large-scale applications—depends largely on increasing the number of available stimulation channels [14]. With only a small number of channels, visual information remains rudimentary and lacks the detail necessary for practical everyday use [14, 18]. Studies estimated that at least 625 phosphenes are required to enable meaningful visual perception for activities such as reading or navigating an environment [18, 19], and future visual prostheses are expected to have more than a thousand channels [6, 19]. However, scaling up to this level introduces substantial engineering and design challenges, particularly related to device power management and efficiency.

Power consumption is a major constraint for large-scale implantable neurostimulators [6, 14, 19]. While conventional systems with fewer electrodes can be powered by implanted batteries, increasing channel counts lead to substantial power demands that make battery operation impractical. For example, commercial vagus nerve stimulators (VNS) with a non-rechargeable battery and a single stimulation channel achieve lifetimes of 2–8 years [20]; scaling to 100 channels with similar parameters would reduce this to less than a month. To overcome this challenge, wireless power transfer (WPT), particularly inductive coupling, has been explored as a way to reduce device size and enable continuous operation in certain applications, such as visual prostheses [21]. Safety-critical devices like cardiac pacemakers, however, continue to rely on implanted batteries to ensure reliability. Regulatory and safety constraints, including limits on tissue heating and electromagnetic exposure, restrict the power that can be safely delivered wirelessly [6, 22–24]. Consequently, optimizing energy efficiency in large-scale multichannel neurostimulators is essential to maximize the number of channels that can operate within the available power budget.

For clinical translation, neurostimulators must also comply with safety and regulatory standards such as ISO 14708-3 [25], which define limits on charge density, leakage currents, thermal rise, and fault tolerance. Energy efficiency directly supports these requirements: reducing power consumption lowers thermal rise, efficient charge delivery minimizes residual currents, and precise control helps maintain safe charge densities. Thus, improving efficiency not only extends device lifetime but also facilitates compliance with safety standards and enhances clinical viability.

1.2. AIM OF THIS WORK

As the number of stimulation channels increases in large-scale neurostimulators, the cumulative power consumed by these channels becomes a dominant factor in overall device power usage. Figure 1.2 depicts the energy flow in an implantable stimulator circuit

from the power source to the final delivery of stimulation pulses at the neural interface [26]. Optimizing energy efficiency in neurostimulation requires a comprehensive approach that accounts for all stages involved, from circuit-level considerations to physiological responses. In this context, energy efficiency is defined as the energy required at the system's input to achieve a desired physiological outcome in the tissue. The challenges addressed in this thesis are also illustrated in Fig. 1.1.

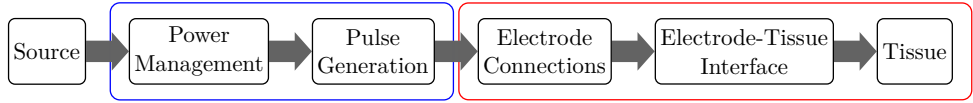


Figure 1.2: Energy flow diagram in an electrical stimulation system [26]. The first part of this thesis focuses on optimizing the energy in the red box using pulse shaping and pulse delivery. The second part of this thesis considers energy optimization in the blue box by focusing on multichannel power management and pulse generation.

This thesis aims to advance the design of large-scale implantable neurostimulators by addressing two key aspects of energy efficiency, represented by the colored boxes in Figure 1.2: stimulation-pulse efficiency (red box) and power management in multichannel systems (blue box). The first aspect examines how stimulation pulse shapes affect energy efficiency (Fig. 1.1(c)). Traditional neurostimulation uses rectangular pulses due to their simplicity. However, research suggests that alternative pulse shapes may reduce the energy required for neural activation [27–29]. While previous studies have explored pulse shaping from a biophysical perspective, the impact on power losses within the stimulator circuit remains largely unexamined. This thesis systematically examines the interplay between pulse shapes, physiological effectiveness, and circuit-level power consumption to identify optimal stimulation strategies.

The second aspect addresses the distribution of power across multiple stimulation channels (Figure 1.1(d)). Due to inherent differences in electrode impedance and stimulation amplitude requirements (Figure 1.1(e)), each channel demands a different amount of power [30–32]. Conventional power-management methods typically do not compensate for this variability, leading to inefficiencies and unnecessary energy losses. Although several methods have been proposed to improve the efficiency, their effectiveness has yet to be fully quantified. This thesis provides a methodology to analyze the power losses in multichannel neurostimulation systems, and proposes an advanced power-management approach specifically tailored to the channel-specific power demands.

1.3. THESIS ORGANIZATION

This thesis is structured into seven chapters, starting with a literature review in Chapters 2 and 3, followed by the three main Chapters 4, 5 and 6, each addressing one of the challenges outlined in the previous section. The work concludes with a summary of findings and recommendations for future research in Chapter 7.

Chapter 2 serves as a theoretical background focusing on the principles of electrical stimulation, covering neurophysiological mechanisms, stimulation methods, waveform characteristics, electrode configurations, and system-level design considerations. Furthermore, modeling of electrical stimulation for different purposes is introduced.

Chapter 3 presents a comprehensive state-of-the-art analysis of the topics relevant to this thesis. The first part focuses on energy-efficient stimulation pulses, discussing pulse shape optimization and the validation and circuit implementations for non-rectangular pulses. The second part covers power management in implantable stimulators, starting with a review of wireless power transfer modalities, followed by the circuit design of rectifiers, voltage regulators, and regulating rectifier implementations. Next, the different power-management strategies in multichannel stimulator systems are discussed. The chapter ends with an analysis of recent multichannel stimulator implementations, highlighting trends and comparing key specifications regarding current-mode stimulation and power management.

Chapter 4 investigates the impact of pulse shaping on the energy efficiency of neural activation in electrical stimulation. Building upon previous studies that explored non-rectangular pulses as a means to enhance efficiency, this chapter extends the analysis to include both biophysical considerations and energy losses associated with the stimulator circuits. The goal is to identify pulse shapes that provide effective neural stimulation while reducing overall power consumption.

Chapter 5 addresses the influence of inter-channel variability on power requirements in multichannel stimulation devices. A methodology to quantify power losses in multichannel stimulation devices is presented. Utilizing previously published experimental data across various stimulation applications, the efficacy various power-management strategies is evaluated.

Chapter 6 introduces a novel approach to efficiently deliver electrical charge to stimulation channels with varying load requirements. It presents a channel-specific regulating rectifier designed for current-mode stimulation, capable of dynamically adjusting its output voltage without compliance monitoring. The proposed rectifier features rapid adaptation to load condition changes, enabling efficient time-division multiplexing and enhanced scalability for multichannel neurostimulation systems.

Finally, Chapter 7 summarizes the main findings, discusses their implications for future neurostimulation systems, and provides recommendations for further research in the field of large-scale multichannel stimulation.

BIBLIOGRAPHY

- [1] R. L. Johnson and C. G. Wilson, “A review of vagus nerve stimulation as a therapeutic intervention”, *Journal of Inflammation Research*, vol. Volume 11, pp. 203–213, May 2018, ISSN: 1178-7031. DOI: 10.2147/JIR.S163248.
- [2] J. Y. Fang and C. Tolleson, *The role of deep brain stimulation in parkinson's disease: An overview and update on new developments*, Mar. 2017. DOI: 10.2147/NDT.S113998.
- [3] J. Li, X. Liu, W. Mao, T. Chen, and H. Yu, “Advances in Neural Recording and Stimulation Integrated Circuits”, *Frontiers in Neuroscience*, vol. 15, Aug. 2021, ISSN: 1662-453X. DOI: 10.3389/fnins.2021.663204.
- [4] T. L. Skarpaas and M. J. Morrell, “Intracranial Stimulation Therapy for Epilepsy”, *Neurotherapeutics*, vol. 6, no. 2, pp. 238–243, Apr. 2009, ISSN: 18787479. DOI: 10.1016/j.nurt.2009.01.022.
- [5] B. S. Wilson and M. F. Dorman, *A Brief History of the Cochlear Implant and Related Treatments*, Second Edi. Elsevier Ltd, 2018, pp. 1197–1207, ISBN: 9780128053539. DOI: 10.1016/b978-0-12-805353-9.00099-1.
- [6] A. Nurmikko, *Challenges for Large-Scale Cortical Interfaces*, 2020. DOI: 10.1016/j.neuron.2020.10.015.
- [7] R. Guan, P. G. Zufria, V. Giagka, and W. A. Serdijn, “Circuit Design Considerations for Power-Efficient and Safe Implantable Electrical Neurostimulators”, *2020 IEEE 11th Latin American Symposium on Circuits and Systems, LASCAS 2020*, pp. 7–10, 2020. DOI: 10.1109/LASCAS45839.2020.9068975.
- [8] Y. Liu *et al.*, “Bidirectional Bioelectronic Interfaces”, *IEEE solid state circuits magazine*, vol. 12, no. 2, pp. 30–46, 2020.
- [9] D. R. Merrill, M. Bikson, and J. G. Jefferys, “Electrical stimulation of excitable tissue: design of efficacious and safe protocols”, *Journal of Neuroscience Methods*, vol. 141, no. 2, pp. 171–198, Feb. 2005, ISSN: 01650270. DOI: 10.1016/j.jneumeth.2004.10.020.
- [10] S. F. Cogan, K. A. Ludwig, C. G. Welle, and P. Takmakov, “Tissue damage thresholds during therapeutic electrical stimulation”, *Journal of Neural Engineering*, vol. 13, no. 2, p. 021001, Apr. 2016, ISSN: 1741-2560. DOI: 10.1088/1741-2560/13/2/021001.
- [11] K. Nanbakhsh *et al.*, “On the longevity and inherent hermeticity of silicon-ICs: evaluation of bare-die and PDMS-coated ICs after accelerated aging and implantation studies”, *Nature Communications*, vol. 16, no. 1, Dec. 2025, ISSN: 20411723. DOI: 10.1038/s41467-024-55298-4.

- [12] H. S. Sohal, K. Vassilevski, A. Jackson, S. N. Baker, and A. O'Neill, "Design and Microfabrication Considerations for Reliable Flexible Intracortical Implants", *Frontiers in Mechanical Engineering*, vol. 2, Jun. 2016, ISSN: 22973079. DOI: 10.3389/fmech.2016.00005.
- [13] A. Najarpour Foroushani, C. C. Pack, and M. Sawan, "Cortical visual prostheses: From microstimulation to functional percept", *Journal of Neural Engineering*, vol. 15, no. 2, p. 021 005, Apr. 2018, ISSN: 17412552. DOI: 10.1088/1741-2552/aaa904.
- [14] E. Fernández, A. Alfaro, and P. González-López, "Toward Long-Term Communication With the Brain in the Blind by Intracortical Stimulation: Challenges and Future Prospects", *Frontiers in Neuroscience*, vol. 14, no. August, Aug. 2020, ISSN: 1662-453X. DOI: 10.3389/fnins.2020.00681.
- [15] E. Fernandez and R. Normann, *Introduction to Visual Prostheses*. Salt Lake City (UT): University of Utah Health, 2016.
- [16] X. Chen, F. Wang, E. Fernandez, and P. R. Roelfsema, "Shape perception via a high-channel-count neuroprosthesis in monkey visual cortex", *Science*, vol. 370, no. 6521, pp. 1191–1196, 2020, ISSN: 10959203. DOI: 10.1126/science.abd7435.
- [17] E. Fernández *et al.*, "Visual percepts evoked with an intracortical 96-channel microelectrode array inserted in human occipital cortex", *Journal of Clinical Investigation*, vol. 131, no. 23, Dec. 2021, ISSN: 1558-8238. DOI: 10.1172/JCI151331.
- [18] K. Cha, K. W. Horch, and R. A. Normann, "Mobility performance with a pixelized vision system", *Vision Research*, vol. 32, no. 7, pp. 1367–1372, Jul. 1992, ISSN: 00426989. DOI: 10.1016/0042-6989(92)90229-C.
- [19] J. Weiland and M. Humayun, "Visual Prosthesis", *Proceedings of the IEEE*, vol. 96, no. 7, pp. 1076–1084, Jul. 2008, ISSN: 0018-9219. DOI: 10.1109/JPROC.2008.922589.
- [20] H. D. Simpson *et al.*, *Practical considerations in epilepsy neurostimulation*, Oct. 2022. DOI: 10.1111/epi.17329.
- [21] S. R. Khan, S. K. Pavuluri, G. Cummins, and M. P. Desmulliez, *Wireless power transfer techniques for implantable medical devices: A review*, Jun. 2020. DOI: 10.3390/s20123487.
- [22] T. P. G. van Nunen, R. M. C. Mestrom, and H. J. Visser, "Wireless Power Transfer to Biomedical Implants Using a Class-E Inverter and a Class-DE Rectifier", *IEEE Journal of Electromagnetics, RF and Microwaves in Medicine and Biology*, vol. 7, no. 3, pp. 202–209, Sep. 2023, ISSN: 2469-7249. DOI: 10.1109/JERM.2023.3267042.
- [23] M. Mariello and C. M. Proctor, "Wireless Power and Data Transfer Technologies for Flexible Bionic and Bioelectronic Interfaces: Materials and Applications", *Advanced Materials Technologies*, Sep. 2024, ISSN: 2365-709X. DOI: 10.1002/admt.202400797.
- [24] M. Kiani, "Wireless Power Transfer and Management for Medical Applications: Wireless power", *IEEE Solid-State Circuits Magazine*, vol. 14, no. 3, pp. 41–52, 2022, ISSN: 1943-0582. DOI: 10.1109/MSSC.2022.3178671.

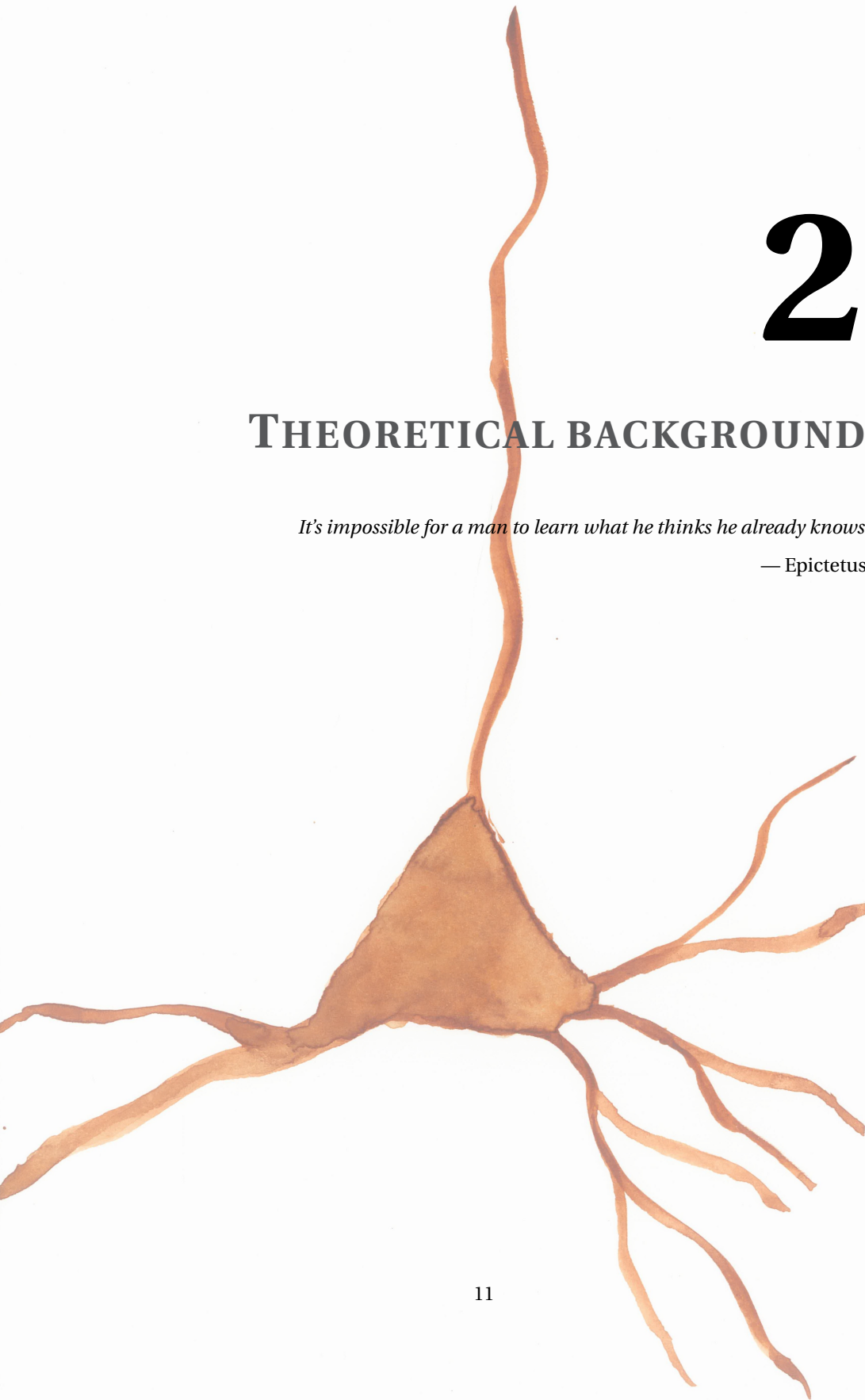
- [25] International Organization for Standardization, “ISO 14708-3:2017: Implants for surgery — Active implantable medical devices — Part 3: Implantable neurostimulators”, International Organization for Standardization, Geneva, Switzerland, Tech. Rep. ISO 14708-3:2017, 2017, Safety and performance requirements for implantable neurostimulators.
- [26] T. Cameron, B. Tranchina, and J. Erickson, “Power”, in *Essential Neuromodulation*, 2011, pp. 253–267, ISBN: 9780123814098. DOI: 10.1016/B978-0-12-381409-8.00011-5.
- [27] A. Wongsarnpigoon and W. M. Grill, “Energy-efficient waveform shapes for neural stimulation revealed with a genetic algorithm”, *Journal of Neural Engineering*, vol. 7, no. 4, p. 046009, Aug. 2010, ISSN: 1741-2560. DOI: 10.1088/1741-2560/7/4/046009.
- [28] T. J. Foutz, D. M. Ackermann Jr., K. L. Kilgore, and C. C. McIntyre, “Energy Efficient Neural Stimulation: Coupling Circuit Design and Membrane Biophysics”, *PLoS ONE*, vol. 7, no. 12, G. Foffani, Ed., e51901, Dec. 2012, ISSN: 1932-6203. DOI: 10.1371/journal.pone.0051901.
- [29] W. M. Grill, “Model-based analysis and design of waveforms for efficient neural stimulation”, *Progress in Brain Research*, vol. 222, pp. 147–162, 2015, ISSN: 18757855. DOI: 10.1016/bs.pbr.2015.07.031.
- [30] T. S. Davis *et al.*, “Spatial and temporal characteristics of V1 microstimulation during chronic implantation of a microelectrode array in a behaving macaque”, *Journal of Neural Engineering*, vol. 9, no. 6, p. 065003, Dec. 2012, ISSN: 1741-2560. DOI: 10.1088/1741-2560/9/6/065003.
- [31] E. Noorsal, H. Xu, K. Sooksood, and M. Ortmanns, “Multichannel Microstimulating SoC”, in *Handbook of Biochips*, New York, NY: Springer New York, 2022, pp. 1285–1316. DOI: 10.1007/978-1-4614-3447-4_18.
- [32] W. Ahn, K.-H. Nguyen, H. Lee, K. S. Min, S. Ha, and M. Je, “An Energy-Efficient Stimulation System Based on Adaptive Dynamic Voltage Switching Control for Cochlear Implants”, *IEEE Transactions on Biomedical Circuits and Systems*, pp. 1–12, 2024, ISSN: 1932-4545. DOI: 10.1109/TBCAS.2024.3497585.

2

THEORETICAL BACKGROUND

It's impossible for a man to learn what he thinks he already knows.

— Epictetus



THIS chapter provides a theoretical background of neural interfaces and electrical neuromodulation, covering, in the first part, the fundamental principles of electrical stimulation, including the relevant aspects of neurophysiology, stimulation techniques, and electronic system design, and in the second part, modeling strategies for predicting and optimizing neural responses.

The chapter begins with an overview of the principles of electrical stimulation in Section 2.1, which introduces the fundamental neurophysiology of excitable tissues. Section 2.1.1 explains the structure and function of neurons, including their electrical properties, ion channel dynamics, and action potential generation. Following this, Section 2.1.2 introduces different methods and neuronal targets in electrical stimulation applications. To understand how stimulation is delivered, Section 2.1.3 describes the two predominant stimulation modes: Current Mode Stimulation (CMS) and Voltage Mode Stimulation (VMS). Next, Section 2.1.4 explores the characteristics of stimulation waveforms, such as pulse shape and duration, and their role in activation thresholds. Another important design choice is the configuration of the electrodes, as described in Section 2.1.5. Building on these foundations, Section 2.1.6 provides a system-level overview of bidirectional neural interfaces, detailing the common components of these systems. Finally, typical stimulation parameters are discussed in Section 2.1.7, with a focus on intracortical visual prostheses as a case study.

The second part of the chapter focuses on the modeling of electrical stimulation (Section 2.2), which is essential for optimizing stimulation efficacy. Here, modeling is considered at three levels: neuronal-level modeling (Section 2.2.1) uses the Hodgkin-Huxley model as a foundational framework for describing ion-channel dynamics and neuron activation; tissue-level models (Section 2.2.2) describe electric field distributions and their use in predicting neuronal activation; and circuit-level models (Section 2.2.3) examine the electrical properties of stimulation electrodes and the typical electrical load as seen by the stimulator circuits.

Finally, Section 2.3 summarizes the key principles covered in this chapter, emphasizing the importance of understanding neuronal dynamics, system design, and modeling approaches for the development of efficient neuromodulation technologies. These concepts provide the necessary foundation for the subsequent discussions on power efficiency and circuit optimization in later chapters.

2.1. PRINCIPLES OF ELECTRICAL STIMULATION

2.1.1. NEUROPHYSIOLOGY OF ELECTRICAL STIMULATION

Neurons are the main components of our nervous system. They are excitable cells that transmit electrical signals and communicate with other neurons via synapses using chemical neurotransmitters [1]. The structure of a typical neuron consists of four parts, depicted in Fig. 2.1a: The soma, dendrites, an axon, and the presynaptic terminal. The soma, or cell body, contains the nucleus and organelles responsible for protein synthesis and other cellular processes. The dendrites typically consist of many branches, forming a dendritic tree. They act as the receivers of the cell, as they receive inputs from other cells through synapses. The axon is the output of the cell, transmitting signals from the soma to the presynaptic terminal. Most neurons only contain one axon, however

it typically branches out to communicate with multiple target neurons. Axons can be non-myelinated or myelinated. In the latter case, the axon is surrounded by an insulation layer named myelin sheath. The myelin sheath is periodically interrupted by small unmyelinated segments known as nodes of Ranvier, which play a crucial role in signal propagation by allowing electrical impulses to jump from node to node via saltatory conduction. Myelination increases the speed of propagation of signals along the axon. At the end of the axon is the presynaptic terminal, which contains synapses that can release neurotransmitters to communicate with other neurons.

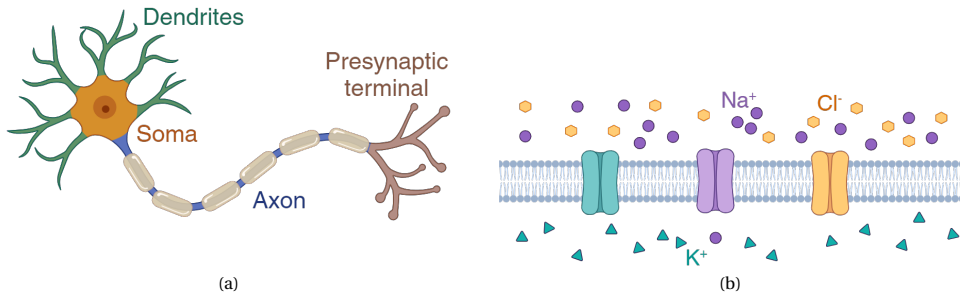


Figure 2.1: (a) The structure of a typical (myelinated) neuron consisting of the dendrites, the soma, an axon, and the presynaptic terminal. (b) The cell membrane with Sodium (Na⁺), Potassium (K⁺), and Chloride (Cl⁻) ion channels at rest. Figures created with BioRender.com.

The neurons are enclosed by a phospholipid bilayer, which is typically referred to as the cell membrane. This membrane is impermeable to ions and forms a barrier between the intra- and extracellular fluids. The presence of different ion concentrations between the inside and outside of the cell forms a membrane voltage:

$$V_m = \phi_{in} - \phi_{out}. \quad (2.1)$$

The membrane contains various proteins, including ion channels, which are essential for facilitating ion movement across it. Figure 2.1b illustrates the cell membrane with ion channels for the most important ions in neuronal signaling (Sodium, Potassium, and Chloride).

Ion channels control the movement of ions across the cellular membrane; when open, ions flow freely in or out of the cell, and when closed, ion movement is restricted. Ion channels can be divided in two types: leaky ion channels and gated ion channels. Leaky ion channels spontaneously open without external stimuli, whereas gated ion channels open only in response to specific triggers or conditions. Voltage-gated ion channels, activated by changes in membrane voltage, are particularly important for electrical stimulation. The movement of a specific ion across the membrane is influenced by two primary forces: concentration gradients and electrical fields. Concentration gradients drive ions from areas of higher concentration to lower concentration through diffusion, while electrical fields direct ions toward regions of opposite charge. These gradients may align or oppose each other, and the combined effect determines the net

ion movement. If these opposing forces are equal in strength but in opposite directions, the ion is in equilibrium, resulting in no net ion movement. The membrane voltage at which an ion is in equilibrium is called the Nernst potential and is calculated using [2]:

2

$$V_k = \frac{RT}{z_k F} \ln \frac{c_{i,k}}{c_{o,k}}, \quad (2.2)$$

where V_k is the equilibrium voltage for ion k , R is the gas constant [8.314 J/(mol · K)], T is absolute temperature [K], z_k is the valence of the ion k , F is Faraday's constant [9.649 × 10⁴ C/mol], and $c_{i,x}$ and $c_{o,x}$ are the intracellular and extracellular concentrations of the ion k , respectively. The Nernst potentials of Sodium, Potassium, and Chloride are 55 mV, −90 mV, and −65 mV, respectively. The balance of these opposing Nernst potentials (described by the Goldman-Hodgkin-Katz equation [2]) results in a resting membrane voltage around −70 mV. If the membrane voltage is increased (depolarized) to a threshold value V_{th} (around −55 mV), it causes voltage-gated sodium channels to open. Crossing this threshold initiates the generation of an action potential, an all-or-nothing event that will propagate along the axon. When the action potential reaches the presynaptic terminal, it causes the release of neurotransmitters that can activate or inhibit the receiving neurons. The progression of an action potential is illustrated in Fig. 2.2. The opening of the voltage-gated sodium channels causes a rapid influx of sodium ions into the cell, resulting in a fast depolarization of the membrane voltage. The depolarization results in the blocking of the sodium channels and the opening of voltage-gated potassium channels, allowing potassium ions to flow out of the cell, which repolarizes the membrane voltage. Due to the repolarization, the potassium channels close. A delay in this process causes the membrane voltage to hyperpolarize (undershoot), after which the cell restores to its resting membrane voltage. In mammals, the repolarization process is largely mediated by passive potassium leakage currents [3]. Once an action potential is created, it causes depolarization of the membrane further down the axon, triggering an action potential at that point. This way, the action potential propagates along the axon.

The working principle of electrical stimulation is the initiation of action potentials by means of applying external electrical stimuli [2]. Through electrodes, electric fields are generated that modulate the cells membrane voltage. This way, neurons can either be activated (by depolarizing V_m to V_{th}) or inhibited (by hyperpolarizing V_m , making it more difficult to reach V_{th}).

2.1.2. METHODS AND TARGETS OF ELECTRICAL STIMULATION

Electrical stimulation is used for a wide range of applications, each requiring careful consideration of physiological targets, electrode placement, and stimulation parameters. Depending on these factors, different stimulation methods may be selected, broadly categorized into transcutaneous [4], percutaneous [5, 6], and implantable approaches [7]. Transcutaneous stimulation, involving the application of electrical currents through electrodes placed on the skin surface, is non-invasive and relatively easy to implement, making it suitable for temporary treatments or diagnostics [4, 8, 9]. However, its effectiveness is often limited by poor current penetration and low spatial resolution, as electrical signals must traverse layers of skin and tissue (including bone) to reach the desired nerve

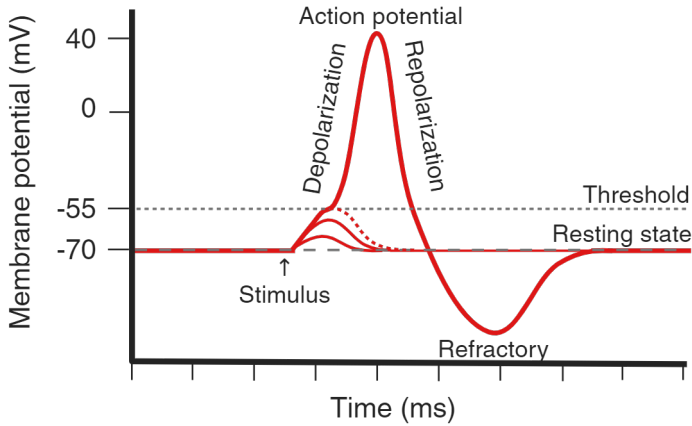


Figure 2.2: The progression of an action potential. Only if the stimulus depolarizes the membrane voltage to its threshold value, the action potential is initiated. Figure created with BioRender.com.

or muscle [10, 11]. In contrast, percutaneous stimulation involves inserting needle electrodes through the skin, positioning them closer to the target tissue [5, 6]. This method improves spatial resolution but introduces risks such as infection or discomfort due to its semi-invasive nature [12–15]. Implantable stimulation devices, such as deep brain stimulators or cochlear implants, are surgically placed near or within the target tissue. Implantable methods offer the highest precision and long-term efficacy but come with surgical risks and higher costs [16, 17].

Regarding the stimulation targets, these can be located either in the central nervous system (CNS) or in the peripheral nervous system (PNS). In the CNS, electrical stimulation is commonly used to treat neurological disorders such as Parkinson's disease and epilepsy [18]. Additionally, stimulation of the visual and auditory systems, as well as the somatosensory cortex, is employed to restore sensory functions. In the PNS, electrical stimulation of the vagus nerve is used to treat epilepsy, depression, and assist in post-stroke rehabilitation [19, 20]. Other peripheral applications include pain management, restoration of motor control, and stimulation for bladder control.

2.1.3. STIMULATION MODES

Electrical stimulation systems employ various modes to generate the electric fields required to modulate excitable tissue. Among these, Current Mode Stimulation (CMS) and Voltage Mode Stimulation (VMS) are the two predominant approaches, each distinguished by its control strategy in generating stimuli. In CMS, the system regulates the current delivered through the electrodes, whereas in VMS, the voltage applied to the electrodes is controlled. CMS offers precise charge control, ensuring that the exact amount of charge required for stimulation is delivered, independent of the electrode-tissue interface (ETI) impedance. This precision arises because, in CMS, the stimulation current, I_{stim} , is explicitly defined, making it less sensitive to variations in tissue or electrode impedance. A simplified model of a stimulation setup with two polarizable electrodes is shown in

Table 2.1: Comparison of current mode stimulation (CMS) and voltage mode stimulation (VMS).

Stimulation mode	CMS	VMS
Control Parameter	Current	Voltage
Charge Control	Direct	Indirect
Impedance Sensitivity	Minimal	High
Power Efficiency	Overhead losses in current source	All energy delivered to load
Circuit Complexity	Higher	Low

Fig. 2.3, where the electrode/electrolyte interface is represented by a capacitive element (C_{dl}), and the tissue is modeled as a resistive element (R_{tis}). In this setup, the voltage over the tissue and thus the electric field strength in the tissue is determined by:

$$V_{stim} = I_{stim} R_{tis}, \quad (2.3)$$

remaining unaffected by changes in C_{dl} . In contrast, VMS determines the stimulation current based on the applied voltage and the load impedance Z_{load} , as expressed by Ohm's law:

$$I_{stim} = V_{stim} / Z_{load}, \quad (2.4)$$

where Z_{load} represents the combined impedance of the tissue and the electrode interface, as depicted in Fig. 2.3. Consequently, additional charge or impedance measurements are required to accurately quantify the injected charge. Furthermore, as C_{dl} charges during stimulation, it can alter the electric field strength in the tissue, adding variability to VMS performance.

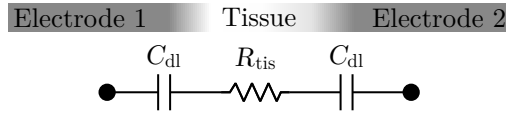


Figure 2.3: Linearized electrical model of a stimulation setup with two electrodes. Both electrodes form a capacitive electrode/electrolyte interface C_{dl} , and the tissue is modeled as a resistive element R_{tis} .

Table 2.1 provides a comparative summary of the two stimulation modes. The advantages of CMS make it the preferred choice for most applications [21, 22], and as such, this thesis focuses primarily on CMS-based stimulation systems.

While pulse-based stimulation is the main focus of this thesis, alternative paradigms have also been proposed. For example, alternating current stimulation strategies such as temporal interference can enable noninvasive targeting of deep brain regions by exploiting interference patterns of multiple high-frequency fields [23]. These approaches illustrate the breadth of stimulation modalities under exploration, though their circuit-level design considerations differ substantially from those of pulse-based systems.

2.1.4. STIMULATION WAVEFORM CHARACTERISTICS

The stimulation waveform typically consists of a train of biphasic pulses. In this biphasic pulse, the first phase (stimulating phase) is used to elicit the desired physiological effect,

while the second phase (reversal phase) is used to reverse the charges of the first phase. The reversal phase prevents harmful electrochemical reactions by neutralizing the charge accumulated during the stimulation phase. Without this phase, the voltage across the electrode-tissue interface (C_{dl} in Fig. 2.3) could reach levels that damage tissue and degrade electrodes over time [22]. A negative stimulation current defines a cathodic phase, while a positive current defines an anodic phase.

Whether a stimulus leads to the triggering of an action potential in a specific neuron, mainly depends on the duration and the amplitude of the stimulation phase. The relationship between the pulse duration and pulse amplitude that leads to activation (I_{th}) is known as the strength-duration curve, shown in Fig. 2.4a. For increasing pulse duration, I_{th} decreases, and for infinitely long pulse duration, I_{th} asymptotically approaches a minimum value known as the rheobase current I_{rh} . The curve can be approximated with the Lapicque equation [24]:

$$I_{th} = \frac{I_{rh}}{1 - \exp(-PW/\tau_m)}, \quad (2.5)$$

where I_{th} is the threshold amplitude, I_{rh} is the rheobase current, PW is the pulse duration, and τ_m is the membrane time constant. The quantitative characteristics of the curve depend on several factors, such as the distance between the neuron and the electrode and the diameter of the neuron.

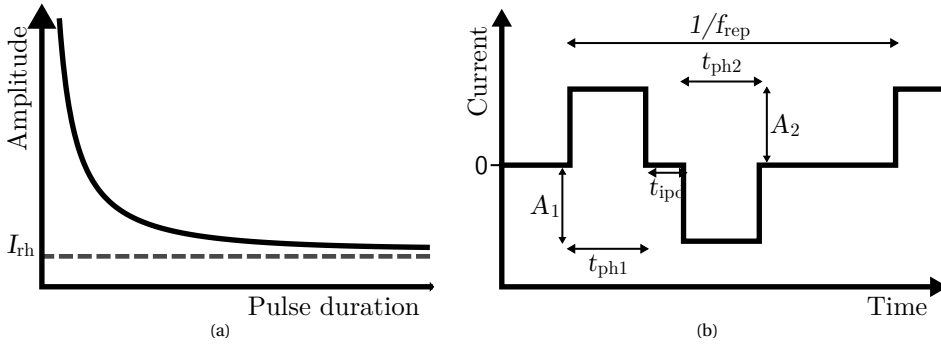


Figure 2.4: (a) Strength-Duration Curve, showing the typical relationship between pulse duration and activation threshold for a neuron. (b) Variable stimulation parameters in a train of biphasic stimulation pulses.

Although biphasic pulses are essential for long-term safety and therapeutic function, the reversal phase may partially negate the desired physiological effects of the activation phase, thereby increasing the stimulation threshold. Introducing a short delay between the two phases, an interphase delay, can reduce this effect allowing for a similar threshold to monophasic pulses [22, 25]. The typical stimulation waveform is illustrated in Fig. 2.4b, where A_1 is the amplitude of the stimulating phase, A_2 is the amplitude of the reversal phase, t_{ph1} , t_{ph2} , and t_{ipd} are the durations of the stimulating phase, the reversal phase, and the interphase delay, respectively, and f_{rep} is the repetition frequency of the stimulation pulses in the pulse train. The effect of pulse shapes on the SD curve, and its effect on the power efficiency of stimulation is the topic of Chapter 4 of this thesis.

2.1.5. ELECTRODE CONFIGURATIONS

To generate an electric field for stimulation, at least two electrodes are required, which can function as either working or return electrodes. The desired activation occurs due to depolarization near the working electrode(s), while the return electrode(s) provide(s) a current path [22]. Various electrode configurations can achieve the desired electric field, as depicted in Fig. 2.5. The most common configurations are monopolar and bipolar [26, 27]. In a monopolar configuration (Fig. 2.5a), the working electrode alternates between negative and positive potentials relative to a distant reference electrode, generating biphasic pulses [26, 28, 29]. The return electrode in this setup is typically much larger than the working electrode to ensure negligible polarization from the stimulation signal [22]. A key advantage of monopolar stimulation is that a single return electrode can serve multiple stimulation channels [2]. The electric field in this configuration resembles a point-source field due to the distant return electrode [29]. Producing biphasic pulses requires two separate current drivers: one current source and one current sink. Often, the return electrode is connected to ground potential, necessitating a negative supply voltage (V_{SS} in Fig. 2.5a) for the current sink [26]. Alternatively, biasing the working electrode to $V_{DD}/2$ allows the current sink to connect to ground potential [30]. In a bipolar configuration (Fig. 2.5b), both electrodes are of similar size and positioned close to each other, forming an electric dipole [26, 28, 29]. A single current driver (either a sink or a source) combined with an H-bridge switch is sufficient to generate biphasic pulses. However, a drawback of the bipolar configuration is that the return electrode experiences similar depolarization to the working electrode, potentially causing unintended activation near the return electrode [31].

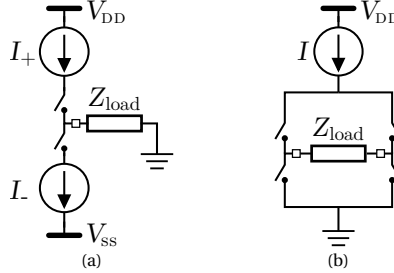
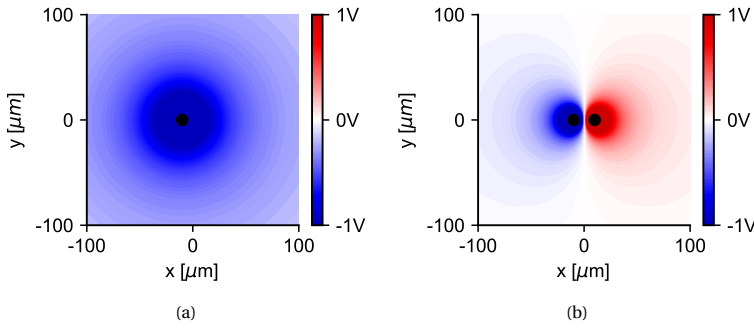


Figure 2.5: (a) Monopolar electrode configuration, where the distant return electrode is connected to the ground potential. Two separate current drivers are used to create biphasic pulses. (b) Bipolar electrode configuration with an H-bridge structure to create biphasic pulses.

As shown in Fig. 2.6, the bipolar configuration creates a more localized electric field, reducing cross-talk between channels [29]. The potential distributions in Fig. 2.6 are calculated in Python, where the electrodes are modeled as a point source as described in Section 2.2 and Eq. (2.16).

Similar to the bipolar configuration, more complex multipolar configurations can be designed using three or more electrodes. For instance, a hexagonal arrangement can include one working electrode surrounded by six return electrodes, forming a guard ring to minimize cross-talk with neighboring channels [32]. Multipolar configurations also enable current steering, where stimulation current is distributed across multiple working



2

Figure 2.6: Simulated potential distribution for (a) monopolar and (b) bipolar electrode configurations, calculated using Eq. (2.16). Both simulations use a stimulation current of $100\mu\text{A}$ and a tissue conductivity of $\sigma = 0.3\text{ S m}^{-1}$. The electrodes are indicated by the black dots.

electrodes [33]. This technique enhances spatial specificity by shaping the electric field.

2.1.6. SYSTEM-LEVEL DESIGN OF NEURAL INTERFACES

Even though different applications have unique system requirements, some essential circuit components can be generalized for all electrical neurostimulation systems [34, 35]. Figure 2.7 illustrates a generic system-level block diagram for an implantable bidirectional neural interface, comprising the following components: wireless power and data transfer, a power management unit (PMU), a processing and/or control unit, a stimulation unit, an analog front-end (AFE), and electrodes.

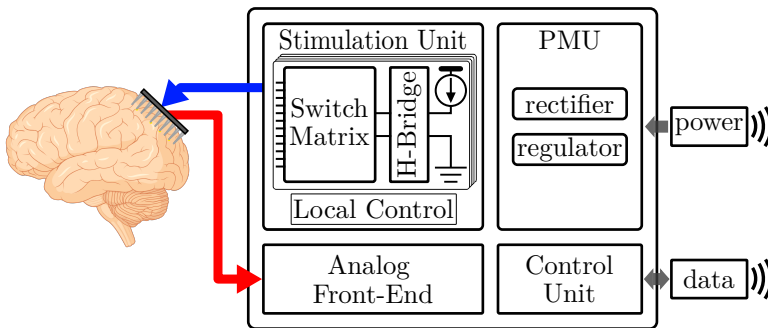


Figure 2.7: System level block diagram depicting the typical system components of a bidirectional implantable neural interface. Figure partly created with BioRender.com.

Wireless power and data transfer serve as the primary link between the implanted system and external devices, enabling efficient energy delivery and secure data communication. Power is commonly transmitted using methods such as inductive or capacitive coupling [36]. More recently, new approaches such as ultrasound, magnetoelectric, and optical power delivery are being explored [36, 37]. These modalities are discussed in more detail in Section 3.2.1. For data transfer, RF communication, inductive coupling, capacitive coupling, ultrasound, and optical links are commonly used [35, 38]. Multiple

configurations for the power and data link are possible. A single link can be used, such as a single inductive link, or two separate links can be used, either two links of the same modality or even different modalities. Using a single link offers the simplest implementation, however conflicting requirements limit the power efficiency and data rates that can be achieved [39]. On the other hand, using separate links allows for optimization for their specific function but increases the complexity of the circuits and antenna structures. The power management unit (PMU) is responsible for regulating and distributing the received power. Conventionally, this block consists of a rectifier followed by voltage regulators. Advanced approaches of the PMU will be discussed in Section 3.2 and is the topic of Chapter 6. The stimulation unit (SU) generates electrical pulses to stimulate neural tissue. Its specific components depend on the chosen stimulation method and electrode configuration. In addition to pulse generation, this unit may include local control circuits and additional safety circuits to prevent damage to the tissue or the electrodes. For multichannel systems, the SU can include multiple stimulation sources operating in parallel, with a switch matrix enabling a single source to address multiple electrodes, thereby improving system configurability. The analog front-end (AFE) amplifies, filters, and digitizes the weak neural signals recorded by the electrodes, preparing these signals for processing in the control unit. In the control unit, received commands are decoded into stimulation and recording commands, and the recorded signals are processed. It also manages communication with external devices through the data link. The arrangement and functionality of these blocks vary depending on the application. For instance, the AFE and stimulation unit (SU) may share the same electrodes or operate with separate groups. Systems can range in their balance of stimulation and recording capabilities from exclusively stimulatory systems to purely recording-based systems. While some applications require continuous power and data connections, others rely on internal energy storage using batteries. The specific design of each block, such as the stimulation unit, depends on factors like the stimulation mode and electrode configuration and application-specific requirements.

2.1.7. TYPICAL STIMULATION PARAMETERS

The range of stimulation parameters differs across applications, depending on the type of electrodes, the placement of the electrodes relative to the neural targets, and the type of neural targets. Here, the application of an intracortical visual prosthesis will be used as a use case for a large-scale multichannel application. Intracortical visual prosthetics aim to restore light perception in profoundly blind patients by directly stimulating the visual cortex using penetrating microelectrode arrays [40]. Activation of the cortical neurons in the visual cortex can elicit dots of light, so called phosphenes, in the visual field of the patient. Although no commercial device currently exists, significant research and clinical trials have advanced the understanding of the stimulation parameters and electrode designs required to evoke meaningful visual perceptions or phosphenes.

Several studies have researched the effect of varying stimulation parameters on the phosphene threshold, the current amplitude required to evoke a phosphene [41–43]. Repetition frequencies in the range of 100 Hz to 200 Hz are most effective for visual stimulation [41]. Frequencies below 150 Hz result in higher phosphene thresholds as the frequency decreases, while thresholds remain unaffected for frequencies above 150 Hz

[42]. Phase durations between $10\ \mu\text{s}$ and $1000\ \mu\text{s}$ have been shown to be effective [41], with thresholds decreasing as phase duration increases. However, a typical phase duration of approximately $200\ \mu\text{s}$ is commonly used for visual stimulation [42–47]. Furthermore, increasing the train duration causes a decrease in phosphene thresholds [41, 42]. Typical train durations for this application range from 125 ms to 300 ms [42–47].

Next to the waveform parameters, the electrode characteristics are important for the design of the stimulator system. The Utah Electrode Array (UEA), shown in Fig. 2.8a, has been widely used for clinical trials of intracortical stimulation in humans [43] and non-human primates (NHP) [48, 49]. The UEA is a silicon-based microelectrode array of penetrating electrodes, where the tips of the electrodes are often coated with sputtered iridium oxide to improve the impedance characteristics. The reported impedance values for these electrodes range from tens of $\text{k}\Omega$ up to a few hundred $\text{k}\Omega$ [43, 48]. Furthermore, phosphene thresholds ranging from a few μA to over $150\ \mu\text{A}$ have been reported in human and NHP studies [43, 48]. This brief overview shows the wide spread of stimulation parameters and load conditions, even within a given application. Although the UEA remains widely used in clinical trials, there is a growing shift toward flexible electrode arrays that better conform to brain tissue. An example is the ultraflexible array developed by Zhao et al. [50], shown in Fig. 2.8b.

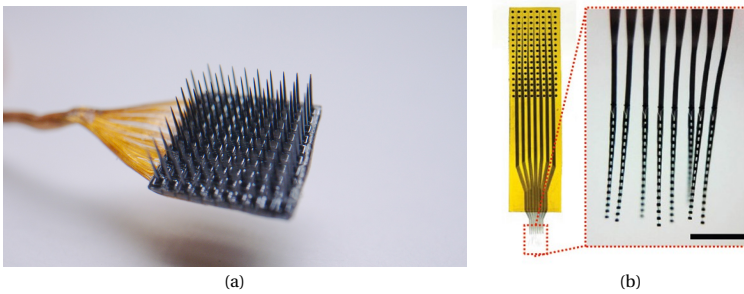


Figure 2.8: (a) The Utah Array with 100 electrodes. ©Blackrock Neurotech. (b) Ultraflexible electrode array by Zhao et al., figure adapted from [50].

2.2. MODELING OF ELECTRICAL STIMULATION

Modeling is essential for the design and optimization of electrical stimulation systems. Simulation of the interactions between electrical signals and biological tissue offers insights into important design parameters, such as the expected load conditions of the electrical circuit. To capture the complexity of electrical stimulation, different modeling approaches are used, each focusing on a specific level of abstraction. These levels range from the membrane dynamics within individual neurons to the interactions of electrodes and tissues. Figure 2.9 illustrates three levels of abstraction. At the neuronal level, models for ion-channel dynamics allow for the simulation of the interaction of electrical signals and neuron activation. At the tissue level, modeling focuses on the interaction of electrodes with tissue and the generation of electric fields. The electric fields can be used to predict activation patterns. Finally, at the circuit level, the interactions between the

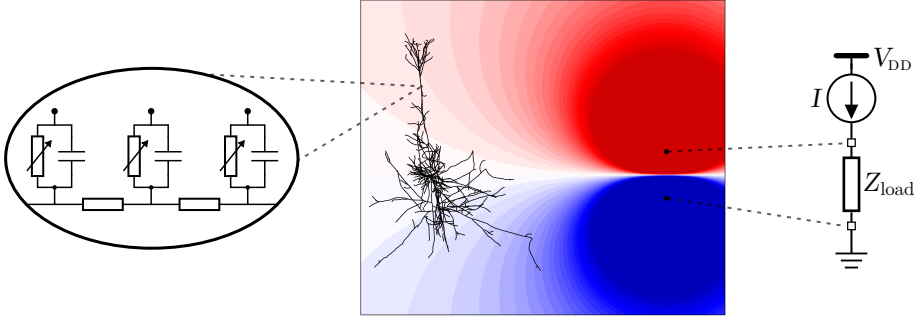


Figure 2.9: Overview of electrical stimulation modeling at different levels of abstraction, from left to right: neuronal, tissue, and circuit levels. The neuronal level simulates neuron activation and cell dynamics based on ion-channel behavior. The tissue level models electric fields generated by electrodes and predicts activation patterns, while the circuit level abstracts the stimulator circuit as an equivalent electrical load.

electrodes and the tissue are combined into an equivalent electrical circuit. These models are used to design stimulator circuits and to optimize the stimulator performance. Each level of abstraction provides insights into different parts of understanding and designing stimulator systems.

2.2.1. MODELING NEURONAL DYNAMICS

The Hodgkin–Huxley (HH) model [51] is a foundational mathematical framework used to simulate the active ion-channel dynamics of neurons. Hodgkin and Huxley experimentally measured ionic currents in the giant squid axon. Based on these measurements, they formulated a mathematical model to capture the activation of voltage-gated ion channels. The equivalent circuit of the Hodgkin–Huxley model is shown in Fig. 2.10. In general, each ionic current can be modeled as a variable conductance in series with a voltage source that reflects the Nernst potential (Eq. (2.2)) of the corresponding ion.

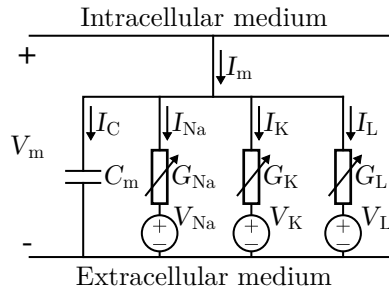


Figure 2.10: Schematic representation of the Hodgkin-Huxley (HH) active membrane model, showing the ionic current pathways and capacitive behavior of the neuronal membrane [51].

The total transmembrane current per unit area can be written in the general form as:

$$I_m = C_m \frac{dV_m}{dt} + \sum_i (V_m - V_i) G_i, \quad (2.6)$$

where I_m is the total membrane current density [μAcm^{-2}], C_m is the membrane capacitance per unit area [μFcm^{-2}], and V_m is the membrane voltage [mV]. For each ionic species i , V_i is the reversal (Nernst) potential [mV] and G_i is the corresponding conductance per unit area [mScm^{-2}]. In the HH framework, the conductance is voltage- and time-dependent, and is expressed as a maximal conductance multiplied by a product of gating variables that describe channel activation and inactivation.

For the specific case studied by Hodgkin and Huxley in the squid giant axon, the model included only sodium, potassium, and a leakage current (Fig. 2.10). In that case, Eq. (2.6) simplifies to:

$$I_m = C_m \frac{dV_m}{dt} + (V_m - V_{\text{Na}}) G_{\text{Na}} + (V_m - V_{\text{K}}) G_{\text{K}} + (V_m - V_{\text{L}}) G_{\text{L}}. \quad (2.7)$$

Hodgkin and Huxley characterized the conductances in this model as:

$$G_{\text{K}} = G_{\text{K,max}} n^4 \quad (2.8)$$

$$G_{\text{Na}} = G_{\text{Na,max}} m^3 h \quad (2.9)$$

$$G_{\text{L}} = \text{constant}, \quad (2.10)$$

where $G_{\text{K,max}}$, $G_{\text{Na,max}}$, G_{L} are 36, 120, and 0.3 mScm^{-2} , respectively. The gating variables n , m , and h , were introduced by Hodgkin and Huxley to fit their measurements. Their value ranges between 0 and 1, and they describe the probability of the related ion gate being open. The gating variables are described with the following differential equation:

$$\frac{dx}{dt} = \alpha_x (1 - x) - \beta_x x, \quad (2.11)$$

where x can be n , m , or h , and α_x and β_x are the transfer rate coefficients for each gating variable. The transfer rate coefficients are voltage-dependent and describe the rate of transition of the gating variables:

$$x \xrightleftharpoons[\beta_x]{\alpha_x} (1 - x). \quad (2.12)$$

For their measurements, the transfer rates were defined as follows:

$$\alpha_n = \frac{0.01 (10 - V')}{\exp((10 - V')/10) - 1}, \quad \beta_n = 0.125 \exp(-V'/80), \quad (2.13)$$

$$\alpha_m = \frac{0.1 (25 - V')}{\exp((25 - V')/10) - 1}, \quad \beta_m = 4 \exp(-V'/18), \quad (2.14)$$

$$\alpha_h = 0.07 \exp(-V'/20), \quad \beta_h = \frac{1}{\exp((30 - V')/10) + 1}. \quad (2.15)$$

where $V' = V_m - V_r$, with V_r the resting voltage (typically, $V_r \approx -65\text{mV}$). These conductances and transfer coefficients are specific to the experiments conducted to the squid giant axon, but the HH framework has since been applied widely to describe neuronal dynamics in many cell types.

To model the spatial propagation of action potentials, the complete neuron can be described as a multi-compartment (cable) model as shown in Fig. 2.11. In this context, a compartment refers to a small, isopotential segment of the neuronal membrane, typically modeled as a cylindrical section with its own membrane capacitance, ion channel dynamics, and axial resistance. By connecting many such compartments in series and branching structures, neurons can be represented as simplified 3D structures rather than point neurons. Even more complex compartment models have been developed to model physiological effects, e.g., of myelination. The NEURON software [52] is specifically designed to simulate neuronal dynamics by numerically solving the differential equations arising from such compartmental HH models.

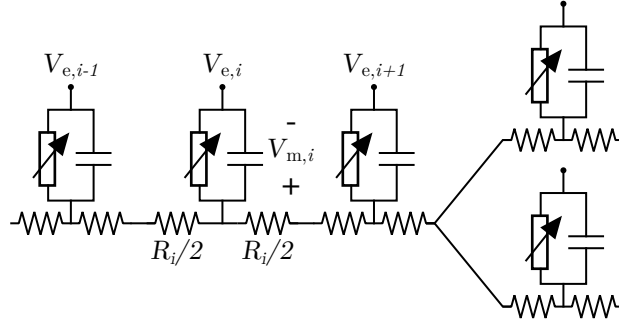


Figure 2.11: Neuron compartment model. In this model, the 3D structure of a neuron is approximated by interconnected compartments. Each compartment is treated as isopotential, containing active membrane dynamics (Fig. 2.10), and is coupled to its neighbors through the intracellular resistance (R_i). This representation enables the simulation of spatially distributed phenomena, such as action potential propagation.

2.2.2. MODELING ELECTRIC FIELDS AND ACTIVATION PATTERNS

At the tissue level, modeling of electrical stimulation is used to calculate electric fields and to predict activation patterns in the tissue. As the simplest approximation, each stimulation electrode can be modeled as an electrical point source in an infinite homogeneous isotropic volume conductor with conductivity σ . In that case, the electric field spreads as a sphere around the electrode, and the potential at a distance r from the electrode can be calculated using:

$$\phi = \frac{I_{\text{stim}}}{4\pi\sigma r}. \quad (2.16)$$

If more than one electrode is used, e.g. in a bipolar or multipolar electrode configuration, the total potential is found by summation of the individual contributions. The point source approximation simplifies calculations when the electrode is small relative to the distance to the observation point, and near-field effects are negligible.

Finite element modeling (FEM) is used to simulate complex electric field distributions

by incorporating detailed electrode geometries, material properties, and tissue inhomogeneity or anisotropy. This method provides greater accuracy when analyzing the effects of electrode designs and spatial configurations.

Electrical field models can be directly linked to the compartment models at the neuronal level, however, the differential equations in the ion channel models increase the computational time, while it is often too detailed for the purpose of the simulations. To simplify the simulations, spatial activation can be predicted based on the cable model of the neuron using the activating function (AF) [53]. Based on the compartment model depicted in Fig. 2.11, the membrane voltage at node n , $V_{m,n}$, can be found by solving the following equation [54]:

$$\frac{V_{m,n}}{dt} = \left[\frac{1}{R_i} (V_{m,n-1} - 2V_{m,n} + V_{m,n+1} + V_{e,n-1} - 2V_{e,n} + V_{e,n+1}) - I_{ionic,n} \right] / C_m, \quad (2.17)$$

where $I_{ionic,n}$ is the ionic current at node n as described by the HH models. After inserting $R_i = 4\rho_i\Delta x/\pi d^2$, and $C_m = \pi dLc_m$, where ρ_i is the intracellular resistivity, Δx is the segmentation length of the fiber, d is the fiber diameter, L is the length of the membrane, and c_m is the membrane capacitance per unit area, Rattay [53] observed that the influence of the extracellular voltage is given by:

$$f_n(t) = \frac{V_{e,n-1} - 2V_{e,n} + V_{e,n+1}}{\Delta x^2}. \quad (2.18)$$

And if $\Delta x \rightarrow 0$, it becomes:

$$f(x, t) = \frac{\partial^2 V_e(x, t)}{\partial x^2}, \quad (2.19)$$

where x is the length coordinate of the fiber, which is the second-order spatial derivative of the extracellular potential along the length of the fiber. Equation (2.19) is called the activating function, as it predicts where the electric field will lead to neuronal activation. At locations where the AF is positive, it leads to depolarization of the membrane, and could thus initiate action potentials. If the AF is negative, it causes hyperpolarization of the membrane. Figure 2.12 shows the simulated AF along an axon near to a cathodic stimulation electrode, the area shaded in gray depicts where the stimulation current causes depolarization of the cell membrane. The potential is calculated in Python using Eq. (2.16) for a point source located at a vertical distance of $50\text{ }\mu\text{m}$ above the axon center, stimulating with a current of $-100\text{ }\mu\text{A}$, and the activating function is obtained by taking the second spatial derivative along the x -direction. Given the simplicity of this approximation with respect to the computationally complex compartment models, it serves as a useful tool to predict activation patterns based on the calculated electric fields.

2.2.3. MODELING THE ELECTRODE-TISSUE INTERFACE (ETI)

Finally, at the circuit level, the goal of modeling is to understand the electrical load of the system and the interactions at the electrode-tissue interface (ETI). The interactions at the ETI can be divided into reversible and irreversible reactions. The reversible interactions are primarily capacitive, resulting from accumulation of charges on both sides of the electrode-electrolyte double layer. In contrast, irreversible interactions involve electrochemical, or faradaic, reactions that permanently alter the electrode or surrounding

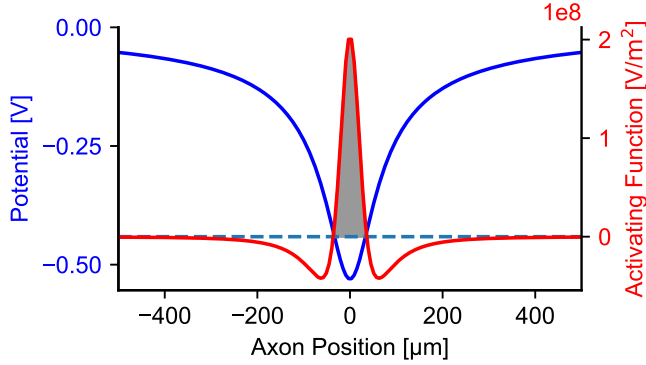


Figure 2.12: Simulated extracellular potential (blue) and activating function (red) along an axon located at a distance of $50\ \mu\text{m}$ from a monopolar electrode stimulating with an amplitude of $-100\ \mu\text{A}$ (cathodic stimulation). The area in gray depicts where this stimulus will cause depolarization of the cell membrane.

tissue. The irreversible processes can lead to damage to the electrodes and the tissue and should be carefully considered to guarantee the safety of the stimulation. The electrical model of the ETI consists of two branches to model both interactions. While the ETI involves complex, non-linear electrochemical reactions, it is often simplified as a linear model for practical analysis. In the linear model (Fig. 2.13), the reversible interactions are modeled by a double-layer capacitance, C_{dl} , or a constant phase element (CPE), and the irreversible interactions by a charge transfer resistor R_{CT} . The values of both components depend on the geometry and materials of the electrodes. For stimulation electrodes, it is important that R_{CT} is sufficiently large, such that charge can be delivered to the tissue without damaging the electrodes and tissue. Furthermore, as the voltage over R_{CT} increases the current through this branch, C_{dl} should generally be big for stimulation electrodes, such that the stimulation charge does not cause a large voltage drop over R_{CT} .

The tissue impedance Z_{tis} is the electrical equivalent of the tissue between the stimulation electrodes. The complex tissue impedance depends on properties such as homogeneity and isotropy. Again, this impedance is often simplified to a resistive component R_{tis} . In some cases, a parallel capacitive branch is added to account for the dynamic properties of the tissue. The value of R_{tis} is also dependent on the electrode geometry, where a large electrode surface leads to a smaller R_{tis} component. Even further simplified,

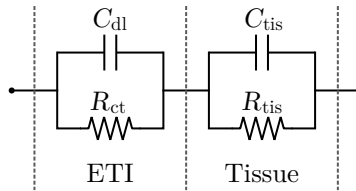


Figure 2.13: Linear electrical model of the tissue and electrode-tissue interface (ETI), illustrating the reversible capacitive interactions and irreversible faradaic reactions.

the electrode impedance is often reported as a single value in literature. This value typically corresponds to the impedance magnitude measured at 1 kHz. Using this model can guide the design of electrical stimulator systems. Depending on the design targets, the complexity of the model can be chosen.

2.3. DISCUSSION

This chapter introduced several fundamental concepts of electrical stimulation and its modeling. In the first part, the electrochemical properties of neurons were introduced, leading to an understanding of how electrical stimulation allows them to interact with this system. Basic design considerations and waveform parameters for stimulator circuits were discussed. The rest of this thesis will focus on current mode stimulation in bipolar electrode configuration. The second part discussed how electrical stimulation can be modeled at different levels of abstraction, covering models for active ion channel dynamics, the activating function for predicting activation patterns, and the ETI and tissue model components used in stimulator circuit design.

BIBLIOGRAPHY

- [1] E. R. Kandel, J. D. Koester, S. H. Mack, and S. A. Siegelbaum, in *Principles of Neural Science*, 6e. New York, NY: McGraw Hill, 2021.
- [2] J. Malmivuo and R. Plonsey, *Bioelectromagnetism: Principles and Applications of Bioelectric and Biomagnetic Fields*. Oxford University Press, Oct. 1995, vol. 15, pp. 1–506, ISBN: 9780195058239. DOI: 10.1093/acprof:oso/9780195058239.001.0001.
- [3] G. R. Tanner and A. V. Tzingounis, “The mammalian nodal action potential: new data bring new perspectives”, *Advances in Physiology Education*, vol. 46, no. 4, pp. 693–702, 2022, ISSN: 15221229. DOI: 10.1152/ADVAN.00171.2021.
- [4] W. Gibson, B. M. Wand, and N. E. O’Connell, *Transcutaneous electrical nerve stimulation (TENS) for neuropathic pain in adults*, Sep. 2017. DOI: 10.1002/14651858.CD011976.pub2.
- [5] G. Plaza-Manzano, G. F. Gómez-Chiguano, J. A. Cleland, J. L. Arias-Buría, C. Fernández-de-las-Peñas, and M. J. Navarro-Santana, *Effectiveness of percutaneous electrical nerve stimulation for musculoskeletal pain: A systematic review and meta-analysis*, Jul. 2020. DOI: 10.1002/ejp.1559.
- [6] S. Mogedano-Cruz *et al.*, *Peripheral Percutaneous Electrical Nerve Stimulation for Neuropathies: A Systematic Review and Meta-analysis*, Feb. 2024. DOI: 10.1016/j.pmn.2024.11.005.
- [7] S. M. Won, E. Song, J. T. Reeder, and J. A. Rogers, *Emerging Modalities and Implantable Technologies for Neuromodulation*, 2020. DOI: 10.1016/j.cell.2020.02.054.
- [8] A. Priori, M. Ciocca, M. Parazzini, M. Vergari, and R. Ferrucci, “Transcranial cerebellar direct current stimulation and transcutaneous spinal cord direct current stimulation as innovative tools for neuroscientists”, *Journal of Physiology*, vol. 592, no. 16, pp. 3345–3369, 2014, ISSN: 14697793. DOI: 10.1113/jphysiol.2013.270280.
- [9] A. Antal *et al.*, “Low intensity transcranial electric stimulation: Safety, ethical, legal regulatory and application guidelines”, *Clinical Neurophysiology*, vol. 128, no. 9, pp. 1774–1809, 2017, ISSN: 18728952. DOI: 10.1016/j.clinph.2017.06.001.
- [10] A. Datta, M. Elwassif, F. Battaglia, and M. Bikson, “Transcranial current stimulation focality using disc and ring electrode configurations: FEM analysis”, *Journal of Neural Engineering*, vol. 5, no. 2, pp. 163–174, Jun. 2008, ISSN: 17412560. DOI: 10.1088/1741-2560/5/2/007.

- [11] M. A. Nitsche *et al.*, “Shaping the effects of transcranial direct current stimulation of the human motor cortex”, *Journal of Neurophysiology*, vol. 97, no. 4, pp. 3109–3117, Apr. 2007, ISSN: 00223077. DOI: 10.1152/jn.01312.2006.
- [12] J. A. George *et al.*, “Long-term performance of Utah slanted electrode arrays and intramuscular electromyographic leads implanted chronically in human arm nerves and muscles”, *Journal of Neural Engineering*, vol. 17, no. 5, Oct. 2020, ISSN: 17412552. DOI: 10.1088/1741-2552/abc025.
- [13] B. M. Ilfeld *et al.*, “Infection Rates of Electrical Leads Used for Percutaneous Neurostimulation of the Peripheral Nervous System”, *Pain Practice*, vol. 17, no. 6, pp. 753–762, Jul. 2017, ISSN: 1530-7085. DOI: 10.1111/papr.12523.
- [14] J. V. L. Hernandez, C. Calvo-Lobo, A. M.-P. Zugasti, J. Fernandez-Carnero, and H. Beltran Alacreu, “Effectiveness of Dry Needling with Percutaneous Electrical Nerve Stimulation of High Frequency Versus Low Frequency in Patients with Myofascial Neck Pain.”, *Pain physician*, vol. 24, no. 2, pp. 135–143, Mar. 2021, ISSN: 2150-1149.
- [15] S. Parikh, A. C. Echevarria, B. R. Cemenski, and T. Small, “The Relevance of Implanted Percutaneous Electrical Nerve Stimulation in Orthopedics Surgery: A Systematic Review”, *Journal of Clinical Medicine*, vol. 13, no. 13, p. 3699, Jun. 2024, ISSN: 2077-0383. DOI: 10.3390/jcm13133699.
- [16] M. Mariello and C. M. Proctor, “Wireless Power and Data Transfer Technologies for Flexible Bionic and Bioelectronic Interfaces: Materials and Applications”, *Advanced Materials Technologies*, Sep. 2024, ISSN: 2365-709X. DOI: 10.1002/admt.202400797.
- [17] IEEE Brain, *Future Neural Therapeutics*, Dec. 2020. DOI: 10.23919/BRAIN.2020.00101.
- [18] A. S. Koivuniemi and K. J. Otto, “Central nervous system stimulation”, in *Neuroprosthetics: Theory and Practice: Second Edition*, 2017, pp. 348–376, ISBN: 9789813207158. DOI: 10.1142/9789813207158_0013.
- [19] D. J. Tyler, “Peripheral Nerve Stimulation”, in *Neuroprosthetics: Theory and Practice: Second Edition*, May 2017, pp. 300–347. DOI: 10.1142/9789813207158_0012.
- [20] A. Kral, F. Aplin, and H. Maier, “Peripheral nerve and spinal stimulation”, in *Prostheses for the Brain*, Elsevier, 2021, pp. 305–328. DOI: 10.1016/b978-0-12-818892-7.00013-4.
- [21] R. Shirafkan and O. Shoaie, “Current-Based Neurostimulation Circuit and System Techniques”, in *Handbook of Biochips*, New York, NY: Springer New York, 2022, pp. 445–469. DOI: 10.1007/978-1-4614-3447-4_42.
- [22] D. R. Merrill, M. Bikson, and J. G. Jefferys, “Electrical stimulation of excitable tissue: design of efficacious and safe protocols”, *Journal of Neuroscience Methods*, vol. 141, no. 2, pp. 171–198, Feb. 2005, ISSN: 01650270. DOI: 10.1016/j.jneumeth.2004.10.020.

- [23] N. Grossman *et al.*, “Noninvasive Deep Brain Stimulation via Temporally Interfering Electric Fields”, *Cell*, vol. 169, no. 6, pp. 1029–1041, Jun. 2017, ISSN: 10974172. DOI: 10.1016/j.cell.2017.05.024.
- [24] L. Lapicque, “Recherches quantitatives sur l’excitation électrique des nerfs traitée comme une polarisation”, *Journal of Physiol Pathol Générale*, 620–635, vol. 9, 1907.
- [25] P. H. Gorman and J. T. Mortimer, “The Effect of Stimulus Parameters on the Recruitment Characteristics of Direct Nerve Stimulation”, *IEEE Transactions on Biomedical Engineering*, vol. BME-30, no. 7, pp. 407–414, Jul. 1983, ISSN: 0018-9294. DOI: 10.1109/TBME.1983.325041.
- [26] C.-Y. Lin and M.-D. Ker, “Overview of On-Chip Stimulator Designs for Biomedical Applications”, *Journal of Neuroscience and Neuroengineering*, vol. 1, no. 2, pp. 204–212, Dec. 2012, ISSN: 21682011. DOI: 10.1166/jnsne.2012.1023.
- [27] J. H. Park, H. Wu, J. S. Y. Tan, and J. Yoo, “Biphasic Current Stimulator for Retinal Prosthesis”, in *Handbook of Biochips*, New York, NY: Springer New York, 2022, pp. 1185–1199. DOI: 10.1007/978-1-4614-3447-4_70.
- [28] M. Zhang, Z. Tang, X. Liu, and J. Van der Spiegel, “Electronic neural interfaces”, *Nature Electronics*, vol. 3, no. 4, pp. 191–200, Apr. 2020, ISSN: 25201131. DOI: 10.1038/s41928-020-0390-3.
- [29] A. Kral, F. Aplin, and H. Maier, “Stimulation rules”, in *Prostheses for the Brain*, Elsevier, 2021, pp. 115–134. DOI: 10.1016/b978-0-12-818892-7.00002-x.
- [30] B. C. Raducanu, J. Aymerich, W. Y. Hsu, P. Hendrickx, and C. M. Lopez, “A 128-channel neural stimulation and recording ASIC for scalable cortical visual prosthesis”, in *European Solid-State Circuits Conference*, vol. 2023-September, IEEE Computer Society, 2023, pp. 301–304, ISBN: 9798350304206. DOI: 10.1109/ESSCIRC59616.2023.10268749.
- [31] Q. Mesnildrey and O. Macherey, “Simulating the dual-peak excitation pattern produced by bipolar stimulation of a cochlear implant: Effects on speech intelligibility”, *Hearing Research*, vol. 319, pp. 32–47, Jan. 2015, ISSN: 18785891. DOI: 10.1016/j.heares.2014.11.001.
- [32] G. Khalili Moghadam, R. Wilke, G. J. Suaning, N. H. Lovell, and S. Dokos, “Quasi-Monopolar Stimulation: A Novel Electrode Design Configuration for Performance Optimization of a Retinal Neuroprosthesis”, *PLoS ONE*, vol. 8, no. 8, A. Ohlmann, Ed., e73130, Aug. 2013, ISSN: 1932-6203. DOI: 10.1371/journal.pone.0073130.
- [33] P. B. Matteucci *et al.*, “Current Steering in Retinal Stimulation via a Quasimonopolar Stimulation Paradigm”, *Investigative Ophthalmology & Visual Science*, vol. 54, no. 6, p. 4307, Jun. 2013, ISSN: 1552-5783. DOI: 10.1167/iovs.13-11653.
- [34] Y. Liu *et al.*, “Bidirectional Bioelectronic Interfaces”, *IEEE solid state circuits magazine*, vol. 12, no. 2, pp. 30–46, 2020.
- [35] S. Drakopoulou, F. Varkevisser, L. Sohail, M. Aqamolaei, T. L. Costa, and G. D. Spyropoulos, “Hybrid neuroelectronics: towards a solution-centric way of thinking about complex problems in neurostimulation tools”, *Frontiers in Electronics*, vol. 4, Sep. 2023, ISSN: 2673-5857. DOI: 10.3389/felec.2023.1250655.

- [36] M. Kiani, "Wireless Power Transfer and Management for Medical Applications: Wireless power", *IEEE Solid-State Circuits Magazine*, vol. 14, no. 3, pp. 41–52, 2022, ISSN: 1943-0582. DOI: 10.1109/MSSC.2022.3178671.
- [37] S. R. Khan, S. K. Pavuluri, G. Cummins, and M. P. Desmulliez, *Wireless power transfer techniques for implantable medical devices: A review*, Jun. 2020. DOI: 10.3390/s20123487.
- [38] A. Koruprolu, S. Nag, R. Erfani, and P. Mohseni, "Capacitive Wireless Power and Data Transfer for Implantable Medical Devices", in *2018 IEEE Biomedical Circuits and Systems Conference (BioCAS)*, IEEE, Oct. 2018, pp. 1–4, ISBN: 978-1-5386-3603-9. DOI: 10.1109/BIOCAS.2018.8584824.
- [39] I. Mayordomo, T. Drager, P. Spies, J. Bernhard, and A. Pflaum, *An overview of technical challenges and advances of inductive wireless power transmission*, 2013. DOI: 10.1109/JPROC.2013.2243691.
- [40] E. Fernández, A. Alfaro, and P. González-López, "Toward Long-Term Communication With the Brain in the Blind by Intracortical Stimulation: Challenges and Future Prospects", *Frontiers in Neuroscience*, vol. 14, no. August, Aug. 2020, ISSN: 1662-453X. DOI: 10.3389/fnins.2020.00681.
- [41] A. Najarpour Foroushani, C. C. Pack, and M. Sawan, "Cortical visual prostheses: From microstimulation to functional percept", *Journal of Neural Engineering*, vol. 15, no. 2, p. 021 005, Apr. 2018, ISSN: 17412552. DOI: 10.1088/1741-2552/aaa904.
- [42] E. M. Schmidt, M. J. Bak, F. T. Hambrecht, C. V. Kufta, D. K. O'Rourke, and P. Vallabhanath, "Feasibility of a visual prosthesis for the blind based on intracortical micro stimulation of the visual cortex", *Brain*, vol. 119, no. 2, pp. 507–522, 1996, ISSN: 0006-8950. DOI: 10.1093/brain/119.2.507.
- [43] E. Fernández *et al.*, "Visual percepts evoked with an intracortical 96-channel microelectrode array inserted in human occipital cortex", *Journal of Clinical Investigation*, vol. 131, no. 23, Dec. 2021, ISSN: 1558-8238. DOI: 10.1172/JCI151331.
- [44] T. S. Davis *et al.*, "Spatial and temporal characteristics of V1 microstimulation during chronic implantation of a microelectrode array in a behaving macaque", *Journal of Neural Engineering*, vol. 9, no. 6, p. 065 003, Dec. 2012, ISSN: 1741-2560. DOI: 10.1088/1741-2560/9/6/065003.
- [45] E. A. DeYoe, J. D. Lewine, and R. W. Doty, "Laminar Variation in Threshold for Detection of Electrical Excitation of Striate Cortex by Macaques", *Journal of Neurophysiology*, vol. 94, no. 5, pp. 3443–3450, Nov. 2005, ISSN: 0022-3077. DOI: 10.1152/jn.00407.2005.
- [46] E. J. Tehovnik and W. M. Slocum, "Depth-dependent detection of microampere currents delivered to monkey V1", *European Journal of Neuroscience*, vol. 29, no. 7, pp. 1477–1489, Apr. 2009, ISSN: 0953816X. DOI: 10.1111/j.1460-9568.2009.06695.x.

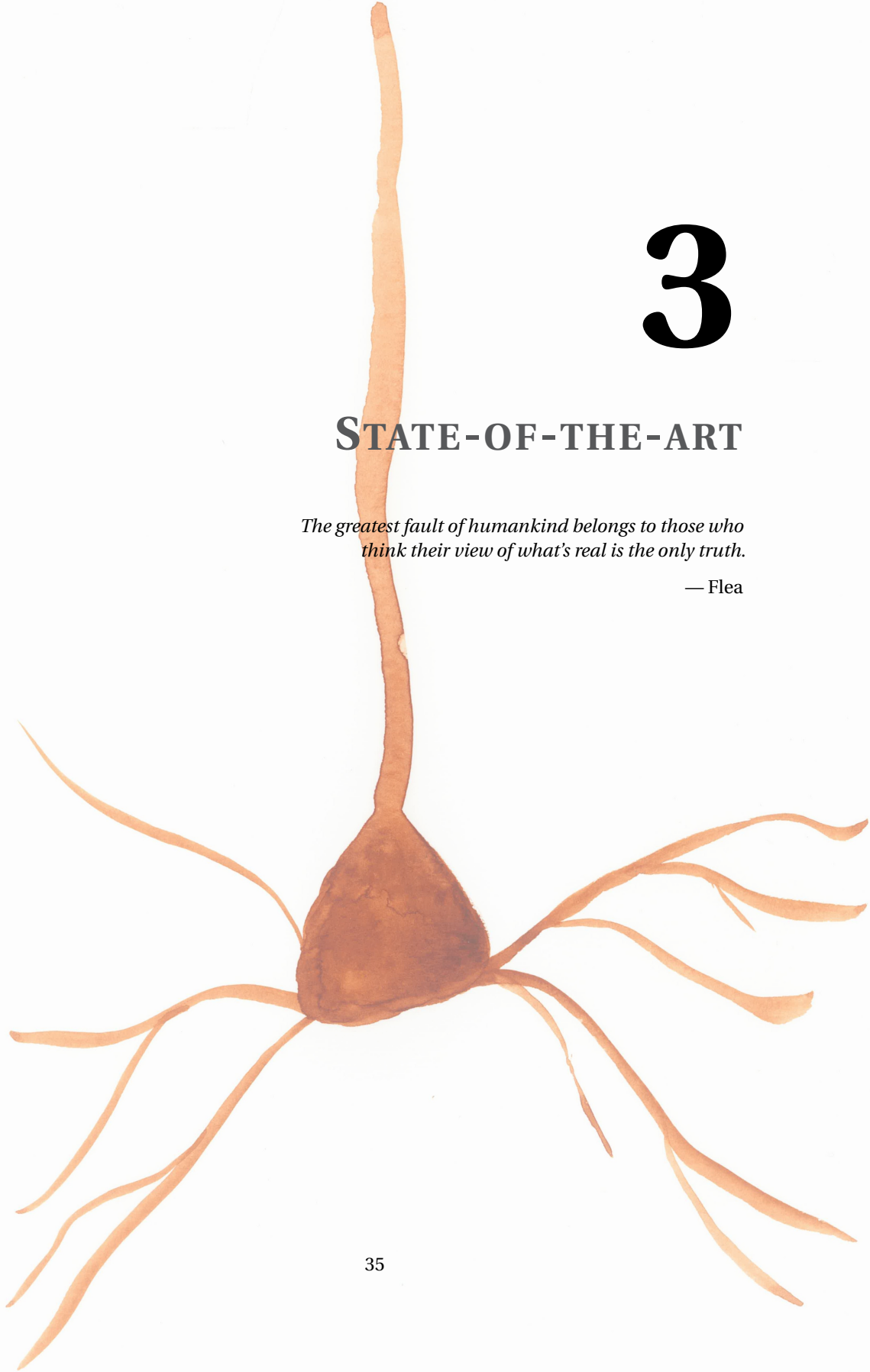
- [47] X. Chen, F. Wang, E. Fernandez, and P. R. Roelfsema, "Shape perception via a high-channel-count neuroprosthesis in monkey visual cortex", *Science*, vol. 370, no. 6521, pp. 1191–1196, 2020, ISSN: 10959203. DOI: 10.1126/science.abd7435.
- [48] X. Chen *et al.*, "Chronic stability of a neuroprosthesis comprising multiple adjacent Utah arrays in monkeys", *Journal of Neural Engineering*, vol. 20, no. 3, Jun. 2023, ISSN: 17412552. DOI: 10.1088/1741-2552/ace07e.
- [49] S. Kim, T. Callier, and S. J. Bensmaia, "A computational model that predicts behavioral sensitivity to intracortical microstimulation", *Journal of Neural Engineering*, vol. 14, no. 1, p. 016012, Feb. 2017, ISSN: 17412552. DOI: 10.1088/1741-2552/14/1/016012.
- [50] Z. Zhao *et al.*, "Ultraflexible electrode arrays for months-long high-density electrophysiological mapping of thousands of neurons in rodents", *Nature Biomedical Engineering*, vol. 7, no. 4, pp. 520–532, Apr. 2023, ISSN: 2157846X. DOI: 10.1038/s41551-022-00941-y.
- [51] A. L. Hodgkin and A. F. Huxley, "A quantitative description of membrane current and its application to conduction and excitation in nerve", *The Journal of Physiology*, vol. 117, no. 4, pp. 500–544, Aug. 1952, ISSN: 0022-3751. DOI: 10.1113/jphysiol.1952.sp004764.
- [52] N. T. Carnevale and M. L. Hines, *The NEURON Book*. Cambridge: Cambridge University Press, 2006, pp. 1–457, ISBN: 9780511541612. DOI: 10.1017/CB09780511541612.
- [53] F. Rattay, "Analysis of models for extracellular fiber stimulation", *IEEE Transactions on Biomedical Engineering*, vol. 36, no. 7, pp. 676–682, Jul. 1989, ISSN: 00189294. DOI: 10.1109/10.32099.
- [54] D. R. McNeal, "Analysis of a Model for Excitation of Myelinated Nerve", *IEEE Transactions on Biomedical Engineering*, vol. BME-23, no. 4, pp. 329–337, Jul. 1976, ISSN: 0018-9294. DOI: 10.1109/TBME.1976.324593.

3

STATE-OF-THE-ART

*The greatest fault of humankind belongs to those who
think their view of what's real is the only truth.*

— Flea



THE design of implantable stimulation systems presents multiple challenges, including energy efficiency, power management, and multichannel architectures. This chapter reviews state-of-the-art techniques aimed at improving power efficiency in electrical stimulation systems.

First, Section 3.1 focuses on energy-efficient stimulation pulses. Specifically, Section 3.1.1 examines pulse-shape optimization strategies, while Section 3.1.2 presents experimental evidence supporting the efficacy of non-rectangular waveforms. Building on these findings, Section 3.1.3 discusses system architectures capable of generating non-rectangular pulses.

Subsequently, Section 3.2 explores power management in implantable stimulators. Various wireless power transfer modalities for implantable devices are introduced in Section 3.2.1, followed by the description of the components of a conventional power management unit consisting of a rectifier (Section 3.2.2) and a voltage regulator (Section 3.2.3) are discussed. Furthermore, Section 3.2.4 explores more advanced power management techniques through regulating rectifiers, and Section 3.2.5 outlines approaches for efficiently distributing power across multiple stimulation channels.

Next, Section 3.3 reviews recent multichannel stimulation system implementations, highlighting the principal trade-offs and design considerations that arise when scaling to larger numbers of channels.

Finally, Section 3.4 summarizes the findings of this chapter, identifies the knowledge gaps and states the research questions that will guide the rest of this thesis.

3.1. ENERGY-EFFICIENT STIMULATION PULSES

Several studies have suggested that using non-rectangular stimulation pulses could improve the energy efficiency of electrical stimulation [1–15]. The research on pulse shaping is based on a range of approaches, including analytical methods [1] and optimization algorithms for shape optimization [2–4], and validation conducted through computational modeling [6–9] and experimental methods [9–15]. These methods are reviewed in the next sub-sections. Two key metrics in shape optimization and validation is the activation charge (Q) and energy (E_{load}) of the stimulation pulses, which are calculated using [2, 8]:

$$Q = \int_0^{\text{PW}} I_{\text{stim}}(t) dt, \quad (3.1)$$

and

$$E_{\text{load}} \propto \int_0^{\text{PW}} I_{\text{stim}}^2(t) dt, \quad (3.2)$$

where $I_{\text{stim}}(t)$ is the stimulation current, and PW the pulse width.

3.1.1. PULSE-SHAPE OPTIMIZATION

An analytical approach to finding energy-efficient pulse shapes was developed in [1]. Using a nerve membrane model similar to the HH-model in Fig. 2.10 and optimal theory of dynamical systems, the optimal pulse shape was derived. An important assumption in this analysis is that the membrane conductance (g_m) for sub-threshold conditions was assumed to be zero or constant. For the case where g_m is zero (non-leaky membrane),

the optimal shape was found to be a square pulse, while for a leaky membrane ($g_m > 0$), the optimal shape was an exponentially rising pulse. However, validation of these pulses with realistic models and *in vivo* experiments showed that the exponentially rising pulse did not perform better than rectangular, ramp, or decaying exponential waveforms [9]. Therefore, the linearization of the membrane seems to be too simplified to lead to any meaningful insights into efficient pulse shapes.

The complexity and nonlinearity of the realistic membrane models make it impossible to derive energy-optimal pulses analytically [2]. Instead, [2] developed an optimization algorithm to reveal energy-efficient waveforms. Their genetic algorithm was applied to a model of extracellular stimulation of a mammalian myelinated axon. The resulting pulse resembled (truncated) Gaussian curves or half-sines, which were also found to be energy-efficient in [6]. An interesting result of the algorithm was that the energy-duration curve was no longer U-shaped; instead, the energy plateaued with increasing pulse durations. This has to do with the definition of the PW, where the algorithm was allowed to have tails of zero amplitude. Therefore, at a given PW, the algorithm could always produce the same waveform of a shorter PW bounded by a zero amplitude tail. As a result, for increasing PW the energy would never increase. Over the PW range of 0.05 ms to 0.2 ms, the optimized waveforms were found to be 5 % to 60 % more energy efficient than either rectangular or decaying exponential waveforms. Furthermore, the results were validated *in vivo* by stimulation of the sciatic nerve in cats. The waveform was found to be more energy-efficient than rectangular pulses but not substantially more efficient than decaying exponential pulses. Although the algorithm was not intended to minimize the charge of the pulse, the resulting waveform was also more charge-efficient than rectangular pulses.

In another approach to shape optimization, [3] applied the Least-Action Principle (LAP) to a model of intracellular stimulation. One finding is that long pulse durations are much more sensitive to the pulse shape, whereas rectangular pulses are generally optimal for short pulse durations. Their approach describes a general and model-independent description of the optimization. Importantly, the LAP is applied to three different models and results in different energy-optimal pulses. In a passive membrane model, the LAP results in an exponentially rising optimal pulse, while for the active models, the optimal shapes are similar to (truncated) Gaussian or half-sine pulses.

Finally, [4] optimized the stimulation pulse shape using a least squares optimization approach. Their cost function minimizes the total charge while keeping the shape of the pulse smooth. They found a dependency of the optimal shape on the maximum applicable current, the required level of smoothness, the pulse duration, and the neuron model. Furthermore, they found a trade-off between pulse smoothness and total delivered charge. All optimal shapes contained a rise in the tail of the pulse.

3.1.2. VALIDATION OF NON-RECTANGULAR PULSES

The efficacy of non-rectangular pulses in electrical stimulation has been extensively validated using computational models, *in vivo* experiments, and practical applications across various domains. Figure 3.1 illustrates the different pulse shapes evaluated in these studies. The definition of the PW for non-rectangular pulses is not consistent throughout the literature, making PW-based comparisons complicated and biased [8, 10, 16]. This

section summarizes the results of the validation studies.

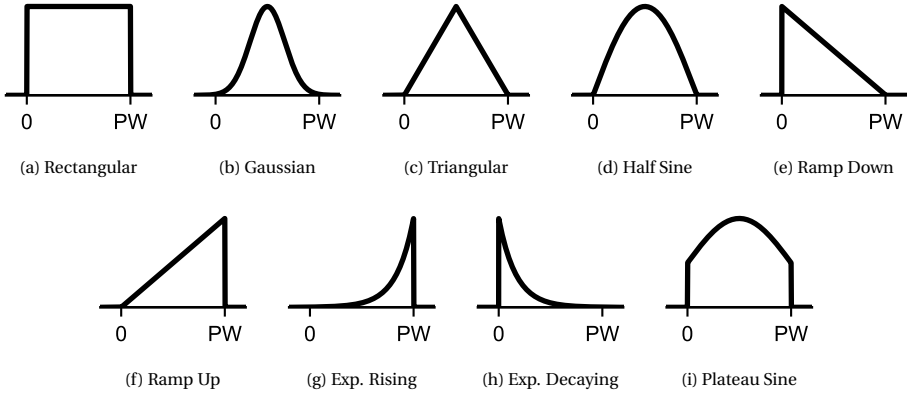


Figure 3.1: Overview of the most common pulse shapes used in the literature. Note that some papers define the pulse width (PW) of the non-rectangular pulses differently from shown here.

Sahin and Tie [6] evaluated several pulse shapes using computational models, including rectangular, ramp-up, ramp-down, exponential increase, exponential decrease, Gaussian, and sine pulses. It was found that ramp-up, Gaussian, and sine pulses exhibited lower energy minima compared to rectangular pulses. The study also investigated the charge efficiency of these waveforms by measuring the shape-dependent charge injection capacity (CIC) of titanium nitride (TiN) electrodes and the corresponding activation charge for each pulse. Using a goal function defined as the ratio of CIC to activation charge, they found that ramp-down, exponential decay, and Gaussian pulses achieved superior performance, enabling smaller electrode designs compared to rectangular pulses.

In the context of deep brain stimulation, Foutz and McIntyre [8] evaluated the efficiency of rectangular, rising exponential, triangular, Gaussian, and half-sine pulse shapes. The Gaussian, sine, and triangular pulses required the lowest energy for activation, with the centered-triangular resulting in a decrease in energy by 65 % compared to a standard 100 μ s rectangular pulse, and by 10 % compared to the most energy efficient rectangular pulse. Building on this work, Foutz *et al.* [10] validated these findings by stimulating the sciatic nerve in rats with rectangular and triangular pulses and measuring the resulting contractile force in the gastrocnemius muscle. They reported a U-shaped, non-monotonic relationship between energy and pulse width (PW) for both shapes, with triangular pulses consuming less energy across all PWs. The most energy-efficient waveform was a triangular waveform with a PW of 50 ms, which was 12 % more efficient than the optimal rectangular waveform, which is consistent with their simulation results that estimated energy savings of 10 % [8]. Furthermore, a comparison of charge and energy demonstrated that the triangular pulses consume less energy for a given level of injected charge compared to the rectangular pulses. In addition to the physiological energy reduction, they also looked at the efficiency of the stimulation circuit. In this context, it was shown that adjusting the voltage supply could reduce the losses in the stimulator circuit, and accordingly, it was suggested that the combination of an adjustable voltage supply with

centered-triangular pulses would lead to efficient stimulation.

Similarly, Wongsarnpigoon and Grill [9] compared square, ramp-up, rising exponential, and decaying exponential pulses in terms of energy, charge, and peak power using computational and *in vivo* methods. Importantly, no waveform was simultaneously energy-, charge-, and power-optimal. Consistently, all waveforms exhibited the following properties: charge-optimal at short PWs, power-optimal at long PWs, and energy-optimal at intermediate PWs. Contrary to the findings of the analytical study, the rising exponential waveform did not provide practical improvements in efficiency compared to the other shapes.

In auditory nerve stimulation, Navaii *et al.*[11] examined the charge, power, and energy efficiency of different shapes (rectangular, rising ramp, triangular, and rising ramp-decaying exponential) in a computational model. Furthermore, they provided a circuit implementation for the non-rectangular pulse generators and evaluated the required additional area and power consumption of these circuits. The power consumption of the three circuits was similar, with the triangular pulse generator occupying the least area. Taking both the efficiencies and circuit considerations into account, the rectangular pulses showed a good performance for short and intermediate durations, while rising ramp-decaying exponential and triangular pulses offered the best option for long durations. Moreover, Yip *et al.*[17] used a genetic algorithm to optimize biphasic waveforms for cochlear implants (CIs), achieving energy reductions of 28 %, 35 % and 54 % for PWs of 25 μ s, 50 μ s and 100 μ s, respectively, compared to a rectangular waveform in simulations. The optimized pulse consisted of a decaying cathodic phase, followed by a rectangular anodic phase. Furthermore, the effectiveness of the waveform was tested in human subjects with implanted CIs. For this, the waveform was changed to an exponentially decaying cathodic phase, followed by an exponentially rising anodic phase to create phase symmetry and ensure charge balancing. Subjective loudness for both waveforms was tested in the subjects. The exponential waveform resulted in a reduction of energy by 25 % and a reduction in charge by 25 %. The difference between the simulations and experimental results is attributed to the change in the anodic phase. Simulations of the experimental waveform showed a similar energy reduction as measured. Furthermore, the subjects reported distinctions in the sounds created by the different waveforms, which is an important consideration for the implementation of non-rectangular pulses. Though energy reduction is important, the first priority of a neuroprosthetic device is to provide the user with usable information. The authors suggest that brain plasticity might help to get used to different pulse shapes.

Furthermore, Deprez *et al.*[12] measured the charge efficiency of Gaussian and triangular pulses by stimulating the motor cortex of rats and measuring limb displacement. Both pulses required less charge than a standard biphasic rectangular pulse, though the advantage was partly attributed to natural interphase delays that arise from the low amplitude tails of these pulses. Therefore, they compared both pulses to a biphasic rectangular pulse with an interphase delay. The pulse with interphase delay produced significantly larger limb displacement for the same charge than the triangular pulse but not significantly larger than the Gaussian pulses.

Moving the focus to chopped stimulation pulses, Dali *et al.*[13] evaluated the efficacy of pulse shaping by stimulating the lateral giant fibers (LGF) and medial giant fiber (MGF)

of earthworms. They compared rectangular chopped pulses with chopped quarter sine and ramp pulses. The non-rectangular pulses required less charge to activate the nerves, with the ramp pulse reducing the required charge for activation by 33.9 % in the MGF and by 17.8 % in the LGE, while the quarter sine reduced the activation charge by 22.8 % and 18.1 %, respectively.

Lee and Im [14] measured the effect of non-rectangular stimulation pulses on network-mediated responses in retinal ganglion cells (RGC) using a patch-clamp technique to record spiking activities in the RGCs. For the same charge, non-rectangular pulses evoked stronger responses, indicating an improved charge efficiency. The increasing ramp was most effective among the tested waveforms (triangular, increasing ramp, decreasing ramp).

Using computational models of the human inner ear, Schier *et al.* [7] evaluated the performance of non-rectangular pulses in the application of a vestibular implant. Their results follow the same conclusions as [6, 8], showing good energy performance for Gaussian and centered triangular pulses. The centered triangular pulse was the most energy-efficient whilst also achieving the highest selectivity at equal amounts of expended energy.

Finally, Eickhoff *et al.* [15] experimentally validated the efficiency of Gaussian-shaped waveforms by stimulating the common peroneal nerve of anesthetized rats and measuring the peak twitch force of the extensor digitorum longus muscle. The energy, charge, and peak power of Gaussian pulses were compared to rectangular pulses. In the range of 50 μ s to 200 μ s, the energy efficiency improvement of Gaussian pulses was 17 %. However, it came at the cost of an increase in maximum peak power of 110 % to 200 %. Furthermore, an improvement in charge efficiency of up to 55 % was found. While the energy improvements would allow for more stimulation pulses from the same energy source, the authors argue that the increase in peak power would lead to an undesired increase in the size of the energy source. Furthermore, the complexity of the Gaussian pulses could also lead to an energy increase in the generation of such pulses. Therefore, it would be necessary to evaluate the effect of these findings on the implications on the circuits that generate the pulses.

3.1.3. SYSTEM IMPLEMENTATIONS FOR NON-RECTANGULAR PULSES

Most validation studies focused on the physiological effects of pulse shaping. However, it is often stressed that implementing non-rectangular pulses might add circuit complexity and additional losses [2, 3, 7–9]. The following works implemented non-rectangular pulse generation into their stimulator designs to assess the added complexity and allow for experimental validation of the shapes.

In [18], a system capable of generating rising exponential as well as rectangular stimulation pulses is presented. The rising exponential generator circuit is shown in Fig. 3.2a. The exponential current is generated by applying a voltage ramp to a current DAC, while maintaining the V_{gs} of M_{dia} below threshold. Since the subthreshold current is too low for neural activation, it is amplified by a current amplifier. The voltage ramp required for this circuit is created by charging a capacitor as shown in Fig. 3.2b. The double current mirror (M_{m1-3}) and subtraction circuit (M_{s1-4}) are used to generate a very small current, to keep the size of C small. Both the current I_{in} and the capacitance C are programmable for

flexibility in the ramp generation. Furthermore, an offset current V_{off} is used to program the time constant of the exponential pulse. The simulator circuit consumed $-0.59 \mu\text{W}$ to $59.22 \mu\text{W}$ (-3% to 276%) more power in exponential mode compared to the rectangular mode. Any additional power would counteract the physiological benefits of using the exponential waveform.

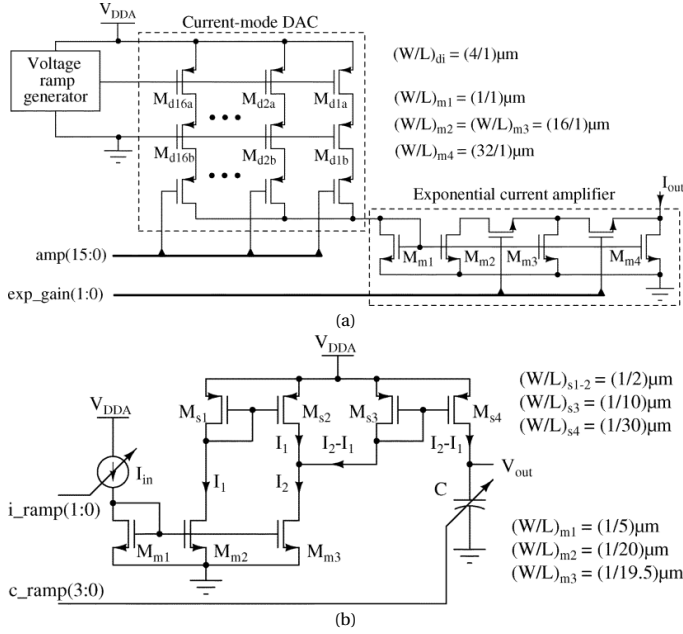


Figure 3.2: (a) Exponential pulse generator from [18] and (b) voltage ramp generator circuit used in (a). Figures from [18] ©2010 IEEE.

The stimulator in [19] can generate half-sine and plateau-sine pulses as these had been identified as being energy-efficient [3]. The half-sine is generated by applying a ramp voltage to two differential pairs of a Gilbert cell, operating in subthreshold region [19, 20]. The ramp voltage for this circuit is generated using a similar circuit as Fig. 3.2b. The non-rectangular pulse generation circuits consume $140 \mu\text{W}$ per channel. It was claimed that a decrease in energy of 3.7% to 29.5% would be possible with these circuits, however, these numbers were estimated and not backed by experimental validation.

Finally, [21] looked at the energy efficiency of decaying exponential waveforms created by a switched capacitor discharge stimulation (SCDS) system, shown in Fig. 3.3. Since the discharging of a capacitor on a resistive load is exponentially decaying, the pulses were generated by discharging a capacitor directly into the tissue. Simulations predicted an energy decrease of 2% to 4% with the decaying exponential waveform, and *in vivo* measurements showed a decrease of 0.4% to 2% . Furthermore, they compared the SCDS method to a constant voltage pulse and predicted that the decaying pulses could save up to 40.7% of energy due to this implementation.

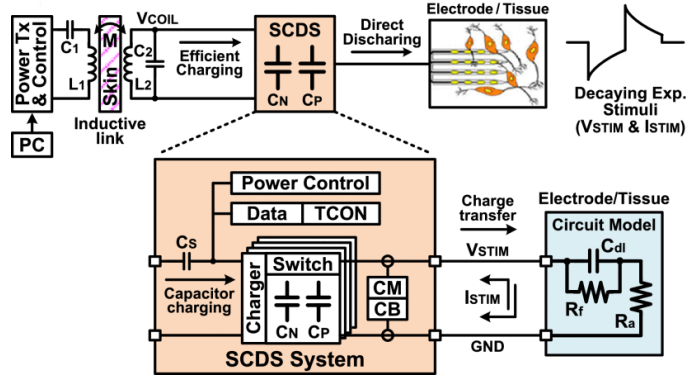


Figure 3.3: Switched capacitor discharging stimulation (SCDS) system proposed in [21]. Capacitors are efficiently charged from the wireless link, and directly discharged into the tissue to generate decaying exponential pulses. Figure from [21] ©2018 IEEE.

3.2. POWER MANAGEMENT IN IMPLANTABLE STIMULATORS

Efficient power management is crucial for ensuring the long-term reliability, safety, and scalability of implantable multichannel stimulation systems. While some low-power applications allow for battery-powered systems, the power demands of advanced implantable systems require active power delivery [22]. Wireless power transfer (WPT) is preferred over a wired solution, as it avoids the risk of infection and improves the safety of the system [23]. Figure 3.4 illustrates a generic block diagram for the WPT and power management in a wirelessly powered implantable device. The wireless link contains a transmitter (Tx) and a receiver (Rx) transducer. The power management unit (PMU) at the receiver side converts the received (ac) power signal into a dc voltage to supply the system. Conventionally, this PMU consists of a rectifier circuit, followed by voltage regulation circuits. This section reviews the different power WPT modalities, implementations for the PMU circuits, and advanced PMU strategies.

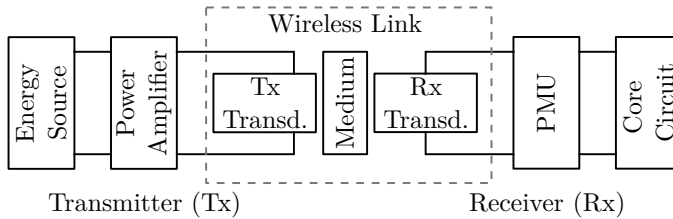


Figure 3.4: Generic block diagram of a wireless power transfer (WPT) link for implantable neurostimulators, consisting of an external transmitter (TX) and an implanted receiver (RX) [24]. Transd. = Transducer, PMU = Power Management Unit.

Several metrics are critical for evaluating the performance of a WPT system. The Power Conversion Efficiency (PCE) is defined as the ratio of the power delivered to the load to the total power received ($PCE = \frac{P_{load}}{P_{RX}}$), reflecting how efficiently the received power is utilized. The Power Transmission Efficiency (PTE) measures the ratio of the power received at the

implant to the power transmitted by the source ($PTE = \frac{P_{RX}}{P_{TX}}$), providing insight into how much of the transmitted power reaches the receiver. Another important metric is the Voltage Conversion Ratio (VCR), which quantifies the effectiveness of the rectification and voltage regulation stages by comparing the DC output voltage to the peak of the AC input voltage ($VCR = \frac{V_{out}}{V_{in,peak}}$). Additionally, the Power Delivered to the Load (PDL) represents the absolute power available at the load (P_{load}).

3.2.1. WIRELESS POWER DELIVERY

WPT can be achieved using different modalities, including inductive coupling [25–47], capacitive coupling [48–50], and ultrasonic [51, 52], RF [53–63], optical [64, 65], and magnetoelectric [66–69] powering. In Fig. 3.5, the different modalities are illustrated. The choice of modality depends on factors such as PTE, PDL, distance, and implant size.

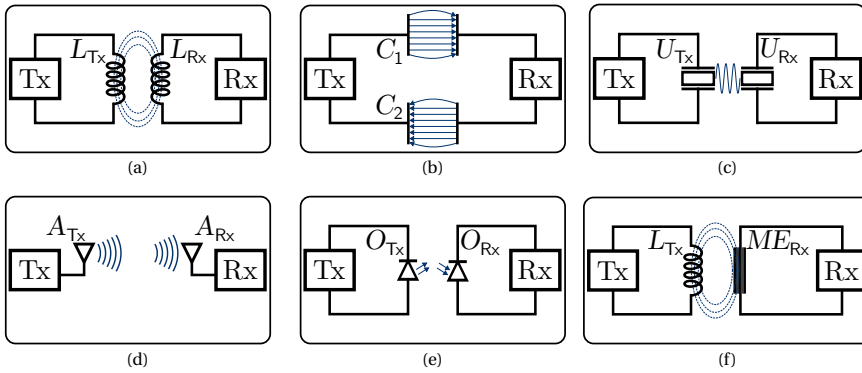


Figure 3.5: Different wireless power transfer modalities. In all figures Tx and Rx denote the power transmitting and receiving circuits, respectively. (a) Inductive WPT, with L_{TX} and L_{RX} representing the transmitting and receiving coils, respectively. (b) Capacitive WPT, where C_1 and C_2 are the two capacitor pairs. (c) Ultrasonic WPT, with U_{TX} and U_{RX} representing the ultrasonic transducer and receiver elements, respectively. (d) Radio Frequency WPT, where A_{TX} and A_{RX} are the transmitting and receiving antennas, respectively. (e) Optical WPT, with O_{TX} and O_{RX} being the optical emitting and receiving elements. (f) Magnetoelectric (ME) WPT, where ME_{RX} is the ME transducer at the receiver side [70].

An inductive WPT link with two coils (Fig. 3.5a) is the most conventional method for powering implantable devices [70]. In this modality, the transmitter (Tx) and receiver (Rx) coils are mutually coupled, enabling power transfer through electromagnetic induction. To improve the coupling, both coils resonate in combination with a capacitor, either in series or in parallel. For the power and distance ranges relevant to biomedical implants, a parallel configuration on the receiver side is usually preferred [34, 71]. The PTE of an inductive link depends on factors such as the alignment and spacing of the coils, the quality factor (Q-factor) of the coils, and their mutual coupling. While inductive WPT is highly efficient over short distances, making it particularly suitable for low-to-medium power implantable medical devices, its efficiency decreases with increasing separation. To mitigate this, multi-coil links with three or four coils have been proposed in the literature, significantly improving PTE over larger distances [70, 72].

In a capacitive WPT link (Fig. 3.5b), two pairs of electrodes are coupled through the

capacitance formed between them. Power transfer is enabled by the displacement current resulting from the application of a time-varying voltage across the Tx electrodes [73]. The efficiency of capacitive WPT is primarily determined by the electrode surface area, the separation distance, and the permittivity of the medium separating the electrodes. While this technique allows for miniaturized receiver designs and reduced magnetic field interference compared to inductive WPT, its practical implementation is constrained by the limited capacitance achievable in implantable configurations and the need for precise electrode alignment.

An ultrasonic (US) WPT link (Fig. 3.5c) uses acoustic waves to transmit power through biological tissue. In this modality, the Tx transducer converts electrical energy into acoustic waves, which propagate through the tissue and are captured by the Rx transducer, where they are converted back into electrical energy. US WPT is advantageous for deeply implanted mm-sized devices because the losses in tissue are smaller than of electromagnetics [70]. Additionally, the allowable ultrasonic intensity for safe operation is higher than that of electromagnetic power transfer methods, enabling efficient power delivery while remaining within safety limits [29, 70]. The use of phased arrays for beam steering further enhances its potential by enabling precise energy delivery, compensating for misalignments, and allowing selective power transmission to multiple implants.

For optical power transfer (Fig. 3.5e), lasers or LEDs are used. The Tx emits focused light, which is captured by a photovoltaic cell at the Rx, converting optical energy into electrical power [64]. Optical WPT offers high energy density and enables precise power delivery, making it advantageous for applications requiring localized and controlled energy transfer. However, its efficiency is significantly reduced by tissue opacity and scattering effects, which attenuate the transmitted light. Furthermore, thermal effects resulting from light absorption in biological tissues pose safety concerns.

Radio-frequency (RF) WPT (Fig. 3.5d) utilizes electromagnetic waves in the RF spectrum to deliver power wirelessly over longer distances compared to near-field techniques such as inductive and capacitive WPT. This modality employs transmitting and receiving antennas to transfer RF energy [53]. While RF WPT enables flexible power delivery to multiple implants and does not require precise alignment like capacitive or inductive coupling, its efficiency is limited by tissue attenuation [74, 75]. Additionally, the relatively high specific absorption rate (SAR) of RF energy in biological tissue raises safety concerns, making it more suitable only for low-power applications [74, 75].

Finally, a magnetoelectric (ME) WPT link (Fig. 3.5f) utilizes the ME effect to convert magnetic energy into electrical energy. In this modality, an alternating magnetic field generated by the Tx induces strain in a magnetostrictive material at the Rx, which is coupled to a piezoelectric layer, resulting in voltage generation [70]. Since ME transducers are more effective at converting magnetic fields into electric fields than inductive coils, they enable operation at lower frequencies, reducing both attenuation and SAR in biological tissue [70]. Additionally, ME receivers can be significantly smaller than the coils used in inductive WPT, making this modality particularly well-suited for small, deeply implanted devices.

Each of these wireless power transfer (WPT) modalities presents distinct advantages and trade-offs, making them suitable for different applications. Inductive WPT remains the most established and widely used approach due to its high power transfer efficiency

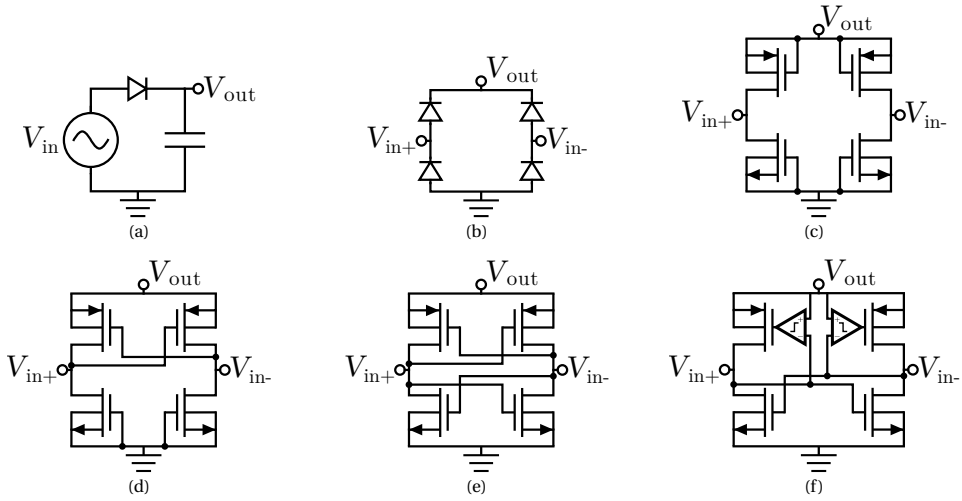


Figure 3.6: Common rectifier topologies [27]: (a) Half-bridge rectifier, (b) Diode-based full-bridge rectifier, (c) Diode-connected MOSFET full-bridge rectifier, (d) Cross coupled passive rectifier, (e) Differential fully cross-coupled passive rectifier, (f) Active rectifier with cross-coupled NMOS pair and comparator-controlled PMOS active diodes.

(PTE) and reliability over short distances, though it requires careful coil alignment and suffers from reduced efficiency with increasing separation [70]. Capacitive WPT, while advantageous for transferring more power, suffers from crosstalk between the capacitor pairs. Increasing the distance between the pairs improves the PTE and PDL, but requires a large area for the link [70]. Ultrasonic WPT offers deep tissue penetration with relatively low attenuation and allows for beam steering, but it is constrained by conversion losses from the acoustic to the electrical domain. Furthermore, the skull poses a challenge for this modality since it reflects a large part of the transmitted power [76]. As a solution, US powering implementations avoid the skull by using a cranial transducer [77] or use another modality to cross the skull [76, 78]. Optical WPT provides precise, high-energy power transfer but suffers from severe tissue scattering and absorption, posing safety and efficiency concerns. RF WPT, while enabling longer-range energy transfer, is limited by tissue attenuation and safety constraints related to SAR, restricting it to low-power applications [22]. Magnetoelectric (ME) WPT presents a promising alternative for ultra-miniaturized, deep implants due to its high magnetic-to-electric conversion efficiency and reduced SAR, though its power transfer capabilities remain lower than inductive methods [70].

3.2.2. RECTIFIER DESIGN

In most WPT modalities introduced in the previous section (except for optical power transfer), the received power signal is alternating and requires rectification to a DC voltage to be used by the rest of the system. Several rectifier topologies exist, which can be divided into passive and active methods. This section describes the different rectifier topologies and their design trade-offs.

Passive rectifiers consist of either diodes or diode-connected MOSFETs with an output capacitor. The simplest implementation, the half-bridge rectifier, only uses a single diode (Fig. 3.6a). When the voltage at V_{in+} is higher than V_{out} , the diode is forward biased and allows for a current path that charges C_{out} . The output capacitor C_{out} filters the output voltage and its size determines the ripple voltage seen at the output. A disadvantage of the diode is the voltage drop, which leads to power loss in the diode and a reduced VCR. Furthermore, the half-bridge topology can only charge C_{out} once every period of the input signal.

The full-bridge implementation (Fig. 3.6b) charges the output twice in each period. As a result, C_{out} can be smaller for the same ripple voltage. However, this topology suffers from two diode voltage drops, increasing the losses and reducing the VCR. In integrated circuits, the diodes are commonly implemented as diode-connected MOSFETs [79], as shown in Fig. 3.6c. While the frequency response is enhanced compared to the diode-based implementation, the conduction losses remain high due to the MOSFETs operating in the saturation region [79]. Cross-coupling the gates of one MOSFET pair, as illustrated in Fig. 3.6d, raises the gate voltage, reducing the voltage drop across the transistors and consequently improving power losses in the cross-coupled transistors [79, 80]. However, the bottom pair is still diode-connected and thus suffers from the low efficiency mentioned before. Finally, a fully cross-coupled rectifier, as shown in Fig. 3.6e, is possible [79, 81]. While this implementation has very low voltage drops in the current path, it is prone to reverse leakage currents from the output to the input, which affects the PCE of the circuit [79, 82, 83]. Recent advancements in passive rectifier circuits use bias tuning [84] or bootstrapping [85, 86] to improve the PCE by reducing conduction losses and reverse currents.

To reduce the voltage drop and conduction losses while preventing reverse currents, active control of the MOSFETs can be used [22, 87]. Active rectifiers typically use the same full-bridge structure, with active circuits driving the gates of one pair in the bridge and the other pair cross-coupled as illustrated in Fig. 3.6f. Alternatively, all four MOSFETs could be actively driven. However, the cross-coupled pair reduces the active circuits, making the implementation smaller and more efficient. A challenge in active rectifier circuits is non-ideal switching due to delays in the comparators, diminishing the PCE. A delay in the turn-on time reduces the effective conduction time leading to less charging of C_{out} , while a delay in the turn-off time causes reverse currents [22] as illustrated in Fig. 3.7. The negative effects of delays become increasingly more important for higher frequencies of the power signal [22]. To improve efficiency, compensation schemes to optimize the switching timing are the focus of many active rectifier implementations. In some works, the delay is compensated by adding a fixed offset voltage to the comparator using unbalanced sized input transistors [88], unbalanced bias currents [89–91], or a combination of both [92, 93]. However, the delay in the comparators is susceptible to process, voltage, and temperature (PVT) variations, and a fixed compensation will not optimize the timing of switching. Therefore, adaptive compensation schemes are designed to optimize the switching timing. These implementations typically use a negative feedback loop to adaptively change the delay compensation. Adaptive compensation designs can be divided into current mode (CM), voltage mode (VM), and delay mode (DM) compensation. In most CM compensation implementations, an offset is created by adding a current to one of the

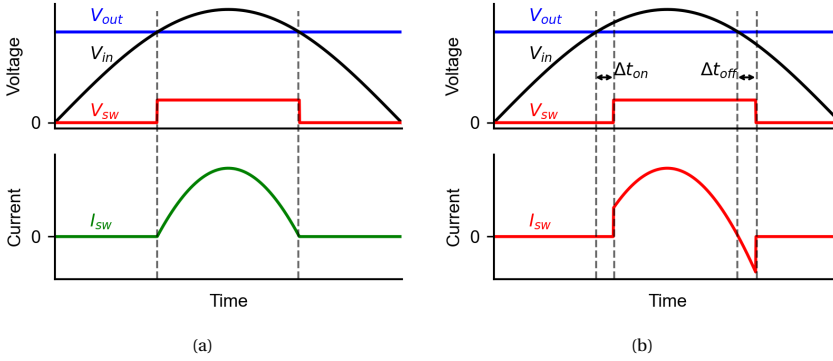


Figure 3.7: Waveforms in the active rectifier circuits, where V_{out} is the output voltage, V_{in} is the input voltage, V_{sw} is the control signal for the active diode, and I_{sw} is the current through the active diode. (a) Ideal switching. (b) Non-ideal switching, where Δt_{on} and Δt_{off} are the on and off-switching delays, respectively.

branches of the comparator [71, 94–96]. Two separate feedback loops are used for the on- and off-switching, injecting a current into the opposite branch. During the conduction pulse, the circuit switches between the on- and off-switching compensation currents. Since this alters the tripping point of the comparator, it could lead to instability, causing the comparator to create multiple pulses. To prevent multiple pulses, most designs use an SR-latch that only allows for a single pulse each period [71, 90, 94]. An alternative implementation of CM compensation is changing the bias current in one of the branches by changing the bulk voltage of the current source [97]. In VM compensation, the offset is generated by adding a voltage in one of the branches of the common-gate comparator [98]. One way to add this voltage is by adding a voltage-controlled resistance in series with the input [98]. Compared to CM, VM has the advantage that it does not affect the power consumption of the comparator. However, the compensation range that can be created is more limited [96]. Alternatively, the switching is regulated with delay elements in DM compensation [99–103]. A clock signal is created from the input waveform, from which the timing is controlled with voltage- or current-controlled delay lines or digital blocks. An advantage of this implementation is that it does not have the problem of multiple pulses and that the feedback can be implemented with low power [96]. However, the compensation range might be a challenge, especially at lower operating frequencies since it requires long delay elements [96]. Finally, some designs use hybrid compensation schemes, such as a combination of VM for on-switching and DM for off-switching [104, 105], or CM for on-switching and VM for off-switching [106].

3.2.3. VOLTAGE REGULATION

In conventional power management for implantable devices, a voltage regulator typically follows the rectifier to ensure a stable supply voltage. Two types of voltage regulation are commonly used: low-dropout (LDO) regulators and switched-mode DC/DC converters. The typical structure of an LDO is illustrated in Fig. 3.8. It consists of an error amplifier that regulates the voltage drop across the pass transistor to maintain a stable output

voltage. In many implementations, V_{out} is attenuated at the input of the amplifier [22]. The amplifier should operate with low power consumption while maintaining a high slew rate to accommodate quick changes in the input voltage or load current [22]. A key limitation of linear regulators is their efficiency, which is constrained by power dissipation in the pass transistor. The PCE is particularly low when the ratio V_{out}/V_{in} is much smaller than one [22, 107]. The pass transistor in an LDO is typically a PMOS device, such that its gate can be driven by a low voltage for it to operate in the active region [87]. One of the primary challenges in LDO design is ensuring stability of the feedback loop, as it contains two dominant poles: one at the gate of the pass transistor and another at the output [87]. To maintain stability, frequency compensation is required to control the location of at least one of these poles and ensure sufficient phase margin.

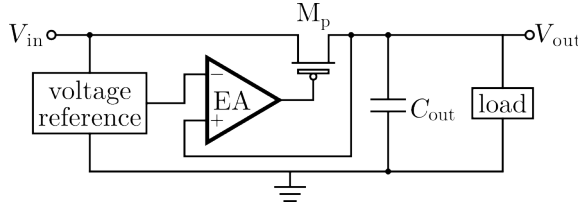


Figure 3.8: Typical schematic of an LDO. The error amplifier (EA) regulates the voltage drop over the pass transistor (M_p) by controlling its gate voltage [22].

Where linear regulators can only regulate an output voltage that is lower than the input, switched mode converters offer more flexibility providing step-down (buck), step-up (boost), or step-up/down (buck-boost) conversion [87]. These converters are implemented using either inductor-based or switched-capacitor (SC) architectures. In inductor-based converters, energy transfer using ideal inductors and switches could be lossless in theory. However, practical implementations suffer from the Q-factor of the inductor and conduction losses in the switches. Additionally, it is difficult to design high-quality inductors on-chip, which limits the scalability of the inductor-based converters [87]. On the other hand, SC converters rely on charge redistribution across capacitors, introducing losses due to parasitic resistances [87]. Despite this drawback, the ability to implement SC converters fully on-chip makes them particularly well-suited for compact implantable devices [87]. Another advantage is the relative ease of ensuring control loop stability, as SC converters introduce only a single dominant pole in the power stage, whereas inductor-based converters typically contain two poles, making stability considerations more complex [87]. Output voltage regulation in SC converters is typically achieved through pulse frequency modulation or capacitor modulation, whereas in inductor-based converters, it is achieved by adjusting the duty cycle of the switches [87].

Compared to LDOs, switched-mode converters typically achieve better PCE, particularly when the difference between V_{in} and V_{out} is large [22]. Furthermore, the ability to perform step-up conversion is useful in applications that require high-voltage supplies. However, the use of inductors or capacitors increases the required area, and the switching operation increases the ripple at the output and adds noise to the system [22, 107].

3.2.4. REGULATING RECTIFIERS

An inherent disadvantage of the conventional power management implementation of a rectifier followed by a voltage regulator is the cascaded losses that lead to low overall efficiency [107]. The total PCE is the product of the efficiencies of each stage, as described by [107]:

$$\text{PCE} = \eta_{\text{rectifier}} \cdot \eta_{\text{regulator}} \quad (3.3)$$

To avoid the cascaded losses and improve efficiency, single-stage regulating rectifier circuits have been introduced. One approach to regulate the output of an active rectifier is by controlling the conduction time of the active diodes (Fig. 3.9) [27, 107–111]. In [108, 109] the conduction time of the active diode is controlled using phase control. Similar to the normal active rectifier circuits, the on-switching is controlled by a comparator. However, in this case, the turn-off timing is controlled by a negative feedback loop that compares the output voltage with a reference voltage and changes the conduction time accordingly (Fig. 3.9b). For light load conditions, the conduction time would be short which leads to low PCE due to switching losses. Therefore, pulse frequency modulation (PFM) was added in [108] to reduce the switching events and increase the conduction time for low-power loads, as illustrated in Fig. 3.9c.

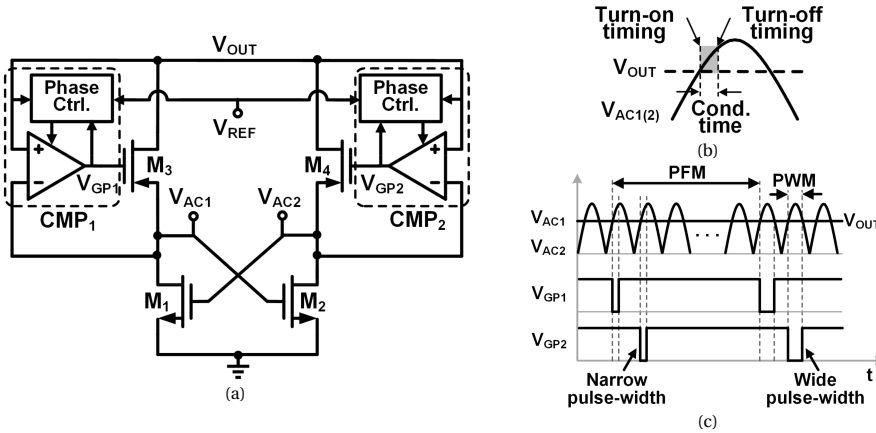


Figure 3.9: Regulating rectifier implementation using turn-on phase control. (a) Schematic of the implementation of [112], (b) timing diagram of phase-controlled rectification, and (c) pulse frequency modulation (PFM) proposed in [108] to avoid short pulse durations for light-load conditions [107]. Figures adapted from [107].

Another method of single-stage regulation is a reconfigurable regulating rectifier (R^3) topology (Fig. 3.10) [31, 113–119]. In this approach, the rectifier can switch between different gain (e.g., 1x, 2x) configurations. By switching between the gain settings, any intermediate gain can be achieved. Using a negative feedback loop that controls the duty cycle of the gain settings, the output is regulated to the desired voltage [107, 113].

A third method uses multi-cycle Q-modulation, also referred to as current-mode regulation (Fig. 3.11) [24, 38, 39, 43, 44]. In this method, the LC tank of an inductive WPT link is switched between two modes: resonant mode (Fig. 3.11b) and charging mode (Fig. 3.11c). During the resonant mode, the tank operates in parallel and remains

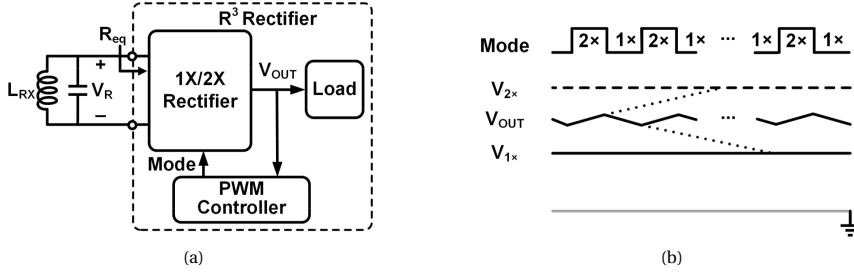


Figure 3.10: (a) Circuit block diagram and (b) regulation principle of the reconfigurable resonant regulating (R^3) rectifier [107, 115]. The circuit regulates the incoming power signal to the desired output voltage in a single stage by reconfiguring between different gain settings. Figures adapted from [107].

disconnected from the circuit for multiple cycles, allowing energy to accumulate within the LC components. In the charging mode, the inductor is connected in series with the load, enabling the transfer of accumulated energy to the load. This method allows for boosting the output voltage when the peak voltage of the incoming power signal is insufficient for the operation of the circuit [107]. However, the PCE is typically lower than voltage-mode regulation methods [44]. The reconfigurable voltage-mode/current-mode integrated power management (VCIPM) in [120] automatically switches between voltage-mode and current-mode regulation depending on the input signal to achieve high PCE and a wide operation range.

3.2.5. POWER MANAGEMENT STRATEGIES IN MULTICHANNEL STIMULATOR SYSTEMS

One challenge in multichannel current mode stimulation (CMS) is the inherent variability in electrode impedance and the current amplitude across channels and over time leading to varying load voltages at each channel [121]. Conventionally, a fixed voltage supply is used to drive all channels leading to excessive power loss on the channels where there is a mismatch between the load voltage and the supply voltage.

To address this, several scalable voltage supply strategies have been proposed to minimize output driver losses. The power management strategies found in multichannel stimulator designs can be categorized into four approaches, as illustrated in Fig. 3.12: (1) conventional fixed voltage supply, (2) global voltage scaling, (3) local voltage regulation, and (4) N-stepped voltage regulation.

In conventional implementations, a single fixed voltage is used for all channels (Fig. 3.12a). This power management strategy has the simplest implementation and commonly uses a rectifier followed by a voltage regulator as discussed in Sections 3.2.2 and 3.2.3. However, the voltage supply is designed to accommodate the worst-case load voltage and leads to low power efficiency in a system with variable load conditions across channels [122].

To reduce the overhead losses, the second strategy employs a single adaptive voltage supply for the entire system (Fig. 3.12b). One method involves adjusting the transmitted power signal to lower the supply voltage post-rectification [123], requiring uplink commu-

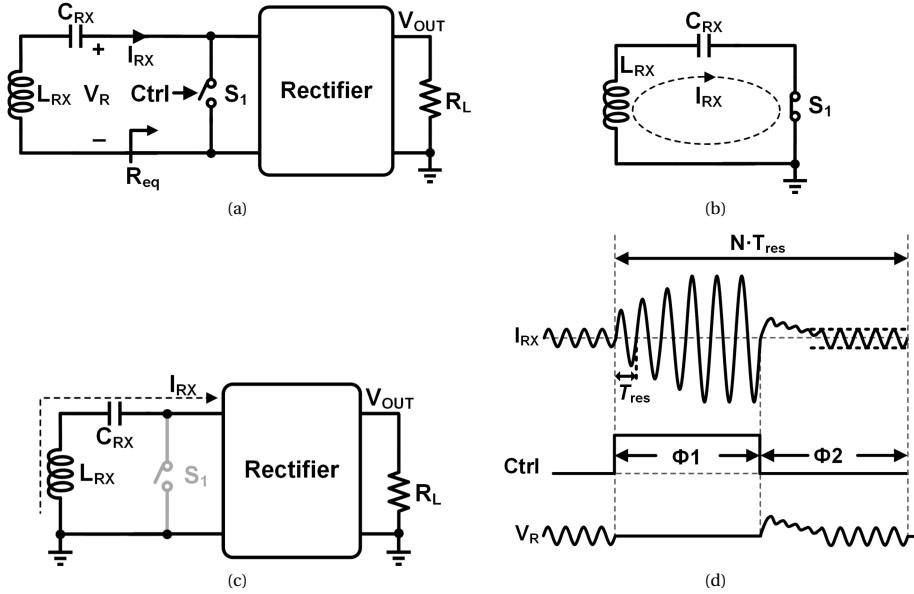


Figure 3.11: (a) Circuit block diagram for the Q-modulation method, which switches between (b) resonant mode and (c) charging mode [24]. (d) Timing diagram for the multi-cycle Q-modulation scheme [38]. Figures adapted from [107].

nication for voltage control. Alternatively, a DC/DC converter can be used to dynamically generate the required voltage [124–129]. Inductor-based DC/DC converters [124] offer high efficiency but require bulky off-chip components, while switched-capacitor DC/DC converters [125–129] enable full integration but provide only discrete voltage steps, limiting precision.

The third approach introduces local voltage regulation at the output driver level (Fig. 3.12c). In [130], each stimulator output features a dedicated charge pump to dynamically adjust the voltage. However, the limited number of voltage steps restricts efficiency gains, and increasing the resolution requires additional capacitors, significantly impacting the area and scalability of each channel.

The last approach employs a parallel DC/DC converter at the global scale (Fig. 3.12d) [111, 131–138]. In this strategy, a multi-output DC/DC converter generates N supply rails that are distributed to all channels, with each output driver selecting the optimal rail via a multiplexer (MUX). While this reduces the area impact compared to local scaling, higher resolution increases routing complexity and MUX complexity.

3.3. DESIGN OF MULTICHANNEL STIMULATION SYSTEMS

Multichannel stimulator systems are widely implemented across various applications. A comparison of recent works is summarized in Tables 3.1 and 3.2. Table 3.1 outlines the primary focus and key specifications of current-mode stimulation, while Table 3.2 examines the power management strategies in these systems. Notably, not all designs

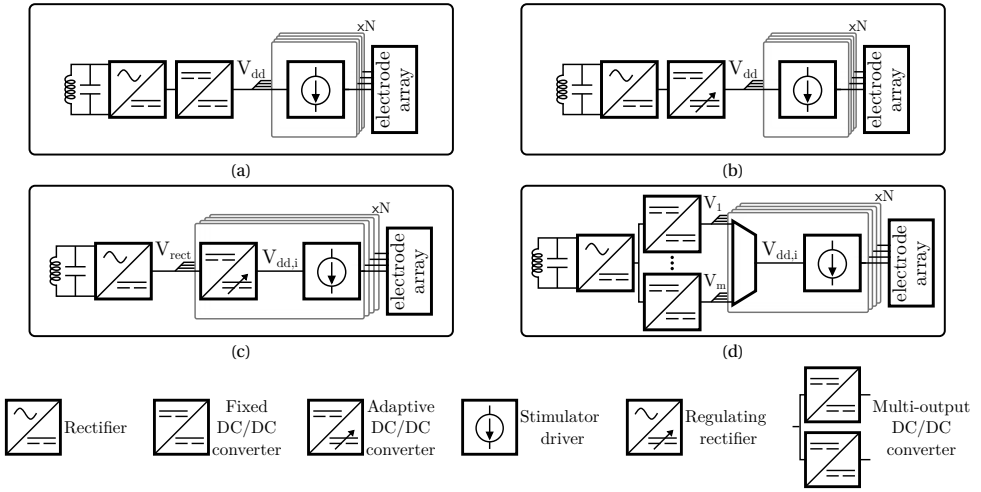


Figure 3.12: Overview of power management strategies for adaptive voltage regulation in multichannel stimulator systems with a modular architecture. Each module contains at least an output driver that can connect to one or more electrodes and may incorporate additional local circuitry. (a) Conventional fixed voltage supply; (b) Global singular voltage regulation, where all modules share a common adaptive V_{dd} ; (c) Localized parallel voltage regulation, employing individual adaptive DC/DC converters within each module; (d) Global parallel voltage regulation, using a multi-output DC/DC converter to generate m voltage rails at the system level, with each module using a multiplexer to select the appropriate voltage.

demonstrated a full system implementation, including the WPT link. Several common trends can be identified, influencing the overall system design and specifications. This section describes the different focus areas in multichannel stimulator development.

One important aspect of multichannel stimulators is the ratio of stimulation drivers to channels. In this context, a stimulation driver refers to a current source delivering stimulation current, while a channel represents either a single electrode (monopolar) or a group of electrodes (bipolar and multipolar) that the driver connects to. Some designs adopt a shared-driver architecture, where a single driver is used across multiple channels to reduce system area. However, this limits stimulation flexibility, as not all channels can be activated simultaneously. Therefore, the ratio offers a trade-off between area and flexibility. While the majority of systems integrate the multichannel stimulator within a single-chip platform, alternative approaches explore distributed networks of low-channel-count implants [56, 139]. In this approach, the transmitter has to power and communicate to many receivers, which results in distinct approaches for the power management.

As described in Section 3.2.5, the power management strategy of a multichannel system is important for overall power efficiency. As shown in Table 3.2, three strategies can be distinguished in the compared designs. Most commonly, a fixed voltage supply is applied as it is the simplest implementation. In [140–142], the global voltage scaling of Fig. 3.12b is applied, and [131, 132, 134] implement dynamic voltage scaling (DVS) using an N-step supply and local multiplexer circuits (Fig. 3.12d). Furthermore, many designs focus on high-voltage (HV) compliance for the stimulator output. Depending on the application,

the amplitude of the stimulation current and the impedance of the electrodes can result in a large load voltage, requiring an HV supply to drive the stimulation. Importantly, not all of these systems are implemented in a HV CMOS technology. Instead, stacked output driver circuits are used to allow HV operation in standard CMOS technology to mitigate the large area typically associated with HV devices [130, 143–147]. The HV supply voltage is often generated using charge pump (CP) circuits, which is a type of SC DC-DC boost converter [19, 130, 134, 139, 140, 146].

Another important specification concerns the long-term safety in electrical stimulation, which requires charge balancing (CB) to prevent irreversible electrochemical reactions from charge building up on the electrodes [148]. Advanced CB techniques have been the topic for many stimulator circuit designs [149]. Some implementations aim for high-resolution amplitude control to minimize charge imbalance [145, 150], while others implement active CB methods that monitor the electrode voltage and dynamically change the stimulation signal accordingly [142]. Another area of focus of several designs is closed-loop stimulation [130, 140–142, 146, 150–153]. In closed-loop systems, the stimulator circuits are combined with neural recording circuits to adaptively control the stimulation signals based on the recorded activity. Finally, while most implementations focus on current mode stimulation (CMS) with rectangular pulses, some designs offer other modalities such as switched-capacitor stimulation (SCS) [139], optogenetic stimulation [151] or voltage mode stimulation (VMS) [144, 153] and non-rectangular stimulation pulses [19, 130, 153]. The design considerations discussed above show the diverse focus areas in multichannel stimulator systems. Each of these topics contributes to the application-specific design requirements, resulting in considerable differences between the implementations.

3.4. DISCUSSION AND RESEARCH QUESTIONS

The advancements in stimulation pulse optimization, power management, and multichannel designs presented in this chapter demonstrate the diverse approaches taken to improve the energy efficiency of implantable stimulators.

As discussed in Section 3.1, the energy efficiency is pulse-shape dependent. The optimization methods have shown that oversimplification of the problem leads to wrong conclusions. Where analytical models predicted optimal performance of exponential pulse shapes, validation in computational models and experimental validation refuted these claims. Computational models identified, Gaussian, triangular, and sine-shaped pulses as promising alternatives for improving energy efficiency. However, the efficiencies in experimental validation are found to be marginal. Most of the studies focused on the energy efficiency in the biological domain and neglected additional losses in the stimulation circuits. Hence, there is a knowledge gap on how to optimize the pulse shapes taking into account the losses in both domains.

Furthermore, Section 3.2, discussed different aspects of power management in implantable devices and power management strategies for multichannel stimulation systems. Traditionally, these systems are powered by a fixed voltage supply. However, as discussed in Section 2.1.7, multichannel applications typically experience varying load conditions on the different channels. While the strategies presented in Section 3.2.5 aim to address these variations, their effectiveness has not been quantified. As a result, com-

Table 3.1: Comparison of recent multichannel electrical stimulation implementations based on the key focus of the design and current mode stimulation parameters. WPT = Wireless Power Transfer, SCS = Switched Capacitor Stimulation, CMS = Current Mode Stimulation, DVS = Dynamic Voltage Scaling, HV compl. = High-Voltage Compliance, VMS = Voltage Mode Stimulation, Rect. = Rectangular, HS = Half-Sine, PS = Plateau-Sine, CB = Charge Balancing, N/S = Not Specified.

Work	Year	Focus	Channels [#]	Current Drivers [#]	Polarity	Pulse shape	Imax [µA]	Resolution [bits]
[56]	2024	Network of implants	8	1	Bipolar	Rectangular	120	5
[139]	2024	Network of implants, Optical WPT, SCS	1	1	Bipolar	Rectangular	400	3
[151]	2020	Closed-loop, Multimodal (Optical & CMS)	8	4	Bipolar	Rectangular	775	5
[140]	2018	Closed-loop	64	8	Bipolar	Rectangular	5100	8
[152]	2017	Closed-loop	64	64	Monopolar	Rectangular	1350	8
[131]	2024	DVS	4	4	Bipolar	Rectangular	1500	8
[132]	2023	DVS	505	505	Bipolar	Rectangular	160	6
[153]	2021	HV compl., Closed-loop, Multimodal (CMS & VMS)	32	32	Multipolar	Arbitrary	10200	5
[19]	2018	Pulse shaping	16	4	Mono/Bipolar	Rect., HS, PS	210	7
[130]	2020	HV compl., pulse shaping, Closed-loop	4	4	Bipolar	Arbitrary	2000	8
[143]	2024	HV compl.	8	8	Mono/Bipolar	Rectangular	70	3
[144]	2023	Multimodal (CMS & VMS)	4	4	Mono/Bipolar	Rectangular	3600	5
[145]	2023	HV compl., CB	16	16	Monopolar	Rectangular	160	7
[150]	2023	Closed-loop, CB	4	4	Bipolar	Rectangular	1800	12.75
[146]	2022	Closed-loop, HV compl.	16	4	Bipolar	Rectangular	600	N/S
[147]	2021	Monopolar, HV compl.	16	2	Monopolar	Rectangular	3000	4
[154]	2022	Monopolar, Time-to-current converter	16	16	Monopolar	Rectangular	550	~10
[141]	2019	Closed-loop	64	4	Bipolar	Rectangular	5000	N/S
[142]	2022	CB, Closed-loop	16	4	Monopolar	Rectangular	12750	8
[134]	2021	DVS	16	16	Monopolar	Rectangular	100	4

Table 3.2: Continuation of comparison of recent multichannel electrical stimulation implementations focused on power management and dimensions. WPT = Wireless Power Transfer, RF = Radio Frequency, Rect. = Rectangular, LDO = Low Drop Out (regulator), CP = Charge Pump, SIMO = Single- Inductor Multiple-Output (regulator), N/S = Not Specified.

Work	WPT modality	Voltage distribution	Power Management	Compliance [V]	CMOS technology [μm]	Total area [mm^2]	Area/Ch [μm^2]
[56]	RF	Fixed	Rect. + LDO	1.2	0.18	1	1000k
[139]	Optical	Fixed	2-stage CP	4.3	0.18	0.06	62.5k
[151]	Inductive	Fixed	Voltage doubler + LDO	4	0.35	15	N/S
[140]	Inductive	Global	4-stage CP	$\pm 3 - \pm 5$	0.18 HV	16.4	N/S
[152]	Inductive	Fixed	Rect. + LDO	2.5	0.13	5.98	13k
[131]	Inductive	3-steps supply	SIMO DC-DC	6-12	0.18	5.65	N/S
[132]	Inductive	4-steps supply	N/S	1.8-5	0.25	9.6	10k
[153]	Inductive	Fixed	External	± 9	0.18 HV	25	460k
[19]	Inductive	Fixed	CP	± 10	0.8 CMOS/DMOS	16	N/S
[130]	-	Fixed	Resonant CP	± 11	0.065	4	360k
[143]	-	Fixed	External	9	0.18	0.79	24k
[144]	-	Fixed	External	± 6	0.18	1.19	52k
[145]	-	Fixed	External	11	0.065	0.23	14k
[150]	-	Fixed	External	± 5	0.18 BCD	9	N/S
[146]	-	Fixed	12-stage CP	8	0.065	3.48	14k
[147]	-	Fixed	External	± 6	0.18	4.1	1141k
[154]	-	Fixed	External	18.2	0.18 HV	N/S	385k
[141]	-	Global	Prog. DC-DC	12	0.18 HV	N/S	N/S
[142]	-	Global	7-stage CP	20-40	0.18 HV	25	6250k
[134]	-	6-steps supply	Multi-output CP	-5.05 - +3.49	0.18	1.41	50k

parative evaluation of different power management strategies remains an understudied area.

Finally, Section 3.3 presented a comparison of recent multichannel stimulator designs. The various focus areas across these systems lead to significant differences in their architectures and performance. Notably, the comparison confirms that most implementations still rely on a fixed voltage supply, overlooking the power losses associated with this approach. To enhance the energy efficiency of such systems, further investigation into optimal power management strategies is warranted.

Hence, there is a knowledge gap on how to achieve the optimal energy distribution in large-scale multichannel electrical stimulation systems. To address this knowledge gap, this work will answer the following research question:

How can the energy distribution in large-scale multichannel electrical stimulation systems be optimized?

This question is broken down into three sub-questions that are addressed in the following three chapters:

1. *What is the most efficient stimulation waveform when both biophysical effects and circuit design losses are taken into account? (Chapter 4)*
2. *What is the effect of channel variability on the power requirements and the efficacy of power management strategies in multichannel stimulation devices? (Chapter 5)*
3. *How can the required charge be efficiently delivered to multiple subsystems with independent output requirements? (Chapter 6)*

BIBLIOGRAPHY

- [1] S. Jezernik and M. Morari, “Energy-Optimal Electrical Excitation of Nerve Fibers”, *IEEE Transactions on Biomedical Engineering*, vol. 52, no. 4, pp. 740–743, Apr. 2005, ISSN: 0018-9294. DOI: 10.1109/TBME.2005.844050.
- [2] A. Wongsarnpigoon and W. M. Grill, “Energy-efficient waveform shapes for neural stimulation revealed with a genetic algorithm”, *Journal of Neural Engineering*, vol. 7, no. 4, p. 046 009, Aug. 2010, ISSN: 1741-2560. DOI: 10.1088/1741-2560/7/4/046009.
- [3] N. I. Krouchev, S. M. Danner, A. Vinet, F. Rattay, and M. Sawan, “Energy-Optimal Electrical-Stimulation Pulses Shaped by the Least-Action Principle”, *PLoS ONE*, vol. 9, no. 3, D. R. Chialvo, Ed., e90480, Mar. 2014, ISSN: 1932-6203. DOI: 10.1371/journal.pone.0090480.
- [4] B. Tahayori and S. Dokos, “Optimal stimulus current waveshape for a hodgkin-huxley model neuron”, in *2012 Annual International Conference of the IEEE Engineering in Medicine and Biology Society*, vol. 2012, IEEE, Aug. 2012, pp. 4627–4630, ISBN: 978-1-4577-1787-1. DOI: 10.1109/EMBC.2012.6346998.
- [5] L. Yan, H. Zhang, Z. Sun, S. Liu, Y. Liu, and P. Xiao, “Optimization of stimulation waveforms for regulating spike-wave discharges in a thalamocortical model”, *Chaos, Solitons and Fractals*, vol. 158, May 2022, ISSN: 09600779. DOI: 10.1016/j.chaos.2022.112025.
- [6] M. Sahin and Y. Tie, “Non-rectangular waveforms for neural stimulation with practical electrodes”, *Journal of Neural Engineering*, vol. 4, no. 3, pp. 227–233, Sep. 2007, ISSN: 1741-2560. DOI: 10.1088/1741-2560/4/3/008.
- [7] P. Schier *et al.*, “Model-based vestibular afferent stimulation: Evaluating selective electrode locations and stimulation waveform shapes”, *Frontiers in Neuroscience*, vol. 12, no. AUG, Aug. 2018, ISSN: 1662453X. DOI: 10.3389/fnins.2018.00588.
- [8] T. J. Foutz and C. C. McIntyre, “Evaluation of novel stimulus waveforms for deep brain stimulation”, *Journal of Neural Engineering*, vol. 7, no. 6, p. 066 008, Dec. 2010, ISSN: 1741-2560. DOI: 10.1088/1741-2560/7/6/066008.
- [9] A. Wongsarnpigoon, J. P. Woock, and W. M. Grill, “Efficiency analysis of waveform shape for electrical excitation of nerve fibers”, *IEEE Transactions on Neural Systems and Rehabilitation Engineering*, vol. 18, no. 3, pp. 319–328, 2010, ISSN: 15344320. DOI: 10.1109/TNSRE.2010.2047610.
- [10] T. J. Foutz, D. M. Ackermann Jr., K. L. Kilgore, and C. C. McIntyre, “Energy Efficient Neural Stimulation: Coupling Circuit Design and Membrane Biophysics”, *PLoS ONE*, vol. 7, no. 12, G. Foffani, Ed., e51901, Dec. 2012, ISSN: 1932-6203. DOI: 10.1371/journal.pone.0051901.

- [11] M. Lotfi Navaii, H. Sadjedi, and M. Jalali, "Waveform efficiency analysis of auditory nerve fiber stimulation for cochlear implants", *Australasian Physical and Engineering Sciences in Medicine*, vol. 36, no. 3, pp. 289–300, 2013, ISSN: 01589938. DOI: 10.1007/s13246-013-0212-2.
- [12] M. Deprez, K. Luyck, L. Luyten, T. Tambuyzer, B. Nuttin, and M. Mc Laughlin, "An evaluation of the effect of pulse-shape on grey and white matter stimulation in the rat brain", *Scientific Reports*, vol. 8, no. 1, Dec. 2018, ISSN: 20452322. DOI: 10.1038/s41598-017-19023-0.
- [13] M. Dali, T. Guiho, P. Maciejasz, O. Rossel, and D. Guiraud, *Investigation of the efficiency of the shape of chopped pulses using earthworm model*. 2018, ISBN: 9781538636466. DOI: 10.0/Linux-x86_64.
- [14] J. I. Lee and M. Im, "Non-rectangular waveforms are more charge-efficient than rectangular one in eliciting network-mediated responses of on type retinal ganglion cells", *Journal of Neural Engineering*, vol. 15, no. 5, Aug. 2018, ISSN: 17412552. DOI: 10.1088/1741-2552/aad416.
- [15] S. Eickhoff and J. C. Jarvis, "An Investigation of Neural Stimulation Efficiency With Gaussian Waveforms", *IEEE Transactions on Neural Systems and Rehabilitation Engineering*, vol. 28, no. 1, pp. 104–112, Jan. 2020, ISSN: 1534-4320. DOI: 10.1109/TNSRE.2019.2954004.
- [16] W. M. Grill, "Model-based analysis and design of waveforms for efficient neural stimulation", *Progress in Brain Research*, vol. 222, pp. 147–162, 2015, ISSN: 18757855. DOI: 10.1016/bs.pbr.2015.07.031.
- [17] M. Yip, P. Bowers, V. Noel, A. Chandrakasan, and K. M. Stankovic, "Energy-efficient waveform for electrical stimulation of the cochlear nerve", *Scientific Reports*, vol. 7, no. 1, pp. 1–10, 2017, ISSN: 20452322. DOI: 10.1038/s41598-017-13671-y.
- [18] S. Ethier and M. Sawan, "Exponential Current Pulse Generation for Efficient Very High-Impedance Multisite Stimulation", *IEEE Transactions on Biomedical Circuits and Systems*, vol. 5, no. 1, pp. 30–38, Feb. 2011, ISSN: 1932-4545. DOI: 10.1109/TBCAS.2010.2073707.
- [19] M. Hasanuzzaman, B. G. Motlagh, F. Mounaim, A. Hassan, R. Raut, and M. Sawan, "Toward an Energy-Efficient High-Voltage Compliant Visual Intracortical Multichannel Stimulator", *IEEE Transactions on Very Large Scale Integration (VLSI) Systems*, vol. 26, no. 5, pp. 878–891, May 2018, ISSN: 1063-8210. DOI: 10.1109/TVLSI.2018.2794445.
- [20] O. Ishizuka, Z. Tang, and H. Matsumoto, "MOS sine function generator using exponential-law technique", *Electronics Letters*, vol. 27, no. 21, pp. 1937–1939, Oct. 1991, ISSN: 0013-5194. DOI: 10.1049/el:19911202.
- [21] H.-M. Lee, B. Howell, W. M. Grill, and M. Ghovanloo, "Stimulation Efficiency with Decaying Exponential Waveforms in a Wirelessly-Powered Switched-Capacitor Discharge Stimulation System", *IEEE Transactions on Biomedical Engineering*, vol. 65, no. 5, pp. 1–1, 2017, ISSN: 0018-9294. DOI: 10.1109/TBME.2017.2741107.

- [22] H. M. Lee and M. Ghovanloo, "Energy management integrated circuits for wireless power transmission", in *Implantable Biomedical Microsystems: Design Principles and Applications*, Elsevier Inc., Jan. 2015, pp. 87–111, ISBN: 9780323261906. DOI: 10.1016/B978-0-323-26208-8.00005-4.
- [23] Y. T. Wong *et al.*, "CMOS stimulating chips capable of wirelessly driving 473 electrodes for a cortical vision prosthesis", *Journal of Neural Engineering*, vol. 16, no. 2, p. 026025, Apr. 2019, ISSN: 17412552. DOI: 10.1088/1741-2552/ab021b.
- [24] M. Kiani, B. Lee, P. Yeon, and M. Ghovanloo, "A Q-Modulation Technique for Efficient Inductive Power Transmission", *IEEE Journal of Solid-State Circuits*, vol. 50, no. 12, pp. 2839–2848, Dec. 2015, ISSN: 00189200. DOI: 10.1109/JSSC.2015.2453201.
- [25] K. Van Schuylenbergh and R. Puers, *Inductive Powering*, K. Van Schuylenbergh and R. Puers, Eds. Dordrecht: Springer Netherlands, 2009, ISBN: 978-90-481-2411-4. DOI: 10.1007/978-90-481-2412-1.
- [26] P. Perez-Nicoli and F. Silveira, "Maximum Efficiency Tracking in Inductive Power Transmission Using Both Matching Networks and Adjustable AC–DC Converters", *IEEE Transactions on Microwave Theory and Techniques*, vol. 66, no. 7, pp. 3452–3462, Jul. 2018, ISSN: 0018-9480. DOI: 10.1109/TMTT.2018.2831676.
- [27] N. Almarri, D. Jiang, P. J. Langlois, M. Rahal, and A. Demosthenous, "High Efficiency Power Management Unit for Implantable Optical-Electrical Stimulators", *IEEE Open Journal of Circuits and Systems*, vol. 4, pp. 3–14, 2023, ISSN: 2644-1225. DOI: 10.1109/OJCS.2023.3240644.
- [28] R. F. Xue, K. W. Cheng, and M. Je, "High-efficiency wireless power transfer for biomedical implants by optimal resonant load transformation", *IEEE Transactions on Circuits and Systems I: Regular Papers*, vol. 60, no. 4, pp. 867–874, 2013, ISSN: 15498328. DOI: 10.1109/TCSI.2012.2209297.
- [29] U. M. Jow and M. Ghovanloo, "Design and optimization of printed spiral coils for efficient transcutaneous inductive power transmission", *IEEE Transactions on Biomedical Circuits and Systems*, vol. 1, no. 3, pp. 193–202, Sep. 2007, ISSN: 19324545. DOI: 10.1109/TBCAS.2007.913130.
- [30] T. P. G. van Nunen, R. M. C. Mestrom, and H. J. Visser, "Wireless Power Transfer to Biomedical Implants Using a Class-E Inverter and a Class-DE Rectifier", *IEEE Journal of Electromagnetics, RF and Microwaves in Medicine and Biology*, vol. 7, no. 3, pp. 202–209, Sep. 2023, ISSN: 2469-7249. DOI: 10.1109/JERM.2023.3267042.
- [31] X. Li, C. Y. Tsui, and W. H. Ki, "Power management analysis of inductively-powered implants with 1X/2X reconfigurable rectifier", *IEEE Transactions on Circuits and Systems I: Regular Papers*, vol. 62, no. 3, pp. 617–624, Mar. 2015, ISSN: 15580806. DOI: 10.1109/TCSI.2014.2366814.
- [32] M. Catrysse, B. Hermans, and R. Puers, "An inductive power system with integrated bi-directional data-transmission", in *Sensors and Actuators, A: Physical*, vol. 115, Sep. 2004, pp. 221–229. DOI: 10.1016/j.sna.2004.02.016.

- [33] K. M. Silay *et al.*, “Load optimization of an inductive power link for remote powering of biomedical implants”, in *Proceedings - IEEE International Symposium on Circuits and Systems*, 2009, pp. 533–536, ISBN: 9781424438280. DOI: 10.1109/ISCAS.2009.5117803.
- [34] R. Jay and S. Palermo, “Resonant coupling analysis for a two-coil wireless power transfer system”, in *2014 IEEE Dallas Circuits and Systems Conference: Enabling an Internet of Things - From Sensors to Servers, DCAS 2014*, Institute of Electrical and Electronics Engineers Inc., Nov. 2014, ISBN: 9781479959235. DOI: 10.1109/DCAS.2014.6965345.
- [35] D. Ahn and M. Ghovanloo, “Optimal Design of Wireless Power Transmission Links for Millimeter-Sized Biomedical Implants”, *IEEE Transactions on Biomedical Circuits and Systems*, vol. 10, no. 1, pp. 125–137, Feb. 2016, ISSN: 19324545. DOI: 10.1109/TBCAS.2014.2370794.
- [36] H. Jiang, S. Liang, J. Zhang, S. Liou, and H. Shahnasser, “Design and optimization of printed spiral coils in wireless power transfer for biomedical implants”, in *2011 4th International Conference on Biomedical Engineering and Informatics (BMEI)*, IEEE, Oct. 2011, pp. 1064–1067, ISBN: 978-1-4244-9352-4. DOI: 10.1109/BMEI.2011.6098398.
- [37] P. Dehghanzadeh, H. Zamani, and S. Mandal, “Fundamental Trade-Offs between Power and Data Transfer in Inductive Links for Biomedical Implants”, *IEEE Transactions on Biomedical Circuits and Systems*, vol. 15, no. 2, pp. 235–247, Apr. 2021, ISSN: 19409990. DOI: 10.1109/TBCAS.2021.3063376.
- [38] B. Lee, P. Yeon, and M. Ghovanloo, “A multicycle Q-modulation for dynamic optimization of inductive links”, *IEEE Transactions on Industrial Electronics*, vol. 63, no. 8, pp. 5091–5100, Aug. 2016, ISSN: 02780046. DOI: 10.1109/TIE.2016.2550009.
- [39] H. S. Gougheri and M. Kiani, “Current-Based Resonant Power Delivery With Multi-Cycle Switching for Extended-Range Inductive Power Transmission”, *IEEE Transactions on Circuits and Systems I: Regular Papers*, vol. 63, no. 9, pp. 1543–1552, Sep. 2016, ISSN: 1549-8328. DOI: 10.1109/TCSI.2016.2579258.
- [40] M. Zargham and P. G. Gulak, “High-efficiency CMOS rectifier for fully integrated mW wireless power transfer”, in *2012 IEEE International Symposium on Circuits and Systems*, IEEE, May 2012, pp. 2869–2872, ISBN: 978-1-4673-0219-7. DOI: 10.1109/ISCAS.2012.6271912.
- [41] G. B. Joung, C. T. Rim, and G. H. Cho, “Integral cycle mode control of series resonant converter.”, in *PESC Record - IEEE Annual Power Electronics Specialists Conference*, Publ by IEEE, 1988, pp. 575–582. DOI: 10.1109/pesc.1988.18183.
- [42] G. Wang, W. Liu, M. Sivaprakasam, and G. A. Kendir, “Design and analysis of an adaptive transcutaneous power telemetry for biomedical implants”, *IEEE Transactions on Circuits and Systems I: Regular Papers*, vol. 52, no. 10, pp. 2109–2117, 2005, ISSN: 10577122. DOI: 10.1109/TCSI.2005.852923.

- [43] H.-S. Lee *et al.*, “A Power-Efficient Resonant Current Mode Receiver With Wide Input Range Over Breakdown Voltages Using Automated Maximum Efficiency Control”, *IEEE Transactions on Power Electronics*, vol. 37, no. 7, pp. 8738–8750, Jul. 2022, ISSN: 0885-8993. DOI: 10.1109/TPEL.2022.3151427.
- [44] J.-H. Kim, N. u. Hassan, S.-J. Lee, Y.-W. Jung, and S.-U. Shin, “A resonant current-mode wireless power transfer for implantable medical devices: an overview”, *Biomedical Engineering Letters*, vol. 12, no. 3, pp. 229–238, Aug. 2022, ISSN: 2093-9868. DOI: 10.1007/s13534-022-00231-1.
- [45] K. Na, H. Jang, S. K. Oruganti, and F. Bien, “An improved wireless power transfer system with adaptive technique for Implantable Biomedical Devices”, in *2013 IEEE MTT-S International Microwave Workshop Series on RF and Wireless Technologies for Biomedical and Healthcare Applications (IMWS-BIO)*, IEEE, Dec. 2013, pp. 1–3, ISBN: 978-1-4673-6096-8. DOI: 10.1109/IMWS-BIO.2013.6756136.
- [46] P. Si, A. P. Hu, S. Malpas, and D. Budgett, “A frequency control method for regulating wireless power to implantable devices”, *IEEE Transactions on Biomedical Circuits and Systems*, vol. 2, no. 1, pp. 22–29, Mar. 2008, ISSN: 19324545. DOI: 10.1109/TBCAS.2008.918284.
- [47] G. Simard, M. Sawan, and D. Massicotte, “High-speed OQPSK and efficient power transfer through inductive link for biomedical implants”, in *IEEE Transactions on Biomedical Circuits and Systems*, vol. 4, Jun. 2010, pp. 192–200. DOI: 10.1109/TBCAS.2009.2039212.
- [48] R. Jegadeesan, K. Agarwal, Y. X. Guo, S. C. Yen, and N. V. Thakor, “Wireless Power Delivery to Flexible Subcutaneous Implants Using Capacitive Coupling”, *IEEE Transactions on Microwave Theory and Techniques*, vol. 65, no. 1, pp. 280–292, Jan. 2017, ISSN: 00189480. DOI: 10.1109/TMTT.2016.2615623.
- [49] A. M. Sodagar and P. Amiri, “Capacitive coupling for power and data telemetry to implantable biomedical microsystems”, in *2009 4th International IEEE/EMBS Conference on Neural Engineering*, IEEE, Apr. 2009, pp. 411–414, ISBN: 978-1-4244-2072-8. DOI: 10.1109/NER.2009.5109320.
- [50] R. Erfani, F. Marefat, A. M. Sodagar, and P. Mohseni, “Modeling and Experimental Validation of a Capacitive Link for Wireless Power Transfer to Biomedical Implants”, *IEEE Transactions on Circuits and Systems II: Express Briefs*, vol. 65, no. 7, pp. 923–927, Jul. 2018, ISSN: 15583791. DOI: 10.1109/TCSII.2017.2737140.
- [51] A. Ballo, M. Bottaro, and A. D. Grasso, “A Review of Power Management Integrated Circuits for Ultrasound-Based Energy Harvesting in Implantable Medical Devices”, *Applied Sciences*, vol. 11, no. 6, p. 2487, Mar. 2021, ISSN: 2076-3417. DOI: 10.3390/app11062487.
- [52] J. Charthad, M. J. Weber, T. C. Chang, and A. Arbabian, “A mm-Sized Implantable Medical Device (IMD) With Ultrasonic Power Transfer and a Hybrid Bi-Directional Data Link”, *IEEE Journal of Solid-State Circuits*, vol. 50, no. 8, pp. 1741–1753, Aug. 2015, ISSN: 00189200. DOI: 10.1109/JSSC.2015.2427336.

- [53] A. M. Almohaimeed, R. E. Amaya, J. A. Lima, and M. C. Yagoub, "An adaptive power harvester with active load modulation for highly efficient short/long range RF WPT applications", *Electronics (Switzerland)*, vol. 7, no. 7, Jul. 2018, ISSN: 20799292. DOI: 10.3390/electronics7070125.
- [54] G. C. Martins and W. A. Serdijn, "An RF Energy Harvesting and Power Management Unit Operating Over -24 to +15 dBm Input Range", *IEEE Transactions on Circuits and Systems I: Regular Papers*, vol. 68, no. 3, pp. 1342–1353, Mar. 2021, ISSN: 1549-8328. DOI: 10.1109/TCSI.2020.3041175.
- [55] Y. Han, O. Leitermann, D. A. Jackson, J. M. Rivas, and D. J. Perreault, "Resistance compression networks for radio-frequency power conversion", *IEEE Transactions on Power Electronics*, vol. 22, no. 1, pp. 41–53, Jan. 2007, ISSN: 08858993. DOI: 10.1109/TPEL.2006.886601.
- [56] C.-E. Lee, J.-H. Park, J. Lim, C. Choi, and Y.-K. Song, "A wireless stimulator system-on-chip with an optically writable ID for addressable cortical microimplants", *Solid-State Electronics*, vol. 216, p. 108914, Jun. 2024, ISSN: 00381101. DOI: 10.1016/j.sse.2024.108914.
- [57] S. Hashemi, M. Sawan, and Y. Savaria, "A novel low-drop CMOS active rectifier for RF-powered devices: Experimental results", *Microelectronics Journal*, vol. 40, no. 11, pp. 1547–1554, Nov. 2009, ISSN: 00262692. DOI: 10.1016/j.mejo.2009.02.007.
- [58] M. Awad, P. Benech, and J.-M. Duchamp, "Design of Dickson rectifier for RF energy harvesting in 28 nm FD-SOI technology", in *2018 Joint International EU-ROSOI Workshop and International Conference on Ultimate Integration on Silicon (EUROSOI-ULIS)*, IEEE, Mar. 2018, pp. 1–4, ISBN: 978-1-5386-4811-7. DOI: 10.1109/ULIS.2018.8354751.
- [59] M. Stoopman, S. Keyrouz, H. J. Visser, K. Philips, and W. A. Serdijn, "Co-design of a CMOS rectifier and small loop antenna for highly sensitive RF energy harvesters", *IEEE Journal of Solid-State Circuits*, vol. 49, no. 3, pp. 622–634, 2014, ISSN: 00189200. DOI: 10.1109/JSSC.2014.2302793.
- [60] A. S. Almansouri, J. Kosel, and K. N. Salama, "A Dual-Mode Nested Rectifier for Ambient Wireless Powering in CMOS Technology", *IEEE Transactions on Microwave Theory and Techniques*, vol. 68, no. 5, pp. 1754–1762, May 2020, ISSN: 15579670. DOI: 10.1109/TMTT.2020.2970913.
- [61] B. K. Kanaujia, N. Singh, and S. Kumar, *Rectenna: Wireless Energy Harvesting System* (Advances in Sustainability Science and Technology). Singapore: Springer Singapore, 2021, ISBN: 978-981-16-2535-0. DOI: 10.1007/978-981-16-2536-7.
- [62] N. De, N. Donaldson, and T. A. Perkins, "Analysis of resonant coupled coils in the design of radio frequency transcutaneous links", Tech. Rep., 1983, pp. 612–627.
- [63] M. W. Baker and R. Sarpeshkar, "Feedback analysis and design of RF power links for low-power bionic systems", *IEEE Transactions on Biomedical Circuits and Systems*, vol. 1, no. 1, pp. 28–38, Mar. 2007, ISSN: 19324545. DOI: 10.1109/TBCAS.2007.893180.

- [64] D. H. Nguyen, "Optical Wireless Power Transfer for Implanted and Wearable Devices", *Sustainability (Switzerland)*, vol. 15, no. 10, May 2023, ISSN: 20711050. DOI: 10.3390/su15108146.
- [65] S. A. H. Mohsan, H. Qian, and H. Amjad, *A comprehensive review of optical wireless power transfer technology*, Jun. 2023. DOI: 10.1631/FITEE.2100443.
- [66] A. Singer *et al.*, "Magnetoelectric materials for miniature, wireless neural stimulation at therapeutic frequencies", *Neuron*, vol. 107, no. 4, 631–643.e5, 2020, ISSN: 0896-6273. DOI: <https://doi.org/10.1016/j.neuron.2020.05.019>.
- [67] B. D. Truong, E. Andersen, C. Casados, and S. Roundy, "Magnetoelectric wireless power transfer for biomedical implants: Effects of non-uniform magnetic field, alignment and orientation", *Sensors and Actuators A: Physical*, vol. 316, p. 112 269, 2020, ISSN: 0924-4247. DOI: <https://doi.org/10.1016/j.sna.2020.112269>.
- [68] S. Hosur, R. Sriramdas, S. K. Karan, N. Liu, S. Priya, and M. Kiani, "A comprehensive study on magnetoelectric transducers for wireless power transfer using low-frequency magnetic fields", *IEEE Transactions on Biomedical Circuits and Systems*, vol. 15, no. 5, pp. 1079–1092, 2021. DOI: 10.1109/TBCAS.2021.3118981.
- [69] Z. Yu *et al.*, "Magni: A magnetoelectrically powered and controlled wireless neurostimulating implant", *IEEE Transactions on Biomedical Circuits and Systems*, vol. 14, no. 6, pp. 1241–1252, 2020. DOI: 10.1109/TBCAS.2020.3037862.
- [70] M. Kiani, "Wireless Power Transfer and Management for Medical Applications: Wireless power", *IEEE Solid-State Circuits Magazine*, vol. 14, no. 3, pp. 41–52, 2022, ISSN: 1943-0582. DOI: 10.1109/MSSC.2022.3178671.
- [71] L. Cheng, W. H. Ki, Y. Lu, and T. S. Yim, "Adaptive On/Off Delay-Compensated Active Rectifiers for Wireless Power Transfer Systems", *IEEE Journal of Solid-State Circuits*, vol. 51, no. 3, pp. 712–723, Mar. 2016, ISSN: 00189200. DOI: 10.1109/JSSC.2016.2517119.
- [72] M. Kiani, U. M. Jow, and M. Ghovanloo, "Design and optimization of a 3-coil inductive link for efficient wireless power transmission", in *IEEE Transactions on Biomedical Circuits and Systems*, vol. 5, Dec. 2011, pp. 579–591. DOI: 10.1109/TBCAS.2011.2158431.
- [73] S. M. Agarwal *et al.*, "Transcranial direct current stimulation in schizophrenia", *Clinical Psychopharmacology and Neuroscience*, vol. 11, no. 3, pp. 118–125, 2013, ISSN: 17381088. DOI: 10.9758/cpn.2013.11.3.118.
- [74] S. R. Khan, S. K. Pavuluri, G. Cummins, and M. P. Desmulliez, *Wireless power transfer techniques for implantable medical devices: A review*, Jun. 2020. DOI: 10.3390/s20123487.
- [75] J. Van Mulders *et al.*, "Wireless Power Transfer: Systems, Circuits, Standards, and Use Cases", *Sensors*, vol. 22, no. 15, p. 5573, Jul. 2022, ISSN: 1424-8220. DOI: 10.3390/s22155573.

- [76] M. Meng and M. Kiani, "A Hybrid Inductive-Ultrasonic Link for Wireless Power Transmission to Millimeter-Sized Biomedical Implants", *IEEE Transactions on Circuits and Systems II: Express Briefs*, vol. 64, no. 10, pp. 1137–1141, Oct. 2017, ISSN: 15583791. DOI: 10.1109/TCSII.2016.2626151.
- [77] M. Gourdouparis *et al.*, "6.2 An Ultrasound-Powering TX with a Global Charge-Redistribution Adiabatic Drive Achieving 69% Power Reduction and 53° Maximum Beam Steering Angle for Implantable Applications", in *Digest of Technical Papers - IEEE International Solid-State Circuits Conference*, Institute of Electrical and Electronics Engineers Inc., 2024, pp. 102–104, ISBN: 9798350306200. DOI: 10.1109/ISSCC49657.2024.10454411.
- [78] E. So, P. Yeon, E. J. Chichilnisky, and A. Arbabian, "An RF-Ultrasound Relay for Adaptive Wireless Powering Across Tissue Interfaces", *IEEE Journal of Solid-State Circuits*, vol. 57, no. 11, pp. 3429–3441, Nov. 2022, ISSN: 1558173X. DOI: 10.1109/JSSC.2022.3171233.
- [79] E. A. Gomez-Casseres, S. M. Arbulu, R. J. Franco, R. Contreras, and J. Martinez, "Comparison of passive rectifier circuits for energy harvesting applications", in *2016 IEEE Canadian Conference on Electrical and Computer Engineering (CCECE)*, IEEE, May 2016, pp. 1–6, ISBN: 978-1-4673-8721-7. DOI: 10.1109/CCECE.2016.7726840.
- [80] M. Ghovanloo and K. Najafi, "Fully integrated wideband high-current rectifiers for inductively powered devices", *IEEE Journal of Solid-State Circuits*, vol. 39, no. 11, pp. 1976–1984, 2004. DOI: 10.1109/JSSC.2004.835822.
- [81] C. Peters, O. Kessling, F. Henrici, M. Ortmanns, and Y. Manoli, "CMOS Integrated Highly Efficient Full Wave Rectifier", in *2007 IEEE International Symposium on Circuits and Systems (ISCAS)*, IEEE, May 2007, pp. 2415–2418, ISBN: 1-4244-0920-9. DOI: 10.1109/ISCAS.2007.377947.
- [82] C.-S. Gong, "IC-Based Rectification Circuit Techniques for Biomedical Energy-Harvesting Applications", *Micromachines*, vol. 13, no. 3, p. 411, Mar. 2022, ISSN: 2072-666X. DOI: 10.3390/mi13030411.
- [83] M. H. Ouda, W. Khalil, and K. N. Salama, "Wide-Range Adaptive RF-to-DC Power Converter for UHF RFIDs", *IEEE Microwave and Wireless Components Letters*, vol. 26, no. 8, pp. 634–636, Aug. 2016, ISSN: 1531-1309. DOI: 10.1109/LMWC.2016.2586077.
- [84] X. Li, F. Mao, Y. Lu, and R. P. Martins, "A VHF Wide-Input Range CMOS Passive Rectifier with Active Bias Tuning", *IEEE Journal of Solid-State Circuits*, vol. 55, no. 10, pp. 2629–2638, Oct. 2020, ISSN: 1558173X. DOI: 10.1109/JSSC.2020.3005814.
- [85] L. Huang, A. Murray, and B. W. Flynn, "A high-efficiency low-power rectifier for wireless power transfer systems of deep micro-implants", *IEEE Access*, vol. 8, pp. 204 057–204 067, 2020, ISSN: 21693536. DOI: 10.1109/ACCESS.2020.3036703.

- [86] S. S. Hashemi, M. Sawan, and Y. Savaria, "A high-efficiency low-voltage CMOS rectifier for harvesting energy in implantable devices", *IEEE Transactions on Biomedical Circuits and Systems*, vol. 6, no. 4, pp. 326–335, 2012, ISSN: 19324545. DOI: 10.1109/TBCAS.2011.2177267.
- [87] Y. Lu and W.-H. Ki, *CMOS Integrated Circuit Design for Wireless Power Transfer* (Analog Circuits and Signal Processing). Singapore: Springer Singapore, 2018, ISBN: 978-981-10-2614-0. DOI: 10.1007/978-981-10-2615-7.
- [88] H. K. Cha, W. T. Park, and M. Je, "A CMOS rectifier with a cross-coupled latched comparator for wireless power transfer in biomedical applications", *IEEE Transactions on Circuits and Systems II: Express Briefs*, vol. 59, no. 7, pp. 409–413, 2012, ISSN: 15583791. DOI: 10.1109/TCSII.2012.2198977.
- [89] S. Guo and H. Lee, "An efficiency-enhanced CMOS rectifier with unbalanced-biased comparators for transcutaneous-powered high-current implants", *IEEE Journal of Solid-State Circuits*, vol. 44, no. 6, pp. 1796–1804, Jun. 2009, ISSN: 00189200. DOI: 10.1109/JSSC.2009.2020195.
- [90] Y. Lu and W. H. Ki, "A 13.56 MHz CMOS active rectifier with switched-offset and compensated biasing for biomedical wireless power transfer systems", *IEEE Transactions on Biomedical Circuits and Systems*, vol. 8, no. 3, pp. 334–344, 2014, ISSN: 19324545. DOI: 10.1109/TBCAS.2013.2270177.
- [91] H.-M. Lee and M. Ghovanloo, "An Integrated Power-Efficient Active Rectifier With Offset-Controlled High Speed Comparators for Inductively Powered Applications", *IEEE Transactions on Circuits and Systems I: Regular Papers*, vol. 58, no. 8, pp. 1749–1760, Aug. 2011, ISSN: 1549-8328. DOI: 10.1109/TCSI.2010.2103172.
- [92] C. Y. Wu, X. H. Qian, M. S. Cheng, Y. A. Liang, and W. M. Chen, "A 13.56 MHz 40 mW CMOS high-efficiency inductive link power supply utilizing on-chip delay-compensated voltage doubler rectifier and multiple ldos for implantable medical devices", *IEEE Journal of Solid-State Circuits*, vol. 49, no. 11, pp. 2397–2407, Nov. 2014, ISSN: 00189200. DOI: 10.1109/JSSC.2014.2356459.
- [93] R. S. Berido and A. C. Lowaton, "13.56 MHz highly-efficient power conditioning unit using an active rectifier and LDO for implantable medical devices (IMD)", *International Journal of Electrical and Electronic Engineering and Telecommunications*, vol. 8, no. 2, pp. 84–88, Mar. 2019, ISSN: 23192518. DOI: 10.18178/ijeetc.8.2.84-88.
- [94] C. Huang, T. Kawajiri, and H. Ishikuro, "A Near-Optimum 13.56 MHz CMOS Active Rectifier with Circuit-Delay Real-Time Calibrations for High-Current Biomedical Implants", *IEEE Journal of Solid-State Circuits*, vol. 51, no. 8, pp. 1797–1809, Aug. 2016, ISSN: 00189200. DOI: 10.1109/JSSC.2016.2582871.
- [95] S. Pal and W. H. Ki, "40.68 MHz Digital On-Off Delay-Compensated Active Rectifier for WPT of Biomedical Applications", *IEEE Transactions on Circuits and Systems II: Express Briefs*, vol. 67, no. 12, pp. 3307–3311, Dec. 2020, ISSN: 15583791. DOI: 10.1109/TCSII.2020.2991797.

- [96] K. Zheng, Y. Hou, X. Wang, and Y. Liu, "An Active Rectifier with Pulse Width Modulation (PWM) Mode On- and Off-Delay Compensation for Wireless Power Transfer (WPT) System", *IEEE Access*, vol. 11, pp. 118 204–118 216, 2023, ISSN: 21693536. DOI: 10.1109/ACCESS.2023.3326472.
- [97] S. Shahsavari and M. Saberi, "A Power-Efficient CMOS Active Rectifier with Circuit Delay Compensation for Wireless Power Transfer Systems", *Circuits, Systems, and Signal Processing*, vol. 38, no. 3, pp. 947–966, Mar. 2019, ISSN: 15315878. DOI: 10.1007/s00034-018-0902-9.
- [98] K. Noh, J. Amanor-Boadu, M. Zhang, and E. Sanchez-Sinencio, "A 13.56-MHz CMOS Active Rectifier with a Voltage Mode Switched-Offset Comparator for Implantable Medical Devices", *IEEE Transactions on Very Large Scale Integration (VLSI) Systems*, vol. 26, no. 10, pp. 2050–2060, Oct. 2018, ISSN: 10638210. DOI: 10.1109/TVLSI.2018.2845369.
- [99] Y. Zhang, J. Ma, and X. Tang, "A CMOS Active Rectifier with Efficiency-Improving and Digitally Adaptive Delay Compensation for Wireless Power Transfer Systems", *Energies*, vol. 14, no. 23, p. 8089, Dec. 2021, ISSN: 1996-1073. DOI: 10.3390/en14238089.
- [100] J. Ahn, H.-S. Lee, K. Eom, W. Jung, and H.-M. Lee, "A 93.5%-Efficiency 13.56-MHz-Bandwidth Optimal On/Off Tracking Active Rectifier with Fully Digital Feedback-Based Delay Control for Adaptive Efficiency Compensation", in *2023 IEEE Symposium on VLSI Technology and Circuits (VLSI Technology and Circuits)*, IEEE, Jun. 2023, pp. 1–2, ISBN: 978-4-86348-806-9. DOI: 10.23919/VLSITechnologyandCir57934.2023.10185395.
- [101] Z. Xue, S. Fan, D. Li, L. Zhang, W. Gou, and L. Geng, "A 13.56 MHz, 94.1% Peak Efficiency CMOS Active Rectifier with Adaptive Delay Time Control for Wireless Power Transmission Systems", *IEEE Journal of Solid-State Circuits*, vol. 54, no. 6, pp. 1744–1754, Jun. 2019, ISSN: 1558173X. DOI: 10.1109/JSSC.2019.2894359.
- [102] Z. Luo, J. Liu, and H. Lee, "A 40.68-MHz Active Rectifier With Cycle-Based On-/Off-Delay Compensation for High-Current Biomedical Implants", *IEEE Journal of Solid-State Circuits*, vol. 58, no. 2, pp. 345–356, Feb. 2023, ISSN: 1558173X. DOI: 10.1109/JSSC.2022.3192523.
- [103] Y.-J. Moon, Y.-S. Roh, C. Yoo, and D.-Z. Kim, "A 3.0-W wireless power receiver circuit with 75-% overall efficiency", in *2012 IEEE Asian Solid State Circuits Conference (A-SSCC)*, IEEE, Dec. 2012, pp. 97–100. DOI: 10.1109/IPEC.2012.6522636.
- [104] L. Hu, L. Cheng, Y. Yao, T. S. Yim, W. H. Ki, and C. Y. Tsui, "A 40.68MHz Active Rectifier with Hybrid Delay Compensation Scheme", in *2018 IEEE Asia Pacific Conference on Circuits and Systems, APCCAS 2018*, Institute of Electrical and Electronics Engineers Inc., Jan. 2019, pp. 501–504, ISBN: 9781538682401. DOI: 10.1109/APCCAS.2018.8605616.

- [105] L. Cheng, X. Ge, L. Hu, Y. Yao, W. H. Ki, and C. Y. Tsui, "A 40.68-MHz active rectifier with hybrid adaptive on/off delay-compensation scheme for biomedical implantable devices", *IEEE Transactions on Circuits and Systems I: Regular Papers*, vol. 67, no. 2, pp. 516–525, Feb. 2020, ISSN: 15580806. DOI: 10.1109/TCSI.2019.2928815.
- [106] K. S. Zheng, X. Liu, X. Wang, Q. Su, and Y. Liu, "A 6.78 MHz CMOS Active Rectifier With Hybrid Mode Delay Compensation for Wireless Power Transfer Systems", *IEEE Access*, vol. 10, pp. 46 176–46 186, 2022, ISSN: 21693536. DOI: 10.1109/ACCESS.2022.3169493.
- [107] Y. Liu, B. Li, M. Huang, Z. Chen, and X. Zhang, "An Overview of Regulation Topologies in Resonant Wireless Power Transfer Systems for Consumer Electronics or Bio-Implants", *Energies*, vol. 11, no. 7, p. 1737, Jul. 2018, ISSN: 1996-1073. DOI: 10.3390/en11071737.
- [108] C. Kim, S. Ha, J. Park, A. Akinin, P. P. Mercier, and G. Cauwenberghs, "A 144-MHz Fully Integrated Resonant Regulating Rectifier With Hybrid Pulse Modulation for mm-Sized Implants", *IEEE Journal of Solid-State Circuits*, vol. 52, no. 11, pp. 3043–3055, Nov. 2017, ISSN: 0018-9200. DOI: 10.1109/JSSC.2017.2734901.
- [109] H. M. Lee and M. Ghovanloo, "A power-efficient wireless capacitor charging system through an inductive link", *IEEE Transactions on Circuits and Systems II: Express Briefs*, vol. 60, no. 10, pp. 707–711, 2013, ISSN: 15583791. DOI: 10.1109/TCSII.2013.2278104.
- [110] E. Ozalevli *et al.*, "A Cost-Effective Adaptive Rectifier for Low Power Loosely Coupled Wireless Power Transfer Systems", *IEEE Transactions on Circuits and Systems I: Regular Papers*, vol. 65, no. 7, pp. 2318–2329, Jul. 2018, ISSN: 1549-8328. DOI: 10.1109/TCSI.2017.2780169.
- [111] H.-S. Lee, K. Eom, and H.-M. Lee, "27.3 A 90.8%-Efficiency SIMO Resonant Regulating Rectifier Generating 3 Outputs in a Half Cycle with Distributed Multi-Phase Control for Wirelessly-Powered Implantable Devices", in *2024 IEEE International Solid-State Circuits Conference ()*, IEEE, Feb. 2024, pp. 448–450, ISBN: 979-8-3503-0620-0. DOI: 10.1109/ISSCC49657.2024.10454403.
- [112] H.-M. Lee, H. Park, and M. Ghovanloo, "A Power-Efficient Wireless System With Adaptive Supply Control for Deep Brain Stimulation", *IEEE Journal of Solid-State Circuits*, vol. 48, no. 9, pp. 2203–2216, Sep. 2013, ISSN: 0018-9200. DOI: 10.1109/JSSC.2013.2266862.
- [113] L. Cheng, W. H. Ki, and C. Y. Tsui, "A 6.78-MHz Single-Stage Wireless Power Receiver Using a 3-Mode Reconfigurable Resonant Regulating Rectifier", *IEEE Journal of Solid-State Circuits*, vol. 52, no. 5, pp. 1412–1423, May 2017, ISSN: 00189200. DOI: 10.1109/JSSC.2017.2657603.
- [114] H.-M. Lee and M. Ghovanloo, "An adaptive reconfigurable active voltage doubler/rectifier for extended-range inductive power transmission", in *2012 IEEE International Solid-State Circuits Conference*, IEEE, Feb. 2012, pp. 286–288, ISBN: 978-1-4673-0377-4. DOI: 10.1109/ISSCC.2012.6177017.

- [115] X. Li, C. Y. Tsui, and W. H. Ki, "A 13.56 MHz Wireless Power Transfer System With Reconfigurable Resonant Regulating Rectifier and Wireless Power Control for Implantable Medical Devices", *IEEE Journal of Solid-State Circuits*, vol. 50, no. 4, pp. 978–989, Apr. 2015, ISSN: 00189200. DOI: 10.1109/JSSC.2014.2387832.
- [116] T. Lu, Z.-Y. Chang, J. Jiang, K. Makinwa, and S. Du, "A 13.56MHz Fully Integrated 91.8% Efficiency Single-Stage Dual-Output Regulating Voltage Doubler for Biomedical Wireless Power Transfer", in *2023 IEEE Custom Integrated Circuits Conference (CICC)*, IEEE, Apr. 2023, pp. 1–2, ISBN: 979-8-3503-9948-6. DOI: 10.1109/CICC57935.2023.10121186.
- [117] J. H. Choi, S. K. Yeo, S. Park, J. S. Lee, and G. H. Cho, "Resonant regulating rectifiers (3R) operating for 6.78 MHz Resonant Wireless Power Transfer (RWPT)", *IEEE Journal of Solid-State Circuits*, vol. 48, no. 12, pp. 2989–3001, Dec. 2013, ISSN: 00189200. DOI: 10.1109/JSSC.2013.2287592.
- [118] Yan Lu, Xing Li, Wing-Hung Ki, Chi-Ying Tsui, and C. P. Yue, "A 13.56MHz fully integrated 1X/2X active rectifier with compensated bias current for inductively powered devices", in *2013 IEEE International Solid-State Circuits Conference Digest of Technical Papers*, IEEE, Feb. 2013, pp. 66–67, ISBN: 978-1-4673-4516-3. DOI: 10.1109/ISSCC.2013.6487639.
- [119] K. Cui, X. Fan, and Y. Ma, "An Energy-Efficient Wireless Power Receiver With One-Step Adiabatic-Bipolar-Supply Generating for Implantable Electrical Stimulation Applications", *IEEE Transactions on Biomedical Circuits and Systems*, vol. 18, no. 5, pp. 1112–1122, Oct. 2024, ISSN: 1932-4545. DOI: 10.1109/TBCAS.2024.3379208.
- [120] H. S. Gougheri and M. Kiani, "Self-Regulated Reconfigurable Voltage/Current-Mode Inductive Power Management", *IEEE Journal of Solid-State Circuits*, vol. 52, no. 11, pp. 3056–3070, Nov. 2017, ISSN: 00189200. DOI: 10.1109/JSSC.2017.2737138.
- [121] T. S. Davis *et al.*, "Spatial and temporal characteristics of V1 microstimulation during chronic implantation of a microelectrode array in a behaving macaque", *Journal of Neural Engineering*, vol. 9, no. 6, p. 065003, Dec. 2012, ISSN: 1741-2560. DOI: 10.1088/1741-2560/9/6/065003.
- [122] M. N. van Dongen and W. A. Serdijn, "A Power-Efficient Multichannel Neural Stimulator Using High-Frequency Pulsed Excitation From an Unfiltered Dynamic Supply", *IEEE Transactions on Biomedical Circuits and Systems*, vol. 10, no. 1, pp. 61–71, Feb. 2016, ISSN: 1932-4545. DOI: 10.1109/TBCAS.2014.2363736.
- [123] E. Noorsal, H. Xu, K. Sooksood, and M. Ortmanns, "Multichannel Microstimulating SoC", in *Handbook of Biochips*, New York, NY: Springer New York, 2022, pp. 1285–1316. DOI: 10.1007/978-1-4614-3447-4_18.
- [124] S. K. Arfin and R. Sarpeshkar, "An Energy-Efficient, Adiabatic Electrode Stimulator With Inductive Energy Recycling and Feedback Current Regulation", *IEEE Transactions on Biomedical Circuits and Systems*, vol. 6, no. 1, pp. 1–14, Feb. 2012, ISSN: 1932-4545. DOI: 10.1109/TBCAS.2011.2166072.

- [125] Z. Luo and M.-D. Ker, "A High-Voltage-Tolerant and Power-Efficient Stimulator With Adaptive Power Supply Realized in Low-Voltage CMOS Process for Implantable Biomedical Applications", *IEEE Journal on Emerging and Selected Topics in Circuits and Systems*, vol. 8, no. 2, pp. 178–186, Jun. 2018, ISSN: 2156-3365. DOI: 10.1109/JETCAS.2018.2796381.
- [126] Z. Luo, M.-D. Ker, T.-Y. Yang, and W.-H. Cheng, "A Digitally Dynamic Power Supply Technique for 16-Channel 12 V-Tolerant Stimulator Realized in a 0.18- μ m 1.8-V/3.3-V Low-Voltage CMOS Process", *IEEE Transactions on Biomedical Circuits and Systems*, vol. 11, no. 5, pp. 1087–1096, Oct. 2017, ISSN: 1932-4545. DOI: 10.1109/TBCAS.2017.2713122.
- [127] K. H. Nguyen *et al.*, "A Fully Integrated Dynamic-Voltage-Scaling Stimulator IC with Miniaturized Reconfigurable Supply Modulator and Channel Drivers for Cochlear Implants", in *Proceedings of the Custom Integrated Circuits Conference*, Institute of Electrical and Electronics Engineers Inc., 2024, ISBN: 9798350394061. DOI: 10.1109/CICC60959.2024.10529043.
- [128] L. Yao, D. I. Made, and Y. Gao, "A 83% peak efficiency 1.65 V to 11.4V dynamic voltage scaling supply for electrical stimulation applications in standard 0.18 μ m CMOS process", in *2016 IEEE Asian Solid-State Circuits Conference (A-SSCC)*, IEEE, Nov. 2016, pp. 205–208, ISBN: 978-1-5090-3699-8. DOI: 10.1109/ASSCC.2016.7844171.
- [129] I. Williams and T. G. Constandinou, "An Energy-Efficient, Dynamic Voltage Scaling Neural Stimulator for a Proprioceptive Prosthesis", *IEEE Transactions on Biomedical Circuits and Systems*, vol. 7, no. 2, pp. 129–139, Apr. 2013, ISSN: 1932-4545. DOI: 10.1109/TBCAS.2013.2256906.
- [130] J. P. Uehlin *et al.*, "A Single-Chip Bidirectional Neural Interface with High-Voltage Stimulation and Adaptive Artifact Cancellation in Standard CMOS", *IEEE Journal of Solid-State Circuits*, vol. 55, no. 7, pp. 1749–1761, Jul. 2020, ISSN: 1558173X. DOI: 10.1109/JSSC.2020.2991524.
- [131] W. Ahn, K.-H. Nguyen, H. Lee, K. S. Min, S. Ha, and M. Je, "An Energy-Efficient Stimulation System Based on Adaptive Dynamic Voltage Switching Control for Cochlear Implants", *IEEE Transactions on Biomedical Circuits and Systems*, pp. 1–12, 2024, ISSN: 1932-4545. DOI: 10.1109/TBCAS.2024.3497585.
- [132] K. Eom *et al.*, "A Low-Stimulus-Scattering Pixel-Sharing Sub-Retinal Prosthesis SoC With Time-Based Photodiode Sensing and Per-Pixel Dynamic Voltage Scaling", *IEEE Journal of Solid-State Circuits*, vol. 58, no. 11, pp. 2976–2989, Nov. 2023, ISSN: 1558173X. DOI: 10.1109/JSSC.2023.3305521.
- [133] K. H. Nguyen *et al.*, "A Neural Stimulator IC with Dynamic Voltage Scaling Supply and Energy Recycling for Cochlear Implant in Standard 180nm CMOS Process", in *Proceedings - International SoC Design Conference 2023, ISOCC 2023*, Institute of Electrical and Electronics Engineers Inc., 2023, pp. 35–36, ISBN: 9798350327038. DOI: 10.1109/ISOCC59558.2023.10396171.

- [134] A. Rashidi, N. Yazdani, and A. M. Sodagar, "Fully implantable, multi-channel microstimulator with tracking supply ribbon, multi-output charge pump and energy recovery", *IET Circuits, Devices & Systems*, vol. 15, no. 2, pp. 104–120, Mar. 2021, ISSN: 1751-858X. DOI: 10.1049/cds2.12007.
- [135] X. Zeng *et al.*, "A 12-V Single-Input Multiple-Independently Configurable-Output Dynamic Voltage Scaling Supply in Standard 0.18- μm CMOS for Electrical Stimulation Applications", *IEEE Solid-State Circuits Letters*, vol. 5, pp. 33–36, 2022, ISSN: 2573-9603. DOI: 10.1109/LSSC.2022.3149570.
- [136] A. Urso, V. Giagka, M. van Dongen, and W. A. Serdijn, "An Ultra High-Frequency 8-Channel Neurostimulator Circuit With 68% Peak Power Efficiency", *IEEE Transactions on Biomedical Circuits and Systems*, vol. 13, no. 5, pp. 882–892, Oct. 2019, ISSN: 1932-4545. DOI: 10.1109/TBCAS.2019.2920294.
- [137] M. Y. Jung, S. H. Park, J. S. Bang, D. C. Park, S. U. Shin, and G. H. Cho, "An error-based controlled single-inductor 10-output DC-DC buck converter with high efficiency at light load using adaptive pulse modulation", in *Digest of Technical Papers - IEEE International Solid-State Circuits Conference*, vol. 58, Institute of Electrical and Electronics Engineers Inc., Mar. 2015, pp. 222–223, ISBN: 9781479962235. DOI: 10.1109/ISSCC.2015.7063006.
- [138] D. Palomeque-Mangut, Á. Rodríguez-Vázquez, and M. Delgado-Restituto, "A 4.2–13.2 V, on-chip, regulated, DC–DC converter in a standard 1.8V/3.3V CMOS process", *AEU - International Journal of Electronics and Communications*, vol. 161, Mar. 2023, ISSN: 16180399. DOI: 10.1016/j.aeue.2023.154527.
- [139] J. Lee *et al.*, "A Sub-mm³ Wireless Neural Stimulator IC for Visual Cortical Prosthesis with Optical Power Harvesting and 7.5-kb/s Data Telemetry", *IEEE Journal of Solid-State Circuits*, vol. 59, no. 4, pp. 1110–1122, Apr. 2024, ISSN: 1558173X. DOI: 10.1109/JSSC.2023.3349179.
- [140] D. Rozgic *et al.*, "A 0.338 cm³, Artifact-Free, 64-Contact Neuromodulation Platform for Simultaneous Stimulation and Sensing", *IEEE Transactions on Biomedical Circuits and Systems*, vol. 13, no. 1, pp. 1–1, 2018, ISSN: 1932-4545. DOI: 10.1109/TBCAS.2018.2889040.
- [141] A. Zhou *et al.*, "A wireless and artefact-free 128-channel neuromodulation device for closed-loop stimulation and recording in non-human primates", *Nature Biomedical Engineering*, vol. 3, no. 1, pp. 15–26, Jan. 2019, ISSN: 2157-846X. DOI: 10.1038/s41551-018-0323-x.
- [142] H. Pu, O. Malekzadeh-Arasteh, A. R. Danesh, Z. Nenadic, A. H. Do, and P. Heydari, "A CMOS Dual-Mode Brain-Computer Interface Chipset With 2-mV Precision Time-Based Charge Balancing and Stimulation-Side Artifact Suppression", *IEEE Journal of Solid-State Circuits*, vol. 57, no. 6, pp. 1824–1840, Jun. 2022, ISSN: 0018-9200. DOI: 10.1109/JSSC.2021.3108578.
- [143] Y. Ding, X. Gu, X. Guo, S. Wu, and H. Lyu, "An 8-Channel 9-V-Compliant Crosstalk-Free Bipolar Biphasic Current-Controlled Neural Stimulator in a Standard CMOS Technology", *IEEE Transactions on Circuits and Systems II: Express Briefs*, vol. 71, no. 7, pp. 3293–3297, 2024, ISSN: 15583791. DOI: 10.1109/TCSII.2024.3365102.

- [144] C.-C. Hsieh, Y.-H. Wu, and M.-D. Ker, "Design of Dual-Configuration Dual-Mode Stimulator in Low-Voltage CMOS Process for Neuro-Modulation", *IEEE Transactions on Biomedical Circuits and Systems*, pp. 1–14, 2023, ISSN: 1932-4545. DOI: 10.1109/TBCAS.2023.3246164.
- [145] M. Feyerick and W. Dehaene, "Dense, 11 V-tolerant, Balanced Stimulator IC with Digital Time-domain Calibration for <100nA Error", *IEEE Transactions on Biomedical Circuits and Systems*, pp. 1–11, 2023, ISSN: 1932-4545. DOI: 10.1109/TBCAS.2023.3287294.
- [146] U. Shin *et al.*, "NeuralTree: A 256-Channel 0.227- μ J/Class Versatile Neural Activity Classification and Closed-Loop Neuromodulation SoC", *IEEE Journal of Solid-State Circuits*, vol. 57, no. 11, pp. 3243–3257, Nov. 2022, ISSN: 1558173X. DOI: 10.1109/JSSC.2022.3204508.
- [147] C.-C. Hsieh and M.-D. Ker, "Monopolar Biphasic Stimulator With Discharge Function and Negative Level Shifter for Neuromodulation SoC Integration in Low-Voltage CMOS Process", *IEEE Transactions on Biomedical Circuits and Systems*, vol. 15, no. 3, pp. 568–579, Jun. 2021, ISSN: 1932-4545. DOI: 10.1109/TBCAS.2021.3087036.
- [148] D. R. Merrill, M. Bikson, and J. G. Jefferys, "Electrical stimulation of excitable tissue: design of efficacious and safe protocols", *Journal of Neuroscience Methods*, vol. 141, no. 2, pp. 171–198, Feb. 2005, ISSN: 01650270. DOI: 10.1016/j.jneumeth.2004.10.020.
- [149] R. Ranjandish, T. Jang, and A. Schmid, "An active charge balancing method suitable for integration in the output-stage of electrical neural stimulators", *Analog Integrated Circuits and Signal Processing*, Jan. 2022, ISSN: 0925-1030. DOI: 10.1007/s10470-021-01951-7.
- [150] Z. Qiu, A. T. Nguyen, K. Su, Z. Yang, and J. Xu, "A High Precision, Wide Dynamic Range Closed-Loop Neuromodulation IC with Rapid Stimulation Artifact Recovery", *IEEE Transactions on Biomedical Circuits and Systems*, 2023, ISSN: 19409990. DOI: 10.1109/TBCAS.2023.3321295.
- [151] Y. Jia *et al.*, "A Trimodal Wireless Implantable Neural Interface System-on-Chip.", *IEEE transactions on biomedical circuits and systems*, vol. 14, no. 6, pp. 1207–1217, Dec. 2020, ISSN: 1940-9990. DOI: 10.1109/TBCAS.2020.3037452.
- [152] H. Kassiri *et al.*, "Rail-to-rail-input dual-radio 64-channel closed-loop neurostimulator", *IEEE Journal of Solid-State Circuits*, vol. 52, no. 11, pp. 2793–2810, Nov. 2017, ISSN: 00189200. DOI: 10.1109/JSSC.2017.2749426.
- [153] S. Reich, M. Sporer, M. Haas, J. Becker, M. Schuttler, and M. Ortmanns, "A High-Voltage Compliance, 32-Channel Digitally Interfaced Neuromodulation System on Chip", *IEEE Journal of Solid-State Circuits*, pp. 1–1, 2021, ISSN: 0018-9200. DOI: 10.1109/jssc.2021.3076510.
- [154] Y. Wu, D. Jiang, and A. Demosthenous, "A Multi-Channel Stimulator With High-Resolution Time-to-Current Conversion for Vagal-Cardiac Neuromodulation", *IEEE Transactions on Biomedical Circuits and Systems*, pp. 1–1, 2022, ISSN: 1932-4545. DOI: 10.1109/TBCAS.2021.3139996.

4

ENERGY EFFICIENCY OF PULSE SHAPING IN ELECTRICAL STIMULATION

What would the electron do?

— Wouter Serdijn

This chapter is based on the following publication: F. Varkevisser, *et al.*, “Energy efficiency of pulse shaping in electrical stimulation: the interdependence of biophysical effects and circuit design losses,” *Biomedical Physics & Engineering Express*, vol. 8, no. 6, p. 065009, Nov. 2022, doi: 10.1088/2057-1976/ac8c47.

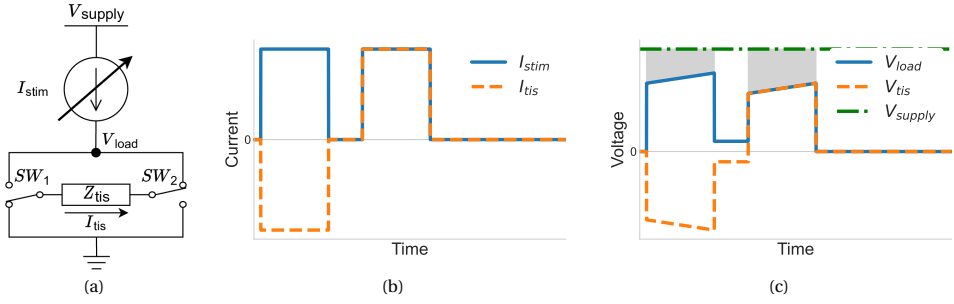


Figure 4.1: (a) Generic circuit diagram for current mode stimulation in a bipolar electrode configuration. (b) Example of rectangular pulses generated by I_{stim} consisting of two phases with equal amplitudes and durations, separated by an interphase delay. During the interphase delay, SW_1 and SW_2 will switch to direct the current through the tissue in the opposite direction during the second phase. (c) Resulting voltage at node V_{load} for a typical tissue load, and the fixed supply voltage. The shaded grey area indicates the voltage drop across I_{stim} as a result of a mismatch between V_{supply} and V_{load} .

4

4.1. INTRODUCTION

ELECTRICAL brain stimulation devices are successfully applied to treat several neural disorders such as Parkinson's disease, hearing loss, and visual impairment. Applications like bidirectional brain-computer interfaces and cortical visual stimulation drive the development of large-scale multichannel stimulator systems. These fully implantable devices interface with the brain by means of electrical pulses through hundreds to thousands of stimulation channels [1]. If battery operation is not an option, the power is transferred to the system via a wireless link. Due to safety regulations on tissue heating and electromagnetic exposure the maximum deliverable wireless power is restricted [2–5]. Therefore, the power efficiency of the stimulator needs to be optimized to increase the number of channels that can be stimulated with the available power.

Current Mode Stimulation (CMS) is often favored over Voltage Mode Stimulation (VMS) due to its inherent control over the injected charge, which is essential for safe operation [6]. However, conventional CMS is power inefficient, especially in multichannel devices [7]. A generic circuit diagram for CMS is depicted in Fig. 4.1a. Rectangular current pulses are generated from a fixed voltage supply and applied to the tissue impedance, Z_{tis} . Switches SW_1 and SW_2 are used to change the direction of the current through Z_{tis} , such that a bipolar pulse is applied to the tissue. The voltage supply needs to be sufficiently high to cope with the voltage drop across the tissue and the overhead voltage required for the current source. The amplitude of V_{load} depends on the amplitude of the current pulse and Z_{tis} , which can be highly variable for different channels in the same system. Any mismatch between V_{supply} and V_{load} leads to a voltage drop across the source I_{stim} , indicated by the grey area in Fig. 4.1c, resulting in energy dissipation—and thus inefficiency—in the current source. In a multichannel system, the voltage supply needs to accommodate the worst-case channel. Therefore, all other channels operate at an unnecessarily high supply voltage, which results in energy waste.

Statement of contribution: The work presented in this chapter was carried out by the candidate. All simulations, analyses, and writing were performed by the candidate under the conceptual guidance of the promotor.

One method to reduce energy consumption in CMS is pulse shaping. Several studies suggest that non-rectangular stimulation pulses might be more energy-efficient than the conventional rectangular stimulation pulses [8–11]. Computational studies using detailed neuron models evaluated the efficiency of alternative shapes. The energy consumption of different pulse shapes for deep brain stimulation was modeled in [8]. Centered-triangular and Gaussian-shaped pulses reduced the energy consumption by approximately 10% compared to the energy-optimal rectangular pulse. In [9], a genetic algorithm was developed to find a pulse shape optimized for energy efficiency. The resulting pulse resembled a truncated Gaussian curve. When comparing the optimized pulses to rectangular pulses of equal duration in the range of 50–200 μs , a decrease in activation energy ranging from 5% to 60% was observed. However, compared to the energy-optimal rectangular pulse, the maximum energy-saving was approximately 20%. The efficiency of Gaussian-shaped pulses was investigated in vivo in [10]. A decrease in activation energy of 17% was reported in the pulse width range of 50–200 μs . Research consistently reports that non-rectangular pulses (preferably Gaussian or centered-triangular) can be more energy-efficient, but it is acknowledged that possible circuit implications could alter this conclusion [9]. What is mostly overlooked in the literature, is that non-rectangular pulses alter the required compliance voltage required at stimulation output stages due to an increase in the peak current. This will cause an increase in the overhead energy losses in the output stage of the device.

A possible solution to reduce the overhead losses in CMS is dynamic voltage scaling (DVS) [12–19]. In DVS, the supply voltage is dynamically scaled to minimize the voltage drop across the current driver. Generally, state-of-the-art DVS techniques can be divided into two methods. The first method scales the supply voltage by modulating the incoming AC power signal [12, 13]. The second method uses (on-chip) adaptive DC/DC converters, for example, inductive buck/boost converters [14, 15] or switched-capacitor charge pumps [16–19]. The signal modulation and inductive DC/DC converter approaches benefit from a continuous output voltage range but suffer from limited scalability. Inductor-based converters require bulky off-chip inductor(s) for each channel, and modulation of the incoming power signal only allows for the adaptation of a single channel. Alternatively, switched-capacitor-based converters allow for a fully integrated implementation that can be shared by many channels but have limited output resolution. This method produces discrete voltage steps, and each step occupies a relatively large area. Therefore, they are usually limited to only a few voltage steps.

Foutz *et al.* [20] suggested that non-rectangular pulse shapes should be combined with scaling of the (constant) voltage supply for optimal energy efficiency. However, they analyzed both methods separately and did not consider the effect of the non-rectangular shapes on the required voltage compliance. It is important to note that the two methods described above reduce the energy consumption of electrical stimulation in two different domains. Voltage scaling techniques reduce overhead energy consumption in the electrical domain, whereas pulse shaping techniques reduce the activation energy in the biological domain. To the best of the authors' knowledge, an efficiency analysis considering both methods concurrently is yet to be performed.

This chapter presents a high-level analysis of the total energy efficiency of pulse shaping techniques generated from scaled voltage supplies. We do so by analyzing

the activation thresholds of different pulse configurations on computational models of cortical neurons—both for biophysically realistic neuron models [21] and for a straight axon model.

4.2. METHODS

4.2.1. STIMULATION WAVEFORMS

We analyzed the current thresholds for monophasic, cathodic stimulation pulses of different shapes. The used shapes are: rectangular, Gaussian, half-sine, centered triangular, ramp-up, and ramp-down. The definitions of the pulse shapes are listed in Eqs. (4.1) to (4.6) and illustrated in Table 4.1. For all definitions, K_x is the peak amplitude, PW is the pulse width, and $u(t)$ is the unit step function. In the simulations of the Gaussian-shaped pulses, the pulse width (PW) was defined as 6σ . All other shapes were non-zero for $0 \leq t \leq PW$ and zero otherwise. The waveforms were applied as monophasic pulses to isolate the effect of pulse shape on activation threshold, since non-rectangular pulses inherently alter the interpulse delay which may cause unfair comparison in biphasic pulses [22]. In practice, stimulation is always delivered as charge-balanced biphasic pulses to meet safety standards. Since the reversal phase serves only to balance charge, its shape can be chosen to minimize the electrical losses.

$$\text{Rectangular: } I_{\text{stim}}(t) = K_r \cdot [u(t) - u(t - PW)] \quad (4.1)$$

$$\text{Ramp-up: } I_{\text{stim}}(t) = K_{ru} \cdot \frac{t}{PW} \cdot [u(t) - u(t - PW)] \quad (4.2)$$

$$\text{Ramp-down: } I_{\text{stim}}(t) = K_{rd} \cdot \left(1 - \frac{t}{PW}\right) \cdot [u(t) - u(t - PW)] \quad (4.3)$$

$$\text{Sine: } I_{\text{stim}}(t) = K_s \cdot \sin\left(\frac{2\pi t}{2 \cdot PW}\right) \cdot [u(t) - u(t - PW)] \quad (4.4)$$

$$\text{Gaussian: } I_{\text{stim}}(t) = K_g \cdot \exp\left[-\frac{(t - PW/2)^2}{2\sigma^2}\right] \quad (4.5)$$

$$\text{Triangular: } I_{\text{stim}}(t) = \begin{cases} K_t \cdot \frac{2t}{PW}, & \text{for } 0 \leq t \leq \frac{PW}{2}, \\ 2K_t - K_t \cdot \frac{2t}{PW}, & \text{for } \frac{PW}{2} < t \leq PW, \\ 0, & \text{otherwise.} \end{cases} \quad (4.6)$$

4.2.2. NEURON MODELS

We used two types of neuron models in the NEURON v8.0 simulation software [23]: a single-axon fiber model and the biophysically realistic models presented in [21]. We will focus on the results for the single-axon fiber for most of this chapter to ease the interpretation of the results. For both models, extracellular electrical stimulation was modeled in a homogeneous, isotropic environment. A point-source electrode delivered the pulses. The spatial component of the electric field along the membrane was calculated using Eq. (4.7), where σ is the extracellular conductivity and r is the distance to the electrode.

$$V_e(r) = \frac{1}{4\pi\sigma r} \quad (4.7)$$

The calculated extracellular potential was applied to each section of the model using NEURON's 'extracellular' mechanism. In each time step, the potential was scaled proportionally to the current amplitude of the stimulus.

AXON FIBER MODEL

The single-axon fiber model is a multi-compartment single-cable model that consists of 101 active nodal sections, representing nodes of Ranvier, connected by 100 passive inter-nodal sections, representing myelin sheath. The fiber dimensions and membrane dynamics are based on the axonal branch of a human L5 thick-tufted pyramidal cell [21]. The inter-nodal sections only have passive membrane properties, while the nodal sections have both passive and active properties. The active properties of the nodal sections include five Hodgkin-Huxley-like ion channels: transient sodium, persistent sodium, transient potassium, persistent potassium, and A-type potassium (Kv3.1) [21]. The model properties are listed in Table 4.2.

The electrode was positioned directly above the center node, at a distance of 100 μm . Simulations were run with a time step of 0.1 μs using implicit Euler integration. A stimulus was considered supra-threshold if the outermost nodes' membrane voltage (V_m) crossed 0 mV. Activation thresholds were determined to an accuracy of 10^{-2} μA using a binary search algorithm for PWs ranging from 10 μs to 1ms in steps of 10 μs .

BIOPHYSICALLY REALISTIC MODELS

In [21], 25 biophysically realistic neuron models representing neurons in different cortical layers are presented. In this chapter, we used the five layer 5 cells shown in Fig. 4.2 as an extra validation step to account for the effects of cell-electrode distance and cell morphology on shape dependency.

The electrode was placed in a grid of equally spaced locations around the cells, separated by steps of 200 μm in x, y, and z directions. The boundaries of the grid were

Table 4.1: Illustration of the used pulse shapes.


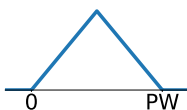
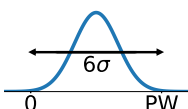
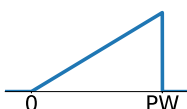
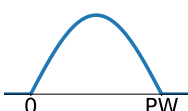
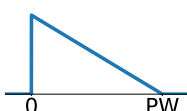
Name	Shape	Name	Shape
Rectangular		Triangular	
Gaussian		Ramp-Up	
Half-Sine		Ramp-Down	

Table 4.2: Model parameters for the single-axon fiber model

Symbol	Description	Value
ρ_a	Axial resistivity	$100 \Omega \cdot \text{cm}$
σ_o	Extracellular conductivity	$0.276 \text{ S} \cdot \text{m}^{-1}$
d_m	Diameter myelin sections	$1.25 \mu\text{m}$
d_n	Diameter nodal sections	$0.93 \mu\text{m}$
L_n	Length nodal sections	$1 \mu\text{m}$
L_m	Length myelin sections	$59 \mu\text{m}$
$C_{m,n}$	Membrane capacitance nodal sections	$1 \mu\text{F} \cdot \text{cm}^{-2}$
$C_{m,m}$	Membrane capacitance myelin sections	$0.02 \mu\text{F} \cdot \text{cm}^{-2}$
$R_{m,n}$	Membrane resistance nodal sections	$33.3 \text{ k}\Omega \cdot \text{cm}^2$
$R_{m,m}$	Membrane resistance myelin sections	$1.125 \text{ M}\Omega \cdot \text{cm}^2$
\bar{g}_{Nap}	Max. conductance persistent sodium	$6.83 \cdot 10^{-3} \text{ S} \cdot \text{cm}^{-2}$
\bar{g}_{Nat}	Max. conductance transient sodium	$6.28 \text{ S} \cdot \text{cm}^{-2}$
\bar{g}_{Kp}	Max. conductance persistent potassium	$9.74 \cdot 10^{-1} \text{ S} \cdot \text{cm}^{-2}$
\bar{g}_{Kt}	Max. conductance transient potassium	$8.93 \cdot 10^{-2} \text{ S} \cdot \text{cm}^{-2}$
$\bar{g}_{\text{Kv3.1}}$	Max. conductance A-type potassium	$5.18 \cdot 10^{-1} \text{ S} \cdot \text{cm}^{-2}$
V_{Na}	Sodium reversal voltage	50 mV
V_{K}	Potassium reversal voltage	-85 mV
V_{L}	Leakage voltage	-75 mV
V_{rest}	Resting potential	-80 mV
T	Temperature	37°C

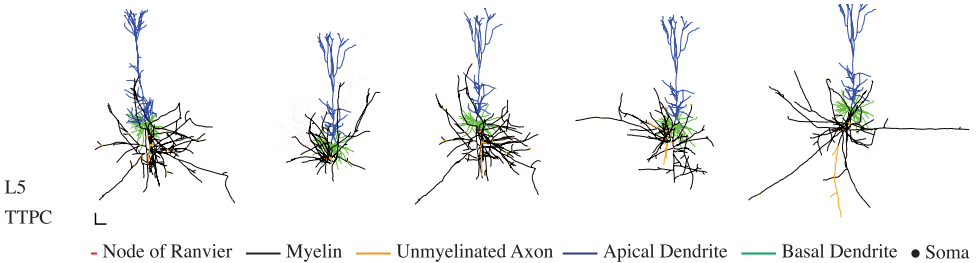


Figure 4.2: Biophysically realistic models of L5 thick-tufted pyramidal cells presented in [21] used in the validation to account for effects of cell-electrode distance and cell morphology on shape dependency. Figure adapted from [21]

determined by the extremities of the cell geometry in all three directions. All locations with a distance to any part of the cell smaller than $30 \mu\text{m}$ or larger than $500 \mu\text{m}$ were removed from the locations set. This resulted in a set of 1800 locations divided over the five models. The time step for these simulations was $5 \mu\text{s}$. A stimulus was considered supra-threshold if the membrane voltage at the soma crossed 0 mV . Current thresholds were determined for PWs ranging from $10 \mu\text{s}$ to 1.5 ms in steps of $50 \mu\text{s}$ to an inaccuracy of $<1\%$. Locations where the optimal energy point for any of the shapes was at maximum pulse duration were omitted, as this might indicate that the minimum energy point has

not been reached yet. Consequently, a total of 1561 locations are included in the results.

4.2.3. SHAPE COMPARISONS

After determining the thresholds for all pulse configurations, we compared the pulse shapes on different metrics. First, the shapes are compared by the peak current at threshold conditions for different PWs in a Strength-Duration curve. Next, the charge threshold of each shape is calculated using Eq. (4.8), and Charge-Duration curves are used to compare the shapes.

$$Q_{th} = \int_0^{PW} I(t) dt \quad (4.8)$$

Furthermore, the energy of each shape is calculated for two scenarios. First, the energy is calculated using Eq. (4.9), which corresponds to energy calculations of stimulation pulses reported in previous literature [8, 9].

$$E_{adiabatic} = \int_0^{PW} P(t) dt = \int_0^{PW} V(t) I(t) dt \propto \int_0^{PW} I(t)^2 dt \quad (4.9)$$

In Eq. (4.9), the quasi-static approximation [24] is used to scale the voltage proportionally to the current. As the voltage is proportional to the current, this would require a fully adaptive (adiabatic) voltage supply to perfectly track the non-rectangular pulses in a practical system.

Second, we consider the case where the current is generated from a constant voltage supply. In this calculation, we scaled the voltage proportional to the peak current of the pulse. This scenario combines pulse shaping and voltage scaling, as proposed in [20]. The energy required to generate the pulse in this case is calculated using:

$$E_{constant} = V_{constant} \int_0^{PW} I(t) dt \propto I_{peak} \int_0^{PW} I(t) dt = I_{peak} \cdot Q \quad (4.10)$$

To illustrate the difference between the calculations, the current, voltage, and power traces in the case of an adiabatic and scaled constant supply voltages are compared in Fig. 4.3 for the example of a half-sine pulse.

For both energy calculations, we calculate the relative energy efficiency of the shapes using Eq. (4.11), where E_x is the threshold energy for shape x , and E_r is the energy needed for a rectangular pulse. Thus, a negative number indicates a decrease in energy with respect to the rectangular pulse, while a positive number indicates an increase in energy. The energy efficiency is assessed based on the minimum required energy for each shape rather than for each PW because the PW definition for non-rectangular pulses can be chosen freely. Consequently, a PW-bound comparison would depend on the chosen definition [20].

$$\eta_E = \left(\frac{\min(E_x)}{\min(E_r)} - 1 \right) \cdot 100\% \quad (4.11)$$

In calculating the energy efficiency for the case of a constant supply, it is assumed that the voltage is scaled proportionally to I_{peak} to maximize efficiency. However, in a practical system, the voltage is usually fixed and can not be scaled to its optimal value at each channel. It shows from Eq. (4.10) that if V_{supply} is fixed, only a decrease in Q can lower the energy threshold. Therefore, we compare the shapes by their Strength-Charge (I_{th} vs. Q) relationship to evaluate energy efficiencies for a fixed supply.

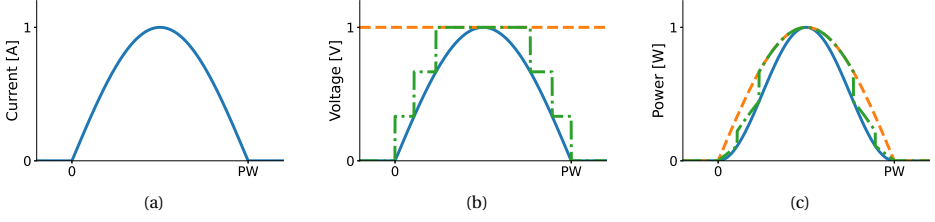


Figure 4.3: (a) current, (b) voltage, and (c) power traces for a half-sine pulse in case of an adiabatic (solid, blue), 3-rail dynamic (dash-dot, green), and scaled constant (dashed, orange) voltage supply.

4.2.4. DYNAMIC VOLTAGE SCALING

As demonstrated in [25], dynamic voltage scaling could improve the energy efficiency for non-rectangular pulses. The total efficiency, including dynamic voltage scaling, can be calculated using:

$$\eta_{\text{total,dvs}} = \eta_{\text{const}} \cdot \eta_{\text{dvs}}, \quad (4.12)$$

where η_{const} is the efficiency of generating the pulses from a constant supply as presented in this chapter, and η_{dvs} is the potential efficiency of applying the dynamic voltage scaling technique as shown in [25]. η_{dvs} is calculated using Eq. (4.13), where E_{dvs} is the required energy in the case of dynamic voltage scaling. In that case, the supply voltage consists of a number of distinct voltage rails and is stepped towards the lowest possible voltage to accommodate the stimulation current at each point in time. In Fig. 4.3, dynamic voltage scaling is illustrated for the example of a 3-rail supply.

$$\eta_{\text{dvs}} = \left(\frac{E_{\text{constant}}}{E_{\text{dvs}}} - 1 \right) \cdot 100\% \quad (4.13)$$

4.2.5. CAPACITIVE EFFECTS OF ELECTRODE-TISSUE INTERFACE

In the previous sections, Z_{tis} is assumed to be resistive in all calculations. A more realistic model includes the electrode-tissue interface (ETI), which has a capacitive nature. Including the ETI will result in reactive components in the voltage during current-controlled stimulation pulses. The amplitude of this effect depends on the geometry and material of the electrodes. Generally, electrodes for electrical stimulation should be designed to minimize the voltage drop over the ETI to prevent harmful electrochemical reactions [26]. For this reason, the error introduced by the assumption of a resistive load should be small. Nevertheless, for completeness of our analysis, we consider the capacitive effects of the ETI in this section.

To include ETI effects, the load of a stimulator circuit is commonly modeled as a combination of a tissue resistance (R_s) in series with a double layer capacitance (C_{dl}). During a current pulse, C_{dl} will be charged, causing an increase in the load voltage. To account for the capacitive charging, the load voltage can be calculated using Eq. (4.14), where $\tau = R_s C_{\text{dl}}$.

$$V_{\text{load}}(t) = R_s \cdot I(t) + \frac{1}{C_{\text{dl}}} \int_0^t I(t) dt = R_s \left(I(t) + \frac{1}{\tau} \int_0^t I(t) dt \right) \quad (4.14)$$

The peak voltage of shape x will increase by a factor β_x as described by Eq. (4.15).

$$\beta_x = \frac{\max[V_{\text{load}}(t)|_{1/\tau>0}]}{\max[V_{\text{load}}(t)|_{1/\tau=0}]} \quad (4.15)$$

Consequently, the energy calculation for the constant-supply-voltage scenario can be expanded to Eq. (4.16) to account for C_{dl} .

$$E_{rc,x} = \beta_x \cdot E_{\text{constant},x} = \beta_x \cdot I_{\text{peak}} \cdot Q \quad (4.16)$$

To compare the effect of C_{dl} between rectangular and non-rectangular shapes, we use Eq. (4.17).

$$\eta_\beta = \left(\frac{\beta_x}{\beta_r} - 1 \right) \cdot 100\% \quad (4.17)$$

4.3. RESULTS

4.3.1. SINGLE-AXON FIBER MODEL

The strength-duration behavior of all shapes was monotonically decreasing (Fig. 4.4). For short PWs, all strength-duration curves approach a vertical asymptote, while for long PWs, they approach a horizontal asymptote. For all PWs, rectangular pulses had the lowest threshold and ramp-down pulses the highest.

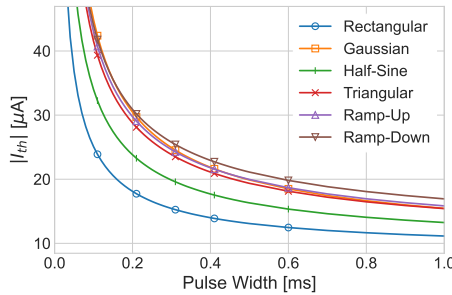


Figure 4.4: Current threshold for different pulse shapes and widths in the single-axon fiber model. The reported threshold is the peak current of the pulses, and the pulse widths are defined in Eqs. (4.1) to (4.6). In agreement with existing literature, the results demonstrate that activation thresholds vary with pulse shape, and rectangular pulses consistently require the lowest peak current.

Furthermore, all shapes had monotonically increasing charge thresholds with increasing PW (Fig. 4.5). For all PWs, rectangular pulses had the highest charge threshold, and Gaussian pulses had the lowest.

In the case of an adiabatic voltage supply, the energy-duration curves show potential energy savings for non-rectangular pulses (Fig. 4.6a). For PWs $> 150 \mu\text{s}$, the rectangular pulses were the least energy-efficient. The energy-optimal shape is PW dependent, but the lowest energy can be achieved using Gaussian pulses with a PW of $240 \mu\text{s}$. The energy efficiencies for the non-rectangular pulses in the case of an adiabatic voltage supply are listed in Table 4.3.

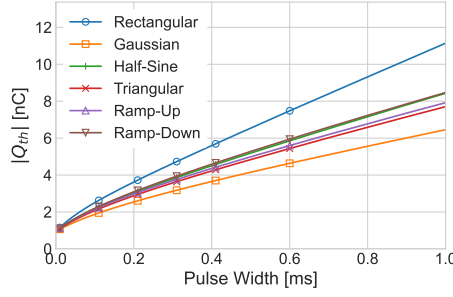


Figure 4.5: Charge threshold for different pulse shapes and widths in the single-axon fiber model. The pulse widths of the non-rectangular pulses are defined in Eqs. (4.1) to (4.6). In contrast to the current threshold results, rectangular pulses consistently exhibit the highest charge threshold.

Table 4.3: Relative energy efficiency of non-rectangular pulses with respect to rectangular pulses in the single-axon fiber model for an adiabatic voltage supply.

	Rectangular	Gaussian	Half-Sine	Triangular	Ramp-Up	Ramp-Down
$\min(E)$ [pJ/kΩ]	62.8	54.6	56.3	55.2	58.9	63.1
η_E [%]	-	-12.9	-10.2	-12.1	-6.1	+0.6

The energy-duration relationships change when the pulses are generated from a scaled constant voltage supply (Fig. 4.6b). Still, no single shape is the most energy-efficient for all PWs; however, the overall least energy can now be achieved with rectangular pulses with a duration of 110 μ s. For PWs < 440 μ s, rectangular pulses have the lowest energy threshold. For longer PWs, the Gaussian pulses require the least amount of energy. The energy efficiencies of non-rectangular pulses in the case of a constant voltage supply are listed in Table 4.4.

Table 4.4: Relative energy efficiency of non-rectangular pulses with respect to rectangular pulses in the single-axon fiber model for a constant voltage supply.

	Rectangular	Gaussian	Half-Sine	Triangular	Ramp-Up	Ramp-Down
$\min(E)$ [pJ/kΩ]	62.8	77.3	71.7	82.8	88.4	94.7
η_E [%]	-	+23.2	+14.3	+31.9	+40.6	+50.9

To compare the efficiency in the case of a fixed voltage supply, the current-charge relationship for the different pulse shapes is depicted in Fig. 4.7. As explained in Section 4.2.3, only a decrease in charge can lower the energy when the supply voltage is fixed. Therefore, a lower charge threshold for a given I_{th} (proportional to V_{supply}) means better energy performance of a circuit generating that pulse from a constant voltage. Rectangular pulses have the lowest charge threshold for all values of I_{th} , while ramp-down pulses have the highest charge threshold for all values of I_{th} .

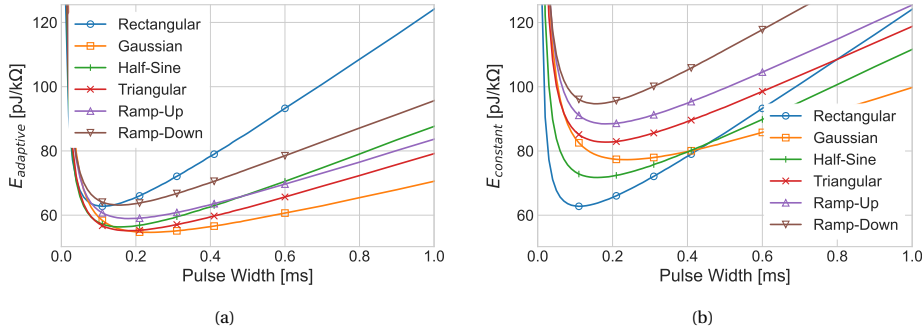


Figure 4.6: Energy threshold for different pulse shapes and widths in the single-axon fiber model for (a) an adiabatic voltage supply and (b) a constant voltage supply. The pulse widths of the non-rectangular pulses are defined in Eqs. (4.1) to (4.6). These results illustrate that the optimal pulse shape depends strongly on the supply voltage. Furthermore, the pulse width that minimizes the energy threshold varies with the selected pulse shape.

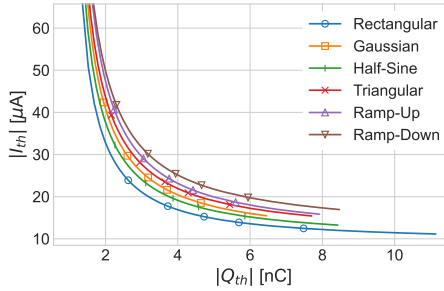


Figure 4.7: Current threshold versus charge threshold for different pulse shapes in the single-axon fiber model. Because the required supply voltage scales with the current threshold, waveforms with lower charge thresholds at a given peak current provide more efficient stimulation under a fixed supply voltage.

4.3.2. BIOPHYSICALLY REALISTIC MODELS

The energy efficiencies for adiabatic and constant-voltage supplies in the biophysically realistic models are shown in Fig. 4.8. The results show similar trends as the single-axon fiber model, supporting the validity of that model. In the case of an adiabatic voltage supply, non-rectangular pulses are more efficient, except for the ramp-down pulses. However, when considering the cost of generating the pulses from a constant supply, an energy increase ranging from $15.9 \pm 1.1\%$ (mean \pm std %) for half-sine pulses to $51.7 \pm 2.5\%$ for triangular pulses is observed.

4.3.3. DYNAMIC VOLTAGE SCALING

Potential energy savings for non-rectangular pulses by scaling the supply voltage to the instant requirements of the channel were calculated in [25]. For a multi-level DC/DC converter with six output steps, this results in an energy reduction of -22%, -15%, and -26% for Gaussian, half-sine, and triangular pulses, respectively. The total efficiency,

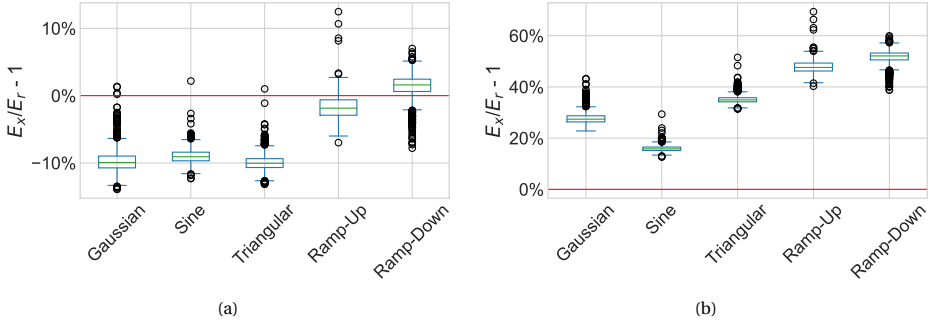


Figure 4.8: Energy efficiency for non-rectangular pulses at multiple locations ($n=1561$) surrounding the biophysically realistic L5 models, presented in [21]. (a) in the case of an adiabatic voltage supply, and (b) for a constant voltage supply.

calculated using Eq. (4.12), for different numbers of voltage steps is listed in Table 4.5. The table shows an increase in energy for most of the shapes. Only in the case of a supply with more than four rails for the Gaussian and half-sine pulses or more than five rails for triangular pulses do they become slightly more efficient than rectangular pulses.

Table 4.5: Overall relative energy efficiency in % of non-rectangular stimulation pulses with respect to rectangular pulses for a system employing dynamic voltage scaling with various numbers of supply rails.

# Supply Rails	$\eta_{\text{total,dvs}}$				
	Gaussian	Half-Sine	Triangular	Ramp-Up	Ramp-Down
1	23.2	14.3	31.9	40.9	50.9
2	8.5	6.7	15.5	23.2	32.3
3	2.5	2.5	7.5	14.7	23.3
4	-0.9	0.0	3.1	10.0	18.2
5	-3.0	-1.7	0.3	7.0	15.0
6	-4.4	-2.9	-1.6	4.9	12.8

4.3.4. EFFECT OF CAPACITIVE ETI

Large-scale multichannel devices will typically interface with arrays of microelectrodes. For microelectrodes, the order of magnitude for the model parameters are $R_s \approx 100\text{k}\Omega$ [27–29] and $C_{\text{dl}} \approx 10\text{--}100\text{ nF}$ [30, 31]. Thus, the expected range of τ is 1–10 ms. Fig. 4.9 depicts η_β for different values of τ over the relevant PW range. The effect of capacitive charging is highly dependent on τ and PW. The energy-duration curves depicted in Fig. 4.10 account for different values of τ , and the total energy efficiencies are listed in Table 4.6. In the expected range of τ , the rectangular pulse is still the most energy-efficient shape. However, its efficiency is affected, especially for longer pulse widths. Next to that, lower values of τ affect the rectangular pulses even further, and at $\tau=0.1\text{ ms}$, the rectangular pulses

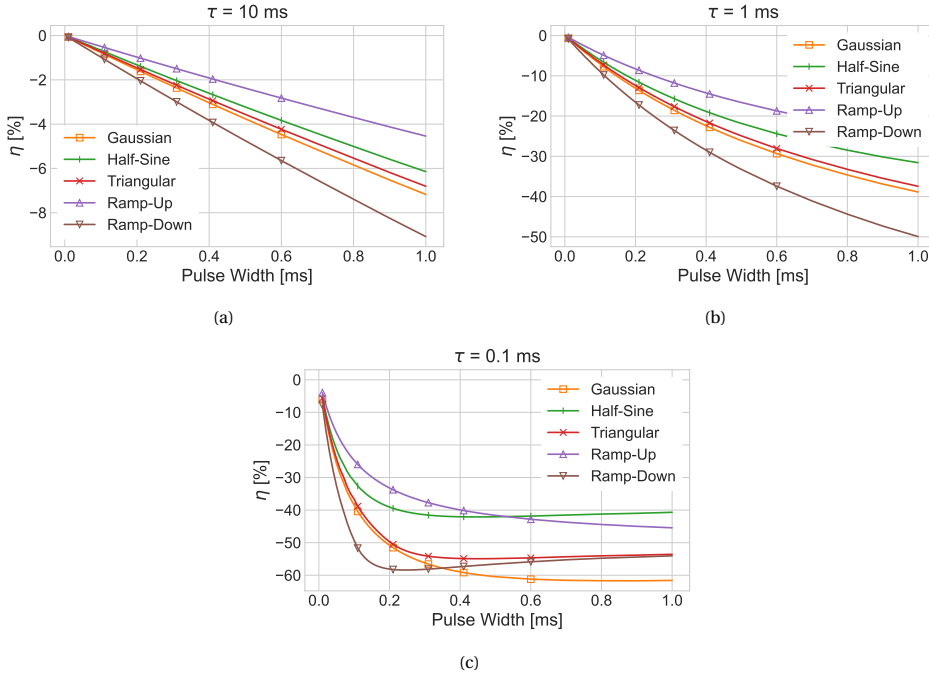


Figure 4.9: Effect of the electrode-tissue interface on the efficiency, η_β , in constant-supply-voltage stimulation for $\tau =$ (a) 10 ms, (b) 1 ms, (c) 0.1 ms. The pulse widths of the non-rectangular pulses are defined in Eqs. (4.1) to (4.6).

are not optimal anymore. However, in the development of electrodes for stimulation, the capacitive transfer should be minimized [32] which will result in high values of τ . Therefore, the capacitive effect is expected to be reduced with further improvement of microelectrodes.

Table 4.6: Overall relative energy efficiency in % of non-rectangular stimulation pulses with respect to rectangular pulses, taking into account charging of the double layer capacitance C_{dl} .

τ [ms]	$\eta_{total,\beta}$				
	Gaussian	Half-Sine	Triangular	Ramp-Up	Ramp-Down
∞	23.2	14.3	31.9	40.9	50.9
10	22.4	13.6	31.0	40.6	49.3
1	17.7	9.4	25.7	39.0	38.1
0.1	3.9	-2.26	8.7	33.8	-1.85

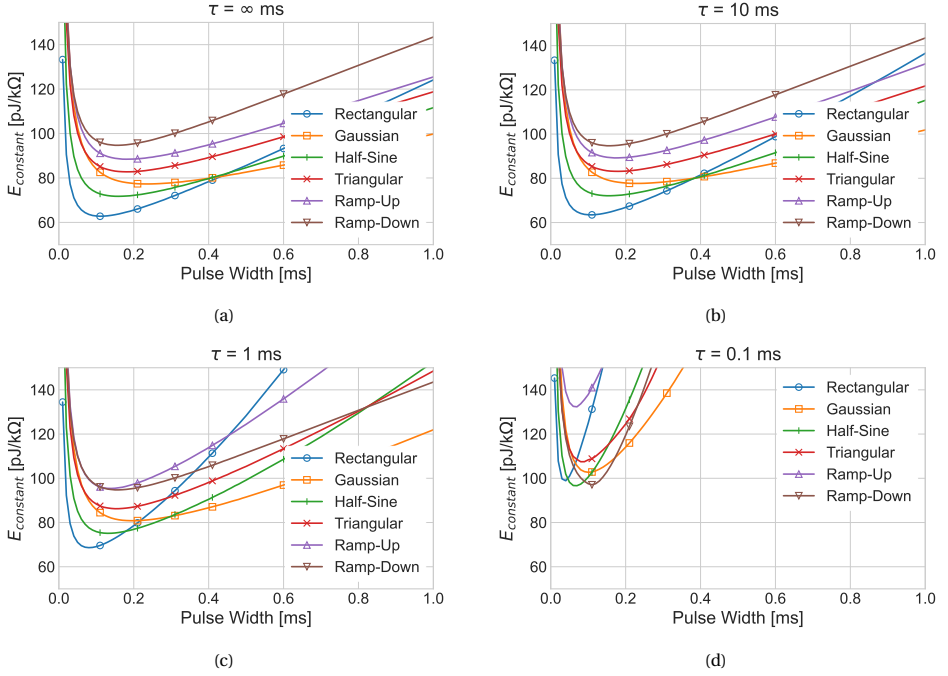


Figure 4.10: Effect of the electrode-tissue interface on the required energy in constant-supply-voltage stimulation for different values of τ . The pulse widths of the non-rectangular pulses are defined in Eqs. (4.1) to (4.6).

4.3.5. GENERALIZATION OF RESULTS

Using the mathematical descriptions of the pulse shapes, one could generalize the obtained results of the proposed energy calculation to other scenarios (e.g., other models or experimental results). By combining Eqs. (4.8) and (4.10), one can calculate the relative threshold value for which the required energy of an arbitrary shape becomes less than that of a rectangular pulse. As an example, the ratio of current thresholds that lead to equal required energy for the triangular and rectangular pulses is given in (4.18)-(4.20).

$$E_{\text{const},r} = I_{\text{th},r} \cdot Q_{\text{th},r} = I_{\text{th},r}^2 \cdot PW \quad (4.18)$$

$$E_{\text{const},t} = I_{\text{th},t} \cdot Q_{\text{th},t} = I_{\text{th},t}^2 \cdot \frac{PW}{2} \quad (4.19)$$

$$E_{\text{const},r} = E_{\text{const},t} \Rightarrow \frac{I_{\text{th},t}}{I_{\text{th},r}} = \sqrt{2} \quad (4.20)$$

$$(4.21)$$

The threshold ratios are calculated similarly for the other shapes used in this chapter and summarized in Table 4.7. The reported ratios are calculated for the shape definitions of this chapter. To use this method to compare the results of other works, one should recalculate the threshold ratio for the appropriate shape definitions. Furthermore, one

could combine the ratio with η_{total} and/or η_{β} to include the effects of dynamic voltage scaling and capacitive charging, respectively.

Table 4.7: Current threshold ratio for which the required energy is equal to that of a rectangular pulse in case of a constant voltage supply.

Shape	Threshold ratio
Gaussian	$\approx \sqrt{6/\sqrt{2\pi}}$
Half-Sine	$\sqrt{\pi/2}$
Triangular	$\sqrt{2}$
Ramp-Up	$\sqrt{2}$
Ramp-Down	$\sqrt{2}$

4.4. DISCUSSION

This study aimed to provide an energy efficiency analysis of different pulse shapes in electrical stimulation that includes losses in the generator circuit. Previously, it was suggested that the combination of non-rectangular pulses and an adjustable compliance voltage would result in the most energy-efficient way of stimulation [20]. First, we presented shape-dependent threshold characteristics for two types of neuron models. In line with previous literature, non-rectangular pulses decreased the charge threshold, while an increase in the strength-duration (current threshold) was observed. When the activation energy is calculated using Eq. (4.9) (assuming an adiabatic voltage supply), non-rectangular pulses show better energy efficiency. However, implementing an adiabatic voltage supply is costly in both area and power. Therefore, large-scale multichannel stimulator systems will typically have limited flexibility in the voltage supply. To account for the losses in the stimulator circuit due to this limited flexibility, we proposed an alternative energy calculation in Eq. (4.10). The results show that the efficiency of non-rectangular pulses is degraded in the proposed energy calculation. This is mainly due to an increase in the peak current, requiring a higher voltage supply.

The losses in the stimulator circuit can partially be reduced using dynamic voltage scaling. We have shown the potential energy reduction in the case of non-rectangular pulses for voltage supplies with up to 6 supply rails. However, it should be noted that the presented efficiencies can only be achieved for channels requiring full-range voltage output. Channels with lower impedance or amplitude requirements can not use all voltage steps, resulting in a decreased efficiency compared to rectangular pulses. As a result, most channels will operate at voltages below the full range in large-scale multichannel systems. Consequently, using rectangular pulses will result in the lowest overall energy consumption of the complete system. Nevertheless, multichannel stimulators can still benefit from voltage scaling when using rectangular pulses. Dynamic voltage scaling saves most energy for channels requiring sub-full-range amplitudes [25]. This is also true for rectangular pulses; thus, the total power consumption of a multichannel stimulator can be reduced by deploying independent voltage supply rails.

The pulse shapes used in this chapter are not always identical to the ones used in pre-

vious works, which might have an effect on the obtained results. The Gaussian-like pulses in [9] were truncated at the tails for small pulse widths, while [10] used Gaussian pulses with a fixed σ for all pulse widths. Furthermore, this chapter focused on monophasic pulses, while biphasic pulses are commonly used in electrical stimulation applications. The second phase—also called the recovery phase—is introduced to recover the charges applied during the first phase to prevent harmful electrochemical reactions [26]. The biphasic pulses can be symmetrical (the shape, amplitude, and duration of the second phase are equal to the first phase) or asymmetrical, but the total charge of both phases should be equal for safety. Previous work has shown that the introduction of the recovery causes an increase in the stimulation threshold compared to monophasic pulses [33]. However, many factors change the extent of this effect. For example, introducing an inter-phase delay and using asymmetrical pulses reduce the threshold increase [26, 34]. We used monophasic pulses to focus on the effects of pulse shaping of the first phase without additional factors of the second phase. Since the second phase is not used to activate the cell, its shape and duration can be designed to minimize the energy consumption, regardless of the shape of the first phase.

The presented analysis does not include any losses introduced by additional circuitry required to generate non-rectangular pulses. The generation of rectangular pulses is relatively easy using a constant current source, while the generation of non-rectangular pulses requires additional circuitry [35, 36]. The power consumption of the additional circuits depends on the specific implementation and can be optimized, but it will degrade the efficiency of non-rectangular pulses even further.

Finally, the results presented in this chapter are based on the quasi-static approximation in a homogeneous and isotropic environment. This model exhibits various limitations due to the simplifications made. For example, it does not consider capacitive wave propagation through the tissue. Thus, it is unlikely that the exact percentages presented here will translate to an in-vivo environment. Further research is required to incorporate these effects into the energy calculations.

4.5. CONCLUSION

Non-rectangular pulses are often presented to be more energy-efficient than rectangular pulses for electrical stimulation. We have shown that it is crucial to incorporate the cost of generating such pulses in assessing energy efficiency. The presented results suggest that losses due to limited flexibility in the voltage supply negate potential energy reductions in the biological domain in the case of non-rectangular pulses. Previously, it was suggested that combining non-rectangular pulses with scaling of the supply to the minimum allowable voltage would result in the most energy-efficient way of stimulation [20]. The current results present an opposite finding that rectangular stimuli can be more energy efficient than the tested non-rectangular pulses in the case of a scalable, constant voltage supply. This provides a different perspective on pulse shaping and energy efficiency optimization of neural implants, specifically for large-scale multichannel systems where the flexibility of the voltage supply is limited.

BIBLIOGRAPHY

- [1] E. Fernández, A. Alfaro, and P. González-López, “Toward Long-Term Communication With the Brain in the Blind by Intracortical Stimulation: Challenges and Future Prospects”, *Frontiers in Neuroscience*, vol. 14, no. August, Aug. 2020, ISSN: 1662-453X. DOI: 10.3389/fnins.2020.00681.
- [2] T. P. G. van Nunen, R. M. C. Mestrom, and H. J. Visser, “Wireless Power Transfer to Biomedical Implants Using a Class-E Inverter and a Class-DE Rectifier”, *IEEE Journal of Electromagnetics, RF and Microwaves in Medicine and Biology*, vol. 7, no. 3, pp. 202–209, Sep. 2023, ISSN: 2469-7249. DOI: 10.1109/JERM.2023.3267042.
- [3] A. Nurmikko, *Challenges for Large-Scale Cortical Interfaces*, 2020. DOI: 10.1016/j.neuron.2020.10.015.
- [4] M. Mariello and C. M. Proctor, “Wireless Power and Data Transfer Technologies for Flexible Bionic and Bioelectronic Interfaces: Materials and Applications”, *Advanced Materials Technologies*, Sep. 2024, ISSN: 2365-709X. DOI: 10.1002/admt.202400797.
- [5] M. Kiani, “Wireless Power Transfer and Management for Medical Applications: Wireless power”, *IEEE Solid-State Circuits Magazine*, vol. 14, no. 3, pp. 41–52, 2022, ISSN: 1943-0582. DOI: 10.1109/MSSC.2022.3178671.
- [6] R. Shirafkan and O. Shoaee, “Current-Based Neurostimulation Circuit and System Techniques”, in *Handbook of Biochips*, New York, NY: Springer New York, 2022, pp. 445–469. DOI: 10.1007/978-1-4614-3447-4_42.
- [7] M. N. van Dongen and W. A. Serdijn, “A Power-Efficient Multichannel Neural Stimulator Using High-Frequency Pulsed Excitation From an Unfiltered Dynamic Supply”, *IEEE Transactions on Biomedical Circuits and Systems*, vol. 10, no. 1, pp. 61–71, Feb. 2016, ISSN: 1932-4545. DOI: 10.1109/TBCAS.2014.2363736.
- [8] T. J. Foutz and C. C. McIntyre, “Evaluation of novel stimulus waveforms for deep brain stimulation”, *Journal of Neural Engineering*, vol. 7, no. 6, p. 066 008, Dec. 2010, ISSN: 1741-2560. DOI: 10.1088/1741-2560/7/6/066008.
- [9] A. Wongsarnpigoon and W. M. Grill, “Energy-efficient waveform shapes for neural stimulation revealed with a genetic algorithm”, *Journal of Neural Engineering*, vol. 7, no. 4, p. 046 009, Aug. 2010, ISSN: 1741-2560. DOI: 10.1088/1741-2560/7/4/046009.
- [10] S. Eickhoff and J. C. Jarvis, “An Investigation of Neural Stimulation Efficiency With Gaussian Waveforms”, *IEEE Transactions on Neural Systems and Rehabilitation Engineering*, vol. 28, no. 1, pp. 104–112, Jan. 2020, ISSN: 1534-4320. DOI: 10.1109/TNSRE.2019.2954004.

- [11] M. Sahin and Y. Tie, "Non-rectangular waveforms for neural stimulation with practical electrodes", *Journal of Neural Engineering*, vol. 4, no. 3, pp. 227–233, Sep. 2007, ISSN: 1741-2560. DOI: 10.1088/1741-2560/4/3/008.
- [12] H.-M. Lee, H. Park, and M. Ghovanloo, "A Power-Efficient Wireless System With Adaptive Supply Control for Deep Brain Stimulation", *IEEE Journal of Solid-State Circuits*, vol. 48, no. 9, pp. 2203–2216, Sep. 2013, ISSN: 0018-9200. DOI: 10.1109/JSSC.2013.2266862.
- [13] E. Noorsal, K. Sooksood, H. Xu, R. Hornig, J. Becker, and M. Ortmanns, "A Neural Stimulator Frontend With High-Voltage Compliance and Programmable Pulse Shape for Epiretinal Implants", *IEEE Journal of Solid-State Circuits*, vol. 47, no. 1, pp. 244–256, Jan. 2012, ISSN: 0018-9200. DOI: 10.1109/JSSC.2011.2164667.
- [14] S. K. Arfin and R. Sarpeshkar, "An Energy-Efficient, Adiabatic Electrode Stimulator With Inductive Energy Recycling and Feedback Current Regulation", *IEEE Transactions on Biomedical Circuits and Systems*, vol. 6, no. 1, pp. 1–14, Feb. 2012, ISSN: 1932-4545. DOI: 10.1109/TBCAS.2011.2166072.
- [15] A. Urso, V. Giagka, M. van Dongen, and W. A. Serdijn, "An Ultra High-Frequency 8-Channel Neurostimulator Circuit With 68% Peak Power Efficiency", *IEEE Transactions on Biomedical Circuits and Systems*, vol. 13, no. 5, pp. 882–892, Oct. 2019, ISSN: 1932-4545. DOI: 10.1109/TBCAS.2019.2920294.
- [16] A. Rashidi, N. Yazdani, and A. M. Sodagar, "Fully implantable, multi-channel microstimulator with tracking supply ribbon, multi-output charge pump and energy recovery", *IET Circuits, Devices & Systems*, vol. 15, no. 2, pp. 104–120, Mar. 2021, ISSN: 1751-858X. DOI: 10.1049/cds2.12007.
- [17] I. Williams and T. G. Constandinou, "An Energy-Efficient, Dynamic Voltage Scaling Neural Stimulator for a Proprioceptive Prosthesis", *IEEE Transactions on Biomedical Circuits and Systems*, vol. 7, no. 2, pp. 129–139, Apr. 2013, ISSN: 1932-4545. DOI: 10.1109/TBCAS.2013.2256906.
- [18] Z. Luo, M.-D. Ker, T.-Y. Yang, and W.-H. Cheng, "A Digitally Dynamic Power Supply Technique for 16-Channel 12 V-Tolerant Stimulator Realized in a 0.18- μm 1.8-V/3.3-V Low-Voltage CMOS Process", *IEEE Transactions on Biomedical Circuits and Systems*, vol. 11, no. 5, pp. 1087–1096, Oct. 2017, ISSN: 1932-4545. DOI: 10.1109/TBCAS.2017.2713122.
- [19] S. Ha *et al.*, "A 16-channel wireless neural interfacing SoC with RF-powered energy-replenishing adiabatic stimulation", in *2015 Symposium on VLSI Circuits (VLSI Circuits)*, IEEE, Jun. 2015, pp. C106–C107, ISBN: 978-4-86348-502-0. DOI: 10.1109/VLSIC.2015.7231341.
- [20] T. J. Foutz, D. M. Ackermann Jr., K. L. Kilgore, and C. C. McIntyre, "Energy Efficient Neural Stimulation: Coupling Circuit Design and Membrane Biophysics", *PLoS ONE*, vol. 7, no. 12, G. Foffani, Ed., e51901, Dec. 2012, ISSN: 1932-6203. DOI: 10.1371/journal.pone.0051901.
- [21] A. S. Aberra, A. V. Peterchev, and W. M. Grill, "Biophysically realistic neuron models for simulation of cortical stimulation", *Journal of Neural Engineering*, vol. 15, no. 6, p. 066023, Dec. 2018, ISSN: 1741-2560. DOI: 10.1088/1741-2552/aadbb1.

- [22] M. Deprez, K. Luyck, L. Luyten, T. Tambuyzer, B. Nuttin, and M. Mc Laughlin, "An evaluation of the effect of pulse-shape on grey and white matter stimulation in the rat brain", *Scientific Reports*, vol. 8, no. 1, Dec. 2018, ISSN: 20452322. DOI: 10.1038/s41598-017-19023-0.
- [23] N. T. Carnevale and M. L. Hines, *The NEURON Book*. Cambridge: Cambridge University Press, 2006, pp. 1–457, ISBN: 9780511541612. DOI: 10.1017/CB09780511541612.
- [24] C. A. Bossetti, M. J. Birdno, and W. M. Grill, "Analysis of the quasi-static approximation for calculating potentials generated by neural stimulation", *Journal of Neural Engineering*, vol. 5, no. 1, pp. 44–53, Mar. 2008, ISSN: 1741-2560. DOI: 10.1088/1741-2560/5/1/005.
- [25] K. Kolovou-Kouri, A. Rashidi, F. Varkevisser, W. A. Serdijn, and V. Giagka, "Energy Savings of Multi-Channel Neurostimulators with Non-Rectangular Current-Mode Stimuli Using Multiple Supply Rails", in *2022 44th Annual International Conference of the IEEE Engineering in Medicine & Biology Society (EMBC)*, vol. 2022-July, IEEE, Jul. 2022, pp. 3443–3446, ISBN: 978-1-7281-2782-8. DOI: 10.1109/EMBC48229.2022.9871145.
- [26] D. R. Merrill, M. Bikson, and J. G. Jefferys, "Electrical stimulation of excitable tissue: design of efficacious and safe protocols", *Journal of Neuroscience Methods*, vol. 141, no. 2, pp. 171–198, Feb. 2005, ISSN: 01650270. DOI: 10.1016/j.jneumeth.2004.10.020.
- [27] E. M. Maynard, C. T. Nordhausen, and R. A. Normann, "The Utah Intracortical Electrode Array: A recording structure for potential brain-computer interfaces", *Electroencephalography and Clinical Neurophysiology*, vol. 102, no. 3, pp. 228–239, Mar. 1997, ISSN: 00134694. DOI: 10.1016/S0013-4694(96)95176-0.
- [28] M. Hasanuzzaman, B. G. Motlagh, F. Mounaim, A. Hassan, R. Raut, and M. Sawan, "Toward an Energy-Efficient High-Voltage Compliant Visual Intracortical Multi-channel Stimulator", *IEEE Transactions on Very Large Scale Integration (VLSI) Systems*, vol. 26, no. 5, pp. 878–891, May 2018, ISSN: 1063-8210. DOI: 10.1109/TVLSI.2018.2794445.
- [29] M. M. Straka, B. Shafer, S. Vasudevan, C. Welle, and L. Rieth, "Characterizing longitudinal changes in the impedance spectra of in-vivo peripheral nerve electrodes", *Micromachines*, vol. 9, no. 11, p. 587, Nov. 2018, ISSN: 2072666X. DOI: 10.3390/mi9110587.
- [30] M. Monge *et al.*, "A Fully Intraocular High-Density Self-Calibrating Epiretinal Prosthesis", *IEEE Transactions on Biomedical Circuits and Systems*, vol. 7, no. 6, pp. 747–760, Dec. 2013, ISSN: 1932-4545. DOI: 10.1109/TBCAS.2014.2298334.
- [31] C.-Y. Lin, Y.-J. Li, and M.-D. Ker, "High-voltage-tolerant stimulator with adaptive loading consideration for electronic epilepsy prosthetic SoC in a 0.18- μ m CMOS process", in *10th IEEE International NEWCAS Conference*, IEEE, Jun. 2012, pp. 125–128, ISBN: 978-1-4673-0859-5. DOI: 10.1109/NEWCAS.2012.6328972.

- [32] F. Alonso, "Models and Simulations of the Electric Field in Deep Brain Stimulation : Comparison of Lead Designs, Operating Modes and Tissue Conductivity.", Ph.D. dissertation, 2018, pp. 30–30, ISBN: 9789176852613.
- [33] J. Reilly and A. M. Diamant, "Waveform and Polarity Effects", in *Electrostimulation : Theory, Applications, and Computational Model*, Artech House, 2011, pp. 26–28, ISBN: 9781608071081.
- [34] R. K. Shepherd and E. Javel, "Electrical stimulation of the auditory nerve: II. Effect of stimulus waveshape on single fibre response properties.", *Hearing research*, vol. 130, no. 1-2, pp. 171–88, Apr. 1999, ISSN: 0378-5955. DOI: 10.1016/S0378-5955(99)00011-8.
- [35] W. M. Grill, "Model-based analysis and design of waveforms for efficient neural stimulation", *Progress in Brain Research*, vol. 222, pp. 147–162, 2015, ISSN: 18757855. DOI: 10.1016/bs.pbr.2015.07.031.
- [36] S. Ethier and M. Sawan, "Exponential Current Pulse Generation for Efficient Very High-Impedance Multisite Stimulation", *IEEE Transactions on Biomedical Circuits and Systems*, vol. 5, no. 1, pp. 30–38, Feb. 2011, ISSN: 1932-4545. DOI: 10.1109/TBCAS.2010.2073707.

5

ANALYSIS OF POWER LOSSES AND THE EFFICACY OF POWER MINIMIZATION STRATEGIES IN MULTICHANNEL ELECTRICAL STIMULATION SYSTEMS

All models are wrong, but some are useful.

— George Box

This chapter is based on the following preprint and is under review for publication at the time of writing: F. Varkevisser, *et al.*, "Analysis of power losses and the efficacy of power minimization strategies in multichannel electrical stimulation systems," 2025. arXiv: 2501.08025 [eess.SY]. Available: <http://arxiv.org/abs/2501.08025>

5.1. INTRODUCTION

IMPLANTABLE neurostimulation devices are widely used to treat neurological disorders such as Parkinson's disease, hearing loss, and visual impairment. These established clinical applications typically rely on relatively low channel counts or even single channel stimulation. In contrast, emerging applications such as visual prostheses and bidirectional somatosensory prostheses demand large-scale multichannel stimulator systems, where hundreds to thousands of electrodes may be required to achieve meaningful perceptual resolution [1–3]. The development of such systems is a complex interdisciplinary challenge, requiring intricate system- and circuit-level considerations for the electronic circuits [4], and the design of biocompatible high-density electrode interfaces [5]. As the number of stimulation channels continues to scale, the available power becomes a major bottleneck. Traditionally, power is delivered wirelessly to the implantable stimulators since it avoids the infection risks posed by wired connections [6]. However, the power that can be transferred to the implant is limited by several safety regulations, such as the specific absorption rate (SAR) limit [6, 7]. Consequently, optimizing the power efficiency of stimulator circuits is essential to enable further channel scaling and ensure these devices can function effectively within the limits of available power. Furthermore, power losses in the circuits lead to heat generation, which should be minimized to prevent damage to the tissue surrounding the implantable device [8]. Improving power efficiency reduces excessive heating and improves the safety of the device.

Stimulator circuits are typically implemented to allow for current mode stimulation (CMS) or voltage mode stimulation (VMS). CMS is often preferred due to its precise control over injected charge, which is critical for safe stimulation [9, 10]. However, CMS suffers from inherent power inefficiency, as illustrated in Fig. 5.1. In a conventional bipolar CMS setup (Fig. 5.1a), rectangular current pulses are generated from a fixed voltage supply, V_{DD} . The stimulation current leads to a voltage drop over the tissue load equal to $V_{load} = I_{stim} Z_{tissue}$ (Fig. 5.1), where I_{stim} is the stimulation current and Z_{tissue} the tissue impedance. Any mismatch between V_{load} and V_{DD} (indicated in grey in Fig. 5.1) leads to excessive power dissipation in the current source, reducing overall efficiency. A possible solution is to scale down the voltage supply, minimizing overhead losses and improving efficiency (η), as illustrated in Fig. 5.1c.

In multichannel systems, however, the variability of tissue impedance and current amplitude between channels complicates this approach. Each channel has different voltage requirements, making the application of voltage scaling more complex [11]. To address this, several voltage scaling strategies are proposed in the literature to reduce the losses at the output driver. The different scaling strategies are illustrated in Fig. 5.2 for a system with five channels with varying load voltage requirements. Figure 5.2a illustrates the conventional approach of using a fixed voltage supply for all channels. Ideally, each channel would have its own dedicated voltage supply precisely matching its load voltage (Fig. 5.2b), a strategy often referred to as adiabatic voltage scaling [12, 13]. However, this approach faces scalability limitations, as each channel requires a separate voltage supply, and implementing adiabatic scaling often demands an impractically large chip

Statement of contribution: The methodology and analyses in this chapter were developed and implemented by the candidate. All computations and writing were performed by the candidate, with feedback and supervision from the promoters.

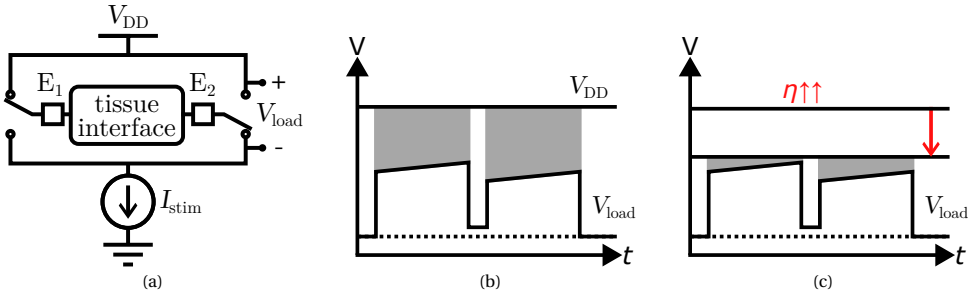


Figure 5.1: Illustration of the overhead losses in current-mode stimulation (CMS) in a bipolar electrode configuration. (a) Conventional output stage for CMS with a fixed voltage supply V_{DD} ; (b) Example of the load voltage (V_{load}) as a result of the current pulses delivered to the tissue. The mismatch between the load voltage and supply voltage (indicated in the grey area) leads to power dissipation in the output driver; (c) Illustration of how a scaled voltage supply can reduce the power dissipation in the output driver and thus increase the power efficiency, for the example in (b).

area, making it unsuitable for scalable solutions. An alternative is to use a single scalable supply (Fig. 5.2c) [14, 15], where the supply voltage is configured to accommodate the worst-case channel (Channel 2 in Fig. 5.2c). While this ensures high efficiency for the worst-case channel, it can result in significant overhead losses for other channels. Another strategy involves creating N voltage rails distributed across all channels [16–19], with each channel connected to the nearest rail above its load voltage (Fig. 5.2d). This approach offers a trade-off between power efficiency and system complexity with the choice of N .

The impact of inter-channel variability on the power efficiency of multichannel stimulation systems is often neglected in conventional designs. This chapter introduces a novel methodology that incorporates these effects to evaluate the efficacy of various supply scaling strategies and quantify the associated power losses. Using experimental data from various multichannel stimulation applications, the methodology calculates channel-specific load voltage requirements and estimates the overhead losses for different voltage scaling strategies. The results provide valuable insights into the trade-offs between power efficiency and design complexity, offering a systematic framework to guide circuit design considerations for large-scale neurostimulation systems.

5.2. METHODS

5.2.1. DATA COLLECTION AND EXTRACTION

Experimental data was collected using a systematic search in the Scopus database for studies on (micro)stimulation. Inclusion criteria required that the selected studies report (perception) thresholds and impedance data and that the subjects are either humans or non-human primates. For some cases with partially available data, the authors were contacted to request additional data. We collected 26 datasets from 7 publications, spanning four applications. The results are organized by application, resulting in categories for intracortical visual prostheses (V1), retinal implants, intrafascicular peripheral nerve stimulation (iPNS), and extraneural PNS. The extracted datasets are detailed below. Each study has its own definitions and methods of collecting and reporting the data. Unless

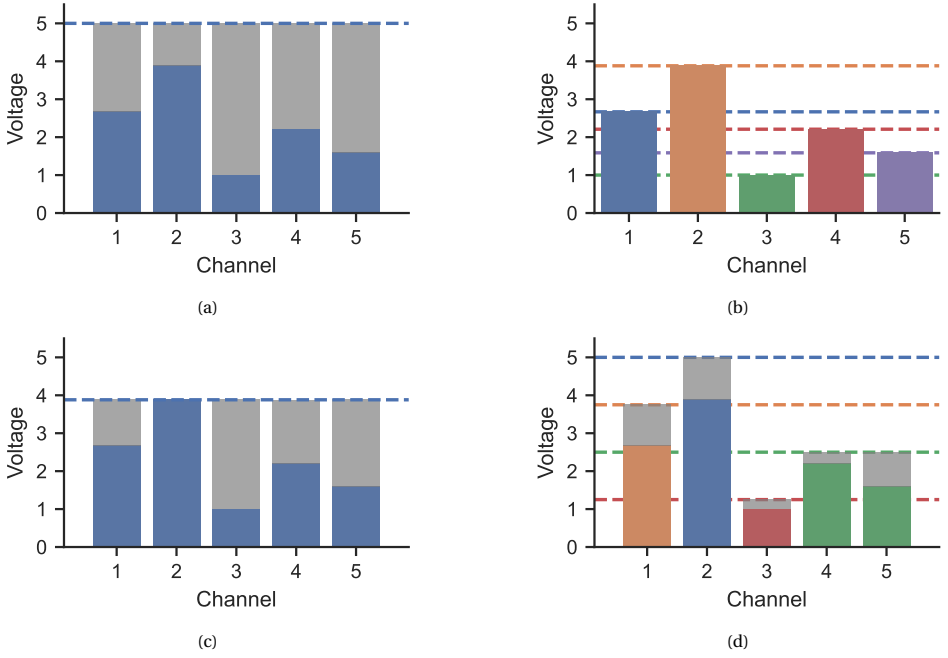


Figure 5.2: Illustration of the overhead losses for different voltage scaling strategies in the example of a system with five channels. Dashed, horizontal lines indicate the available voltage rails, and the colored bars the load voltage (V_{load}) of the specific channel, where the color indicates to which voltage rail the channel is connected. Grey rectangles indicate the overhead losses. (a) In the case of a fixed voltage supply, all channels share the same voltage supply. (b) In the case of ideal supply scaling, each channel has a specific voltage supply matched to its load voltage. Thus, the overhead losses are zero. (c) With a global supply scaling strategy, a shared supply voltage is scaled to the worst-case V_{load} (channel 2 in the example), eliminating all overhead losses for that channel and reducing overhead losses in the other channels compared to the fixed voltage strategy. (d) A stepped voltage supply strategy with 4 rails. Multiple voltage rails are available, and each channel is connected to the nearest rail above its load voltage.

stated otherwise, all values are reported as (mean \pm sd).

The study by Fernández et al. [20] explored the use of a Utah Electrode Array (UEA) with 96 electrodes implanted in the visual cortex of a human patient. The authors applied stimulation trains of 50 monopolar charge-balanced cathodic-first biphasic stimuli, with a pulse width (PW) of 170 μ s, an interphase delay (IPD) of 60 μ s, and a repetition frequency of 300 Hz for the threshold procedure. A binary search procedure was used to determine the stimulation threshold that led to a visual perception in 50 % of the trials. The magnitude of the electrode impedance was measured at 1 kHz. The current threshold for single-electrode stimulation was $(66.8 \pm 36.5) \mu$ A, while electrode impedances of $(47.0 \pm 4.8) \text{ k}\Omega$ were recorded.

Building on similar stimulation parameters, Chen et al. [21] implanted 1024 micro-electrodes (16 64-channel UEAs) in the visual cortex of two monkeys ('Monkey A' and 'Monkey L'). For both monkeys, two current thresholds are reported, one in the early stage after implantation (μ_{early}) and one in the late stage of the experiments (μ_{late}). The

reported thresholds are $\mu_{\text{early}} = (65 \pm 45) \mu\text{A}$ and $\mu_{\text{late}} = (60 \pm 58) \mu\text{A}$ for Monkey A, and $\mu_{\text{early}} = (19 \pm 17) \mu\text{A}$ and $\mu_{\text{late}} = (80 \pm 71) \mu\text{A}$ for Monkey L. Additionally, we received the dataset of recorded electrode impedances from the authors. From this dataset, we obtained the impedance values (at 1 kHz) for both monkeys in the first and last experiment sessions. These values were filtered to include only electrodes with impedance below 300 k Ω for Monkey A and below 150 k Ω for Monkey L, as these electrodes were used for the current threshold measurements [21]. In Monkey A, the recorded electrode impedance was $(144.7 \pm 72.6) \text{ k}\Omega$ and $(71.1 \pm 70.6) \text{ k}\Omega$ in the early and late stages, respectively, and for Monkey L, it was $(75.1 \pm 36.3) \text{ k}\Omega$ and $(74.9 \pm 36.4) \text{ k}\Omega$.

While Fernández and Chen focused on cortical implants, De Balthasar et al. [22] investigated epiretinal implants in six human subjects (S1-S6). Since the impedance data is only reported for subjects S4-S6, the other subjects are not included in this analysis. The array consisted of 16 (4x4) platinum electrodes in a checkerboard arrangement with alternating electrode sizes of 260 μm and 520 μm . The stimulation thresholds were determined using single-pulse symmetric cathodic-first pulses with a PW of 0.975 ms and an IPD of 0.975 ms. The perceptual thresholds, in this case, are defined as the current amplitude that causes a percept in 79 % of the trials. The electrode impedance was reported separately for the two sizes and are therefore treated as separate datasets in this analysis. The reported current thresholds ($\mu_{\text{subject, size}}$) are: $\mu_{S4, 260} = (233.0 \pm 20.9) \mu\text{A}$, $\mu_{S5, 260} = (30.3 \pm 1.7) \mu\text{A}$, $\mu_{S6, 260} = (40.9 \pm 6.1) \mu\text{A}$, $\mu_{S4, 520} = (222.9 \pm 16.0) \mu\text{A}$, $\mu_{S5, 520} = (26.9 \pm 1.3) \mu\text{A}$, $\mu_{S6, 520} = (37.8 \pm 4.9) \mu\text{A}$. Furthermore, the reported impedances are as follows: $Z_{S4, 260} = (25.6 \pm 3.0) \text{ k}\Omega$, $Z_{S5, 260} = (40.8 \pm 1.5) \text{ k}\Omega$, $Z_{S6, 260} = (36.5 \pm 1.8) \text{ k}\Omega$, $Z_{S4, 520} = (13.6 \pm 1.1) \text{ k}\Omega$, $Z_{S5, 520} = (22.9 \pm 0.3) \text{ k}\Omega$, $Z_{S6, 520} = (18.7 \pm 0.4) \text{ k}\Omega$.

Similarly targeting retinal stimulation, Demchinsky et al. [23] implanted one human patient with the Argus II [24] retinal prosthesis. The Argus II has an epiretinal electrode array of 6x10 platinum electrodes with a diameter of 200 μm [24]. The parameters for stimulation thresholds and impedance measurements are not specified in this study, but the perception threshold is reported as the amplitude evoking a visual percept in 50 % of the trials. The measured perception threshold and electrode impedance after six months of implantation were $(251 \pm 197) \mu\text{A}$ and $(5.10 \pm 1.77) \text{ k}\Omega$ ¹, respectively.

Instead of targeting the central nervous system, Tan et al. [25] examined extraneural peripheral nerve stimulation (PNS) in two human amputees. They implanted flat interface nerve electrodes (FINE) around the median and ulnar nerves in their mid-forearm and Case Western Reserve University (CWRU) electrodes around the radial nerve to produce selective sensory responses. The FINE electrode around the ulnar nerve in subject 2 did not retain good contact with the nerve and is therefore not included in the results. The stimulation pattern was a pulse train (100 Hz) of monopolar, bi-phasic, charge-balanced, cathodic-first square pulses, with a sinusoidal modulated pulse width (1 Hz) to evoke a natural, pulsing perception. Furthermore, the PW, as well as the amplitude, were stepped during the threshold process. As a result, the stimulation charge is used to report the perception threshold. However, the current amplitude is required for the power loss calculations presented in this chapter. To estimate the current amplitude from the reported

¹In [23], the current and impedance values are reported in mA and Ω , respectively in Table 2. Based on impedance and current values reported in other Argus II studies, it is assumed that this is a mistake and that these values should be μA and k Ω instead.

charge thresholds, the average PW is estimated at 100 μ s, and the current threshold is calculated as $I_{th,i} = Q_{th,i} / 100 \mu$ s. The resulting perception current thresholds are: $\mu_{S1,median} = (0.96 \pm 0.43)$ mA, $\mu_{S1,ulnar} = (0.71 \pm 0.59)$ mA, $\mu_{S1,radial} = (0.41 \pm 0.12)$ mA, $\mu_{S2,median} = (1.26 \pm 0.42)$ mA, $\mu_{S2,radial} = (1.20 \pm 0.33)$ mA. To measure the electrode impedance, 0.3 mA and 50 μ s pulses at 20 and 100 Hz between pairs of electrodes within each cuff were used. The mean of eight measures of the resulting peak voltage drop between each pair of contacts was measured to calculate the impedance. The reported impedances are: $Z_{S1,median} = (3.12 \pm 0.15)$ k Ω , $Z_{S1,ulnar} = (2.66 \pm 0.15)$ k Ω , $Z_{S1,radial} = (2.91 \pm 0.22)$ k Ω , $Z_{S2,median} = (2.92 \pm 0.21)$ k Ω , $Z_{S2,radial} = (3.09 \pm 0.19)$ k Ω .

Finally, Davis et al. [26] and George et al. [27] focused on intrafascicular PNS (iPNS) using Utah Slanted Electrode Arrays (USEA). In [26], two human amputees were implanted with a USEA of 96 electrodes in the sensory nerves in the forearm. The USEA delivers intrafascicular microstimulation, in contrast to the electrodes used in [25], which wrap around the nerve. In subject 1, the array was implanted in the median nerve, while in subject 2, it was implanted in the ulnar nerve. Biphasic, cathodic-first stimulation was used to determine the perception threshold. In most thresholding experiments, a constant frequency of 200 Hz and train duration of 0.2 s were used. The resulting perception thresholds were $\mu_{S1} = (27.0 \pm 20.0)$ μ A, $\mu_{S2} = (12.0 \pm 11.0)$ μ A. The electrode impedance was measured using a sinusoidal current at 1 kHz through a reference electrode. Electrodes with an impedance <500 k Ω were defined as working electrodes. The measured impedances for the working electrodes are $Z_{S1} = (222 \pm 133)$ k Ω and $Z_{S2} = (143 \pm 76)$ k Ω . The number of working electrodes in subject 1 rapidly dropped over the duration of the study.

A complementary study by George et al. [27] provides further insight into the long-term viability of iPNS in humans. In [27], two human amputees (S5 & S6) were chronically implanted with USEAs in their residual arm nerves to restore sensorimotor function. In both participants, one array was implanted in the median nerve and one in the ulnar nerve. The study included a third participant (S7). However, the stimulation thresholds are only reported for S5 & S6. Therefore, S7 is excluded from the analysis in this chapter. Contrary to the other studies, the perception threshold values in [27] are reported in the format 'median (IQR).' The perception thresholds are reported for the first and last session, leading to a total of 8 datasets; however, since the last session in S6-ulnar contains a very limited set of electrodes, it is left out of the analysis in this chapter. The reported perception thresholds are as follows: $\mu_{S5M,first} = 25$ μ A (17 μ A), $\mu_{S5U,first} = 31$ μ A (31 μ A), $\mu_{S6M,first} = 21$ μ A (11 μ A), $\mu_{S6U,first} = 36.5$ μ A (42.5 μ A), $\mu_{S5M,last} = 60$ μ A (40 μ A), $\mu_{S5U,last} = 70$ μ A (52.5 μ A), $\mu_{S6M,last} = 72.5$ μ A (25 μ A). The electrode impedance data is only shown in figure format in the paper. The data behind this figure was provided to us by the authors and we used the impedance data of the first and last sessions of each participant for our analysis. The recorded impedance data is as follows: $Z_{S5M,first} = 81.6$ k Ω (99.6 k Ω), $Z_{S5U,first} = 77.5$ k Ω (101.5 k Ω), $Z_{S6M,first} = 67.6$ k Ω (130.6 k Ω), $Z_{S6U,first} = 49.0$ k Ω (71.4 k Ω), $Z_{S5M,last} = 131.3$ k Ω (163.8 k Ω), $Z_{S5U,last} = 178.6$ k Ω (65.9 k Ω), $Z_{S6M,last} = 50.6$ k Ω (42.8 k Ω).

The datasets are summarized in Table 5.1.

Table 5.1: Summary of the datasets used in this chapter. All numerical data is presented as 'mean \pm sd,' except for [27], where it is presented as 'median (IQR).' U(S)EA = Utah (Slanted) Electrode Array, FINE = Flat Interface Nerve Electrode, V1 = Primary visual cortex, and (i)PNS = (intrafascicular) Peripheral Nerve Stimulation.

#	Source	Dataset	Electrode impedance [k Ω]	Current threshold [μ A]	Target	Electrodes
1	[20]	Human	47.0 \pm 4.8	67 \pm 37	V1	UEA
2	[21]	Monkey A early	144.7 \pm 72.6	65 \pm 45	V1	UEA
3	[21]	Monkey A late	71.1 \pm 70.6	60 \pm 58	V1	UEA
4	[21]	Monkey L early	75.1 \pm 36.3	19 \pm 17	V1	UEA
5	[21]	Monkey L late	74.9 \pm 36.4	80 \pm 71	V1	UEA
6	[22]	S4 260 μ m	25.6 \pm 0.3	233 \pm 21	Retina	Custom
7	[22]	S5 260 μ m	40.8 \pm 1.5	30 \pm 2	Retina	Custom
8	[22]	S6 260 μ m	36.5 \pm 1.8	41 \pm 6	Retina	Custom
9	[22]	S4 520 μ m	13.6 \pm 1.1	222 \pm 16	Retina	Custom
10	[22]	S5 520 μ m	22.9 \pm 0.3	27 \pm 1	Retina	Custom
11	[22]	S6 520 μ m	18.7 \pm 0.4	38 \pm 5	Retina	Custom
12	[23]	Human	5.1 \pm 1.8	251 \pm 197	Retina	Argus II
13	[25]	S1 median	3.1 \pm 0.2	955 \pm 425	PNS	FINE
14	[25]	S1 ulnar	2.7 \pm 0.2	707 \pm 592	PNS	FINE
15	[25]	S1 radial	2.9 \pm 0.2	407 \pm 124	PNS	FINE
16	[25]	S2 median	2.9 \pm 0.2	1260 \pm 415	PNS	FINE
17	[25]	S1 radial	3.1 \pm 0.2	1200 \pm 325	PNS	FINE
18	[26]	S1 median	222 \pm 133	27 \pm 20	iPNS	USEA
19	[26]	S2 ulnar	143 \pm 76	12 \pm 11	iPNS	USEA
20	[27]	S5-M first	81.6 (99.6)	25 (17)	iPNS	USEA
21	[27]	S5-U first	77.5 (101.5)	31 (31)	iPNS	USEA
22	[27]	S6-M first	67.6 (130.6)	21 (11)	iPNS	USEA
23	[27]	S6-U first	49.0 (71.4)	37 (43)	iPNS	USEA
24	[27]	S5-M last	131.3 (163.8)	60 (40)	iPNS	USEA
25	[27]	S5-U last	178.6 (65.9)	70 (53)	iPNS	USEA
26	[27]	S6-M last	50.6 (42.8)	73 (25)	iPNS	USEA

5.2.2. DATA ANALYSIS

The power losses at the output are the result of a mismatch between the supply voltage and the channel-specific load voltage. To compare the impact of different voltage scaling strategies, channel-specific voltage requirements need to be calculated. To that purpose, a numerical dataset with 10 000 entries per subject listed in Table 5.1 was created. The current amplitude and electrode impedance data for these datasets were calculated using three different methods, depending on the available information. For variables reported as mean \pm sd, the dataset was assumed to follow a truncated normal distribution with the given parameters. The distribution was truncated at the reported extreme values or at the minimal step size of the parameter, ensuring no negative values were generated. For data provided as a dataset by the authors, the probability density function (PDF) of the variable was estimated using kernel density estimation. The dataset was then filled with

values such that the variable followed the estimated PDF. In cases where the data was reported as the median and IQR, the distribution is also estimated to be normal. Although [27] mentions that the data is not normally distributed, the lack of additional information on the distribution led us to assume a normal distribution as a reasonable estimation. Similar to the mean \pm sd data, the dataset followed a truncated normal distribution, with the mean and standard deviation estimated from the median and IQR values, respectively.

In the resulting dataset, each entry received a random value for the current amplitude (I_{th}) and electrode impedance (Z), following these distributions. For simplification of the calculations, this chapter assumes the combined impedance of the electrode-tissue interfaces and the tissue, Z , to be real (resistive) and equal to the impedance magnitude measured at 1 kHz. The required load voltage at each entry was then calculated using the following equation

$$V_{load,i} = I_{th,i} Z_i. \quad (5.1)$$

Using this dataset, the power losses of different voltage scaling strategies were calculated as described in Section 5.2.3. The resulting data is available at [28].

5

5.2.3. CALCULATING POWER LOSSES

To calculate the power losses for each scaling strategy, a Monte Carlo sampling method is used. This method involves the following steps:

1. For each subject in the dataset, a subset of M samples is randomly chosen from the dataset described in Section 5.2.2. The size of M is tailored to the target application.
2. On each subset, the power losses on each channel are calculated with the methods outlined below.
3. The efficiencies and power losses of the subset are averaged to obtain the expected average efficiency and power loss per channel for each application.
4. The sampling method is repeated for $n_{repeats}$ repetitions on each subject. In this chapter a repetition rate of $n_{repeats} = 1000$ was used.

For the first step, the size of M needs to be determined for each application. The size of M matters mainly for the calculation of the power losses in case of a global scaling supply, but the subset is applied to the calculation for all methods to ensure fair comparison of the methods. For intracortical visual prostheses, current efforts are aimed at developing systems with more than 1000 channels to provide high-resolution visual information that could restore useful vision [1]. In retinal prostheses, it has been estimated that 625 channels would be sufficient for useful vision [29]. However, using smaller and more electrodes could improve the field of view and efficacy of the implant [30]. In the case of PNS applications, the channel requirements are generally much lower. For intrafascicular interfaces, such as those using the USEA, one or two arrays, each with 100 channels, can provide sufficient information for neuroprosthetic applications [27]. This suggests that a total channel count of approximately 200 may be adequate for many tasks. On the other hand, extraneural electrodes, such as the FINE, offer much lower resolution, with individual electrodes typically containing only 8 channels. Therefore, a system utilizing two FINE electrodes would have only 16 channels in total [25]. Additionally, only a subset

of the total channel will be active at the same time. For this analysis, it is assumed that only 20 % of the channels will be active simultaneously. Consequently, in this study, the sample size M is set to 200, 125, 40, and 4 for V1, Retinal, iPNS, and extraneural PNS applications, respectively. Note that the exact value for M is not important, but the order of magnitude is, as will be shown in the results. When repeating this method for a new application, the sample size can be iterated to evaluate the impact of the number of channels on the efficacy of each scaling strategy.

To calculate the power loss at the output, the load power in the ideal case, when the voltage supply tracks the load voltage accurately for each channel (Fig. 5.2b), is used as a reference. In the ideal case, all the power at the output is delivered to the load. Using the current and impedance information of the samples, the load power can be calculated as:

$$P_{\text{load},i} = I_{\text{th},i}^2 Z_i. \quad (5.2)$$

Subsequently, the efficiency for all non-ideal cases is calculated using:

$$\eta = \frac{P_{\text{load},i}}{P_{\text{load},i} + P_{\text{loss},i}}, \quad (5.3)$$

where P_{loss} are the losses associated with the voltage scaling strategy.

In the case of a fixed voltage supply (Fig. 5.2a), the power losses at each channel can be calculated using:

$$P_{\text{loss,fixed},i} = (V_{\text{fixed}} - V_{\text{load},i}) I_{\text{th},i}, \quad (5.4)$$

where V_{fixed} is the same for all channels. When designing a system to deliver the stimulation from a fixed voltage supply, different considerations could lead to the choice of V_{fixed} . In this chapter, V_{fixed} is based on grouping all data with the same target (in Table 5.1) together. Furthermore, a reasonable design consideration is the trade-off between channel yield and efficiency. Here, channel yield is defined as the percentage of the total number of available channels that can be stimulated. If $V_{\text{fixed}} < \max(V_{\text{load,target}})$, not all channels can be stimulated, resulting in a lower yield, but the overall system efficiency will improve. Whether it can be tolerated to allow for yield < 100 % depends on the application and the design requirements. In this chapter, a yield of 75 % is chosen for most calculations, unless stated differently. In other words, V_{fixed} is equal to the third quantile (Q_3) of $V_{\text{load,target}}$. Note that a yield of 75 % might be considered low for some applications and that higher yields are desirable. This will favor the more flexible scaling strategies as the variability in load voltages increases. The effect on the yield choice will also be considered in the results section. In practice, the technology used to design the stimulator circuit will also influence the choice of V_{fixed} as some values (e.g., 3.3 V, 5 V, 10 V) are common for given technologies. This consideration is not included in the analyses presented in this chapter, but the method could be repeated if these constraints are known.

The first supply scaling strategy considered in this chapter is the use of a globally scaled supply voltage (Fig. 5.2c). In this case, the global supply would have to accommodate for the worst-case channel that is being stimulated. To power losses for this strategy are calculated as:

$$P_{\text{loss,global},i} = (\max(V_{\text{load},j}) - V_{\text{load},i}) I_{\text{th},i}, j \in M. \quad (5.5)$$

Thus, the maximum load voltage in the subset M is used as the supply voltage for all channels in the sampled subset.

The other supply scaling strategy is the use of a stepped supply voltage (Fig. 5.2d). In this case, N voltage steps are created, and each channel is connected to the nearest available step above the load voltage. Thus, the power losses can be calculated as:

$$P_{\text{loss,stepped},i} = (V_{\text{step},i} - V_{\text{load},i})I_{\text{th},i}, \quad (5.6)$$

where $V_{\text{step},i}$ is the nearest available voltage rail above $V_{\text{load},i}$. The available supply rails depend on the numbers of steps chosen. For the results in this chapter, the voltage rails are calculated using a uniform distribution of the rails between 0 V and V_{fixed} . As an example, in the case of $V_{\text{fixed}} = 5$ V and $N = 4$, the available voltage steps will be 1.25 V, 2.5 V, 3.75 V and 5 V. The methodology is not limited to a uniform distribution and could be repeated using any desired distribution of the voltage rails.

5.3. RESULTS

5.3.1. VOLTAGE AND LOAD POWER DISTRIBUTIONS

The calculated load voltage distributions (Eq. (5.1)) are shown in Fig. 5.3a. The resulting load voltage for the different applications are 3.5 V (5.3 V) (median (IQR)), 3.9 V (6.1 V), 1.3 V (2.2 V), and 2.8 V (2.4 V) for iPNS, V1, Retina, and PNS, respectively. These results suggest that PNS and Retina stimulation operate at relatively lower voltages compared to iPNS and V1, reflecting varying requirements across applications.

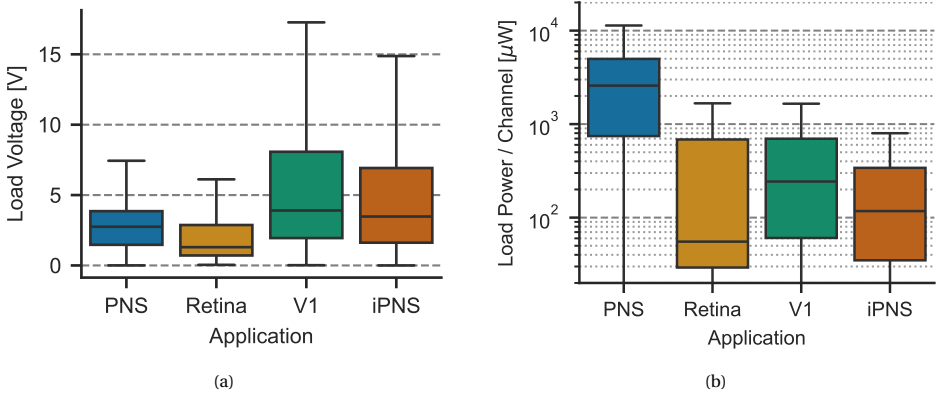


Figure 5.3: Distributions of (a) load voltage and (b) load power per channel across the four applications (PNS, Retina, V1, iPNS). Variations in stimulation thresholds and electrode impedances lead to substantial differences between applications. While the load voltages are comparable, the corresponding per-channel power requirements differ by more than an order of magnitude.

The corresponding load power distributions (Eq. (5.2)) are presented in Fig. 5.3b. The resulting values are as follows: 117 μW (306 μW) for iPNS, 243 μW (637 μW) for V1, 55 μW (656 μW) for Retina, and 2.6 mW (4.2 mW) for PNS. These results show that the median load power per channel is highly application-dependent, spanning more than one order of magnitude between Retinal and PNS stimulation.

To further explore inter-subject differences, the load voltage and power distributions of all subjects are compared in Fig. 5.4. This figure highlights the differences between applications. For Retinal stimulation, the load power spans a wide range on the application level, while the range within each subject is small. On the other hand, both iPNS and V1 stimulation show wide ranges both on the application level and on the subject level.

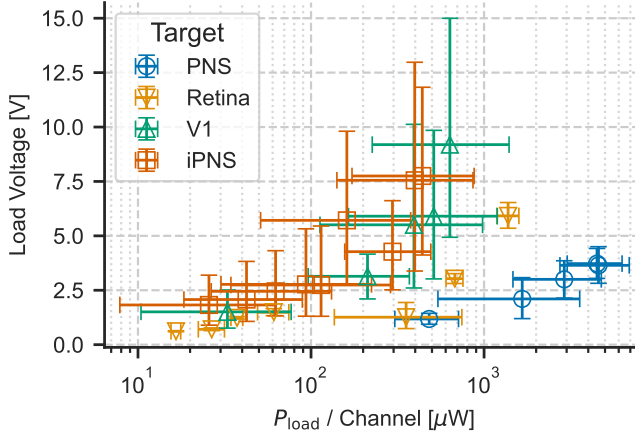


Figure 5.4: Load voltage and power distributions across the individual datasets, with markers showing the median and error bars the interquartile range. The figure highlights variability, both within subjects and between subjects, which differs across applications.

The application-specific voltage supplies for a channel yield of 75 %, used in subsequent power loss calculations, are listed in Table 5.2. The effect of channel yield on the voltage supply is illustrated in Fig. 5.5. As shown there, a yield of 100 % would require a supply voltage of 44 V and 54 V for the applications of iPNS and V1, respectively. Next to the inefficiency that this would cause, it would also require special circuits that can generate and handle such voltage levels.

Table 5.2: Application-specific voltage supply (for a channel yield of 75 %) used for the power loss calculations.

Application	V_{fixed} [V]
iPNS	7.0
V1	8.1
Retina	2.9
PNS	3.9

5.3.2. POWER LOSSES FOR A FIXED VOLTAGE SUPPLY

The power losses per channel for a conventional fixed voltage supply are shown in Fig. 5.6, where the markers denote the different subjects in Table 5.1. Most subjects exhibit efficiencies below 60 %, with power losses typically in the range of 100 μW per channel.

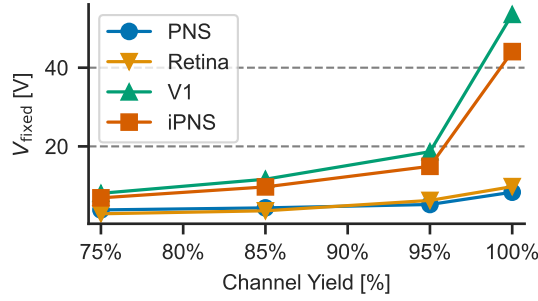


Figure 5.5: V_{fixed} for different channel yield settings across the different applications. Outlier channels drive up the required supply voltage to achieve high channel yield.

5

However, PNS subjects display higher efficiencies despite experiencing greater power losses in the order of 1 mW per channel. This emphasizes that even though efficiencies may be high, it could still be worth improving to save significant power. Except for the PNS subjects, the plot shows small variations within each subject, which can be attributed to two factors. In the Retina subjects, the spread in load power and load voltage within each subject is small, as shown in Fig. 5.4. For the V1 and iPNS subjects, the small variation is likely an effect of the sample size for resampling since the resampling and averaging filters out extreme values. This shows that, within a subject, the losses for a fixed voltage supply would be predictable and constant for different subsets of channels.

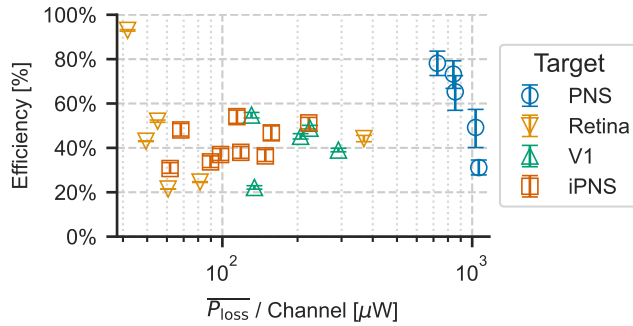


Figure 5.6: Average power loss per channel (Median & IQR) and the corresponding efficiencies for a conventional fixed voltage supply (V_{fixed}). Each marker corresponds to one subject.

5.3.3. POWER LOSSES FOR GLOBAL SUPPLY SCALING

The efficiencies and power loss per channel for global supply scaling are compared to fixed voltage supplies in Fig. 5.7. In applications with high channel counts and wide spread in load conditions (iPNS and V1) the efficiency is negligible due to the fact that the supply has to accommodate the worst case channel. However, in low-channel-count applications like

PNS, the approach can reduce power losses substantially. For PNS, the median power loss per channel is reduced from 914 μW to 404 μW , while the median efficiency is increased from 62.9 % to 77.3 %. Furthermore, if the variability in load conditions within subjects is small, as is the case for the Retina data, global supply scaling also leads to significant improvements. In the Retina data, the median power loss per channel is reduced from 58 μW to 14 μW , while the median efficiency is increased from 43.1 % to 80.2 %. These results show that global scaling is most effective when the channel count is low and the variability in voltage requirements within subjects is small.

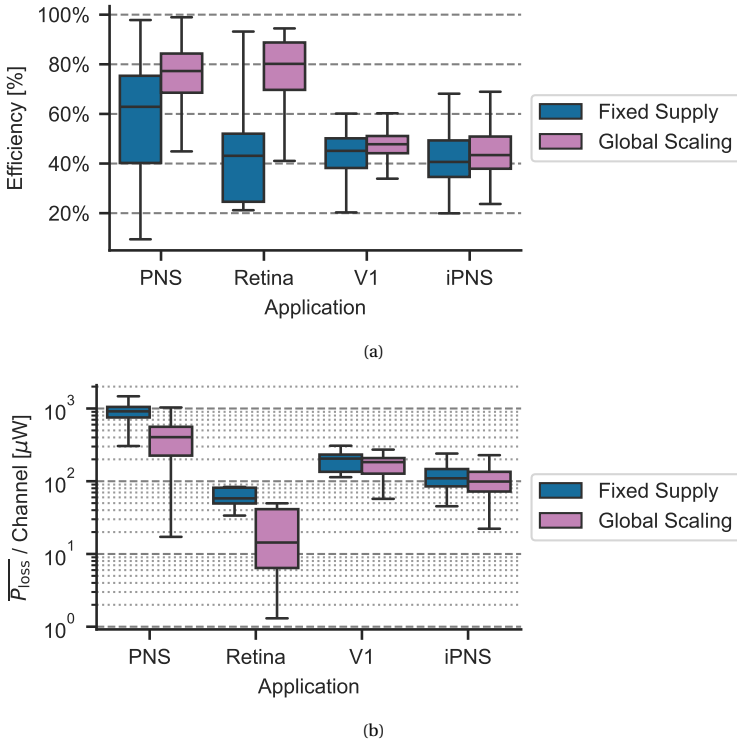


Figure 5.7: The effect of a global supply scaling strategy on (a) efficiency and (b) per-channel power loss across the different applications. Outliers are omitted for clarity. Substantial improvements are observed in low-channel-count applications (PNS) and those with limited intra-subject variation (Retina), whereas the benefits are negligible in large-scale applications with wide intra-subject variability (V1, iPNS).

5.3.4. POWER LOSSES FOR A STEPPED SUPPLY

For the stepped supply strategy, the power loss reduction and efficiency improvements are calculated for uniformly distributed supplies of 1 (fixed), 2, 4, and 8 voltage rails. This strategy demonstrates efficiency improvements across all applications (Fig. 5.8), with efficiencies exceeding 81 % when using eight voltage rails. Compared to the fixed voltage supply, this yields an increase in efficiency of 43 % (PNS) to 100 % (iPNS and Retina). However, the incremental benefit of adding more rails diminishes with each step.

Nonetheless, the flexibility to tune each channel specifically makes this strategy broadly applicable.

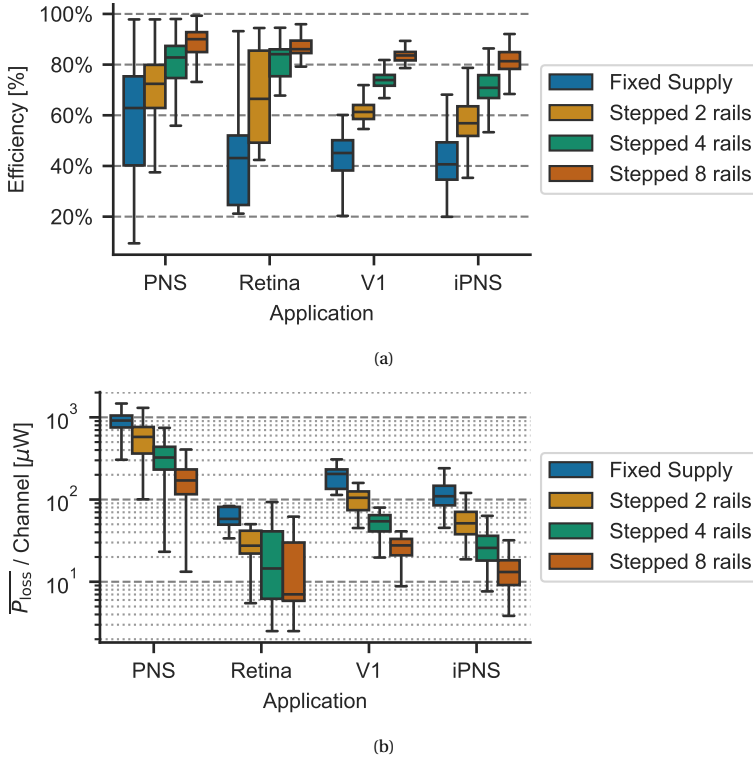


Figure 5.8: Effect of a stepped-voltage supply strategy from an application-specific supply on the (a) efficiency and (b) power loss per channel in the different applications. Outliers are not shown in the plot. All applications benefit from this scaling approach, though the incremental improvements diminish as the number of supply rails increases.

5.3.5. COMPARISON OF SCALING STRATEGIES

The comparative performance of all strategies is summarized in Fig. 5.9. Furthermore, the normalized efficiencies and power losses are listed in Table 5.3, where each value is normalized to the Fixed Voltage configuration for each respective application. It is shown that stepped supplies with 4 and 8 rails outperform the global scaling across all applications, although for Retina stimulation the performance of global scaling and stepped 4 rails is comparable. Furthermore, in some cases, one strategy outperforms the others, but other factors, such as design complexity and circuit losses, may still favor another strategy. For example, in Retina data, the relative improvement from 4 rails to 8 rails is 2 % corresponding to a reduction of $7 \mu\text{W}$ per channel, which is likely not worth the extra circuits. Considerations regarding circuit implementations will be discussed in Section 5.4.1.

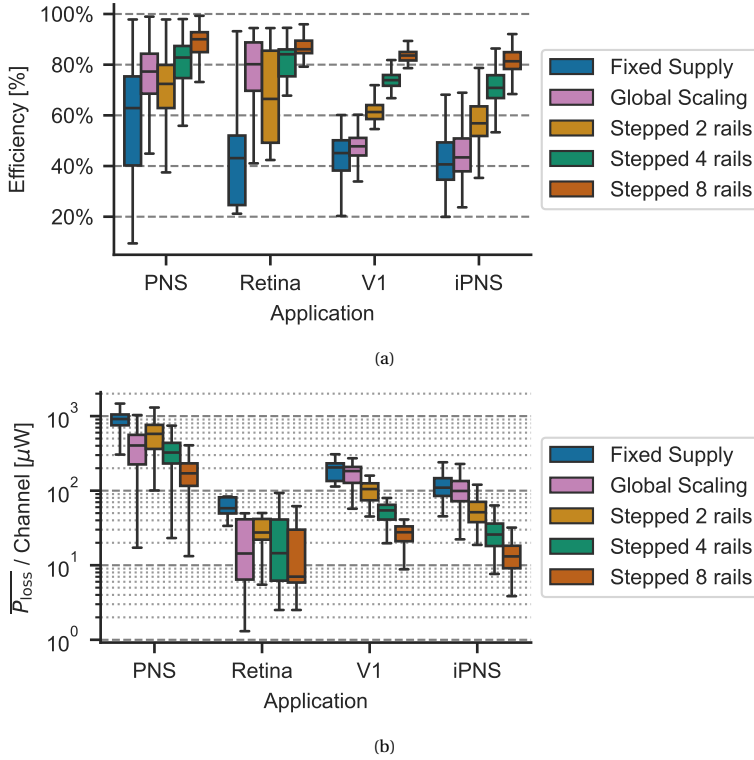


Figure 5.9: Comparison of the impact of the scaling strategies on the (a) efficiency and (b) power loss per channel in the different applications. Outliers are not shown in the plot. The stepped supply strategy with 8 rails outperforms the global scaling strategy across all applications.

Table 5.3: Comparison of normalized efficiency (η) and normalized power loss (P_{loss}) across different applications and scaling strategies. All values are normalized to the Fixed Supply configuration for each respective application.

Application	Retina		V1		PNS		iPNS	
	η/η_{ref}	$P_{\text{loss}}/P_{\text{ref}}$	η/η_{ref}	$P_{\text{loss}}/P_{\text{ref}}$	η/η_{ref}	$P_{\text{loss}}/P_{\text{ref}}$	η/η_{ref}	$P_{\text{loss}}/P_{\text{ref}}$
Fixed Supply	1.00	1.00	1.00	1.00	1.00	1.00	1.00	1.00
Global Scaling	1.86	0.25	1.06	0.89	1.23	0.44	1.07	0.90
Stepped 2 rails	1.54	0.47	1.36	0.51	1.15	0.63	1.40	0.47
Stepped 4 rails	1.95	0.25	1.64	0.27	1.32	0.36	1.74	0.24
Stepped 8 rails	2.00	0.12	1.85	0.14	1.43	0.19	2.00	0.12

Even though the evaluated strategies show substantial improvements in efficiency, there is still room for further reduction of the power losses. For each application, the total power loss can be calculated by multiplying the number of channels in that application with the channel losses presented in Fig. 5.9b. For the best scaling strategy in each

application, this results in a total system power loss of 525 μW (366 μW), 5.5 mW (2.4 mW), 879 μW (3016 μW), 683 μW (466 μW) for iPNS, V1, Retina, and PNS, respectively.

5.3.6. EFFECT OF CHANNEL YIELD

All results so far were calculated with a channel yield of 75 %. The effect of the channel yield on the efficiency and power losses is shown in Figs. 5.10 and 5.11. First of all, increasing the yield diminishes the efficiency and increases the power losses for all strategies across all applications. However, the global scaling strategy is more robust to changes in the yield. At several conditions the global scaling becomes more efficient than the stepped 4 rail supply, and for a yield of 100 % it is the most efficient strategy for the Retina data. One possible improvement for the stepped voltage supplies would be to use non-uniformly distributed voltage rails. Furthermore, as mentioned in Section 5.3.1, achieving a higher yield also increases the circuit complexity due to the increased voltage supply. Therefore, the trade-off between channel yield and power efficiency will also be impacted by practical limitations of the implementation. The proposed method allows to evaluate each condition to guide the design process.

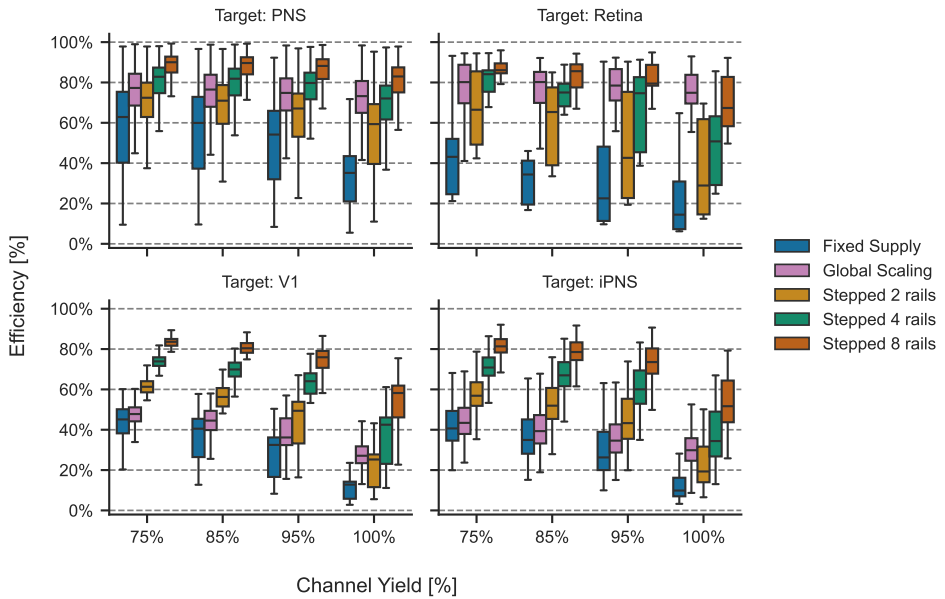


Figure 5.10: Effect of channel yield on efficiency across applications and supply strategies. Scaling approaches remain more robust under increasing yield requirements, with global scaling showing particular benefits in PNS and Retina applications.

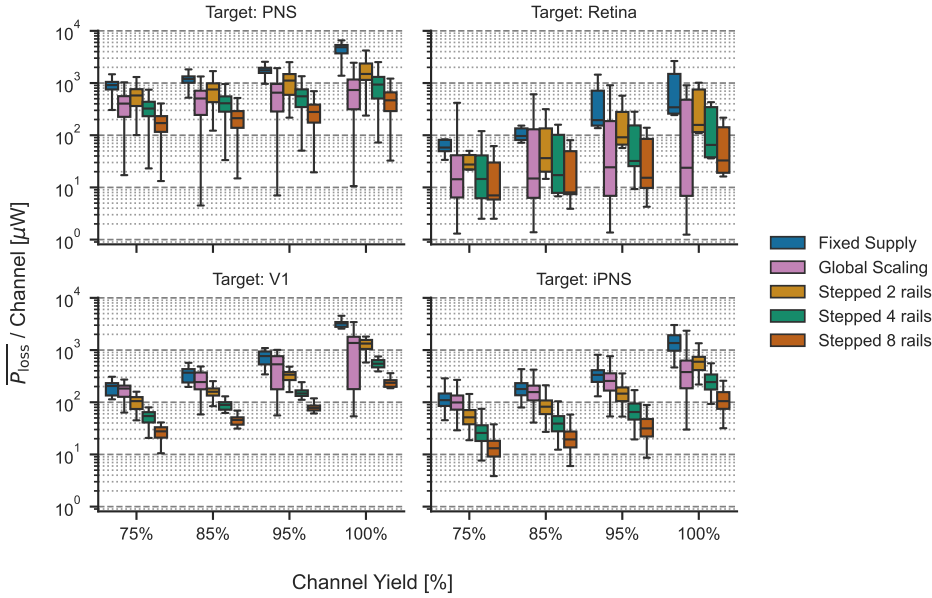


Figure 5.11: Effect of channel yield on power losses across different applications and supply scaling strategies. Higher yield requirements increase power losses under a fixed-voltage supply, making scaling strategies comparatively more advantageous.

5.4. DISCUSSION

5.4.1. CIRCUIT DESIGN CONSIDERATIONS

The voltage supply levels in this chapter are based on the available datasets, without taking into account the implementation of these voltage rails. In reality, most systems will be designed adhering to common voltage levels depending on the technology used for the circuit design. The first use of the proposed method could be to get an estimation of the channel yield for a given voltage supply level to decide if that is sufficient for the application. Furthermore, the method can be used to decide whether implementing more complex supply strategies is worthwhile.

In the analyzed applications, global scaling showed limited benefit over a fixed supply voltage in scenarios with high channel counts and a wide spread of load conditions. However, in applications with fewer channels or when within-subject load variation is low, global scaling can significantly improve efficiency—up to 86 % in the Retina dataset. Several designs in the literature adopt a global scaling supply [31–33]. The added complexity of these implementations is a voltage compliance monitor at every channel to determine what the supply voltage should be.

A stepped voltage supply with four or more rails generally outperformed global scaling, especially when intrasubject variability was high (e.g., in V1 and iPNS). In principle, increasing the number of voltage rails reduces losses, but it also raises complexity at both the system and channel levels. At the system level, increasing the number of voltage rails

in the multi-output supply increases its complexity. Each voltage rail requires a storage capacitor to make it possible to deliver power, which can increase the area requirements. Furthermore, all voltage rails need to be distributed towards all channels. In high-channel-count applications, this can become a bottleneck for increasing the number of rails. At the channel level, more rails require a larger selector circuit. Since the area requirements are highly technology-dependent, it is difficult to estimate the cost of each implementation. However, once the technology parameters are known, the presented analysis can serve to make a trade-off between efficiency, area, and complexity.

Finally, for each scaling strategy, additional power losses should be considered. Additional losses could come from reduced rectifier efficiency, extra conversion steps, and additional control and compliance circuitry. In this respect, the power per channel for the application is an important weighting factor. When the load power per channel is low, overhead losses in the channel can quickly diminish the efficiency improvements gained by the scaling strategy. Sharing resources among multiple channels helps to reduce the impact on the efficiency. When the power per channel is high, the design requirements for the scaling circuitry are easier in terms of power consumption since overhead losses are less important.

5

5.4.2. TEMPORAL CHANGES

The datasets used in this study all represent a static set of parameters. However, impedance and stimulation thresholds are known to change over time [11, 21, 27]. Therefore, the voltage requirements of the channels and resulting losses will change accordingly. Flexibility in the voltage supply helps to accommodate changes and reduce power losses over time. In the long term, this will lead to the best power efficiency during the lifetime of the implant.

5.4.3. LIMITATIONS OF CURRENT WORK

The analysis presented here is based on previously published data. Here, we reflect on the limitations of the assumptions necessary to perform the analysis.

First, for most datasets, the distribution of the parameters was assumed to be (truncated) Gaussian. This assumption was made due to a lack of information; in reality, the distributions could have been different. As described in Section 5.2.2, an extended analysis was performed when more information regarding the data distribution was available.

Furthermore, the impedance and current data are assumed to be uncorrelated. While [22] found a negative correlation between the two parameters, the other studies did not report the correlation. Variations in electrode impedance are caused by many factors, which might change the correlation between impedance and threshold values. In [22], the critical factor influencing impedance and threshold was the distance between the electrode and the retina. If the correlation of these parameters is known for a specific application, it could be added to the generation of the dataset to evaluate its effects.

Additionally, the size of the electrodes used in the retina data is relatively big. The development trend in retinal implants is to reduce the size of the electrodes to bring them closer to the retina and achieve higher electrode count and density [34, 35]. However, no data could be found on human subjects for the smaller electrodes, where both impedance

measurements and perception thresholds were reported. Generally speaking, reducing the electrode size will increase the impedance, and bringing the electrodes closer to the cells will reduce stimulation thresholds [22].

Last, the electrode impedance is more complex than the 1 kHz value used in this chapter to calculate the losses. A more realistic model includes the capacitive effects of the electrode-tissue interface (ETI). This capacitive component affects the load voltage and will change the load power. The extent of this effect depends on the ratio between the resistive and capacitive components of the load impedance, as well as the delivered charge [36]. Therefore, it depends on the type of electrodes used. Ideally, the capacitance of stimulation electrodes should be large to prevent depolarization of the ETI, which can lead to non-reversible charge transfer [10]. Specifically, in microelectrodes, the resistive component is typically dominant, and the effect of the capacitance on the power calculations will be minimal.

5.5. CONCLUSION

This chapter introduces a novel methodology for analyzing power losses in multichannel electrical stimulation systems, integrating both electrophysiological and electronic considerations. Traditional stimulator systems are often designed for fixed load conditions, overlooking the significant impact of inter-channel variability in electrode impedance and current thresholds. By incorporating these variabilities into the analysis, the proposed method enables more elaborate assessments of the power efficiency across various scaling strategies and applications. Furthermore, the method serves as a tool for guiding the design of new systems, providing insights into which scaling strategy performs best under specific conditions.

Applied to experimental data from multiple multichannel systems, the methodology reveals that a stepped voltage supply with 8 voltage rails can increase efficiency by 43 % to 100 %, proving to be most effective for high-channel-count applications with significant inter-channel variation. Conversely, global voltage scaling emerged as a viable option for applications with fewer channels or minimal inter-channel variability. These findings underscore the critical role of application-specific parameters, such as channel count and load variance, in selecting the most suitable voltage scaling approach.

Furthermore, while advanced supply strategies can substantially reduce power losses, they invariably add complexity at both the system and channel levels. The specific cost-benefit trade-offs depend on the underlying technology and target application, making generalization challenging. Nonetheless, when specific design targets and technology limitations are known, the proposed methodology can guide the design trade-offs to choose the best approach.

From a practical design perspective, two insights stand out. First, the benefits of adding more supply rails diminish beyond four rails, suggesting that additional rails may not justify the extra circuit complexity. Second, channel-specific supply scaling only provides substantial advantages when inter-channel variability is high, whereas in low-variability applications, simpler global scaling could be sufficient.

Finally, the calculated total system power losses indicate that there is still room for improvements in more advanced methods to increase power efficiency even further. By developing novel systems that support voltage scaling techniques, power efficiency can be

enhanced, allowing for increasing the number of stimulation channels in next-generation, large-scale neural interfaces.

BIBLIOGRAPHY

- [1] E. Fernández, A. Alfaro, and P. González-López, “Toward Long-Term Communication With the Brain in the Blind by Intracortical Stimulation: Challenges and Future Prospects”, *Frontiers in Neuroscience*, vol. 14, no. August, Aug. 2020, ISSN: 1662-453X. DOI: 10.3389/fnins.2020.00681.
- [2] E. Musk, “An integrated brain-machine interface platform with thousands of channels”, *Journal of Medical Internet Research*, vol. 21, no. 10, Oct. 2019, ISSN: 14388871. DOI: 10.2196/16194.
- [3] T. Jung *et al.*, *Stable, chronic in-vivo recordings from a fully wireless subdural-contained 65,536-electrode brain-computer interface device*, bioRxiv: 2024.05.17.594333, 2024. DOI: 10.1101/2024.05.17.594333.
- [4] Y. Liu *et al.*, “Bidirectional Bioelectronic Interfaces”, *IEEE solid state circuits magazine*, vol. 12, no. 2, pp. 30–46, 2020.
- [5] S. Drakopoulou, F. Varkevisser, L. Sohail, M. Aqamolaei, T. L. Costa, and G. D. Spyropoulos, “Hybrid neuroelectronics: towards a solution-centric way of thinking about complex problems in neurostimulation tools”, *Frontiers in Electronics*, vol. 4, Sep. 2023, ISSN: 2673-5857. DOI: 10.3389/felec.2023.1250655.
- [6] T. P. G. van Nunen, R. M. C. Mestrom, and H. J. Visser, “Wireless Power Transfer to Biomedical Implants Using a Class-E Inverter and a Class-DE Rectifier”, *IEEE Journal of Electromagnetics, RF and Microwaves in Medicine and Biology*, vol. 7, no. 3, pp. 202–209, Sep. 2023, ISSN: 2469-7249. DOI: 10.1109/JERM.2023.3267042.
- [7] IEEE International Committee on Electromagnetic Safety (SCC39), “IEEE Std C95.1TM-2005: IEEE Standard for Safety Levels with Respect to Human Exposure to Radio Frequency Electromagnetic Fields, 3 kHz to 300 GHz”, Institute of Electrical and Electronics Engineers (IEEE), New York, NY, USA, Tech. Rep., 2005, ISBN: 978-0-7381-4772-3. DOI: 10.1109/IEEESTD.2006.99501.
- [8] International Organization for Standardization, “ISO 14708-3:2017: Implants for surgery — Active implantable medical devices — Part 3: Implantable neurostimulators”, International Organization for Standardization, Geneva, Switzerland, Tech. Rep. ISO 14708-3:2017, 2017, Safety and performance requirements for implantable neurostimulators.
- [9] R. Shirafkan and O. Shoaee, “Current-Based Neurostimulation Circuit and System Techniques”, in *Handbook of Biochips*, New York, NY: Springer New York, 2022, pp. 445–469. DOI: 10.1007/978-1-4614-3447-4_42.
- [10] D. R. Merrill, M. Bikson, and J. G. Jefferys, “Electrical stimulation of excitable tissue: design of efficacious and safe protocols”, *Journal of Neuroscience Methods*, vol. 141, no. 2, pp. 171–198, Feb. 2005, ISSN: 01650270. DOI: 10.1016/j.jneumeth.2004.10.020.

- [11] T. S. Davis *et al.*, “Spatial and temporal characteristics of V1 microstimulation during chronic implantation of a microelectrode array in a behaving macaque”, *Journal of Neural Engineering*, vol. 9, no. 6, p. 065 003, Dec. 2012, ISSN: 1741-2560. DOI: 10.1088/1741-2560/9/6/065003.
- [12] S. K. Arfin and R. Sarpeshkar, “An Energy-Efficient, Adiabatic Electrode Stimulator With Inductive Energy Recycling and Feedback Current Regulation”, *IEEE Transactions on Biomedical Circuits and Systems*, vol. 6, no. 1, pp. 1–14, Feb. 2012, ISSN: 1932-4545. DOI: 10.1109/TBCAS.2011.2166072.
- [13] S. K. Kelly, “Adiabatic Electrode Stimulator”, in *Handbook of Biochips*, New York, NY: Springer New York, 2022, pp. 1157–1183. DOI: 10.1007/978-1-4614-3447-4_19.
- [14] Z. Luo, M.-D. Ker, T.-Y. Yang, and W.-H. Cheng, “A Digitally Dynamic Power Supply Technique for 16-Channel 12 V-Tolerant Stimulator Realized in a 0.18- μm 1.8-V/3.3-V Low-Voltage CMOS Process”, *IEEE Transactions on Biomedical Circuits and Systems*, vol. 11, no. 5, pp. 1087–1096, Oct. 2017, ISSN: 1932-4545. DOI: 10.1109/TBCAS.2017.2713122.
- [15] I. Williams and T. G. Constandinou, “An Energy-Efficient, Dynamic Voltage Scaling Neural Stimulator for a Proprioceptive Prosthesis”, *IEEE Transactions on Biomedical Circuits and Systems*, vol. 7, no. 2, pp. 129–139, Apr. 2013, ISSN: 1932-4545. DOI: 10.1109/TBCAS.2013.2256906.
- [16] K. Eom *et al.*, “A Low-Stimulus-Scattering Pixel-Sharing Sub-Retinal Prosthesis SoC With Time-Based Photodiode Sensing and Per-Pixel Dynamic Voltage Scaling”, *IEEE Journal of Solid-State Circuits*, vol. 58, no. 11, pp. 2976–2989, Nov. 2023, ISSN: 1558173X. DOI: 10.1109/JSSC.2023.3305521.
- [17] K. H. Nguyen *et al.*, “A Neural Stimulator IC with Dynamic Voltage Scaling Supply and Energy Recycling for Cochlear Implant in Standard 180nm CMOS Process”, in *Proceedings - International SoC Design Conference 2023, ISOCC 2023*, Institute of Electrical and Electronics Engineers Inc., 2023, pp. 35–36, ISBN: 9798350327038. DOI: 10.1109/ISOCC59558.2023.10396171.
- [18] A. Rashidi, N. Yazdani, and A. M. Sodagar, “Fully implantable, multi-channel microstimulator with tracking supply ribbon, multi-output charge pump and energy recovery”, *IET Circuits, Devices & Systems*, vol. 15, no. 2, pp. 104–120, Mar. 2021, ISSN: 1751-858X. DOI: 10.1049/cds2.12007.
- [19] H.-S. Lee, K. Eom, and H.-M. Lee, “27.3 A 90.8%-Efficiency SIMO Resonant Regulating Rectifier Generating 3 Outputs in a Half Cycle with Distributed Multi-Phase Control for Wirelessly-Powered Implantable Devices”, in *2024 IEEE International Solid-State Circuits Conference ()*, IEEE, Feb. 2024, pp. 448–450, ISBN: 979-8-3503-0620-0. DOI: 10.1109/ISSCC49657.2024.10454403.
- [20] E. Fernández *et al.*, “Visual percepts evoked with an intracortical 96-channel microelectrode array inserted in human occipital cortex”, *Journal of Clinical Investigation*, vol. 131, no. 23, Dec. 2021, ISSN: 1558-8238. DOI: 10.1172/JCI151331.

- [21] X. Chen *et al.*, “Chronic stability of a neuroprosthesis comprising multiple adjacent Utah arrays in monkeys”, *Journal of Neural Engineering*, vol. 20, no. 3, Jun. 2023, ISSN: 17412552. DOI: 10.1088/1741-2552/ace07e.
- [22] C. De Balthasar *et al.*, “Factors affecting perceptual thresholds in epiretinal prostheses”, *Investigative Ophthalmology and Visual Science*, vol. 49, no. 6, pp. 2303–2314, Jun. 2008, ISSN: 01460404. DOI: 10.1167/iovs.07-0696.
- [23] A. M. Demchinsky *et al.*, “The first deaf-blind patient in Russia with Argus II retinal prosthesis system: What he sees and why”, *Journal of Neural Engineering*, vol. 16, no. 2, 2019, ISSN: 17412552. DOI: 10.1088/1741-2552/aafc76.
- [24] Y. H.-L. Luo and L. da Cruz, “The Argus® II Retinal Prosthesis System”, *Progress in Retinal and Eye Research*, vol. 50, pp. 89–107, Jan. 2016, ISSN: 13509462. DOI: 10.1016/j.preteyeres.2015.09.003.
- [25] D. W. Tan, M. A. Schiefer, M. W. Keith, J. R. Anderson, and D. J. Tyler, “Stability and selectivity of a chronic, multi-contact cuff electrode for sensory stimulation in human amputees”, *Journal of Neural Engineering*, vol. 12, no. 2, p. 026002, Apr. 2015, ISSN: 1741-2560. DOI: 10.1088/1741-2560/12/2/026002.
- [26] T. S. Davis *et al.*, “Restoring motor control and sensory feedback in people with upper extremity amputations using arrays of 96 microelectrodes implanted in the median and ulnar nerves”, *Journal of Neural Engineering*, vol. 13, no. 3, Mar. 2016, ISSN: 17412552. DOI: 10.1088/1741-2560/13/3/036001.
- [27] J. A. George *et al.*, “Long-term performance of Utah slanted electrode arrays and intramuscular electromyographic leads implanted chronically in human arm nerves and muscles”, *Journal of Neural Engineering*, vol. 17, no. 5, Oct. 2020, ISSN: 17412552. DOI: 10.1088/1741-2552/abc025.
- [28] F. Varkevisser, W. A. Serdijn, and T. L. Costa, *Data underlying manuscript: Analysis of power losses and the efficacy of power minimization strategies in multichannel electrical stimulation systems*, <https://doi.org/10.4121/b8098fe4-3f33-4691-9e55-54bf2cc255c3>, 2025. DOI: 10.4121/b8098fe4-3f33-4691-9e55-54bf2cc255c3.
- [29] E. Margalit *et al.*, “Retinal Prosthesis for the Blind”, *Survey of Ophthalmology*, vol. 47, no. 4, pp. 335–356, Jul. 2002, ISSN: 00396257. DOI: 10.1016/S0039-6257(02)00311-9.
- [30] D. Palanker, A. Vankov, P. Huie, and S. Baccus, “Design of a high-resolution opto-electronic retinal prosthesis”, *Journal of Neural Engineering*, vol. 2, no. 1, S105–S120, Mar. 2005, ISSN: 1741-2560. DOI: 10.1088/1741-2560/2/1/012.
- [31] M. Ortmanns, A. Rocke, M. Gehrke, and H.-J. Tiedtke, “A 232-Channel Epiretinal Stimulator ASIC”, *IEEE Journal of Solid-State Circuits*, vol. 42, no. 12, pp. 2946–2959, Dec. 2007, ISSN: 0018-9200. DOI: 10.1109/JSSC.2007.908693.
- [32] E. Noorsal, K. Sooksood, H. Xu, R. Hornig, J. Becker, and M. Ortmanns, “A Neural Stimulator Frontend With High-Voltage Compliance and Programmable Pulse Shape for Epiretinal Implants”, *IEEE Journal of Solid-State Circuits*, vol. 47, no. 1, pp. 244–256, Jan. 2012, ISSN: 0018-9200. DOI: 10.1109/JSSC.2011.2164667.

- [33] H.-M. Lee, H. Park, and M. Ghovanloo, "A Power-Efficient Wireless System With Adaptive Supply Control for Deep Brain Stimulation", *IEEE Journal of Solid-State Circuits*, vol. 48, no. 9, pp. 2203–2216, Sep. 2013, ISSN: 0018-9200. DOI: 10.1109/JSSC.2013.2266862.
- [34] E. Ho *et al.*, "Characteristics of prosthetic vision in rats with subretinal flat and pillar electrode arrays", *Journal of Neural Engineering*, vol. 16, no. 6, Oct. 2019, ISSN: 17412552. DOI: 10.1088/1741-2552/ab34b3.
- [35] D. Palanker, Y. Le Mer, S. Mohand-Said, M. Muqit, and J. A. Sahel, "Photovoltaic Restoration of Central Vision in Atrophic Age-Related Macular Degeneration", *Ophthalmology*, vol. 127, pp. 1097–1104, 2020, ISSN: 01616420. DOI: 10.1016/j.optha.2020.02.024.
- [36] F. Varkevisser, T. L. Costa, and W. A. Serdijn, "Energy efficiency of pulse shaping in electrical stimulation: the interdependence of biophysical effects and circuit design losses", *Biomedical Physics & Engineering Express*, vol. 8, no. 6, p. 065 009, Nov. 2022, ISSN: 2057-1976. DOI: 10.1088/2057-1976/ac8c47.



6

AUTONOMOUS OUTPUT SUPPLY SCALING FOR EFFICIENT MULTICHANNEL STIMULATION SYSTEMS

Pain is inevitable. Suffering is optional.

— Haruki Murakami

This chapter is under review for publication at the time of writing.

6.1. INTRODUCTION

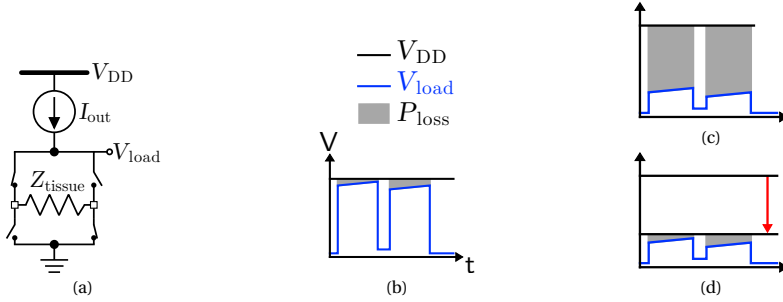


Figure 6.1: Illustration of the power efficiency drawback of (multichannel) current-mode stimulation (CMS) in a bipolar configuration. (a) Conventional output stage for CMS with a fixed voltage supply V_{DD} ; (b) Example of the output voltage in the case of a good match between the load voltage V_{load} and voltage supply. The gray area indicates overhead losses in the output driver; (c) Example of the output voltage in case of a mismatch between the load voltage and supply voltage, leading to high power dissipation in the output driver; (d) Illustration how a scaled voltage supply can reduce the power dissipation in the output driver, and thus increase the power efficiency, for the example in (c). Figure modified from [1].

6

IMPLANTABLE neuromodulation devices have become integral to treating neurological disorders and advancing innovative applications like visual and somatosensory prostheses [2–4]. These applications require large-scale, multichannel stimulation systems capable of driving hundreds to thousands of channels [5–7]. Designing these systems necessitates addressing interdisciplinary challenges, including system-level electronics [8] and high-density, biocompatible electrodes [9].

One of the primary constraints in scaling these systems is efficient power management. Wireless power delivery is preferred for its reduced risk of infection compared to wired approaches. However, safety regulations severely limit the amount of power transferable to the implant [10]. For example, inductive power transfer at 13.56 MHz has a safe exposure limit of $544 \mu\text{W}/\text{mm}^2$ [11], which translates to a maximum available power in millimeter-sized implants in the order of tens of mW. These limitations emphasize the need for power-efficient stimulator circuits to enable channel scaling.

Current-mode stimulation (CMS) stands out as the preferred method for neural tissue stimulation, primarily for its ability to precisely control the delivered amount of charge, a critical aspect of ensuring patient safety [12]. However, the inherent variability in electrode-tissue-interface impedance and the current amplitude requirements across channels and over time [13] pose significant challenges to the power efficiency of multichannel CMS, as illustrated in Fig. 6.1. In the conventional approach, a fixed voltage is used to supply all output drivers; hence, it needs to accommodate the channel with the highest tissue voltage requirements. Every channel for which the tissue voltage requirement is below the fixed voltage supply will contribute to an excessive voltage drop over the output driver, leading to increased power dissipation. Consequently, energy is

Statement of contribution: The candidate designed the circuits, carried out simulations, and performed measurements. Electrode fabrication was performed by collaborators at the Neural Waves Lab, Ghent University, Belgium. The candidate integrated these devices into the experimental setup and wrote the chapter, with input from the promotor.

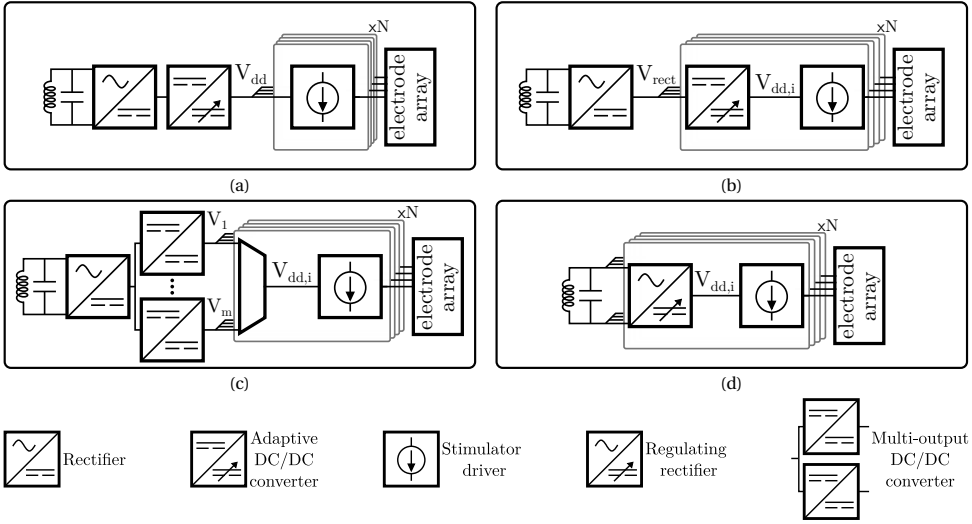


Figure 6.2: Overview of power management strategies for adaptive voltage regulation in multichannel stimulator systems with a modular architecture. Each module contains at least an output driver that can connect to one or more electrodes and can have more local circuitry. (a) Global singular voltage regulation, using the same V_{dd} for all modules; (b) Parallel voltage regulation on a local scale, using local variable DC/DC converters in each module; (c) Parallel voltage regulation on a global scale, using a multi-output DC/DC converter on the system level and a multiplexer in each module to select the appropriate voltage level, (d) Proposed strategy using local regulating rectifiers in each module.

needlessly wasted, highlighting the need for more efficient power management strategies in large-scale multichannel systems.

Given the limitations of the conventional fixed voltage supply, several approaches for scalable voltage supplies have been proposed in the literature to reduce the losses at the output driver. These approaches can be categorized into three groups: global singular voltage regulation, parallel voltage regulation on a local scale, and parallel voltage regulation on a global scale. The first group uses a single scalable voltage supply for the whole system (Fig. 6.2a). One approach is to reduce the transmitted power signal and subsequently lower the supply voltage after rectification [14]. This approach requires uplink data communication to inform the external power transmitter about the required output voltage. Alternatively, a DC/DC converter (DDC) can be used to create an adaptive voltage supply [15–20]. The DDC topology is often based on an inductive buck/boost [15] or a switched-capacitor topology [16–20]. The inductive topology comes at the cost of bulky (off-chip) inductor(s). While a switched-capacitor approach could be fully implemented on-chip, it typically generates only a small number of discrete voltage steps. Due to the resulting low resolution, the generated supply voltage cannot accurately track the required load voltage, and the power losses remain high in most situations [21]. Furthermore, using the same voltage for all output channels results in minimal efficiency improvement compared to a fixed voltage supply [21]. In large-scale multichannel systems with widespread load voltages, most channels will still operate inefficiently, as the output

voltage must suit the worst-case channel. Channel-specific voltage scaling is required to improve the efficiency of large-scale multichannel systems. In the second group, this is achieved by moving the adaptive DDC to the local scale of the output drivers (Fig. 6.2b). In [22], each stimulator output has a dedicated charge pump to dynamically scale the voltage necessary to drive the output current. As mentioned above, having a limited number of output voltages results in minor efficiency gains [21]. Increasing the number of voltage steps requires additional capacitors per step, however, since the adaptive DDCs are implemented on a local scale, this leads to a significant increase in the area of each channel, and limits scalability. To reduce the area impact, the last group implements parallel DDC on a global scale (Fig. 6.2c) [23–29]. In [23–28], a multi-output DDC generates various voltage supply rails that are distributed to all channels. The output driver uses a multiplexer (MUX) to select one of the available rails. In this approach, the area of the DDC has less impact on the overall system area. However, improving the resolution comes at the cost of increased area and complexity for the routing and MUX implementation. In [21], we analyzed the efficacy of these approaches for several multichannel stimulation applications. As shown there, there is still room for improvement in the efficiency, specifically for applications with a wide range of stimulation thresholds and electrode impedances, such as intracortical visual prosthetics, where the total power losses with the best scaling strategy would still be in the mW range [21].

6

Next to the limitations of the various implementations listed above, a common drawback of most is the use of multiple conversion stages to achieve the scaled output voltage. This leads to cascaded power losses and low overall power efficiency. To avoid cascaded losses, several single-stage regulating rectifier topologies have been proposed [30–33]. This approach commonly uses a phase-controlled active rectifier to regulate the output voltage. A disadvantage of these implementations is that they are designed to scale the global voltage supply. As a result, a large output filter capacitor is used, limiting the design's scalability and the speed of the voltage regulation [31]. Furthermore, the feedback loop uses a DAC-generated reference voltage that sets the output voltage [30]. Therefore, the resolution of the output voltage is limited by the resolution of the reference voltage. Moreover, the required output voltage is unknown since the channel impedance and current can vary widely. Therefore, an additional compliance monitor will be needed to select the appropriate reference voltage for each channel, which increases the power consumption and area of each channel.

In this chapter, we present a new power management strategy based on the parallel operation of channel-specific regulating rectifiers. We distribute the received AC power signal to the different channels and perform on-channel regulated rectification. This regulated rectification is triggered when the input AC voltage is equal to the sum of the load voltage for the desired stimulation current and a fixed compliance voltage for the current source. The triggering mechanism is implemented by a feedback topology that, based on the fixed headroom voltage of the current source, is automatically adjusted to account for the unpredictability of the output voltage requirements. This single-step power conversion, apart from omitting multi-stage power conversion losses, allows the current-mode stimulator to have a power supply that is continuously and automatically matched to the needs of the load for given impedance and stimulation current ranges,

hence maximizing the power efficiency at the output. Furthermore, the proposed channel-specific regulating rectifier is designed to achieve scalability for large-scale multichannel systems, allowing for efficient and precise regulation of the output voltage for each channel.

This chapter expands on a previously presented conference paper [1] with an extension on the design methodology and the inclusion of measurement results. The chapter is organized as follows. Sections 6.2 and 6.3 describe the system architecture and circuit design of the proposed system. In Section 6.4, we present measurement results and in vitro validation of the presented ASIC. The results are discussed in Section 6.5, and Section 6.6 concludes the chapter.

6.2. SYSTEM ARCHITECTURE

The proposed power management strategy is illustrated in Fig. 6.3. For simplicity of analysis, a system with two stimulation modules is considered. However, this same approach can be used for a higher number of modules. At the global level, the incoming AC power signal is converted into two half-bridge rectified voltage signals and distributed over the system modules. Each module has a local regulating rectifier that regulates the channel-specific output voltage. The output voltage is automatically matched to the required level for the load, minimizing the energy losses at the output driver and improving the power efficiency.

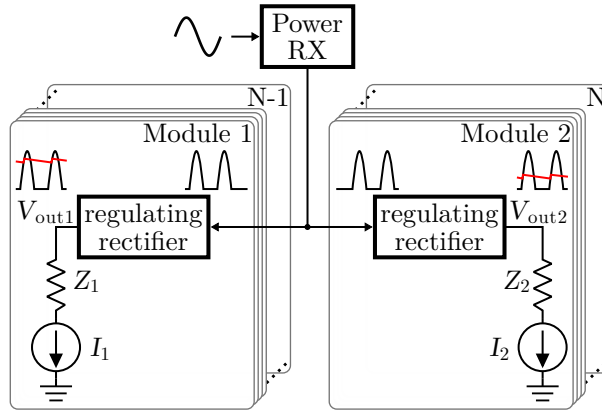


Figure 6.3: The proposed power management strategy is implemented using a modular architecture with N modules, each containing local regulating rectifier circuits. Both phases of the incoming AC signal are used by distributing them to the different modules.

The proposed strategy uses a modular system architecture, in which each module implements local power management and control functionality, as depicted in Fig. 6.4. Each module contains a configurable current DAC (I-DAC), a switch matrix, digital control logic, and a local regulating rectifier consisting of a phase-controlled rectifier switch (M_p) and an output capacitor (C_o). A bipolar current output is generated between V_o and V_{fb} , and the switch matrix is used to direct this current to multiple electrodes. Furthermore, the switch matrix is used to create biphasic stimulation pulses.

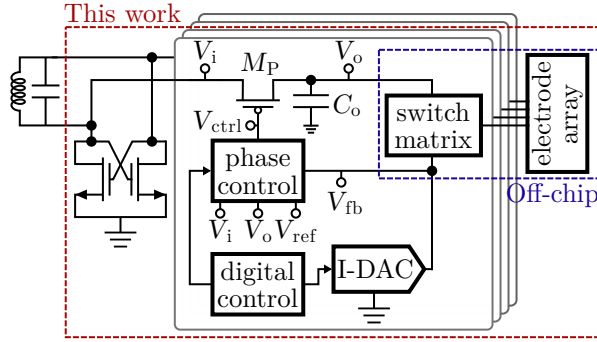


Figure 6.4: Proposed system architecture. The regulating rectifier is implemented as a phase-controlled rectifier switch (M_p), in which the phase control is based on the headroom voltage of the current DAC (V_{fb}). An off-chip switch matrix connects the generated output current to an external electrode array. Figure modified from [1].

6

On the system level, the incoming power is assumed to be received by means of an inductive link. However, the proposed approach would work with other (wireless) sources that produce an AC power signal (i.e., ultrasound, capacitive, or RF). The incoming AC power signal is split into two half-wave rectified sine waves using a cross-coupled NMOS pair at the input. The half-wave rectified signals are distributed equally over the modules in the system. Due to the variance in the output voltage requirements, the parallel regulating rectifiers will extract power from the input signal at different voltage levels. Moreover, although full-wave rectification would also be possible, using only half of the input signal at the input of the rectifiers omits copies of the control circuits that would be needed to rectify the other half of the input [31]. This simplifies the local control and reduces the area of the rectifiers. Since multiple modules operate in parallel, the entire input signal will still be used.

Existing regulating rectifier designs, such as those in [30, 31], have several drawbacks. In these designs, the output voltage V_o is used as the input of the controller. This approach typically requires an attenuator at the input of the controller, where a voltage divider with an impedance in the $M\Omega$ range is needed to minimize static power losses. However, this increases the overall circuit area. Additionally, in the conventional approach, the output voltage V_o is directly regulated by the reference voltage, resulting in discrete regulation steps. This can lead to overhead losses if $V_o > V_{tissue}$. Furthermore, due to the nonlinear and temporally variable nature of the load [13], the required output voltage at each channel is unknown, necessitating a compliance monitor to scale V_o as needed. Another drawback is that the conventional approach requires a separate DAC per channel to produce channel-specific output voltages, increasing the system's complexity and cost.

The proposed implementation addresses these limitations with a novel active phase controller. As shown in Fig. 6.5, the proposed design uses the headroom voltage of the current source, V_{fb} , as the control node in the active rectifier, which has several advantages. First, V_{fb} can be designed to be in the range of 100 to 200 mV, allowing direct detection by a low-voltage amplifier without requiring a high-impedance voltage divider, thereby reducing circuit area. Second, the proposed design regulates the output voltage to $V_o = V_{ref} + I_{out} Z_{tis}$, enabling the output to automatically track the required voltage. This

minimizes overhead losses and removes the need for a compliance monitor. Finally, V_{ref} is the same for all modules in the system, allowing a single reference voltage to be used while producing separate output voltages at each channel. This significantly reduces the complexity compared to the conventional approach, which requires a separate DAC per channel. A comparison of the proposed implementation with conventional regulating rectifiers is shown in Fig. 6.5.

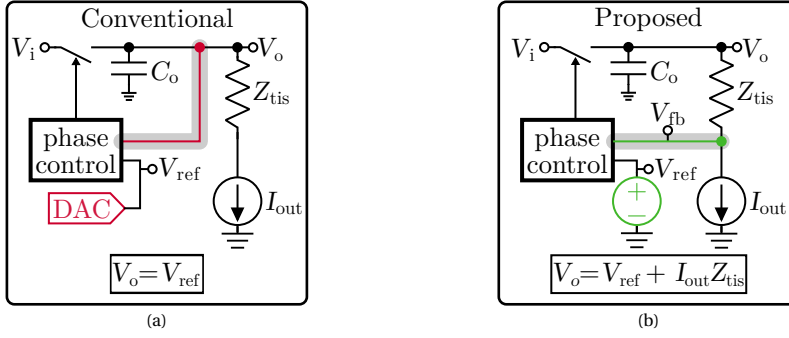


Figure 6.5: Comparison of (a) a conventional regulating rectifier structure and (b) the proposed implementation. In the conventional design, the output voltage is fixed to the reference voltage, which requires separate regulation for each channel. In contrast, the proposed implementation uses the feedback from the headroom voltage of the current source to automatically adjust the output voltage. This allows each channel to track its specific load requirement with a global reference voltage.

6.3. CIRCUIT DESIGN

A system with two parallel modules has been designed to demonstrate the proposed architecture (Fig. 6.4): In each module, a current is generated that flows from V_o to V_{fb} , which corresponds to the nodes where the load impedance is connected. An off-chip switch matrix allows biphasic current pulses to be sent through an external electrode array. This section describes the design of the on-chip module, where system-level specifications are first derived, followed by the design of the sub-blocks. Regarding the system level specifications, the circuit is designed to operate from a wirelessly received power signal with a central frequency of 13.56 MHz, commonly used in biomedical implants. Furthermore, the reconfigurable current DAC is specified with 4 bits of resolution between $20\mu\text{A}$ and $95\mu\text{A}$, which corresponds to typical threshold values often reported in intracortical visual prostheses [2]. The DAC is binary coded with wide-swing cascode current sources in each branch, with the LSB branch sinking $5\mu\text{A}$. Additionally, there is a parallel branch of $20\mu\text{A}$ to offset the current range. Moreover, C_o has a value of 40pF , resulting in a ripple voltage ΔV_o of 175mV at the maximum output current of $95\mu\text{A}$. Since the current is regulated by the I-DAC, the ripple voltage is allowed to be larger than for applications requiring a steady voltage supply. The size of C_o is a fundamental design trade-off with the allowed ripple voltage. Finally, the maximum voltage allowed at the output is 5V such that 5V -transistors can be used, which allows for load impedances in the range of tens of $\text{k}\Omega$, matching the impedances of Utah electrode arrays commonly used in cortical stimulation applications [2, 34]. A detailed description of the sub-blocks

and their design considerations are given below.

6.3.1. PHASE CONTROLLER

The design of the phase controller is depicted in Fig. 6.6. The rectifier switch (M_p in Fig. 6.4) is controlled by two loops. The first loop (indicated by the red arrow in Fig. 6.6), consisting of a comparator and a NAND gate, closes M_p at the cross-over point between V_o and V_i in each period. The conduction time of the pulse, t_d , is controlled by the second loop (indicated by the green arrow in Fig. 6.6), consisting of an error amplifier, a voltage-controlled delay line (VCDL) and the NAND gate. The error amplifier compares V_{fb} to the desired reference voltage V_{ref} and adjusts the delay time accordingly with the bias voltage of the VCDL, V_b . A timing diagram of the (ideal) signals in the controller at steady state is shown in Fig. 6.7. When the output driver is inactive (output current disabled), M_p is configured as a diode-connected transistor acting as a passive rectifier. Most of the components in the phase controller are operating from a 1.8 V supply to reduce power consumption. Therefore, a level shifter (LS) is needed between the control logic and the rectifier switch. The LS and MUX are part of the rectifier switch driver described in Section 6.3.5.

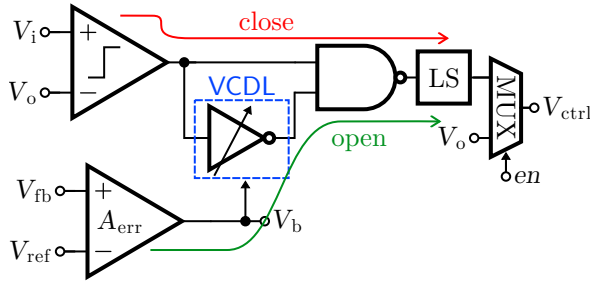


Figure 6.6: Implementation of the phase controller. The rectifier switch is closed via the signal path through the comparator, while the error amplifier and voltage-controlled delay line (VCDL) determine the pulse duration. Figure modified from [1].

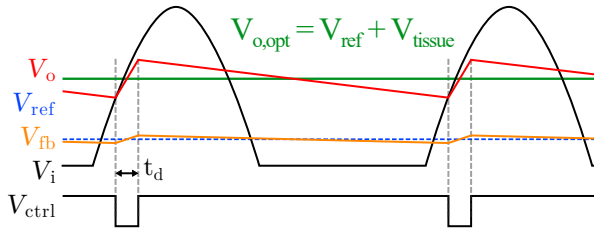


Figure 6.7: Timing diagram of the signals in steady state. In each cycle, the rectifier charges the output capacitor when the input waveform intersects the ideal output voltage. The signals are not to scale to highlight important properties. Figure modified from [1].

6.3.2. ERROR AMPLIFIER

The error amplifier is implemented as a 5T-OTA followed by a frequency compensation network with two poles and one zero, as depicted in Fig. 6.8. When the rectifier is disabled, the amplifier is also disabled. However, the input at V_{fb} can reach 5 V, and thus the amplifier is implemented using 5 V devices to avoid device breakdown. On the other hand, when the rectifier and the amplifier are enabled, the input at V_{fb} is in the range of V_{ref} , which is typically 200 mV. Therefore, the voltage supply of the amplifier is 1.8 V (V_L) to reduce its power consumption. The input pair is implemented using PMOS devices as the input voltage in active mode will be close to 0 V. At the start of a current pulse, the output of the amplifier will be saturated to V_L , which gives the shortest t_d . In turn, the filter capacitor (C_o in Fig. 6.4) is discharged by the DAC current, and V_{fb} drops until the amplifier gets out of saturation. At that point, the gain of the feedback loop restores to control the voltage to the desired level. Since the phase controller is a switched feedback loop, the output of the error amplifier needs frequency compensation to ensure loop stability. For stability, the frequency compensation has to dominate the overall loop gain. The design procedure of the compensation components is discussed in Section 6.3.6

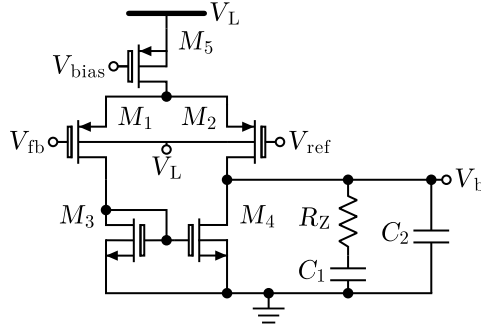


Figure 6.8: Implementation of the error amplifier.

6.3.3. VOLTAGE-CONTROLLED DELAY LINE

The VCDL is implemented as a single-sided current-starved inverter, depicted in Fig. 6.9. The delay of the element needs to be controlled only at the output transition from logic high to low. The element is reset at the output transition from low to high; hence, its transition time is irrelevant to the circuit's operation.

The output delay can be calculated using Eq. (6.1), assuming that C_L is charged to V_L at the beginning of the pulse and that the tipping point of INV_2 is at half the supply voltage, $V_L/2$. I_{M6} is regulated by V_b through M_2 and M_3 .

$$t_d = \frac{V_L}{2} \frac{C_L}{I_{M6}} \quad (6.1)$$

In the implementation, C_L is created by sizing INV_2 to get a large input capacitance. This improves the drive strength of INV_2 , minimizing the additional (overhead) delay. The simulated delay time of the VCDL is between 33 ns and 800 ps for $V_{th} \leq V_b \leq 1.8$ V.

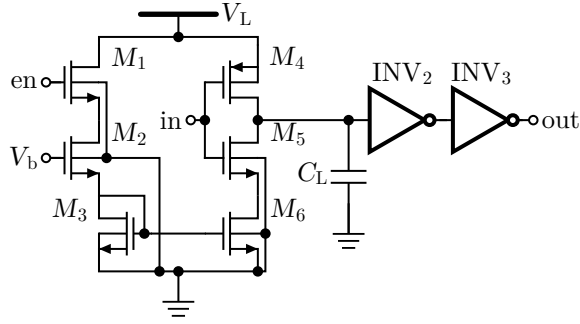


Figure 6.9: Implementation of the voltage-controlled delay line

The circuit produces an infinite delay when $V_b < V_{th}$. However, the comparator will turn the rectifier switch off when V_i drops below V_o in this implementation. Thus, the infinite delay does not pose a problem to the circuit's operation.

6.3.4. COMPARATOR

The design of the comparator is shown in Fig. 6.10. A common-gate input pair is used to allow for inputs above the supply rail of V_L . This omits the need for a steady, high-voltage supply for correct circuit operation. Using a dynamic bulk-biasing (DBB) circuit, the bulk terminals of the input pair are biased to the highest voltage of the two inputs. A single-bit multiplexer is used at the gates of M_3 and M_4 , controlled by the enable signal. When the comparator is enabled, the gates are connected to the bias voltage V_{bn} , which is generated using an (external) bias current and a current mirror. When disabled, V_{gs} of M_3 is 0 V, and V_{gs} of M_4 is V_L . Furthermore, M_5 is used to pull up the gates of M_1 and M_2 when the comparator is disabled. This way, the comparator uses no static power when disabled. The buffer at the output ($M_6 - M_9$) is used to convert the output voltage of the comparator to the low-voltage domain for the following logic gates.

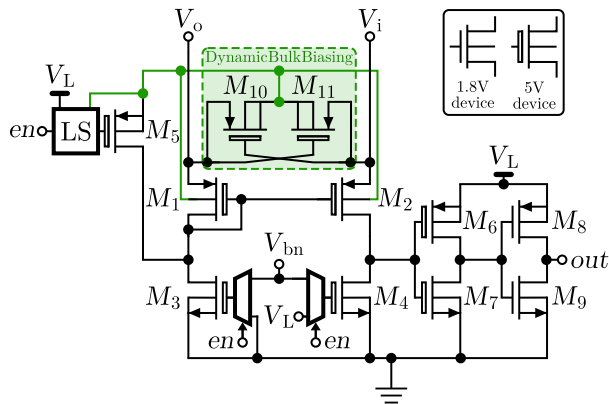


Figure 6.10: Implementation of the comparator. Figure modified from [1].

6.3.5. RECTIFIER SWITCH DRIVER

The rectifier switch, M_p , is a PMOS device with a size of $10\mu\text{m}/500\text{ nm}$ (W/L). The driver circuit for this switch is shown in Fig. 6.11. The bulk of M_p is biased using a DBB circuit. A MUX controls the gate of M_p to select active or passive rectification mode. When the feedback loop is disabled, the MUX connects the gate of M_p to the output, creating a passive rectifier. Contrarily, when the rectifier is enabled, the gate of M_p is actively controlled by the feedback loop. The pulse signal *trig* is level-shifted to the appropriate voltage level and buffered to drive M_p . The driving voltage for the output of the level shifter, the buffer, and the MUX are also created using a (separate) DBB circuit.

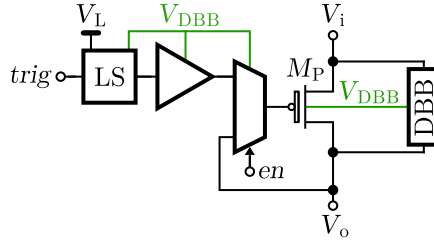


Figure 6.11: Implementation of the driver circuit for the rectifier switch.

6.3.6. DESIGN OF THE FEEDBACK LOOP

The loop gain of the phase controller is calculated by Eq. (6.2), where A_{err} is the gain of the error amplifier, A_{vcdl} the gain of the VCDL, A_{sw} the gain of the rectifier switch, and A_{out} the gain from V_o to V_{fb} (which will be <1). The frequency compensation components at the error amplifier are designed to be dominant in the total loop transfer.

$$A_L = A_{\text{err}} A_{\text{vcdl}} A_{\text{sw}} A_{\text{out}} \quad (6.2)$$

The magnitude of the transfer function of the error amplifier with frequency compensation is depicted in Fig. 6.12. It can be seen that the compensation adds two poles and one zero to the transfer function, where the dominant pole is created by the output resistance of the amplifier, R_o , and capacitor C_1 . To boost the phase margin, resistor R_z is added to create a zero at $f_z = 1/(2\pi R_z C_1)$. The non-dominant pole at $f_{p2} = 1/(2\pi R_z C_2)$ filters out high frequency signals. The phase controller is designed to operate at a switching frequency, f_{sw} , of 13.56 MHz. Since the cross-over frequency f_c should be lower than $f_{\text{sw}}/2$ to ensure stability, a design target for f_c is chosen at $f_{\text{sw}}/10$ to allow for a margin. Several design trade-offs can be derived from the Bode magnitude plot in Fig. 6.12. First, a high DC gain is desired to minimize the steady-state error. On the other hand, increasing the DC gain requires a bigger value of C_1 (and thus area) to achieve the same f_c . Furthermore, the wide operating range of the circuit will cause variance in the (non-linear) transfer functions of the other sub-blocks. Separating the zero and the non-dominant pole makes the increase of the phase margin effective over broad operating conditions. Taking into account the trade-offs above, the amplifier was designed to have low static power consumption and a small area for scalability. The implemented amplifier consumes $1\mu\text{A}$ from a 1.8 V supply, with a DC open-loop gain of 33 dB. The compensation components are chosen as $C_1 = 3.2\text{ pF}$, $C_2 = 160\text{ fF}$, and $R_z = 100\text{ k}\Omega$.

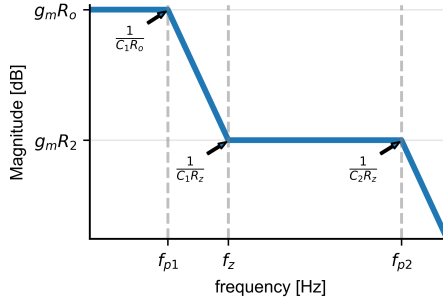


Figure 6.12: Bode magnitude plot of the transfer function of the error amplifier with frequency compensation (Fig. 6.8). R_o and g_m are the output resistance and transconductance of the amplifier, respectively.

Regarding the VCDL, the transfer function is given by:

$$A_{\text{vcdl}} = \frac{dt_d}{dV_b}. \quad (6.3)$$

Since an increase in V_b will increase the discharge current and thus decrease t_d , A_{vcdl} is negative by design. Furthermore, A_{sw} and A_{out} are both positive. Therefore, A_{err} is designed to be positive to achieve an overall negative loop gain. The transfer function of the VCDL has two asymptotes since the delay goes to infinity when $V_b < V_{\text{th}}$, and approaches the minimum delay for V_b close to 1.8 V. Therefore, the gain of this block can vary over a wide range depending on the operating point of the overall circuit.

The next component in the architecture is the rectifier switch, for which the transfer function can be obtained from:

$$A_{\text{sw}} = \frac{dV_o}{dt_d}. \quad (6.4)$$

The output current I_{DAC} determines the discharge rate of the output capacitor and, thus, how much charge needs to be transferred in t_d . When conducting, the charging current can be calculated using

$$I_{\text{in}} = \frac{V_i - V_o}{R_{\text{sw,on}}}. \quad (6.5)$$

Where $R_{\text{sw,on}}$ is the on-resistance of M_p . The DC gain of this stage depends on many variables, such as the slope of the input signal, the size of C_o , the output current I_{DAC} , and the on-resistance of the rectifier switch. Furthermore, a pole is introduced by the low-pass filter at $f_{p,\text{sw}} = D/(2\pi R_{\text{sw,on}} C_o)$, where D is the duty cycle of the rectifier switch. To reduce conduction losses, the on-resistance of the rectifier switch should be low. However, this also reduces D and the location of p_{sw} . Therefore, the sizing of the rectifier switch should be done carefully to prevent p_{sw} from becoming dominant. Finally, the transfer function of the output stage is given by $A_{\text{out}} = V_{\text{ref}}/V_o$. Again, the attenuation depends on impedance and current at the output. When V_o is close to V_{ref} , A_{out} approaches 1, and at the maximum output voltage $A_{\text{out}} = V_{\text{ref}}/5$.

The total loop gain of the designed circuit is simulated for all possible output current amplitudes (20 to 95 μA) and a load resistance ranging from 20 k Ω to 70 k Ω . The resulting

loop gain magnitude and phase are shown in Fig. 6.13. The phase margin ranges between 52° and 74° for the simulated conditions. When the output is disabled, the loop gain is zero since the output of the OTA saturates. Therefore, the beginning of a current pulse causes a large step, and stability should be confirmed using transient simulations. The transient response to a $35\mu\text{s}$ current pulse at the output was simulated for the same range of output current amplitudes and load resistances. The results, shown in Fig. 6.14, show that all conditions result in a stable voltage at V_{fb} . For low output currents, the transient response is slower because the output current needs to discharge C_o , while a minimum amount of charge is deposited each cycle due to the minimum pulse width that the feedback loop can produce.

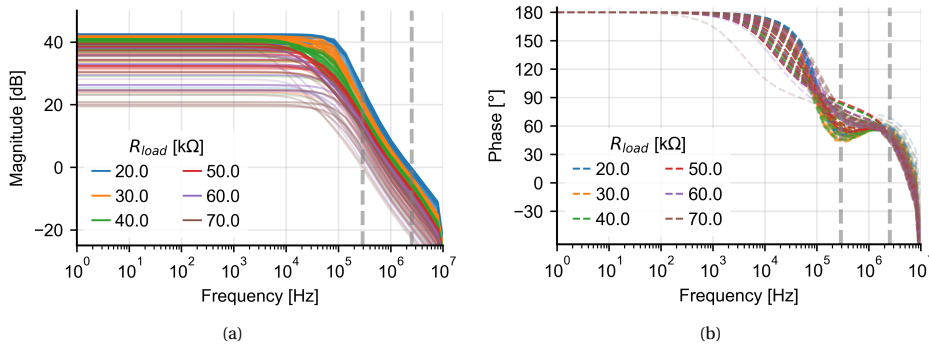


Figure 6.13: Simulated loop gain magnitude (a) and phase (b) of the implemented regulator for a wide range of load conditions: $R_{load} = 20\text{ k}\Omega$ to $70\text{ k}\Omega$ and $I_{load} = 20\mu\text{A}$ to $95\mu\text{A}$ ^a. The opacity of the traces indicates I_{load} , where high current equals high opacity.

^aIf the required output voltage, V_o , exceeds the maximum output voltage the circuit can provide, the output is no longer regulated, and the loop gain deteriorates. These output conditions are not included in the figure.

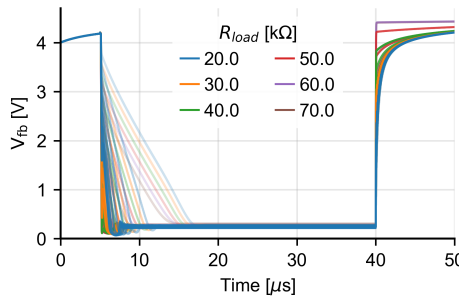


Figure 6.14: Simulated transient response for a stimulation pulse with a duration of $35\mu\text{s}$ starting at $t = 5\mu\text{s}$, while sweeping the conditions: $R_{load} = 20\text{ k}\Omega$ to $70\text{ k}\Omega$ and $I_{load} = 20\mu\text{A}$ to $95\mu\text{A}$. The opacity of the traces indicates I_{load} , where high current equals high opacity.

6.4. SYSTEM VALIDATION

The circuit was implemented in a 180 nm CMOS TSMC process. The chip micrograph is shown in Fig. 6.15. The design has an active area of $800\mu\text{m} \times 126\mu\text{m}$ (excluding pads) and a channel area of $368\mu\text{m} \times 126\mu\text{m}$ (of which 52 % is occupied by C_o). The measure-

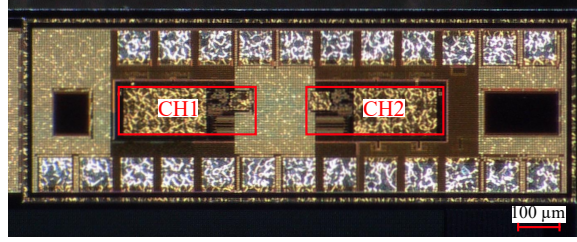


Figure 6.15: Micrograph of the implemented chip with the two channels indicated by the red boxes.

ment setup is illustrated in Fig. 6.16. A 10 V_{pp} , 13.56 MHz sine wave is generated using a signal generator (*Rigol dg4202*) and ac-coupled to the input of the chip using an RF 1:1 transformer (COILCRAFT SWB1010). The low-voltage supply V_L (1.8 V) is provided to the chip using a bench-top DC supply (*GW Instek GPP-4323*). For some measurements, an external H-bridge, created using analog switches (*ADG1211*), was used to generate biphasic current pulses. Furthermore, the necessary bias currents and reference voltage V_{ref} are generated on a PCB using commercially available ICs. In the final application, the low-voltage supply could be generated from a separate rectifier in parallel with the proposed voltage regulators, and the bias currents should be generated on-chip. Finally, the control signals for the ASIC are created using an FPGA module (Digilent CMOD S7). In all presented measurements, V_{ref} is set to 250 mV.

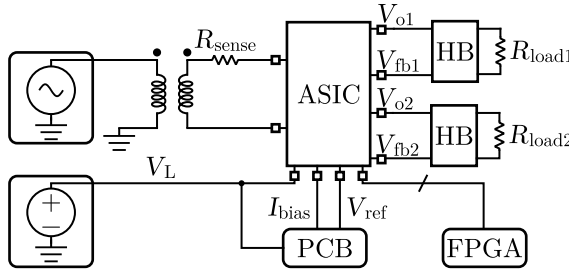


Figure 6.16: Illustration of the measurement setup. The input signal is generated from a signal generated and ac-coupled to the chip using a 1:1 RF transformer. The voltage supply, bias currents, and reference voltage are supplied externally. The output nodes of both channels are connected to the loads using external H-bridges (HB). The ASIC is controlled using an FPGA module. R_{sense} is used to measure the input power.

6.4.1. OUTPUT PULSES

To demonstrate the operation of the circuit, the two channels are configured for different current amplitudes and load impedances. Both channels produce a current pulse with a duration of $100\mu\text{s}$. The amplitude is configured to $50\mu\text{A}$ and $40\mu\text{A}$ for Channels 1 and

2, respectively, and a resistive load of 30 k Ω and 70 k Ω is applied at the outputs. The resulting output voltages are shown in Fig. 6.17a. It can be seen that for both channels, V_{fb} is regulated to V_{ref} , while the output voltages $V_{o,1}$ and $V_{o,2}$, differ for both channels, depending on the output conditions. The effective output currents, shown in Fig. 6.17b, are found by subtracting these voltages and dividing them by the load impedance. For these output conditions, the error on the load current compared to the configured current is $-2.8 \mu\text{A}$ (6 %) for Channel 1 and $-1.1 \mu\text{A}$ (3 %) for Channel 2. Next, an external H-bridge

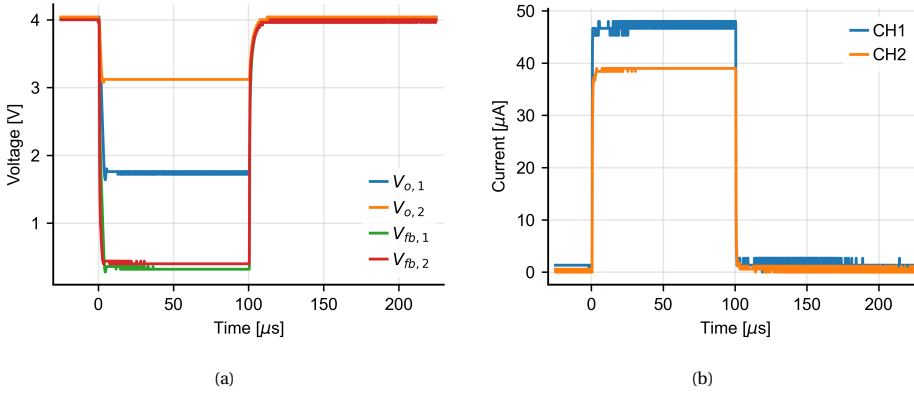


Figure 6.17: Example of measured output voltages (a) for load impedances of 30 k Ω and 70 k Ω , and current amplitudes of 50 μA and 40 μA on Channels 1 and 2, respectively. (b) Effective measured load current.

is used to create biphasic current pulses. Figure 6.18a shows the measured voltages at the two output nodes of the H-bridge for a biphasic current pulse of 50 μA on a 30 k Ω resistive load. The resulting load current is depicted in Fig. 6.18b. These measurements show that the output voltages of both channels are automatically and independently regulated to the voltage required by the load during the stimulation pulses.

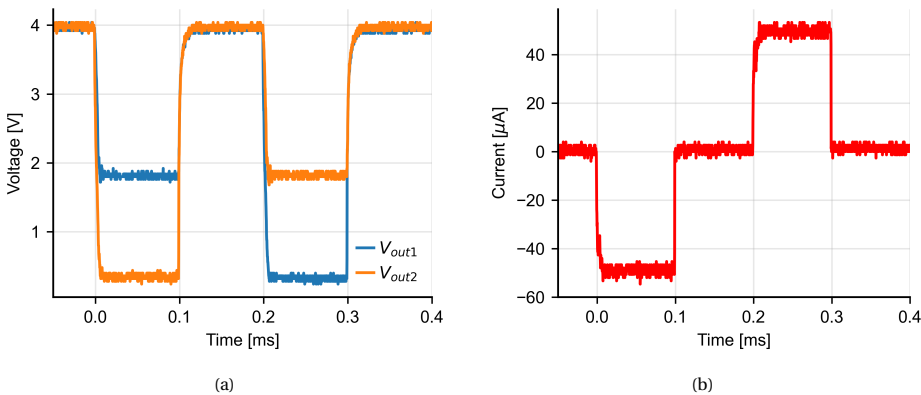


Figure 6.18: (a) Measured voltages at the output of the H-bridge for a biphasic current pulse of 50 μA on a 30 k Ω load. (b) Effective current as seen by the load.

6.4.2. VARYING OUTPUT CONDITIONS

To characterize the output of the chip for varying load conditions, one of the channels is configured to produce a constant output current, as shown in Fig. 6.19. It can be seen that the maximum current is limited for larger load impedances, which is due to the maximum output voltage that the circuit can produce (around 4.2 V). The measured

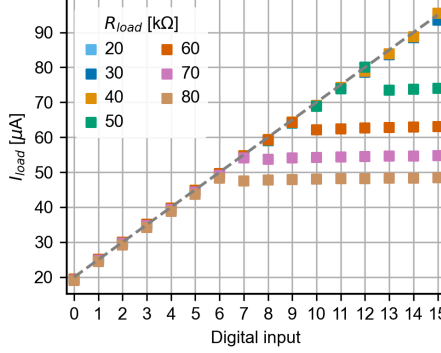


Figure 6.19: Measured output current vs DAC configuration bits for different load impedances. At higher impedances, the maximum achievable current is constrained by the circuit's voltage compliance.

6

output voltages for three different load impedances are depicted in Fig. 6.20, where I_{set} is the configuration setting of the I-DAC. The measurements show a wide range of regulated output voltages, depending on the current and load impedance at the output. The broad operating conditions allow for accurate tracking of the required output voltage, resulting in a high power efficiency at the output. It is evident that V_{fb} is not regulated as desired for low-current output conditions, which is due to the minimum pulse width that the switch driver could produce. When the output current is small, the discharge rate of C_o is low, and the charge delivered to C_o for minimum t_d is too high to properly discharge the node to V_{ref} . This could be improved by making the minimum t_d smaller or skipping pulses for low current conditions. Furthermore, it can also be seen that the maximum output voltage of the circuit is only around 4 V for a 5 V input signal. This is due to the large on-resistance of the implemented rectifier switch. The limitation on the maximum output voltage causes the deviation of I_{load} from its intended value in Fig. 6.19. To improve the maximum VCR of the circuit, the sizing of M_p should be improved. For the following measurements, the results for load conditions where the circuit can not produce the required output voltage are discarded.

6.4.3. POWER EFFICIENCY

For the power measurements, the transformer in Fig. 6.16 is omitted, and a 5V half-sine signal is directly applied from the signal generator to the input of the chip. Each load condition is repeated 20 times in a random order, and the measured quantities are averaged. The efficiency at the output, calculated using Eq. (6.6), is shown in Fig. 6.21.

$$\eta_{out} = \frac{P_{load}}{P_{out}} \quad (6.6)$$

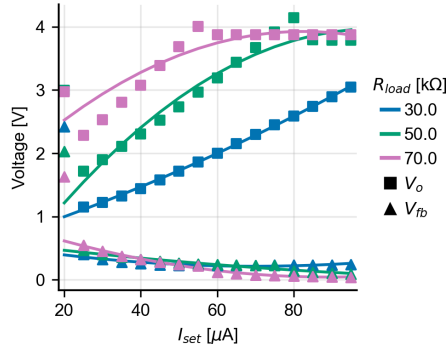


Figure 6.20: Measured output voltages for varying load conditions. Markers indicate measured data; solid lines represent quadratic fits to the data.

As a reference, the output efficiency for a fixed voltage supply of 5 V is also plotted in the same figure. The proposed rectifier achieves efficiencies above 80 % for almost all load conditions, reaching 94 % for a load of 50 k Ω , which represents a substantial improvement over a conventional fixed 5 V supply. The low efficiency for an output current of 20 μ A is due to the effect that V_{fb} is not properly regulated, as explained in the previous section. This results in excessive voltage drop, and thus power dissipation, over the current source.

6

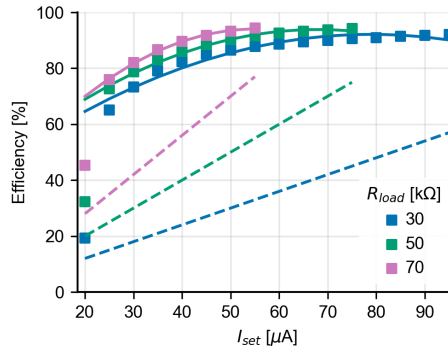


Figure 6.21: Measured power efficiency (solid) at the output for three load impedances compared to the efficiency of a fixed 5 V voltage supply (dashed). Markers indicate measured data; solid lines represent quadratic fits to the data.

A sense resistor of 47 Ω is used in series with the input to measure the input power. Parasitics on the PCB introduce a large offset in the measured power levels since the power to the load is small in this application. To compensate for this offset, the power at the input for all conditions is measured twice: once with the output of the chip enabled and once with the output disabled. The power measurements are obtained by subtracting

P_{off} from P_{on} for a wide range of load conditions, with the measured results presented in Fig. 6.22. The total efficiency of the circuit is calculated using Eq. (6.7) and depicted in Fig. 6.23.

$$\eta_{\text{total}} = \frac{P_{\text{load}}}{P_{\text{in}}} \quad (6.7)$$

It can be seen that the overall efficiency is relatively low compared to the output efficiency shown in Fig. 6.21, which is mainly due to conduction losses in M_p . In Section 6.5, we discuss several opportunities to improve the overall efficiency.

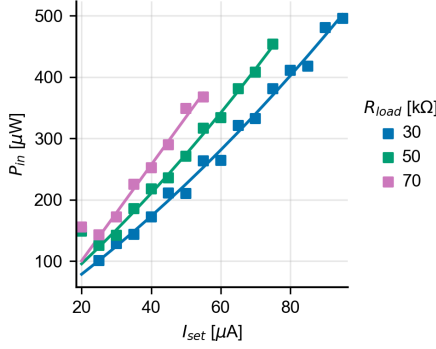


Figure 6.22: Measured input power for a wide range of load impedances and output currents. Markers indicate measured data; solid lines represent quadratic fits to the data.

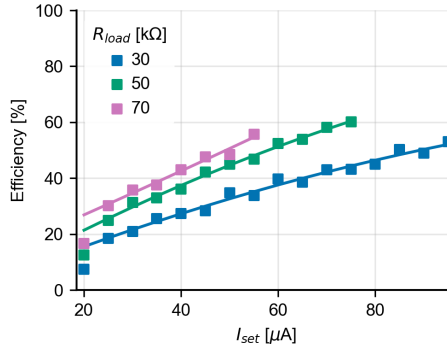


Figure 6.23: Measured overall efficiency of the rectifier for three load impedances. Markers indicate measured data; solid lines represent quadratic fits to the data.

6.4.4. EFFICIENCY IN MULTICHANNEL APPLICATIONS

To see how the measured efficiencies translate to a multichannel application (intracortical visual prosthesis), we applied the analysis presented in Chapter 5 to this system. For this

analysis, we used the experimental data from [2] and [3]. In total, we used five datasets, one from [2] (Human), and four from [3] (Monkey A early, Monkey A late, Monkey L early, Monkey L late). The current thresholds and electrode impedances for these data sets are listed in Table 6.1. Using these distributions, we created a new dataset with 10000 entries for each of the subjects. In this dataset, all electrode impedances are rounded to a multiple of 10 k Ω , and all current thresholds are rounded to a multiple of 5 μ A. Furthermore, the current data is truncated over the range of 20 μ A to 95 μ A, and the impedance data is truncated to the range of 20 k Ω to 80 k Ω . The truncation and rounding of the entries are based on the measurement data obtained for the circuit. For the resulting dataset, efficiencies for each entry are calculated as described in Chapter 5 while taking into account a headroom voltage of 250 mV and a resampling size of $M = 200$. Furthermore, the measured efficiency at the output of the proposed circuit is mapped to the data based on the current threshold and electrode impedance of each entry. As a result, we can compare the efficiency distributions for the different scenarios based on experimental data.

The resulting efficiencies are shown in Fig. 6.24. The proposed work shows a median efficiency of 84 % on this data, representing an improvement of 74 %, 17 %, and 6 % compared to a fixed supply and stepped voltage supplies with 4 and 8 steps, respectively.

Table 6.1: Summary of the datasets used in this chapter. All numerical data is presented as mean \pm sd.

#	Source	Dataset	Electrode impedance [k Ω]		Current threshold [μ A]
1	[2]	Human	47.0 \pm	4.8	67 \pm 37
2	[3]	Monkey A early	144.7 \pm	72.6	65 \pm 45
3	[3]	Monkey A late	71.1 \pm	70.6	60 \pm 58
4	[3]	Monkey L early	75.1 \pm	36.3	19 \pm 17
5	[3]	Monkey L late	74.9 \pm	36.4	80 \pm 71

6.4.5. TIME DIVISION MULTIPLEXING

Time-division multiplexing (TDM) can be employed in electrical stimulation circuits to enable efficient resource sharing by utilizing a single stimulation driver across multiple channels [35]. However, existing multiplexed implementations overlook the need for precise voltage scaling for varying load conditions. Instead, they rely on fixed voltage supplies or regulating rectifiers with large output capacitors [35–40]. Fixed supply implementations lead to low power efficiency (Fig. 6.24), while large output capacitors in regulating rectifiers limit the speed of voltage regulation, making them unsuitable for applications requiring rapid switching between channels with differing load impedances and current amplitudes. The proposed circuit overcomes these limitations by enabling scalable TDM for systems with a large number of electrodes, even when load conditions differ significantly between channels. The small output capacitor in this design allows for rapid voltage regulation and ensures seamless transitions between channels. Furthermore, the circuit automatically adjusts to changing load conditions, maintaining appropriate output voltage. In contrast, implementations with large output capacitors in

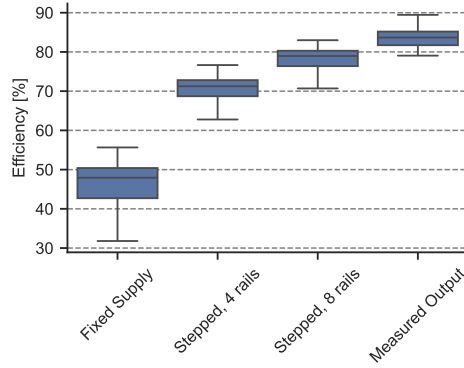


Figure 6.24: Performance comparison of the output efficiency of the proposed design with other supply strategies. Efficiencies are calculated for experimental datasets of intracortical visual prostheses [2, 3] using the analysis method presented in Chapter 5.

regulating rectifiers exhibit slower response times, which hinder their ability to efficiently switch between channels. The flexibility of the proposed circuit for TDM is demonstrated via post-layout simulations of six consecutive current pulses, each lasting $100\text{ }\mu\text{s}$, applied to two channels under varying output conditions (load impedance and current amplitude), as illustrated in Fig. 6.25. An interpulse delay of $1\text{ }\mu\text{s}$ is used to reconfigure the output current and to switch the load impedance. For channel one, the current and load impedance sequences are $90, 50, 30, 30, 50$ and $70\text{ }\mu\text{A}$ and $40, 30, 70, 80, 60$ and $50\text{ k}\Omega$, respectively. For channel two the corresponding sequences are $40, 45, 80, 50, 90$ and $40\text{ }\mu\text{A}$ and $40, 80, 50, 40, 40$ and $60\text{ k}\Omega$. These simulations highlight the circuit's ability to rapidly regulate the output voltage for each pulse, maintaining optimal power efficiency across diverse load conditions. The multiplexing frequency is limited by the duration of the stimulation pulses and the configuration of the current source, which can be in the range of nanoseconds. Therefore, the effective TDM rate is constrained primarily by the pulse duration, and, if present, the interpulse delay of each channel.

6.4.6. IN VITRO MEASUREMENTS

Finally, the chip is tested using custom-made¹ flexible and conformable electrodes immersed in a phosphate-buffered saline (PBS) solution.

Cleaned 4-inch silicon wafers were coated with a $2\text{ }\mu\text{m}$ -thick parylene layer, which provided a conformable substrate. The Au electrodes and interconnects (3 cm) are patterned via photolithography and lift-off processes. AZnLOF2020 was spin-coated, baked on a proximity hot plate at $110\text{ }^{\circ}\text{C}$, exposed using a Suss MA6 Mask Aligner, and developed with AZ 726 MIF developer. Ti (10 nm) and Au (150 nm) layers were deposited with an e-beam metal evaporator. Lift-off was performed by immersing the substrates in a bath with TechniStrip Ni555. An additional $2\text{ }\mu\text{m}$ parylene layer was coated on the samples to electrically isolate the Au electrodes. The adhesion of the second parylene layer was im-

¹The custom electrode probes were developed and fabricated in the Neural Waves Lab at Ghent University, Belgium

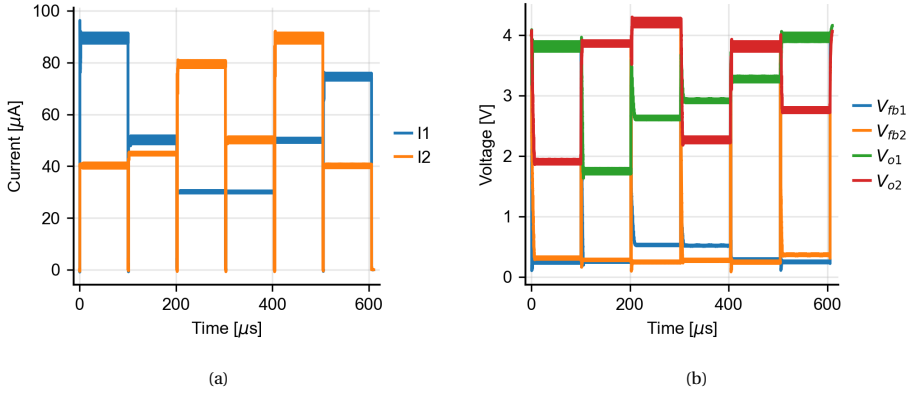


Figure 6.25: Post-layout simulation of (a) output current and (b) output voltages during time-division multiplexing of the proposed circuit. Six current pulses of $100 \mu\text{s}$ each are applied consecutively with varying load impedance and current amplitude. An interpulse delay of $1 \mu\text{s}$ is used to configure the output conditions. For channel one, the current and load impedance sequences are 90, 50, 30, 30, 50 and $70 \mu\text{A}$ and 40, 30, 70, 80, 60 and $50 \text{ k}\Omega$, respectively, while for channel two they are 40, 45, 80, 50, 90 and $40 \mu\text{A}$ and 40, 80, 50, 40, 40 and $60 \text{ k}\Omega$.

proved by using silane during coating. Then 5 % of micro 90 in DI water was spin-coated to form an anti-adhesive layer. A sacrificial third parylene layer ($2 \mu\text{m}$) was deposited on top. AZ10xT was spin-coated, baked at 110°C , exposed using a Suss MA6 Mask Aligner, and developed with AZ400K developer. The areas corresponding to electrodes and contact pads were etched via successive photolithography and reactive ion etching steps. After the fabrication, the probe's contact pads (ball gate array) are flip-chip bonded to a custom-made PCB.

The electrodes have an area of $50 \mu\text{m} \times 50 \mu\text{m}$ with an inter-electrode distance of $950 \mu\text{m}$. The output of the chip is connected to the electrodes in a bipolar configuration using the external H-bridge. First, the impedance of the electrodes is characterized using a Zurich Instruments MFIA digital impedance analyzer. The measured magnitude and phase of the impedance are shown in Fig. 6.26. The impedance at 1 kHz is approximately $15 \text{ k}\Omega$.

Next, biphasic current pulses of $50 \mu\text{A}$ and $95 \mu\text{A}$ are applied to the electrodes. The measured voltages at the output nodes are shown in Fig. 6.27a. The resulting load voltages, depicted in Fig. 6.27b, are obtained by subtracting these voltages. The measured load voltages are typical voltage transients for stimulation electrodes upon applying rectangular current pulses, where the ramp in the voltage is the effect of capacitance at the electrode-tissue interface that is charged by the stimulation current. These measurements show the capability of the circuit to follow a change in required output voltage.

6.4.7. PERFORMANCE COMPARISON WITH PREVIOUS WORK

Table 6.2 and Table 6.3 compare the proposed design with existing regulating rectifier topologies and multichannel stimulator implementations, respectively. Compared to existing regulating rectifier designs (Table 6.2), the proposed design demonstrates advan-

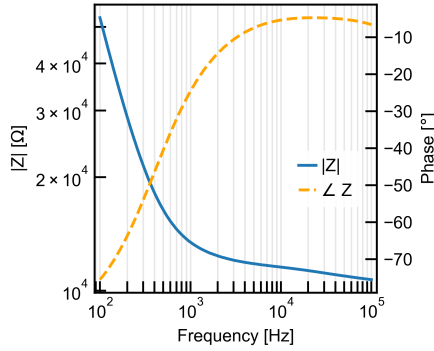


Figure 6.26: Measured impedance magnitude and phase for the bipolar electrode pair in a PBS solution.

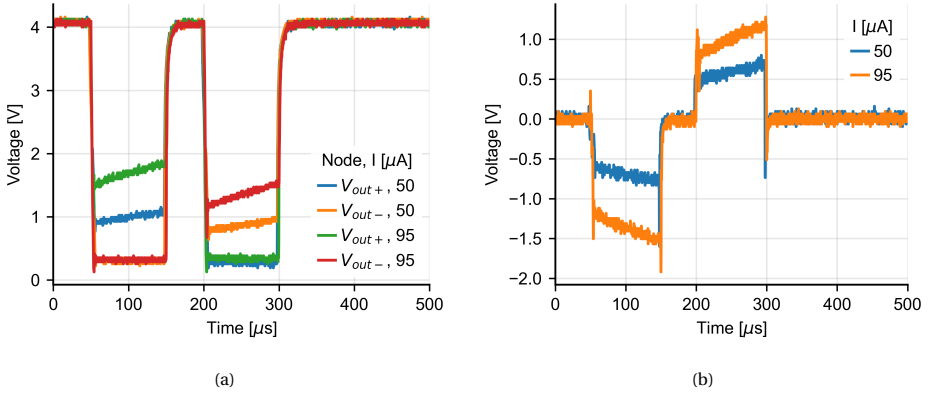


Figure 6.27: In vitro measurements of the (a) output voltage and resulting (b) differential load voltage for current amplitudes of 50 μA and 95 μA . The circuit is able to track the voltage ramp at the output, caused by the capacitive component of the electrode-tissue interface.

tages in terms of area efficiency, adaptability, and scalability. It is the only implementation that achieves continuous voltage regulation with parallel output regulation, allowing for precise control over the output voltage for individual channels. Furthermore, it achieves the smallest area per channel at $368\mu\text{m} \times 126\mu\text{m}$, which is 43 % smaller than the next smallest design [31]. Additionally, it operates with a significantly smaller output capacitor (40 pF), which increases the speed of the output regulation and allows for TDM operation. Finally, the implementation is not fundamentally limited to the number of parallel regulators, while [27] is limited to a maximum of 6 output voltages.

When compared to other multichannel stimulator implementations employing dynamic voltage scaling (Table 6.3), the proposed design offers a continuous output voltage while allowing parallel output regulation. Most prior works utilize compliance monitors or external control circuits to manage voltage regulation. In contrast, our design leverages a local regulating rectifier that autonomously adjusts the voltage supply based on the

Table 6.2: Comparison against regulating rectifier topologies.

Work	2013 [30]	2017 [31]	2015 [33]	2024 [27]	This work
Technology (μm)	0.5	0.18 (SOI)	0.35	0.25	0.18
Resonant frequency (MHz)	2	144	13.56	2	13.56
Area/Channel (mm^2)	0.15	0.08	N.A.	0.52	0.046
Max. output voltage (V)	4.6	0.8	3.6	4.5	5
Max. output current	2.48 mA	700 μA	N.A.	22.5 mA	95 μA
Output capacitor	N.A.	1 nF	N.A.	10 μF (off-chip)	40 pF
Number of voltage steps	8	1 (fixed)	PWM-regulated	N.A.	Continuous
Parallel output regulation	No	No	No	Yes	Yes
Scalability output channels	-	-	-	max. 6	Unlimited

Table 6.3: Comparison against (multichannel) stimulator implementations with dynamic voltage scaling.

Work	2023 [41]	2023 [24]	2023 [25]	2021 [26]
Technology (μm)	0.18	0.25	0.18	0.18
Max. output voltage	12 V	5 V	12 V	-5.4 V/+3.6 V
Max. output current	-	160 μA	2 mA	100 μA
Area/Channel (mm^2)	-	0.01	0.042	0.088
Number of voltage steps	3	4	4	5
Parallel output regulation	Yes	Yes	Yes	Yes
Voltage regulation	Compliance monitor + MUX	Compliance monitor + MUX	Compliance monitor + MUX	Compliance monitor + MUX

Table 6.3: (continued)

Work	2022 [28]	2024 [42]	This work
Technology (μm)	0.18	0.18	0.18
Max. output voltage	12 V	$\pm 6\text{ V}$	5 V
Max. output current	1 mA ¹	2.5 mA	95 μA
Area/Channel (mm^2)	0.11	0.73	0.046
Number of voltage steps	4	Continuous	Continuous
Parallel output regulation	Yes	No	Yes
Voltage regulation	External control	Current sensing fb loop	Headroom voltage fb loop + regulating rectifier

¹ External current sources

headroom voltage, eliminating the need for additional compliance monitoring circuits.

While prior works evaluate efficiency based on selected load conditions, Table 6.3 emphasizes that different designs target varying load scenarios, which may influence benchmarking results in favor of specific designs. In contrast, our approach addresses the challenges posed by variability and unpredictability in output conditions by generating a continuous output voltage, ensuring consistently high efficiency across a wide range of load scenarios. The objective of this chapter is not to optimize efficiency for a single load condition but to enable power-efficient operation across diverse operating scenarios. In this respect, we have shown that the proposed circuit offers high efficiency at the output for realistic output conditions in the application of intracortical visual stimulation

(Fig. 6.24), with an increase of 17 % compared to implementations with 4 voltage steps.

6.5. DISCUSSION

The presented power management strategy of parallel regulating rectifiers that regulate the output voltage based on the headroom voltage of the current source offers high adaptability in the output voltage. Due to the implementation of the feedback circuit, the rectifier matches the output voltage without the need for a compliance monitor that is required for existing implementations [30]. This implementation reduces the complexity of the local controller associated with the other forms of local voltage regulation (Figs. 6.2b and 6.2c) [22, 24–27]. The adaptability results in high power efficiency at the output driver, compared to the conventional fixed-voltage implementation (Fig. 6.21), achieving efficiency as high as 94 % for 50 k Ω , and >80 % across almost all load conditions. Furthermore, the flexibility of the circuit results in a median efficiency at the output of 84 % when applied to experimental data from intracortical visual prostheses, boosting the efficiency with 74 % compared to the conventional fixed supply. The regulation speed of the output voltage allows the circuit to be used for efficient TDM between multiple electrodes, where the output requirements for each electrode will be different. The implemented design only occupies 368 $\mu\text{m} \times 126 \mu\text{m}$ per channel, achieving the lowest area among circuits employing continuous and parallel output regulation. The area could be further improved if part of the circuit is placed under the filter capacitor, C_o . These features collectively establish the proposed implementation as a scalable and power-efficient solution for systems with many stimulation channels.

Yet, there is room for further improvement, which is discussed here. The overall efficiency of the current design is not yet optimized and is mainly limited by conduction losses in M_p . There are several opportunities to improve the overall efficiency of the rectifier further. First, the size of M_p could be increased to reduce R_{on} and thereby the conduction losses. Additionally, the delay introduced by the comparator and switch driver leads to a voltage drop over the switch at the onset of the pulses, which leads to increased conduction losses. Offset compensation at the input of the comparator could improve the overall efficiency by minimizing the delays of the feedback [43–46]. Reducing the voltage drop over M_p by sizing and offset compensation would also improve the maximum VCR of the rectifier. Furthermore, pulse frequency modulation (PFM) could improve the efficiency for small output currents [31]. When the output current is small, the switching losses become relatively dominant. By skipping one or more pulses, the switching losses can be reduced. Since the DAC controls the output current in this system, there is no need for additional circuits to determine the appropriate PFM rate. Lastly, since a half-wave rectified input signal is used, the comparator could be disabled for 50 % of the time to reduce static power losses of the feedback loop. Alternatively, an adaptive-bias comparator can be used [31, 47].

Although the design is demonstrated here with two channels, it is designed to be scalable to many parallel channels. Other designs are fundamentally limited to provide only a few output rails. Scaling the number of output channels of the presented design is a matter of putting multiples of the same circuit in parallel. With the current dimensions, a system with 100 channels would take up less than 5 mm². Note that this includes an integrated output capacitor on-chip for each channel, whereas the output capacitance

in some other works is off-chip [27]. As mentioned before, the area per channel could be reduced by placing circuits under C_o . Combined with time-division multiplexing, the number of channels could be increased to over 1000 for large-scale multichannel applications. Given that each rectifier only provides the output power for a single channel, the impact on the input signal from a wireless link from a single rectifier should be small. Furthermore, since the load conditions for each channel are different, the conduction periods of the different rectifiers will be spread in time. To spread the conduction periods even more, one could design the proposed circuit to operate at the falling phase of the input signal, similar to the peak right rectifier in [27], and distribute the designs over the system such that half of the channels rectify on the falling phase. The impact of many parallel rectifiers on the wireless link should be investigated in future work.

Finally, the safety and reliability of the proposed circuit warrant more detailed consideration. Since the rectifier does not include a global compliance limit, additional safeguards such as overvoltage or overcurrent protection are required to ensure safe operation under fault conditions.

6.6. CONCLUSION

Variability in the load conditions between channels leads to low power efficiency in large-scale multichannel stimulator systems. This chapter introduced a novel power management strategy that offers adaptive regulation of the output voltage for each channel individually. The presented design implements a regulating rectifier for bipolar electrode configurations, where the headroom voltage on the current source is used as feedback voltage. In this way, the channel-specific output voltage is automatically scaled to the requirements of the load without the need to characterize the load impedance.

The scaled voltage results in high power efficiency at the output driver over a wide range of load conditions. In particular, the circuit sustained efficiencies at the output above 80 % across almost all tested load scenarios Fig. 6.21. Using experimental data from intracortical prosthesis studies, the methodology of Chapter 5 showed a median efficiency of 84 % Fig. 6.24, representing a substantial improvement compared to fixed and stepped supply strategies.

We further demonstrated the scalability of the proposed circuit by showing the suitability for time-division multiplexing of the output driver to many channels. In addition, the design was tested on realistic electrode impedances, where it could track the required output voltage. Lastly, we have listed recommendations to further improve the efficiency of the proposed power management strategy.

BIBLIOGRAPHY

- [1] F. Varkevisser, T. L. Costa, and W. A. Serdijn, “Multichannel current-mode stimulator with channel-specific regulated power supply”, in *2023 IEEE Biomedical Circuits and Systems Conference (BioCAS)*, IEEE, Oct. 2023, pp. 1–5, ISBN: 979-8-3503-0026-0. DOI: 10.1109/BioCAS58349.2023.10388577.
- [2] E. Fernández *et al.*, “Visual percepts evoked with an intracortical 96-channel microelectrode array inserted in human occipital cortex”, *Journal of Clinical Investigation*, vol. 131, no. 23, Dec. 2021, ISSN: 1558-8238. DOI: 10.1172/JCI151331.
- [3] X. Chen *et al.*, “Chronic stability of a neuroprosthesis comprising multiple adjacent Utah arrays in monkeys”, *Journal of Neural Engineering*, vol. 20, no. 3, Jun. 2023, ISSN: 17412552. DOI: 10.1088/1741-2552/ace07e.
- [4] S. N. Flesher *et al.*, “Intracortical microstimulation of human somatosensory cortex”, *Science Translational Medicine*, vol. 8, no. 361, Oct. 2016, ISSN: 1946-6234. DOI: 10.1126/scitranslmed.aaf8083.
- [5] E. Fernández, A. Alfaro, and P. González-López, “Toward Long-Term Communication With the Brain in the Blind by Intracortical Stimulation: Challenges and Future Prospects”, *Frontiers in Neuroscience*, vol. 14, no. August, Aug. 2020, ISSN: 1662-453X. DOI: 10.3389/fnins.2020.00681.
- [6] E. Musk, “An integrated brain-machine interface platform with thousands of channels”, *Journal of Medical Internet Research*, vol. 21, no. 10, Oct. 2019, ISSN: 14388871. DOI: 10.2196/16194.
- [7] T. Jung *et al.*, *Stable, chronic in-vivo recordings from a fully wireless subdural-contained 65,536-electrode brain-computer interface device*, May 2024. DOI: 10.1101/2024.05.17.594333.
- [8] Y. Liu *et al.*, “Bidirectional Bioelectronic Interfaces”, *IEEE solid state circuits magazine*, vol. 12, no. 2, pp. 30–46, 2020.
- [9] S. Drakopoulou, F. Varkevisser, L. Sohail, M. Aqamolaei, T. L. Costa, and G. D. Spyropoulos, “Hybrid neuroelectronics: towards a solution-centric way of thinking about complex problems in neurostimulation tools”, *Frontiers in Electronics*, vol. 4, Sep. 2023, ISSN: 2673-5857. DOI: 10.3389/felec.2023.1250655.
- [10] T. P. G. van Nunen, R. M. C. Mestrom, and H. J. Visser, “Wireless Power Transfer to Biomedical Implants Using a Class-E Inverter and a Class-DE Rectifier”, *IEEE Journal of Electromagnetics, RF and Microwaves in Medicine and Biology*, vol. 7, no. 3, pp. 202–209, Sep. 2023, ISSN: 2469-7249. DOI: 10.1109/JERM.2023.3267042.

- [11] I. International Committee on Electromagnetic Safety SCC, *IEEE Standard for Safety Levels with Respect to Human Exposure to Radio Frequency Electromagnetic Fields, 3 kHz to 300 GHz*, Piscataway, NJ, USA, Oct. 2005. DOI: 10.1109/IEEESTD.2006.99501.
- [12] D. R. Merrill, M. Bikson, and J. G. Jefferys, “Electrical stimulation of excitable tissue: design of efficacious and safe protocols”, *Journal of Neuroscience Methods*, vol. 141, no. 2, pp. 171–198, Feb. 2005, ISSN: 01650270. DOI: 10.1016/j.jneumeth.2004.10.020.
- [13] T. S. Davis *et al.*, “Spatial and temporal characteristics of V1 microstimulation during chronic implantation of a microelectrode array in a behaving macaque”, *Journal of Neural Engineering*, vol. 9, no. 6, p. 065 003, Dec. 2012, ISSN: 1741-2560. DOI: 10.1088/1741-2560/9/6/065003.
- [14] E. Noorsal, H. Xu, K. Sooksood, and M. Ortmanns, “Multichannel Microstimulating SoC”, in *Handbook of Biochips*, New York, NY: Springer New York, 2022, pp. 1285–1316. DOI: 10.1007/978-1-4614-3447-4_18.
- [15] S. K. Arfin and R. Sarpeshkar, “An Energy-Efficient, Adiabatic Electrode Stimulator With Inductive Energy Recycling and Feedback Current Regulation”, *IEEE Transactions on Biomedical Circuits and Systems*, vol. 6, no. 1, pp. 1–14, Feb. 2012, ISSN: 1932-4545. DOI: 10.1109/TBCAS.2011.2166072.
- [16] Z. Luo, M.-D. Ker, T.-Y. Yang, and W.-H. Cheng, “A Digitally Dynamic Power Supply Technique for 16-Channel 12 V-Tolerant Stimulator Realized in a 0.18- μ m 1.8-V/3.3-V Low-Voltage CMOS Process”, *IEEE Transactions on Biomedical Circuits and Systems*, vol. 11, no. 5, pp. 1087–1096, Oct. 2017, ISSN: 1932-4545. DOI: 10.1109/TBCAS.2017.2713122.
- [17] Z. Luo and M.-D. Ker, “A High-Voltage-Tolerant and Power-Efficient Stimulator With Adaptive Power Supply Realized in Low-Voltage CMOS Process for Implantable Biomedical Applications”, *IEEE Journal on Emerging and Selected Topics in Circuits and Systems*, vol. 8, no. 2, pp. 178–186, Jun. 2018, ISSN: 2156-3365. DOI: 10.1109/JETCAS.2018.2796381.
- [18] K. H. Nguyen *et al.*, “A Fully Integrated Dynamic-Voltage-Scaling Stimulator IC with Miniaturized Reconfigurable Supply Modulator and Channel Drivers for Cochlear Implants”, in *Proceedings of the Custom Integrated Circuits Conference*, Institute of Electrical and Electronics Engineers Inc., 2024, ISBN: 9798350394061. DOI: 10.1109/CICC60959.2024.10529043.
- [19] L. Yao, D. I. Made, and Y. Gao, “A 83% peak efficiency 1.65 V to 11.4V dynamic voltage scaling supply for electrical stimulation applications in standard 0.18 μ m CMOS process”, in *2016 IEEE Asian Solid-State Circuits Conference (A-SSCC)*, IEEE, Nov. 2016, pp. 205–208, ISBN: 978-1-5090-3699-8. DOI: 10.1109/ASSCC.2016.7844171.
- [20] I. Williams and T. G. Constandinou, “An Energy-Efficient, Dynamic Voltage Scaling Neural Stimulator for a Proprioceptive Prosthesis”, *IEEE Transactions on Biomedical Circuits and Systems*, vol. 7, no. 2, pp. 129–139, Apr. 2013, ISSN: 1932-4545. DOI: 10.1109/TBCAS.2013.2256906.

- [21] F. Varkevisser, W. A. Serdijn, and T. L. Costa, *Analysis of power losses and the efficacy of power minimization strategies in multichannel electrical stimulation systems*, arXiv: 2501.08025 [eess.SY], 2025. arXiv: 2501.08025 [eess.SY].
- [22] J. P. Uehlin *et al.*, “A Single-Chip Bidirectional Neural Interface with High-Voltage Stimulation and Adaptive Artifact Cancellation in Standard CMOS”, *IEEE Journal of Solid-State Circuits*, vol. 55, no. 7, pp. 1749–1761, Jul. 2020, ISSN: 1558173X. DOI: 10.1109/JSSC.2020.2991524.
- [23] W. Ahn, K.-H. Nguyen, H. Lee, K. S. Min, S. Ha, and M. Je, “An Energy-Efficient Stimulation System Based on Adaptive Dynamic Voltage Switching Control for Cochlear Implants”, *IEEE Transactions on Biomedical Circuits and Systems*, pp. 1–12, 2024, ISSN: 1932-4545. DOI: 10.1109/TBCAS.2024.3497585.
- [24] K. Eom *et al.*, “A Low-Stimulus-Scattering Pixel-Sharing Sub-Retinal Prosthesis SoC With Time-Based Photodiode Sensing and Per-Pixel Dynamic Voltage Scaling”, *IEEE Journal of Solid-State Circuits*, vol. 58, no. 11, pp. 2976–2989, Nov. 2023, ISSN: 1558173X. DOI: 10.1109/JSSC.2023.3305521.
- [25] K. H. Nguyen *et al.*, “A Neural Stimulator IC with Dynamic Voltage Scaling Supply and Energy Recycling for Cochlear Implant in Standard 180nm CMOS Process”, in *Proceedings - International SoC Design Conference 2023, ISOCC 2023*, Institute of Electrical and Electronics Engineers Inc., 2023, pp. 35–36, ISBN: 9798350327038. DOI: 10.1109/ISOCC59558.2023.10396171.
- [26] A. Rashidi, N. Yazdani, and A. M. Sodagar, “Fully implantable, multi-channel microstimulator with tracking supply ribbon, multi-output charge pump and energy recovery”, *IET Circuits, Devices & Systems*, vol. 15, no. 2, pp. 104–120, Mar. 2021, ISSN: 1751-858X. DOI: 10.1049/cds2.12007.
- [27] H.-S. Lee, K. Eom, and H.-M. Lee, “27.3 A 90.8%-Efficiency SIMO Resonant Regulating Rectifier Generating 3 Outputs in a Half Cycle with Distributed Multi-Phase Control for Wirelessly-Powered Implantable Devices”, in *2024 IEEE International Solid-State Circuits Conference ()*, IEEE, Feb. 2024, pp. 448–450, ISBN: 979-8-3503-0620-0. DOI: 10.1109/ISSCC49657.2024.10454403.
- [28] X. Zeng *et al.*, “A 12-V Single-Input Multiple-Independently Configurable-Output Dynamic Voltage Scaling Supply in Standard 0.18- μm CMOS for Electrical Stimulation Applications”, *IEEE Solid-State Circuits Letters*, vol. 5, pp. 33–36, 2022, ISSN: 2573-9603. DOI: 10.1109/LSSC.2022.3149570.
- [29] A. Urso, V. Giagka, M. van Dongen, and W. A. Serdijn, “An Ultra High-Frequency 8-Channel Neurostimulator Circuit With 68% Peak Power Efficiency”, *IEEE Transactions on Biomedical Circuits and Systems*, vol. 13, no. 5, pp. 882–892, Oct. 2019, ISSN: 1932-4545. DOI: 10.1109/TBCAS.2019.2920294.
- [30] H.-M. Lee, H. Park, and M. Ghovanloo, “A Power-Efficient Wireless System With Adaptive Supply Control for Deep Brain Stimulation”, *IEEE Journal of Solid-State Circuits*, vol. 48, no. 9, pp. 2203–2216, Sep. 2013, ISSN: 0018-9200. DOI: 10.1109/JSSC.2013.2266862.

- [31] C. Kim, S. Ha, J. Park, A. Akinin, P. P. Mercier, and G. Cauwenberghs, "A 144-MHz Fully Integrated Resonant Regulating Rectifier With Hybrid Pulse Modulation for mm-Sized Implants", *IEEE Journal of Solid-State Circuits*, vol. 52, no. 11, pp. 3043–3055, Nov. 2017, ISSN: 0018-9200. DOI: 10.1109/JSSC.2017.2734901.
- [32] T. Lu, Z.-Y. Chang, J. Jiang, K. Makinwa, and S. Du, "A 13.56MHz Fully Integrated 91.8% Efficiency Single-Stage Dual-Output Regulating Voltage Doubler for Biomedical Wireless Power Transfer", in *2023 IEEE Custom Integrated Circuits Conference (CICC)*, IEEE, Apr. 2023, pp. 1–2, ISBN: 979-8-3503-9948-6. DOI: 10.1109/CICC57935.2023.10121186.
- [33] X. Li, C. Y. Tsui, and W. H. Ki, "A 13.56 MHz Wireless Power Transfer System With Reconfigurable Resonant Regulating Rectifier and Wireless Power Control for Implantable Medical Devices", *IEEE Journal of Solid-State Circuits*, vol. 50, no. 4, pp. 978–989, Apr. 2015, ISSN: 00189200. DOI: 10.1109/JSSC.2014.2387832.
- [34] X. Chen, F. Wang, E. Fernandez, and P. R. Roelfsema, "Shape perception via a high-channel-count neuroprosthesis in monkey visual cortex", *Science*, vol. 370, no. 6521, pp. 1191–1196, 2020, ISSN: 10959203. DOI: 10.1126/science.abd7435.
- [35] Hai-Peng Wang, Zhi-Gong Wang, Xiao-Ying Lu, Zong-Hao Huang, and Yu-Xuan Zhou, "Design of a pulse-triggered four-channel functional electrical stimulator using complementary current source and time division multiplexing output method", in *2015 37th Annual International Conference of the IEEE Engineering in Medicine and Biology Society (EMBC)*, IEEE, Aug. 2015, pp. 1671–1674, ISBN: 978-1-4244-9271-8. DOI: 10.1109/EMBC.2015.7318697.
- [36] Yi-Kai Lo, Kuanfu Chen, P. Gad, and Wentai Liu, "A Fully-Integrated High-Compliance Voltage SoC for Epi-Retinal and Neural Prostheses", *IEEE Transactions on Biomedical Circuits and Systems*, vol. 7, no. 6, pp. 761–772, Dec. 2013, ISSN: 1932-4545. DOI: 10.1109/TBCAS.2013.2297695.
- [37] S. Kameda, Y. Hayashida, Y. Tanaka, D. Akita, and T. Yagi, "A multichannel current stimulator chip for spatiotemporal pattern stimulation of neural tissues", in *2014 36th Annual International Conference of the IEEE Engineering in Medicine and Biology Society*, IEEE, Aug. 2014, pp. 5011–5015, ISBN: 978-1-4244-7929-0. DOI: 10.1109/EMBC.2014.6944750.
- [38] M. Hasanuzzaman, B. G. Motlagh, F. Mounaim, A. Hassan, R. Raut, and M. Sawan, "Toward an Energy-Efficient High-Voltage Compliant Visual Intracortical Multichannel Stimulator", *IEEE Transactions on Very Large Scale Integration (VLSI) Systems*, vol. 26, no. 5, pp. 878–891, May 2018, ISSN: 1063-8210. DOI: 10.1109/TVLSI.2018.2794445.
- [39] D. Rozgic *et al.*, "A 0.338 cm³, Artifact-Free, 64-Contact Neuromodulation Platform for Simultaneous Stimulation and Sensing", *IEEE Transactions on Biomedical Circuits and Systems*, vol. 13, no. 1, pp. 1–1, 2018, ISSN: 1932-4545. DOI: 10.1109/TBCAS.2018.2889040.

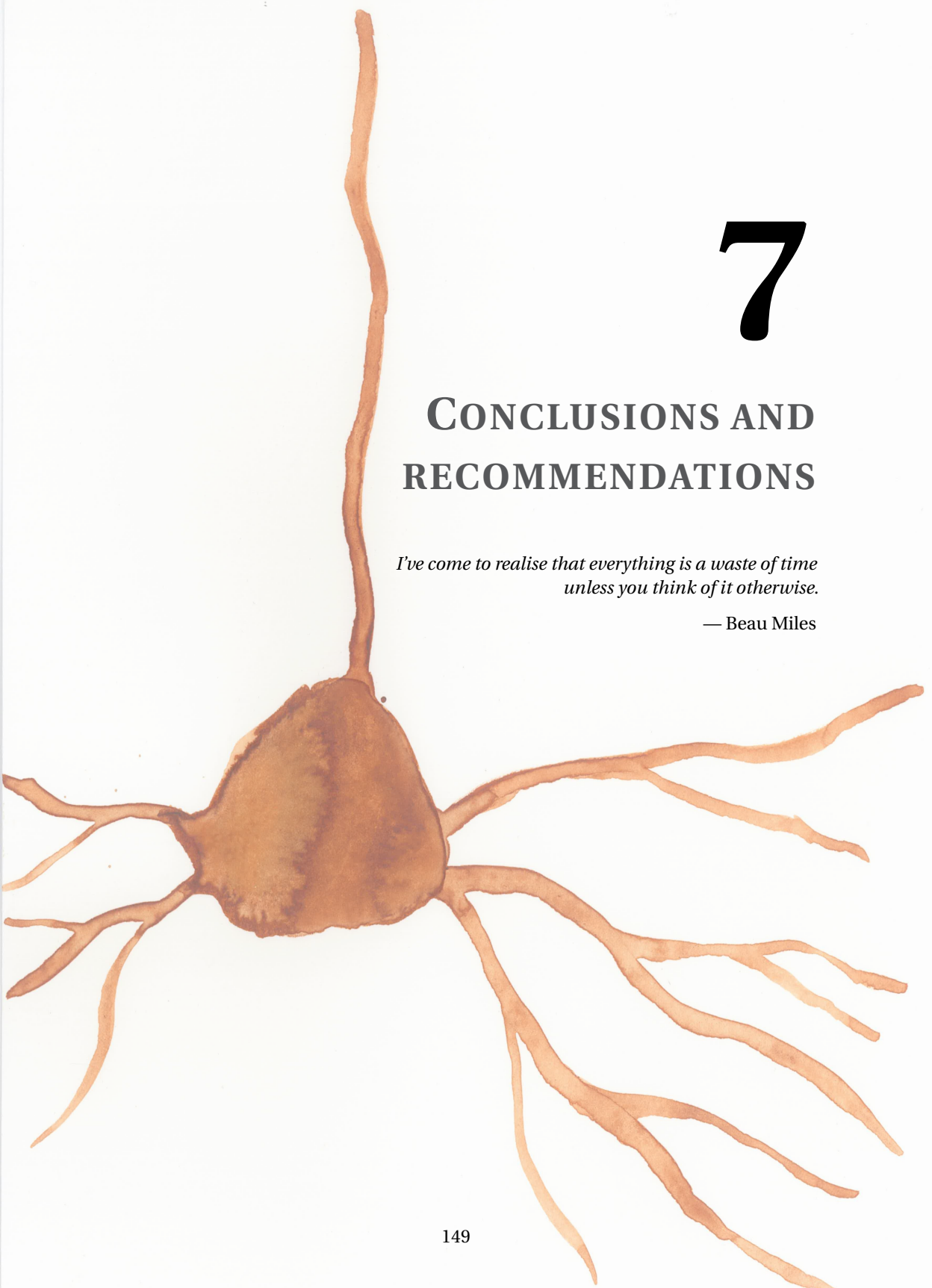
- [40] Y. Hayashida, S. Kameda, Y. Umehira, S. Ishikawa, and T. Yagi, "Multichannel stimulation module as a tool for animal studies on cortical neural prostheses", *Frontiers in Medical Technology*, vol. 4, Sep. 2022, ISSN: 2673-3129. DOI: 10.3389/fmedt.2022.927581.
- [41] W. Ahn *et al.*, "An Energy-Efficient, Scalable Neural Stimulation IC with Adaptive Dynamic Voltage Switching for Cochlear Implant System", in *2023 IEEE International Symposium on Circuits and Systems (ISCAS)*, IEEE, May 2023, pp. 1–5, ISBN: 978-1-6654-5109-3. DOI: 10.1109/ISCAS46773.2023.10181719.
- [42] K. Cui, X. Fan, and Y. Ma, "An Energy-Efficient Wireless Power Receiver With One-Step Adiabatic-Bipolar-Supply Generating for Implantable Electrical Stimulation Applications", *IEEE Transactions on Biomedical Circuits and Systems*, vol. 18, no. 5, pp. 1112–1122, Oct. 2024, ISSN: 1932-4545. DOI: 10.1109/TBCAS.2024.3379208.
- [43] Z. Luo, J. Liu, and H. Lee, "A 40.68-MHz Active Rectifier With Cycle-Based On-/Off-Delay Compensation for High-Current Biomedical Implants", *IEEE Journal of Solid-State Circuits*, vol. 58, no. 2, pp. 345–356, Feb. 2023, ISSN: 1558173X. DOI: 10.1109/JSSC.2022.3192523.
- [44] N. Almarri, D. Jiang, P. J. Langlois, M. Rahal, and A. Demosthenous, "High Efficiency Power Management Unit for Implantable Optical-Electrical Stimulators", *IEEE Open Journal of Circuits and Systems*, vol. 4, pp. 3–14, 2023, ISSN: 2644-1225. DOI: 10.1109/OJCAS.2023.3240644.
- [45] L. Cheng, W. H. Ki, Y. Lu, and T. S. Yim, "Adaptive On/Off Delay-Compensated Active Rectifiers for Wireless Power Transfer Systems", *IEEE Journal of Solid-State Circuits*, vol. 51, no. 3, pp. 712–723, Mar. 2016, ISSN: 00189200. DOI: 10.1109/JSSC.2016.2517119.
- [46] J. Ahn, H.-S. Lee, K. Eom, W. Jung, and H.-M. Lee, "A 93.5%-Efficiency 13.56-MHz-Bandwidth Optimal On/Off Tracking Active Rectifier with Fully Digital Feedback-Based Delay Control for Adaptive Efficiency Compensation", in *2023 IEEE Symposium on VLSI Technology and Circuits (VLSI Technology and Circuits)*, IEEE, Jun. 2023, pp. 1–2, ISBN: 978-4-86348-806-9. DOI: 10.23919/VLSITechnologyandCir57934.2023.10185395.
- [47] G. C. Martins and W. A. Serdijn, "An RF Energy Harvesting and Power Management Unit Operating Over -24 to +15 dBm Input Range", *IEEE Transactions on Circuits and Systems I: Regular Papers*, vol. 68, no. 3, pp. 1342–1353, Mar. 2021, ISSN: 1549-8328. DOI: 10.1109/TCSI.2020.3041175.

7

CONCLUSIONS AND RECOMMENDATIONS

*I've come to realise that everything is a waste of time
unless you think of it otherwise.*

— Beau Miles



EMERGING applications and technological advancements continue to drive the development of large-scale multichannel electrical stimulation systems. This thesis has focused on optimizing energy efficiency in such systems, addressing key challenges related to pulse shaping, inter-channel variability, and power distribution. The main research question — "*How can the energy distribution in large-scale multichannel electrical stimulation systems be optimized?*" — was addressed by deconstructing the energy flow in electrical stimulation and formulating sub-questions that corresponded to different stages of the system. Each of these sub-questions was explored in a dedicated chapter.

7.1. EFFICIENCY IMPROVEMENTS OF PULSE SHAPING

Chapter 4 examined the impact of pulse shaping on the energy efficiency of electrical stimulation, addressing the research question: *What is the most efficient stimulation waveform when both biophysical effects and circuit design losses are taken into account?*

7.1.1. SUMMARY OF SCIENTIFIC CONTRIBUTIONS

This chapter added a new multidisciplinary perspective to the literature on pulse shaping. Most importantly, the results challenge prior work in the field demonstrating that rectangular pulses have less drawbacks in terms of circuit design losses making them competitive with non-rectangular alternatives. These results suggest that rectangular pulses might be the best choice in practical stimulator implementations. Furthermore, a generalized framework was proposed to compare different pulse shapes based on their peak-amplitude ratios.

7.1.2. DETAILED CONCLUSIONS

While non-rectangular pulses are often proposed as more energy-efficient alternatives to conventional rectangular pulses, previous studies have primarily focused on biological losses while overlooking circuit inefficiencies. The aim of this chapter was to provide a comprehensive analysis of the losses in both the biological and electrical domains. The approach involved first computing biological losses using biophysically realistic computational models, followed by incorporating circuit losses based on different stimulation circuit implementations. Consistent with previous findings, non-rectangular pulses required less activation energy in the biological domain, with triangular, sine, and Gaussian pulses being the most efficient. However, when accounting for circuit losses under a non-ideal voltage supply, rectangular pulses emerged as the most efficient. In scenarios where a constant voltage supply was scaled to the peak of the pulse, non-rectangular pulses exhibited an activation energy increase of 14 % to 51 % compared to the most optimal rectangular pulse. This efficiency reduction was attributed to the increased peak current of non-rectangular pulses, whereas rectangular pulses resulted in the lowest peak amplitude. Additionally, the efficacy of voltage stepping for generating non-rectangular pulses was assessed, as this technique can reduce generation losses. It was found that using four or more voltage rails reduced the activation energy of some non-rectangular pulses sufficiently to surpass the efficiency of rectangular pulses. However, this analysis did not account for additional losses associated with generating and controlling multiple voltage rails. The study also examined efficiency variations due to the capacitive com-

ponent of the ETI. Efficiency was calculated for different ratios of the ETI's resistive and capacitive components, expressed as a time constant τ . Within a relevant range of τ for microstimulation electrodes, rectangular pulses remained the most efficient when generated from a constant voltage supply. Finally, a generalized framework was introduced to compare non-rectangular pulses with rectangular ones based on peak-amplitude ratios.

7.2. IMPACT OF CHANNEL VARIABILITY ON POWER EFFICIENCY

Chapter 5 assessed the impact of channel variability on power requirements in multichannel stimulation devices, addressing the research question: *What is the effect of channel variability on the power requirements and the efficacy of power management strategies in multichannel stimulation devices?*

7.2.1. SUMMARY OF SCIENTIFIC CONTRIBUTIONS

The chapter proposes a method to quantify power losses resulting from channel variability in multichannel stimulation systems. The method serves as a tool to evaluate the effectiveness of existing power management strategies and to benchmark emerging approaches. Additionally, it was applied to analyze the performance of various strategies across different applications using previously published experimental data. The analysis reveals that power management efficacy is application-dependent, highlighting the need for application-specific strategies.

7.2.2. DETAILED CONCLUSIONS

While variability-induced overhead losses are acknowledged in the literature, their quantitative impact and the efficacy of different voltage scaling strategies remain uncertain. This chapter introduced a method to quantify power losses using statistical data on electrode impedance and threshold amplitude for individual subjects. The proposed method was applied to previously published experimental data across four different applications: visual cortex stimulation (V1), retinal stimulation (Retina), peripheral nerve stimulation (PNS) and intrafascicular peripheral nerve stimulation (iPNS). The analysis assessed the efficacy of the global voltage scaling and stepped voltage scaling power management strategies. It was shown that the efficacy of scaling strategies varies across applications. Across applications, the stepped strategy using 8 voltage rails performed best, improving the efficiency by 43 % to 100 % compared to the fixed voltage supply. Especially in applications with high channel-counts and large inter-channel variation (V1 and iPNS), the stepped supply strategy performed well, while global scaling showed little efficiency improvement. However, in applications with fewer channels or minimal inter-channel variability (Retina and PNS), global scaling is still a viable option. For example, in the Retina dataset, global voltage scaling improved efficiency by 86 %. The proposed method serves as a tool for guiding design decisions when impedance and amplitude data are available from (pre)clinical trials. Moreover, the method can be extended to evaluate new power-management strategies against existing approaches.

7.3. POWER DISTRIBUTION IN MULTICHANNEL STIMULATOR SYSTEMS

Chapter 6 presented a novel power management strategy to address the question: *How can the required charge be efficiently delivered to multiple subsystems with independent output requirements?*

7.3.1. SUMMARY OF SCIENTIFIC CONTRIBUTIONS

A new power-management strategy is proposed, based on a regulating rectifier for channel-specific voltage regulation to reduce overhead losses. The circuit achieves high efficiency at the output over relevant conditions for intracortical visual prosthetics. Furthermore, the system is scalable and supports time-division multiplexing, making it well-suited for future large-scale neural interfaces.

7.3.2. DETAILED CONCLUSIONS

The results in Chapter 5 highlighted the necessity for high flexibility in large-scale multichannel applications with wide load conditions. In response, a novel power-management strategy was developed for an intracortical visual prosthesis. A stimulator output stage with a channel-specific regulating rectifier was designed, enabling automatic output voltage adjustments without compliance monitoring. The implemented circuit achieves an efficiency at the output >80 % across almost all tested load conditions. Moreover, using the methodology of Chapter 5, the performance was compared to other power-management strategies. On the available data for intracortical visual prostheses, the median efficiency at the output was 84 %, which is an improvement of 74 %, 17 %, and 6 % compared to the fixed supply and stepped supplies with four and eight rails, respectively. Furthermore, simulation results showed the fast adaptability of the circuit to changes in load conditions. This allows the output to be shared among multiple channels using time-division multiplexing. With typical stimulation parameters of a visual prosthesis, up to 12 channels could be shared by a single stimulation source based on this method. While the circuit demonstrates promising efficiency at the output, conduction losses in the rectifier impact the overall efficiency and require further optimization. Several potential improvements have been outlined in the chapter.

7.4. DISCUSSION

Together, the chapters highlight several important aspects of the energy efficiency in multichannel electrical stimulation. The contributions in this thesis may support the advancement of next-generation large-scale multichannel stimulator systems. A central observation is the interdependence of various factors, necessitating a holistic approach to system optimization. The analyses in Chapters 4 and 5 bring important perspectives in terms of power efficiency of pulse shaping and power management strategies. Chapter 4 has shown that the efficacy of pulse shaping is dependent on the voltage supply, and that in most practical cases, rectangular pulses outperform non-rectangular alternatives. Furthermore, it was also shown that the optimal pulse width for minimizing activation energy is shape-dependent, highlighting the importance of co-optimization of

the stimulation parameters considering both the desired physiological effects and the energy efficiency. In Chapter 5, it was shown that the efficacy of the power-management strategies is application-dependent and that the optimal strategy thus cannot be generalized. Additionally, circuit area and associated losses vary depending on implementation, making generalization difficult but essential to consider in system design. The proposed methodology can guide designers in the choice of the power management strategy and can be used to benchmark the performance of new power management implementations in multichannel systems. Finally, the power management strategy in Chapter 6 shows promising results for the efficiency at the output and scalability of the approach. Beyond efficiency considerations, the translation of stimulator systems into clinical devices requires compliance with safety and regulatory standards such as ISO 14708 (active implantable medical devices), IEC 60601 (electrical safety), and ISO 14971 (risk management). These frameworks impose design constraints including guaranteed charge balancing, single-fault protection, and demonstrated long-term reliability under accelerated aging. The introduction of non-standard stimulation waveforms and power management strategies may necessitate additional verification and validation steps. While these aspects were beyond the scope of this thesis, they represent critical considerations for eventual translation.

7.5. RECOMMENDATIONS FOR FUTURE WORK

The developments presented in this thesis open up new directions for future research. The following topics are recommended for further exploration.

SHORT-TERM DEVELOPMENTS:

- **Experimental validation of the results in Chapter 4.**
Experimental validation of the results in Chapter 4 would provide valuable insights into multiple aspects. It would be a useful contribution to the validation of the physiological benefits of non-rectangular pulses, could reveal practical limitations to the design of the dynamic voltage supplies capable of following non-rectangular pulses, and validate the conclusions on the effects of the ETI in practical electrodes.
- **Extending the analysis in Chapter 5 with advancements in stimulation applications.**
Technological advancements will lead to the use of different stimulation parameters and electrodes for the applications in the analysis. Furthermore, more data will become available for other applications as well. Incorporating these developments into the analysis can guide the research directions for power-management strategies and multichannel system designs.
- **Reducing conversion losses in the proposed design of Chapter 6.**
The circuit developed in Chapter 6 demonstrated high output efficiency and rapid adaptability to changing load conditions. However, its overall efficiency was not optimized. Several potential improvements are identified in this chapter, including optimizing the sizing of the rectifier switch M_p , applying offset compensation in the feedback loop, using pulse frequency modulation for low-current load conditions,

and implementing adaptive biasing in the comparator. These suggestions should be explored and validated to enhance total energy efficiency of the proposed design.

- **Investigating the impact of multiple parallel rectifiers from Chapter 6 on the WPT link.**

In the validation of Chapter 6, the input power was supplied from a signal generator. Given that each rectifier only delivers a low-power load, it was assumed that the loading effect on a WPT link would be negligible. However, if many rectifiers are operating in parallel, as is suggested for a large-scale implementation of the power-management strategy, the loading effect might alter the operation and efficacy of the circuit. Further studies should assess these effects to ensure robust system performance.

- **Evaluating the efficiency of the power-management strategy in Chapter 6 for non-rectangular pulses.**

The conclusions of Chapter 4 are based on the assumption of limited flexibility in the voltage supply. However, the circuit proposed in Chapter 6 demonstrated a high degree of adaptability to varying load conditions, including changes in current amplitude. This suggests that the new voltage regulation method might achieve high efficiency for non-rectangular pulses. However, in its current implementation, the circuit requires a settling period at the start of each pulse, particularly for low current amplitudes. Consequently, the most promising non-rectangular shapes (Gaussian, half-sine, and triangular) might require a long settling time due to their low-amplitude tails and result in low efficiency. Interestingly, this could result in alternative pulse shapes offering superior energy performance. Another approach would be to integrate pulse-shape considerations into the regulator circuit design. For example, in its current embodiment, the output voltage is always charged to its maximum when the output current is inactive. If the pulse begins at a low amplitude and thus requires a lower load voltage, circuit performance might be improved by discharging the output voltage during inactive phases.

- **Investigating perceptual changes in time-division multiplexing.**

From an engineering perspective, time-division multiplexing (TDM) offers an effective approach to enhancing the scalability of stimulator circuits. By enabling resource sharing, it reduces the overall system area while distributing power consumption over time, thereby lowering peak-power demands and reducing the load on the WPT link. Furthermore, TDM could reduce the cross-talk between channels, as the active channels could be separated further from each other with proper scheduling, given that fewer channels are active simultaneously. However, in prosthetic applications, the perception of the stimuli by the patient is one of the main concerns. Therefore, more research is needed to assess how TDM affects perception and to incorporate these findings into stimulator designs.

- **Exploring advanced methods for multichannel stimulation.**

Most multichannel electrical stimulation systems are based on a combination of predefined channels. One advancement on this uses current steering, where virtual channels are created by using ratios of currents through neighboring electrodes.

More recent developments in vector field shaping take this concept further, discarding individual channels in favor of shaping the overall electric field using all available electrodes. Using a pipeline of predicting the desired electric field and an optimizer for the required currents to achieve that field, complex stimulation patterns can be achieved, possibly reaching higher resolution and better use of the available resources. This method fundamentally changes the system driving the electrodes, raising new research questions regarding optimal resource allocation (current drivers, voltage regulators) and possible combinations of this paradigm with TDM. Although vector field shaping has not been part of this thesis, it relates closely to the research questions and aim of this work.

LONG-TERM CHALLENGES:

- **Biological validation of the stimulator proposed in Chapter 6.**

While the design has been electrically validated on ETI models and demonstrated the ability to track the voltage on electrodes as load, further validation of the circuit *in vivo* is required to show its usability in future applications.

- **Designing a large-scale multichannel system incorporating the power-management strategy from Chapter 6.**

Following validation and improvements as outlined in previous recommendations, the power-management strategy could be implemented in a large-scale multichannel system to advance the power efficiency and scalability of future applications.

- **Clinical translation and regulatory approval.**

Translation of the proposed supply strategy will require evaluation within the framework of medical device safety and regulatory standards (e.g., ISO 14708, IEC 60601, ISO 14971).

7.6. OUTLOOK

The idea of prosthetic vision dates back several decades. Yet, despite the long history, clinical results remain at an early stage. Present-day implants can elicit rudimentary percepts, but these are still far from restoring natural vision. This apparent paradox—an old field still in its infancy—reflects both the difficulty of the challenge and the determination of the research community. Still many different approaches (e.g., retinal, intracortical, and thalamic stimulation) are being explored, each with their own benefits and hypotheses. The breadth of this landscape is inspiring, and the community behind it even more so. Throughout this project, I have experienced the willingness of this niche field to share insights and help others across labs.

One major obstacle for progress is the enormous parametric space of neural interfaces. Electrode size and placement, waveform characteristics, current steering strategies, and system-level architectures all interact in ways that are difficult to explore through trial and error. At the same time, patient-specific variability adds another layer of complexity. Advances in computational modeling and artificial intelligence will be crucial for systematically exploring this landscape and identifying designs that achieve both efficacy and efficiency.

Underlying these technological efforts is the broader challenge of interfacing with the brain, arguably the most complex organ we know. Here, the guiding principle should be to develop technology that aligns with biological function, which requires strong interdisciplinary collaborations. System-level decisions are often driven less by theoretical efficiency and more by clinical demands for reliability and safety. Indeed, conventional approaches may appear inefficient, but they have the advantage of being proven and accepted. Advanced techniques such as adaptive supply scaling, as proposed in this thesis, will only reach patients if they can also demonstrate compliance with safety standards, reliability under long-term use, and robustness to failure.

Another reality is that stimulation parameters are typically chosen for efficacy rather than efficiency. While models such as those in Chapter 4 have well-defined thresholds that can be tuned for minimal energy use, in a clinical setting thresholds are stochastic and subject to adaptation. As a result, supra-threshold pulses are typically used to maximize the probability of eliciting a percept in clinical trials. This inherently leads to non-optimal energy use. Collaborative research across engineering, neuroscience, and clinical practice will be required to better understand these relationships and move towards parameter choices that balance efficacy and efficiency. In this context, the contributions of this thesis provide multidisciplinary insights and offer a framework for designing the next generation of neural implants.

Future interfaces will increasingly incorporate bidirectional capabilities and closed-loop control. Recording and stimulation combined can enable real-time optimization of parameters, adapt to patient variability, and reduce reliance on supra-threshold operation. Large-scale cortical interfaces, such as those explored in ongoing human trials, remain at a very early stage. Present demonstrations of multi-phosphene patterns show that meaningful images can be evoked, but the percepts remain coarse and rudimentary. Moving beyond the notion of artificial vision as a combination of individual phosphenes requires holistic approaches that consider the emergent properties of cortical networks. Neural network models and artificial intelligence will be instrumental in developing such approaches to connect the dots between stimulation and perception. In parallel with academic and clinical efforts, commercial initiatives are playing a major role in accelerating development. Companies such as Neuralink, Synchron, and Cortigent are investing heavily in large-scale interfaces, pushing rapid advances in hardware integration, surgical approaches, and long-term validation.

Neurotechnology stands at a remarkable point in history. The coming decades will fundamentally change how humans can interact with and augment the brain. The outlook for cortical prosthetics and brain-machine interfaces is uncertain, but continued multidisciplinary efforts are steadily pushing the field forward. With the combined progress of engineering innovation, clinical insight, and computational intelligence, the step from rudimentary percepts to meaningful restoration of function may be closer than it appears today.

ACKNOWLEDGEMENTS

If you're lonely you're far from alone.

— Saba

At times, the PhD journey can feel lonely. However, I have been fortunate to share this adventure with many people around me, and I am forever grateful for the support, guidance, and encouragement I received.

First of all, I want to thank my promotors **Wouter** and **Tiago** for the opportunity to be part of the INTENSE project and for the guidance throughout the years.

Wouter, thank you for inspiring me from my first year in Delft and onward. I remember following your lectures in Linear Circuits in my first year, connecting with you through the ETV, and finally ending up under your supervision in the Bioelectronics section (for quite some time). Thank you for fostering the amazing social environment in our group, for listening and for your open mindset to many things in life. You know how to find something positive in almost everything, and you radiate this positivity to many people around you. On the other hand, I feel acknowledged and appreciated when you come to me for advice on any matter. I cherish the memories of the BioCAS conferences in Taiwan and Canada that we visited together, especially for the social parts of these trips. I also appreciate (and admire) that you keep the BE stairs challenge alive.

Thank you **Tiago**, for showing me what it truly means to push yourself to the limit, both mentally and physically. I enjoy our shared passion for cycling a lot, from trying your limits on Harry Slinger to discussing new bike upgrades and making crazy cycling plans. You have drawn me to the dark side of ultra cycling and I am very thankful for that. As I wrote in my propositions, I see many similarities to doing a PhD and also there you've been a great source of inspiration for being ambitious and for encouraging me to believe in myself.

I would like to thank all the committee members: **Prof. Frijns, Prof. French, Prof. Constandinou, Prof. Degenaar, and Dr. Ghoreishizadeh**, for accepting to be part of the promotion committee and for the valuable feedback to this thesis.

Personally, I get highly motivated and energized from working with others. I want to thank all the students that I had the honour of supervising over the years **Niels, Remco, Inés, Fabio, Ariana, Erwin, Robin, Bram, Olivier**, my co-authors **Amin, Konstantina, Vasso, Masoumeh, George, Linta, and Sofia**. I enjoyed working together with you all, and you have been a spark to many new ideas. I am also thankful for the interactions within the INTENSE project and at conferences such as The Brain and the Chip, the Dutch BME Conference, and BioCAS. The community behind neural interfaces has been a constant source of inspiration and motivation throughout this journey.

Next, I would like to thank my paranymphs **Chris and Stefan** for the support in organizing this important milestone. With you in the team, I am sure that I don't have to worry about a good party. **Chris**, within your first week in Delft, we had already planned our first concert together. Our shared passion for music has brought us to many nice places and concerts. We have shared a lot of good memories, concerts, karaoke nights, jazz sessions, band practices, occasional nights at the kurk, Oude Jan or Schouw and, of course, long nights on your balcony. I love how easy you connect with people and your passion for many things: Music, (Italian) food, and above all Scotland. Thank you for everything. **Stefan**, I feel like we have grown through so many different eras together. Starting at the middenberm, we went on many skate trips, enjoyed some good parties together and then grew into the 'burger' life sharing many dinners, walks, ijsjes at the Lelie and many other things together with **Demi and Lucia**. Who would have thought we would both end up doing (and finishing) a PhD? Thank you for listening to me talk about the struggles of my PhD even though you had no idea what I was talking about most of the time. Thanks for the fun times together, for always showing up after I send a picture from the karaoke bar, but also for the support and serious talks in difficult times.

I also want to thank all my colleagues at the Bioelectronics section. Of course, my officemate **Bakr**, thank you for being a dear friend, for listening to me complain about my problems and trusting me with yours. I deeply value our open communication. Even though our life perspectives are so different, I've always felt that we are able to discuss difficult topics in a very respectful way. For me, this certainly has opened my eyes more than once, and I hope the same is true for you. Take good care of Shaggy when I'm gone, and never forget that her growth is the sign of prosperity in our office. Thank you **Hassan** and **Ghandi** for sharing the load of being Tiago's first students. Although I didn't do anything with ultrasound, I feel we have shared a big part of this journey together. For me, it was very convenient that you both started before me, so that you could lead me through the bureaucratic processes. **Hassan**, thank you for your guidance and patience during tape-out. Your ability to stay calm (on the outside) under stress is impressive. **Gandhi**, thank you for acting like an old man. Not only does it make you limp every other week, it also makes you say some very wise words (sometimes). **Brian**, it still feels funny to call you a colleague. Starting our masters writing an essay about TMS together and ending up in the BE section. Next to joining many of the party plans with Chris, you are always up for any kind of sport. I have enjoyed the many games of spikeball, volleyball, padel, ping-pong, and stress ball, and I hope to beat you many more times. **Ronald**, next to being incredibly awkward at times, you are also incredibly smart and you never fail to amaze me in both of these. I have enjoyed our times as roommates and our discussions about work, music, and life in general. Please try to negotiate better conditions for yourself in the stupid bets you make with friends, or even better, try to make bets that you can actually win. **Maria**, I remember being part of Achilleas' random BE interview session and being impressed by your perspective on life. In many ways you are naïve, but this brings you a lot of good things (it even gets you into doing a PhD). Thank you for the many cafecito walks, for making me enjoy papallonas at 7 a.m., and for being a listening ear. **Samuel**, thank you for always being up for the most random last-minute plans. Starting from joining our new years eve party after you just started in our group, I know I can always count on you. **Bea**, tta, thank you for providing us with high-quality stickers, memes, and

dance moves. They have been proven very useful over the years. **Diogo**, your Portuguese pessimism can sometimes be a burden, for example when I try to let you sleep on my couch instead of on a bench in the train station, but you are a good guy. I love your enthusiasm for stupid ideas and self-irony. I hope your big startup dream one day comes true, just so you can make the joke in your ads. Also, keep playing the bass. One day we will play your Tom Jones song. **Limitha**, kiddo, it is dangerous to start a conversation with you because it will never last less than an hour or two. You are a great person and I wish you can learn to acknowledge that and appreciate yourself and your work. Until then, I will always be there to listen to all the drama or to give you a big hug. I hope you find your prince on a white horse one day, even if he is Dutch. **Christos**, thank you for your Greek courtesy of never refusing 'one last beer' in the oude Jan. As a result of that, we still have one big promise to deliver in Athens this year, and I am sure it will be an amazing adventure. To the Berlin team: **Andra, Raphael, and Konstantina**. It's sad that we shared so much time apart. I enjoyed every time we met, the week of BioEl brought so many good memories, and I was always looking forward to your visits in Delft. **Vasso**, thank you for your enthusiasm and encouragement. I am very grateful for your guidance and I am sorry if I scared your students with my (pessimistic) advice. Finally, thank you **Kellen** for your enthusiasm and organizing so many social activities in the group. Of course, you had an amazing party planning committee with an even more amazing advisor to help you, but you are really bringing a lot of people together. I am still waiting for the day we get to taste the famous cupcake vodka on your birthday.

Of course, this list could go on and on. I want to thank all the other members of the BE section. In particular, **Masoumeh, Ignasi, Chris, Niloufar, Dario, Johan, Suman, Achilles, Dante, Frans, Leon, Tarique, Arash, Kimia, Yihan, Stefania, Mustafeez, Liwen, Hoda, Xiao, Tao, Chenyan, Eshani, Joshua, David, Zeyao, Peng, Nasim, Anna, Ronaldo, Gustavo, Sampi, Kambiz, and Alessandro**. And our amazing adoption colleagues, **Paul, Milica, Hande and Shriya**.

Also outside the university I am blessed with a group of very special people, that have helped me mostly to distract me from work when that was very much needed.

Ben and Hidde, living together at the BWS was an amazing time. Movie nights on the couch, with me and Hidde sleeping after five minutes, something that will forever be incomprehensible (and annoying) to Ben. The boardgames, random house challenges, our long discussions about pretty much everything and nothing, and just the good vibes we created at home. I cherish our friendship and you will always be special to me.

Tim, I think our lives couldn't be more different when we met, but somehow they crossed and I'm grateful for that. What started with krokante-kipschnitzel-wraps at the Röntgenweg grew into a special friendship. I'm always amazed by your ability to make everything you touch look great and I hope to share many more cool projects and memories together.

Yoshi, thank you for the most random plans and parties, which always turn out to be great. Your knowledge and self-confidence about the most random topics never fails to amaze me.

Alex, lexie, thank you for taking care of me (us) on sliptrips, binkie adventures, cycling trips, or any other occasion. With papa Alex in your team, you can be certain that everything will be alright. Jane will have nothing to worry about.

Also a big thank you to the rest of the NGG — **Demi, Stefan, Wouter, Yanni, Bender, Gijs, Chris, Willemijn, Dion, Gwen, Karin, Lucia, Puck, Simon, Timo, Tristan** — for the many good memories, boardgame nights, dinners, parties, skate trips and all the other (nerdy) stuff. Special thanks to the binkies for making me suffer on our amazing adventures together.

I want to thank all the cycling friends I met on the road: **Filipe, Nicolas, Gemma, and Paula**. Sharing some suffering kilometers on the bike is a great way to get very close very quickly. I'm grateful our routes passed each other and I hope to share many more kilometers with all of you.

To my other sport friends at AV40 — **Odilia, Martijn, Bernard, Sára, Niels, David, Tanno, Florian, Honorata**, and many more — thank you for pulling me through the trainings with nice conversations and for motivating me with some healthy competition at times.

Thank you to the NeuroTechHub team, **Antonio, Patricija, Stijn and Samantha**, I am so proud of us to make this happen. The nights of dreaming and visioning (with the help of vermut) are invaluable to me. No matter where we will get with the NTH, I am super proud of our team and friendship, and I am happy to share this journey together.

Merlin, It's sad that you moved away, but I think it is better for your own health (and mine) to be far away from the Hanno. I always feel very welcome in your (and **Miguel's**) place, thank you for that. I miss you and I hope we keep finding excuses to visit each other.

Dennis, we have shared so many hobbies over the years (trumpet, skating, swimming, triathlon, bikepacking). I love how we can motivate each other for trying new things, pushing ourselves and sometimes also reminding the other to relax a little bit more. I am sure we will share many more bike adventures (or any other hobby we still don't know) and eat a lot of suikerwafels and pain au chocolat (or maybe pain aux raisins...) to keep us energized.

Demi, for the majority of my PhD (and for all my time in Delft), you were the most important person in my life. I can say with certainty that without your encouragement, distraction, and relativisation, this thesis would not be finished by now. I am sorry that we go our own ways now, but I want you to know that you are an amazing person, and that you will always have a special place in my heart.

Finally, thank you **Luc, Philip, Roel, and Declan**, for the nice dinners catching up on all of our lives, **Florine** for the videocalls, **Lisa** for our shared writing sessions and deep talks, and **Cathelijan** for the fun at parties and long conversations.

Of course, I realize this list is far from complete, and there is no way to thank everyone. I am sorry if I forgot you, but remember that friendship is much more than a couple of words at the end of a thesis.

Above all, my greatest gratitude goes to my family. Mam, Pap, and N ria, thank you for your love and support, and for shaping me into the person I am today.

*Bij nader inzien, altijd achteraf.
Hadden we alle tijd, vergaten alle tijd.*

— Spinvis

CURRICULUM VITÆ

Francesc VARKEVISSER

11-03-1996 Born in Leiden, The Netherlands.

EDUCATION

2014–2018 Bachelor's degree in Electrical Engineering
Delft University of Technology, The Netherlands

2018–2020 Master's Degree in Microelectronics
Specialization in Bioelectronics
Delft University of Technology, The Netherlands

2021–2025 Ph.D. degree in Bioelectronics
Delft University of Technology, The Netherlands
Thesis: Energy efficiency optimization in large-scale
multichannel electrical neuromodulation

Promotor: Prof. dr. Wouter A. Serdijn

Copromotor: Dr. Tiago L. Costa

LIST OF PUBLICATIONS

JOURNAL ARTICLES

2. S. Drakopoulou, **F. Varkevisser**, L. Sohail, M. Aqamolaie, T. L. Costa, and G. D. Spyropoulos, "*Hybrid neuroelectronics: towards a solution-centric way of thinking about complex problems in neurostimulation tools*," *Frontiers in Electronics*, vol. 4, Sep. 2023.
1. **F. Varkevisser**, T. L. Costa, and W. A. Serdijn, "*Energy efficiency of pulse shaping in electrical stimulation: the interdependence of biophysical effects and circuit design losses*," *Biomedical Physics & Engineering Express*, vol. 8, no. 6, p. 065009, Nov. 2022.

CONFERENCE PAPERS

3. **F. Varkevisser**, T. L. Costa and W. A. Serdijn, "*Multichannel current-mode stimulator with channel-specific regulated power supply*," 2023 IEEE Biomedical Circuits and Systems Conference (BioCAS), Toronto, ON, Canada, 2023, pp. 1-5.
2. K. Kolovou-Kouri, A. Rashidi, **F. Varkevisser**, W. A. Serdijn and V. Giagka, "*Energy Savings of Multi-Channel Neurostimulators with Non-Rectangular Current-Mode Stimuli Using Multiple Supply Rails*," 2022 44th Annual International Conference of the IEEE Engineering in Medicine & Biology Society (EMBC), Glasgow, Scotland, United Kingdom, 2022, pp. 3443-3446
1. **F. Varkevisser**, A. Rashidi, T. L. Costa, V. Giagka and W. A. Serdijn, "*Pre-Filtering of Stimuli for Improved Energy Efficiency in Electrical Neural Stimulation*," 2022 IEEE Biomedical Circuits and Systems Conference (BioCAS), Taipei, Taiwan, 2022, pp. 312-316.

